State-dependent disordered potential for studies of Anderson transition with ultracold atoms

Musawwadah Mukhtar

To cite this version:

Musawwadah Mukhtar. State-dependent disordered potential for studies of Anderson transition with ultracold atoms. Optics [physics.optics]. Université Paris Saclay (COmUE), 2019. English. NNT : 2019SACLO001 . tel-02068720

HAL Id: tel-02068720
https://pastel.hal.science/tel-02068720

Submitted on 15 Mar 2019

université
PARIS-SACLAY

NNT: 2019SALCO001

Thèse de doctorat

INSTITUT
d'OPTIQUE
GRADUATE SCHOOL
ParisTech

State-dependent disordered potential for studies of Anderson transition with ultracold atoms

Thèse de doctorat de l'Université Paris-Saclay
préparée à l'Institut d'Optique Graduate School

École doctorale n° 572
Ondes et Matière (EDOM)

Thèse soutenue à Palaiseau, le 11 février 2019, par

Musawwadah Mukhtar

Composition du jury:

M. Fabien BRETENAKER	Président	Université Paris-Sud (LAC)
M. Guillaume LABEYRIE	Rapporteur	Institut Non Linéaire de Nice
M. Pascal SZRIFTGISER	Rapporteur	Université de Lille (LPhLAM)
Mme Juliette BILLY	Examinatrice	Université Toulouse III
M. Vincent JOSSE	Directeur de thèse	Institut d'Optique Graduate School (LCF)

Remerciement

> All accomplishments in my life, including this PhD work, are due to God's favor. I recognize my own shortcomings. To overcome my self-doubt, I have countlessly recited Moses' prayer (pbuh)[1]: "O my Lord! Open for me my chest [2], and ease my task for me, and loose the knot from my tongue[3], so they understand my speech".

When I firstly came to France on June 2009, I could only speak few words in french but I was very excited to learn a new language and a whole new culture. I stayed for one month, then another month in the same year, two years at Ecole polytechnique, and finally three years for my PhD!

These three years have been invaluable experience. I would like firstly thank my PhD advisor, Vincent Josse, who had accepted me to work in his team. I'd like to thank him for the opportunity, guidance for my research,his patience, and countless suggestions. In particular, his thorough remarks for my writings and presentations.

I also feel honored to have Fabien Bretenaker as the president of the jury of my PhD defense. Also, I'd like to thank Guillaume Labeyrie, Pascal Szriftgiser, and Juliette Billy for accepting being members of the jury. I am extremely happy that the defense was a good show.

It is also a great honor to make acquaintance with Amazing Alain Aspect. I firstly saw him during his public colloquium in Singapore on December 2008. I and my friends were looking for idea for our first research experience. Alain's presentation was inspirational and remarkable. In the following year, we started pursuing projects related to quantum control and decoherence till my departure to Ecole polytechnique. Somehow, I had him later on as my quantum optics professor. Hence, I would like also thank him for his teachings and advices .... since 2011!

Intellectually, this thesis work has been the craziest adventure I ever have! I'd like to express my gratitude to all my teammates. First, Valentin V., who was a great mentor to me ... and inspired me to learn German. Unfortunately, I only benefited his mastery for one semester. Secondly, Vincent D., who taught me the most about the experiment, and with whom I shared a lot of glorious and tough moments. He is excellent not only in physics, but also in drawing. Third, Baptiste L., joined

---

[1] QS Ṭāhā(20): 25-28

[2] grant me self-confidence, contentement, and boldness

[3] remove the incorrectness from my speech

me in the last year. He learns fast and hopefully I have done a decent job transferring my skills. Fourth, Adrien, who were also great friend and mentor. I wished he arrive earlier, I believed he could be a good role model for many PhD students. I wish the best luck for Baptiste, Adrien, and Vasiliki (who joined us recently).

Througout the journey, I have benefited a lot from discussions with my colleagues in the atom optics group. I'd like to mention here, the permanent researchers (Denis B., Marc C., Christophe W., Thomas B., Isabelle B., David C., Laurent S.-P.), other members of "Le bureau du swag" (Anaïs, Clémence, Ziyad), "nearest neighbors" (Pierre, Steven, Maxime, Amaudric, Guillaume, Alessandro), "next nearest neighbors" (Aisling, Max, Cécile Ca., Hugo, Quentin, Rockson, Marco, Antoine, Lorenzo), and "long-range neighbors" (Cécile Cr., Hepeng, Julien). I also had pleasure collaborating with Michael Pasek and Dominique Delande for the spectral function project.

The research group is part of a larger ecosystem, the *Laboratoire Charles Fabry.* I wish the best to Patrick Georges as the head, the researchers, the *thésards*, and the post-docds. In particular, I'd like to thank the personnels with whom I have the opportunity to teach, François Marquier (*Electromagnétisme*, c'était super bien organisé!), Hervé Sauer (*Calcul scientifique avec MATLAB* & *Projet MATLAB*, j'apprecie beaucoup ses attentions aux détails), Charles Bourassin (*Calcul scientifique avec MATLAB*), Rosa Toualle-Brouri (*Mécanique Quantique*), Nathalie Westbrook (*Polarisation optique*), Mathieu Boffety (*Polarisation optique* & *Projet MATLAB*). It was great opportunity to hone my pedagogy.

I'd like also to thank for assistance from the electronics workshop (especially Fréderic Moron for his kind helps, and also André V.), mechanical workshop (Jean-Réné, André G., Patrick R.), technical service (Nicolas and Jean-Luc), Service d'achat (Ghislaine C. Nicole E.-M., Abdelaziz A.), and service médiathèque (Marie-Laure E.).

My doctoral experience is also enriched with my participation in the board of the EDOM graduate school (*Conseil d'EDOM*) and my contribution as treasurer to conference Rencontres des jeune physicien • ne • s (RJP 2017); both are inspired by Pierre. I'd like to thank the head of EDOM Jean-Jacques Greffet and other members for such wonderful opportunity. For the conference, it was full of fun and we fortunately had enough fund. Hence, I'd like to acknowledge the co-organisers: Louis d'E., Raphaël A., SFP (Pierre-François Cohadon and Samuel Guibal), Audrey, Pascal N., Marion, Lucile, Elena, Simon, Dmitri, Bruno, & Clément.

Also best wishes to my friends at Ecole polytechnique, who were in binet X-AMEP (Mouad M., Omar S., Youssouf M., Mohamed Boul., and Mohamed Benz.), Hassan B., Ahmat T., and Adama M.

Looking back in 2005, the *annus mirabilis*, from being student in multiple difficulties, to being part of physics school team (from rank 6th), to enter the national team for physics olympiad, and to dream of being a Doctor in physics, I have to mention these three amazing persons: my physics teacher Iding Sirojudin (thank you for being wonderful teacher, for helping me with my financial difficulty, and for providing me the emotional support), the school principal Mr. Djumadi (I'd like to express my gratitude for his emotional support and his encouragement for pursuing studies abroad till PhD, may God grant him paradise), and Prof. Yohanes Surya (thank you for months of rigorous training in physics, the opportunity making friends with gifted and highly-driven students from all over Indonesia, and other opportunities during and after the olympiad).

In addition to my family (my parents and my siblings), I have discovered new families in this country. I'd like to express my gratitudes to Mohamed D. (and family), Abdelaziz S. (and family), Chiheb, Mohamed M., and many more! I can't forget the moments Mohamed D. brought couscous to cheer me up; Khadija, his spouse, is an excellent cook. During holiday with his family and other families, I also get to learn how to handle kids. And what can be more entertaining than being surrounded by my adorable nieces and nephews–*qu'ils deviennent sages*! I would like also thank friends who make effort to attend my PhD defense, Anis C., Mohamed N., Yazid, and Zakaria. I am determined to stay for many more years in this country.

Résumé

Abstract Dans ce manuscrit, nous présentons notre avancement pour réaliser une méthode spectroscopique pour étudier la transition d'Anderson avec des atomes froids. Cela repose sur la réalisation d'un potentiel désordonné sélectif en état de spin, le désordre n'étant significatif que pour l'un des deux états de spin impliqués. En combinant cela avec la technique de transfert par radiofréquence d'un état insensible au désordre à un état exclusivement sensible au désordre, il devient possible de charger une onde de matière dans le désordre dans des états d'énergie bien définies. Pour prouver le concept, nous avons effectué des mesures des fonctions spectrales d'atomes ultrafroids dans des potentiels désordonnés, qui sont directement proportionnels au taux de transfert des atomes. Nous présentons les résultats en montrant un excellent accord avec les calculs numériques. Cela a ouvert des perspectives pour d'autres études sur la transition d'Anderson. En particulier, nous cherchons à observer la transition entre les états diffusifs et les états localisés séparés par une énergie critique, appelée le seuil de mobilité. Une telle étude nécessite la réalisation d'un désordre sélectif en état de spin qui permet un long temps de propagation dans le désordre afin de distinguer les deux phases. À cette fin, nous présentons un nouveau schéma du désordre sélectif en état de spin avec deux lasers du *speckle* (*speckle bichromatique*). Cela ouvre la voie à une approche spectroscopique de la transition d'Anderson avec des atomes froids avec une résolution en énergie bien supérieure à celles des expériences précédentes.

Ce manuscrit se décompose en sept chapitres. Le premier chapitre introduit le contexte scientifique autour des études sur la localisation d'Anderson notamment avec des atomes froids. On se focalise ensuite sur le système à 3D où une transition de phase existe, dite la transition d'Anderson. Cette transition de phase admet une énergie critique appelée seuil de mobilité qui sépare les états diffusifs et les états localisés. Pour introduire le contexte de cette thèse, nous rappelons trois expériences qui donnent une estimation du seuil de mobilité et nous soulignons le problème de la résolution en énergie dans ces expériences ainsi que le rôle de la fonction spectrale dans leur analyse.

Dans le chapitre 2, nous effectuons un rappel sur la physique de la localisation d'Anderson en commençant par la description de la propagation des ondes dans un milieu désordonné. Elle permet d'introduire le concept de localisation faible et de localisation d'Anderson. Nous relions ces concepts à quelques expériences notamment avec des atomes froids telles que la mesure du temps élastique

de diffusion, l'observation du pic de rétro-diffusion cohérente, les observations de la localisation d'Anderson à 3D et l'estimation du seuil de mobilité. Dans la dernière section du chapitre, nous nous focalisons sur l'enjeu actuel de la mesure du seuil de mobilité. Nous nous appuyons sur un travail récent qui compare le résultat numérique avec trois résultats expérimentaux ; nous allons ensuite remarquer quelques désaccords entre ces résultats. Nous discutons aussi l'utilisation de la fonction spectrale pour estimer le seuil de mobilité. Nous remarquons aussi que la fonction spectrale a été obtenue à partir des travaux numériques exigeants sans validation de la mesure expérimentale. Il est donc désirable d'effectuer une mesure fiable de la fonction spectrale.

Dans le chapitre 3, nous présentons la réalisation d'ondes de matière avec le condensat de Bose-Einstein (BEC) d'atomes de rubidium-87. Le nuage atomique final contient typiquement 10^5 atomes avec température de 5 nK. On peut donc le considérer comme une onde quasi-plane. Le dispositif expérimental comprend le ralentisseur Zeeman, le piège magnéto-optique, le piège magnétique, l'évaporation radio-fréquence, le transport dans une pince optique, le piège dipolaire (croisé), et la lévitation magnétique.

La lévitation magnétique joue un rôle critique dans notre expérience. Elle permet notamment de compenser l'effet gravitationnel ce qui rend possible le temps d'observation de plusieurs secondes. Elle impose ainsi le choix des états de spin ; ce sont des états d'horloge $|1\rangle \equiv |F = 1, m_F = -1\rangle$ et $|2\rangle \equiv |F = 2, m_F = 1\rangle$. Par ailleurs, pour un biais magnétique «magique», $B_0^\star = 3.229$ G, ces deux états possèdent la même susceptibilité magnétique ; l'énergie de transition entre ces deux états devient quasiment insensible à la variation du champ magnétique.

Le couplage entre les deux états d'horloge est réalisé avec un transfert radio-fréquence basé sur le mécanisme de la transition à deux photons. Avec cette technique, nous réalisons également une méthode spectroscopique qui nous sert ensuite pour introduire l'onde de matière dans le désordre avec des états d'énergie bien définies.

Ensuite, le chapitre 4 est consacré à la réalisation du désordre à partir du champ de tavelures optique (en anglais *speckle*). Nous commençons par un rappel sur le *speckle* : l'extension de la tache du *speckle*, les longueurs de corrélation et la statistique de l'intensité. Puis, nous présentons la mise en œuvre du *speckle* : le montage expérimental et la caractérisation par les mesures des corrélations spatiales. Ces dernières montrent un caractère anisotrope du désordre et nous en déduisons l'énergie de corrélation associée (notée E_σ).

Dans ce même chapitre, nous présentons aussi la réalisation du désordre sélectif en état de spin. Avec la fréquence de laser quasi-résonant par rapport à la transition de l'état $|2\rangle$, le potentiel dipolaire géneré sur l'état $|2\rangle$ est beaucoup plus significatif que celui sur l'état $|1\rangle$. Ce dernier est devenu négligeable. Puis nous identifions le paramètre V_R associé à la moyenne du potentiel désordonné généré sur l'état $|2\rangle$. En jouant sur le désaccord par rapport à la transition de l'état $|2\rangle$, nous pouvons réaliser un désordre attractive ($V_R < 0$) ou répulsive ($V_R > 0$). Et en jouant sur l'intensité du laser, nous contrôlons l'amplitude du désordre.

Dans le chapitre 5, nous présentons notre travail sur les mesures de fonctions spectrales d'atomes froids dans les potentiels désordonnés. Nous commençons par un rappel théorique sur la définition de la fonction spectrale, la self-energy, et les deux régimes du désordre (le désordre classique et le désordre quantique). Puis, nous présentons les résultats expérimentaux. Les fonctions spectrales ont été mesurées pour des désordres attractif et répulsif, pour une amplitude $|V_R|/h$ variant de 60 Hz à 4008 Hz. Pour toute la gamme d'amplitude, les résultats expérimentaux sont en accord avec les résultats numériques fournis par nos collaborateurs, Dominique Delande et Michael Pasek.

En outre, les résultats des mesures de fonctions spectrales montrent un crossover entre les deux régimes du désordre que l'on peut identifier en comparant l'amplitude $|V_R|$ à l'énergie de corrélation E_σ. Pour la régime du désordre quantique ($|V_R|/E_\sigma \ll 1$), la fonction spectrale est relativement étroite, symétrique, et centrée proche de la moyenne du désordre, i.e. l'amplitude V_R. Pour la régime du désordre classique ($|V_R|/E_\sigma \gg 1$), la fonction spectrale s'approche de la distribution en potentiel du désordre. Néanmoins, nous constatons une différence entre les cas attractif et répulsif. Pour le cas répulsif, un pic prononcé est observé ; il est associé à une accumulation des états liés au fond des minima de potentiels.

Par ailleurs, nous pouvons estimer le temps de diffusion élastique à partir de la largeur de la fonction spectrale. La comparaison entre ce dernier et le temps de diffusion élastique mesuré précédemment ne peut que renforcer les résultats des mesures de fonctions spectrales.

De plus, la méthode spectroscopique utilisée pour la mesure de la fonction spectrale permet également de réaliser un transfert de l'onde de matière dans le désordre dans les états d'énergie bien définies. Ceci ouvre une perspective pour les études de la transition d'Anderson, en s'appuyant sur l'expansion du paquet d'onde dans le désordre avec une résolution en énergie bien supérieure à celles des expériences précédentes. Néanmoins, ceci nous oblige à surmonter la limitation sur le temps de vie de notre nuage atomique dans le désordre.

Dans le chapitre 6, afin d'adapter notre réalisation du désordre sélectif en état de spin pour les études de la transition d'Anderson, nous proposons une solution qui consiste à réaliser le désordre avec deux lasers *speckle*, dit *speckle bichromatique*. Nous avons effectué des études numériques qui consistent essentiellement à calculer le temps de vie dans des états d'horloge en fonction de l'amplitude du désordre. Nous montrons que le temps de vie dans le désordre peut être amélioré par trois ordres de grandeur; pour $|V_R|/h = 4$ kHz, il passe de 0.5 ms à 0.68 s (voir Tab. 6.1).

Néanmoins, nous avons identifié une nouvelle limitation à cause d'un potentiel résiduel dans l'état $|1\rangle$. Ceci est un résultat dû à la décorrélation entre les deux champs de *speckle* de longueur d'onde différentes. En augmentant la différence en longueur d'onde, le temps de vie devient plus long et le potentiel s'agrandit. Ceci nous oblige à trouver une solution équilibrée. Nous avons étudié théoriquement l'effet du potentiel résiduel. En effectuant quelques applications numériques, nous montrons que pour la gamme des paramètres de désordre utilisé dans les mesures de fonctions spectrales, les études de la transition d'Anderson sont envisageables. Dernièrement, nous avons aussi présenté la mise en œuvre du *speckle bichromatique* en utilisant deux faisceaux lasers combinés pour générer le *speckle*.

Dans le chapitre 7, nous concluons nos travaux par une discussion sur la faisabilité de notre méthode spectroscopique pour étudier la transition d'Anderson, ainsi que quelques possibilités d'observation de signatures de la localisation dans l'espace des impulsions, ou encore un test de la théorie du potentiel effectif caché.

Contents

Chapter 1

Introduction

Wave propagation in disordered media is an ubiquitous subject in physics. It applies to many kind of waves such as electromagnetic wave, acoustic wave, or seismic wave [1–3]. The wave description also applies to quantum particles due to their matter-wave duality. For a particle with a momentum p, we associate de Broglie wavelength [4],

$$\lambda = \frac{h}{p}. \tag{1.1}$$

Such description applies to electrons in crystals within the band theory of solids. Understanding their interaction with defect (impurities), phononic vibration, and other kinds of disorder has led to better description of material conductivity [5]. Hence, understanding of the matter-wave phenomena in disorder can also lead to technological applications.

In the description of electronic propagation in disordered systems, interference effects resulting from multiple wave scattering by the disorder are often neglected. In certain studies in condensed matter physics, these effects result in non-trivial behaviors of transport properties, for instance, conductivity behavior beyond the Ohmic law [6]. Other related phenomena include quantum Hall effect, fractional quantum Hall effect, negative magnetoresistivity, and Anderson localization [5–7].

Sixty years of Anderson localization

One much celebrated phenomenon related to the wave propagation in disordered media is Anderson localization [8, 9]. In 1958, Philip W. Anderson considered a problem of quantum particle diffusion in a disordered lattice [10] as an attempt to describe the anomalously long relaxation times of electron spins in certain doped semiconductors [11]. He has demonstrated that the disorder could cause particle localization, i.e. vanishing diffusion. Indeed, such description does not conform with the conventional diffusion picture. This phenomenon has led to a new quantum mechanical view of metal-insulator transitions. In 1977, Philip W. Anderson received the Nobel prize in physics jointly with Sir Nevill Francis Mott and John Hasbrouck van Vleck “for their fundamental theoretical investigations of the electronic structure of magnetic and disordered systems" [12].

The physics of the Anderson localization depends on the dimensionality of the system. In year 1979, Abrahams, Anderson, Licciardello and Ramakrishnan, known as "gang of four", have introduced the scaling theory of localization, in a published work in the journal *Physical Review Letters*[1] [13]. This theory predicts a phase transition in three dimensional systems between metallic and localized phases, also called the Anderson transition.

Anderson localization is a wave phenomenon that has prompted experimental efforts with many kinds of classical wave such as acoustic wave and photonic wave, and also electronic wave [7,8]. Anderson localization has also been observed in various dimensions. For instance, in one-dimensional systems, the localization signature has been observed in a photonic crystal system [14]. For two-dimensional systems, the phenomenon has been observed, for examples, in a system of waveguide arrays [15] and in disordered glass optical fibers [16]. For three-dimensional systems, there were studies with ultrasound [17] and doped semiconductor system [18]. In 2018, sixty years after its initial publication, there are still many works carried out related to the phenomenon.

Anderson localization of ultracold atom

Ultracold atoms are versatile tools and cold-atom techniques have plenty of applications such as atom laser [19], atomic interferometry [20], optical lattice clock [21], and atomtronics [22]. Ultracold atoms are excellent sources of matter wave [23]. They feature techniques that allow control of dimensionality of the physical systems, fine tuning of the interparticle interactions, tailoring the Hamiltonian, and development of novel detection schemes [24,25]. For these reasons, ultracold atoms have become convenient tools to simulate certain condensed matter systems such as superfluidity [26], superfluid-MOT transition [27], BCS-BEC transition [28], and spin ising models [29]. For Anderson localization, the quest for its signature with ultracold atoms has started in early 2000s. In many studies, the matter wave is realized with Bose-Einstein condensation [30–32]. Typically, the disordered potential is realized with laser speckle [33,34]. It has advantages of being controllable and highly tunable. Besides, there have also been efforts to realize the disordered potential with incommensurable optical lattices [35], impurity atoms in the cold atomic cloud [36], and disordered intensity pattern created using digital mirror device [37]. In order to observe the localization effect, we examine the expansion of the atomic cloud in the presence of the disorder.

Direct signatures of Anderson localization with ultracold atoms were successfully observed in 2008 [38, 39]. Fig. 1.1 depicts the experimental images of the atomic cloud expansion in presence of disorder from atom optics group in Palaiseau and from Inguscio's group in Florence. The Anderson localization manifests as a halt in the expansion of the cold atomic cloud. In the experiment in Palaiseau (Fig. 1.1(a)), the cloud density converges to an exponential decay profile

---

[1] This work is enlisted among the milestones Letters of the journal.

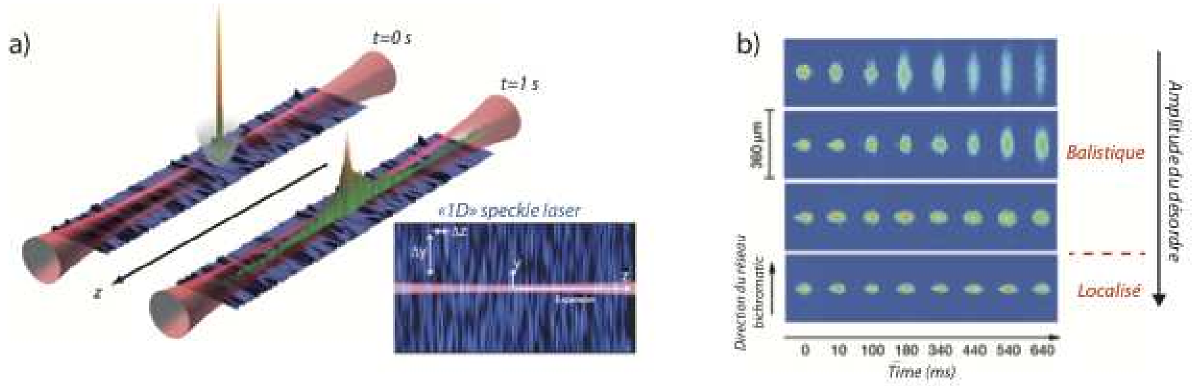

Figure 1.1: **Observations of Anderson localization with ultracold atoms**. (a) Experiment in Palaiseau: inside a one-dimensional waveguide, atomic cloud expansion in the presence of the disordered potential created by laser speckle converges into exponential decay profile, which constitutes a direct signature of Anderson localization (Figure taken from Ref. [38]). (b) Similar experiment carried out in Florence (Figure taken from Ref. [39]).

which constitutes a direct signature of Anderson localization. For three-dimensional systems, Anderson localization has been observed in three different experiments [40–42]; in De Marco's group in Urbana-Champaign, in atom optics group in Palaiseau, and in the group of Modugno and Inguscio in Florence. In these experiments, the evidence of phase transition has been confirmed from the copresence of atoms in diffusive and localized states; diffusive and localized states correspond to the metallic and localized phases respectively and are separated by a so-called mobility edge, E_c. Furthermore, mobility edge, i.e. the critical energy of the Anderson transition, was also estimated from the experimental results. These experiments have encouraged further studies related to the phase transition, which is central to this thesis work.

The scientific context of the thesis

In the three experiments related to Anderson localization in three-dimensional systems, direct measurement of the mobility edge was not possible. The introduction of the disorder induced enlargement of the energy distribution. A fraction of atoms are found in the localized states associated with energies below the mobility edge ($E < E_c$), while the remaining atoms are in the diffusive states (with energies above the mobility edge, $E > E_c$). The two phases can be distinguished because the localized atoms have effectively zero expansion. Fig. 1.2 depicts the snapshots of the atomic cloud expansion in disorder from the experiment in Palaiseau [41] and illustration of the effect of wide energy distribution. Due to the difference of the expansion rate, after few seconds, only localized atoms are left around the initial position. Therefore, the fraction of atoms in the localized states, f_{loc}, can be deduced experimentally.

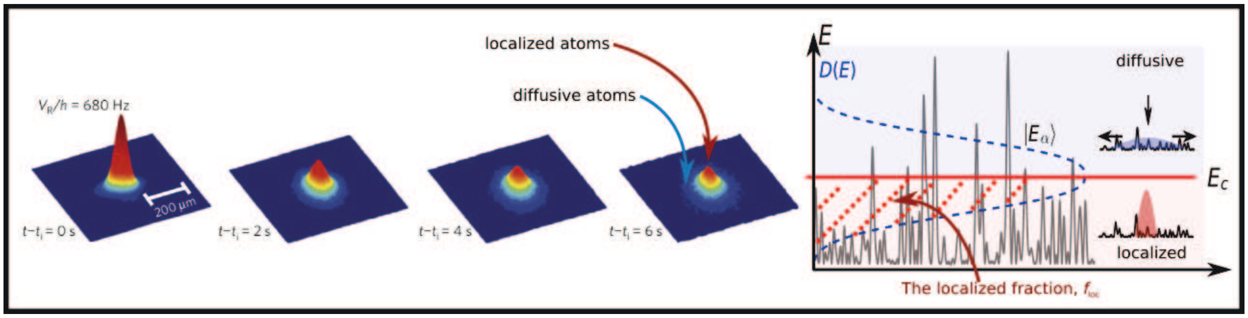

Figure 1.2: (Left) Observation of Anderson localization in three-dimensional system, taken from Ref. [41]. (Right) Due to the wide energy distribution, only a fraction of atoms, f_{loc}, is found in the localized states associated with energies below the mobility edge, E_c.

Despite the poor energy resolution due to the disorder-induced energy broadening, the mobility edge can be estimated provided the information of the energy distribution, $D(E)$ (see Fig. 1.2). In the experiment in Palaiseau, the disorder was quenched such that the energy distribution was effectively the spectral function associated with quasi-null momentum. In the experiment in Florence, the spectral function was also used to deduce the mobility edge [42]. The spectral function has become an invaluable resource in the determination of the mobility edge. However, in these works, the spectral function was obtained through numerical calculations without any supporting experimental work.

A recent result of numerical calculation of the mobility edge offers direct comparison with the three existing experimental results [43]. It has highlighted important discrepancies, especially when the spectral function was not taken into account in the analyses [40]. The imprecision in the measurement of mobility edge would constitute a major obstacle for exploring the Anderson transition in the critical regime. In addition, the implication of this result renders the precise measurement of the spectral function also becomes desirable.

In this thesis work, we develop an approach that solves two challenges, direct measurement of the mobility edge and direct measurement of the spectral function. It is summarized in Fig. 1.3. It has two important features. The first one is state-dependent disorder, a disordered optical potential which is selective in spin states. It involves two spin states, state $|1\rangle$ which is insensitive to the disorder and state $|2\rangle$ which senses the disorder. The second feature is radio-frequency transfer between the two states. In this way, it becomes possible to load matter wave into the disorder with controllable energy and without disorder-induced energy broadening. This approach promises direct measurement of the mobility edge with huge improvement of the energy resolution. In addition, the transfer rate between the two states is proportional to the spectral function, allowing its direct measurement. Our solution constitutes a spectroscopic approach for exploring the Anderson transition.

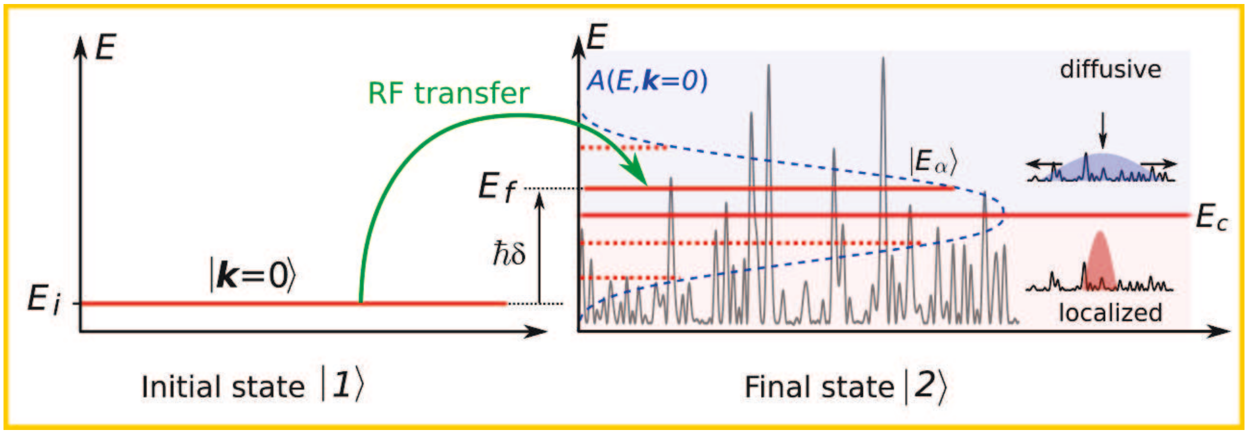

Figure 1.3: Spectroscopic approach of Anderson transition with energy-resolved matter wave in disordered potentials. Matter wave with well-defined momentum is realized with ultracold atoms and is prepared in an initial spin-state $|1\rangle$ which is insensitive to the disorder. These atoms are transferred to spin-state $|2\rangle$ which can sense the disorder. The transfer is based on radio-frequency transfer which allows control of the matter wave energy in the disorder, shown as $\hbar\delta$, defined by the resonance condition of the transfer. This technique aims to explore the critical regime of the Anderson transition, including the direct measurement of the mobility edge E_c.

The course of the PhD work

The PhD work essentially consists of experimental works carried out in the atom optics group at Laboratoire Charles Fabry in Palaiseau. The experiment is currently led by Dr. Vincent Josse who is also my PhD advisor. The quest for Anderson localization with this experiment started in 2008. This work cannot be disassociated with Alain Aspect who initiated the experiment with Philippe Bouyer. There are already several notable works associated with this experiment such as the direct observation of Anderson localization in one-dimensional system [38] and in three dimensional system [41], followed by the observation of coherent backscattering signature in momentum space [44], and its the time-reversal effect [45]. Details regarding these works can be found in the thesis work of Juliette Billy in 2010 [46], Alain Bernard in 2010 [47], Fred Jendrzejewski in 2012 [48], and Kilian Müller in 2014 [49].

I arrived at the laboratory on October 2015 at the end of the thesis work of Jérémie Richard [50]. In the first year, the research work was focalized in the technique of the radio-frequency transfer and the measurement of the spectral functions. Valentin Volchkov, who was a postdoc at that time, was in charge of the daily progress of the experiment. I also started the long work-partnership with Vincent Denechaud who was in his second year of PhD. We also had a fruitful collaboration with the group of Dominique Delande at Laboratoire Kastler Brossel in Paris. He and Michael Pasek, who was a postdoc at that time, have provided us the numerical works of the spectral function for direct comparison with the experimental results. From this collaboration, we have a published work in journal Physical Review Letter in 2018 [51]. At the same time, I have taken the initiative of "upgrading" the state dependent disorder which allows not only measurement of the spectral function but also the study of the critical regime of the Anderson phase transition. The initiative already started in the second semester.

Starting from the second year, we started to face many unexpected experimental hurdles. The main obstacle came mainly from the module generating the programed TTL and analog signals. We had a homemade module which was programmable by software MATLAB. Both fortunately and unfortunately, around April 2017, in the middle of the PhD period, we have decided to replace the module with a new one purchased from *National Instrument* which is programmable using software CICERO. Starting from the third year, the module was fully installed, the programming aspect was mastered and the quest for the BEC production was resumed. Around this time, Vincent Denechaud had started the redaction of his thesis [52] and Baptiste Lecoutre had joined the team as new PhD student. In November 2017, Adrien Signoles joined our team which alleviated the manpower shortage. Unfortunately, in March 2018, there was leaking problem of the water cooling system forcing a temporary halt for the experiment. During the last semester of the PhD studies, we also tried to look into some connection between the spectral-function results and the measurement results of the elastic scattering time obtained in 2015. At the same time, I also started the redaction of this PhD thesis.

Outline of the manuscript

This manuscript comprises seven chapter, including this chapter of introduction. The remaining chapters aim to present the progress towards the realization of the experimental schema shown in Fig. 1.3. In the second chapter, we review several theoretical notions related to the Anderson localization and mesoscopic physics in general, which are relevant to our experiment.

Chapter 3 and 4 concern the matter wave and the disorder respectively. Chapter 3 summarizes experimental details of the realization of the matter wave with Bose-Einstein condensation of rubidium-87 (^{87}Rb) atoms and the radio-frequency (rf) transfer based on two-photon transition. The rf-transfer allows spectroscopy of the matter wave energy in the disorder (the external energy $\hbar\delta$ shown in Fig. 1.3) with excellent resolution. Chapter 4 focuses on the realization of the state-dependent disordered potential created using single laser speckle. This allows introduction of pertinent disorder parameters.

In chapter 5, we present our work on the measurement of the spectral functions of ultracold atoms in disordered potentials. The experimental results have shown excellent agreement with the numerical calculation. The results highlight crossover between two different regimes of disorder, so-called "quantum" and "classical" disorder. Besides, we also show compatibility of the measurement results of the spectral functions and the measurements of the elastic scattering time. Most importantly, the success of the spectral function measurements constitutes a proof of concept of controlled transfer of atoms to well-defined energy in the disorder.

Nevertheless, there is still one major obstacle for our goal to study the Anderson transition. The current state-dependent disorder does not allow long enough observation time for the atomic cloud expansion in the disorder. In chapter 6, we present a solution to circumvent such limitation consisting of speckle disordered potential created from two laser speckles. Finally, chapter 7 present the conclusion, the feasibility of the direct measurement of the mobility edge and the study of the critical regime of the Anderson transition, the current work, and some possible future works.

Chapter 2

Anderson localization of matter wave

Contents

We attempt to review some aspects of quantum transport and the Anderson localization with several associated experiments. The discussion starts from the description of wave scattering in a disordered medium, with focus on the elastic scattering time (the mean time between two successive scattering events). Such description can also be found in many references related to mesoscopic physics. Thus, it can also apply to the description of transport properties in complex media, such as light in the atmosphere or in biological tissues and electrons in solid-state systems [6, 53]. We continue the review with the weak localization effect. With the discussion, we hope to provide appropriate intuition of Anderson localization and Anderson transition. Furthermore, we highlight current problem in the experimental determination of the mobility edge in cold atom experiments. The discussion focuses on three existing experimental results and a recent numerical work which has carefully compared the experimental and numerical results. In particular, we also highlight the role of the spectral function in the determination of the mobility edge in these experiments.

2.1 Wave scattering in disordered potentials

We are interested in the effect of disordered potentials on the diffusion of an initial wave packet. Analogous to particle diffusion, for a wave packet associated with a group velocity v, we can associate diffusion constant D which is given by

$$D = \frac{v\ l_B}{d} = \frac{v^2 \tau_B}{d}, \tag{2.1}$$

where d is the dimension of the system and l_B is the transport mean free path; l_B follows $l_B = v\tau_B$, where τ_B is called the transport mean free time. For isotropic elastic scattering, the time τ_B also corresponds to the mean time between two successive scattering events, i.e. the elastic scattering time.

For anisotropic scattering, the transport time τ_B is no longer equivalent to the elastic scattering time, τ_s. However, the relation between these two characteristic times can be deduced provided that the information about the anisotropic scattering rate is known. Besides, the time τ_s is related to the dephasing whereas the time τ_B is related to the loss of memory of the initial state. Intuitively, τ_s is shorter and is more rudimentary than τ_B. Detailed account of these quantities requires the microscopic details of the disorder, from which the anisotropic scattering rate could be determined.

Since τ_s is not directly related to transport properties, its experimental determination is rather challenging. Some of the techniques developed for its measurement are Shubnikov-de Hass oscillations of the magneto-conductivity in electronic systems [54–56], ballistic transmission [57, 58], microscopy techniques [59–61], and intensity or phase correlations [62–65] for classical waves. In our experimental studies, elastic scattering time τ_s is a measurable quantity; see for example Refs. [44, 45, 48, 50, 66]. With the same experiment, we can also study the transport time τ_B and the weak localization effect. In the following two subsections, we discuss the elastic scattering within the first-order Born approximation and some generalities related to the experiments; only speckle disorder is considered in this section.

2.1.1 Elastic scattering and Born approximation

Fig. 2.1 depicts wave scattering in a speckle correlated disordered potential. Fig. 2.1(a) shows physical picture of scattering based on the 1st-order Born approximation (simply referred as Born approximation in the following). The disorder is considered weak such that perturbative treatment applies. The time τ_s can be interpreted as the finite lifetime of the initial free state $|\boldsymbol{k_i}\rangle$, as it is scattered towards a continuum of final momenta $|\boldsymbol{k'}\rangle$ with $|\boldsymbol{k'}| = |\boldsymbol{k_i}|$. Fig. 2.1(b) depicts the

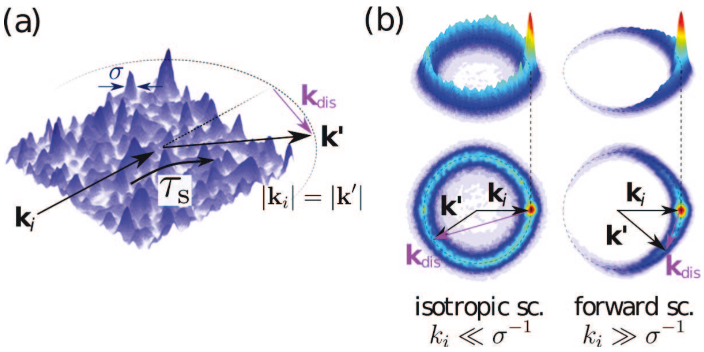

Figure 2.1: (a) Elastic wave scattering of a matter-wave by a laser speckle disordered potential of typical correlation length σ. $\boldsymbol{k_i}$ represents the initial momentum. A scattering event is characterized by an impulse $\boldsymbol{k}_{\text{dis}}$ in a certain duration, whose average is the elastic scattering time τ_s. In the Born approximation, the final momentum, $\boldsymbol{k'} = \boldsymbol{k_i} + \boldsymbol{k}_{\text{dis}}$ lies on the elastic scattering ring (dotted circle). (b) Illustration of the two-dimensional momentum distribution $n(\boldsymbol{k}, t)$ (1st row : side view, 2nd row : top view) for isotropic ($k_i \ll \sigma^{-1}$) and forward ($k_i \gg \sigma^{-1}$) scattering regimes. Figures are taken from Ref. [66].

momentum distribution $n(\boldsymbol{k}, t)$, shown for two-dimensional case. The peaks (see first row) are associated with the initial momentum $\boldsymbol{k_i}$. The elastic scattering condition $|\boldsymbol{k'}| = |\boldsymbol{k_i}|$ results in the depletion of the peak accompanied with the transfer into the ring of momentum $\boldsymbol{k'}$. In this regime, the distribution at initial momentum decays exponentially, with the characteristic time τ_s :

$$n(\boldsymbol{k}_i, t) = n(\boldsymbol{k}_i, 0) e^{-t/\tau_s}, \tag{2.2}$$

where t is the propagation time in the disorder.

The disordered potential determines the allowed range of $\boldsymbol{k}_{\text{dis}} = \boldsymbol{k'} - \boldsymbol{k_i}$. The weight of the scattering in this direction is related to the spatial frequency distribution of the disorder $\tilde{C}(\boldsymbol{k}_{\text{dis}})$, i.e., the Fourier transform of the two-point correlation function[1] $C(\boldsymbol{\Delta r}) = \overline{V(\boldsymbol{r})V(\boldsymbol{r} + \boldsymbol{\Delta r})}$. Using the Fermi golden rule, the elastic scattering time in Born approximation τ_s^{Born} is obtained by summing the contributions coming from the scattering in all directions, yielding [6] :

$$\frac{\hbar}{\tau_s^{\text{Born}}} = 2\pi \sum_{\boldsymbol{k'}} \tilde{C}(\boldsymbol{k'} - \boldsymbol{k_i})\ \delta(\epsilon_{\boldsymbol{k'}} - \epsilon_{\boldsymbol{k_i}}), \tag{2.3}$$

where $\epsilon_{\boldsymbol{k}} = \hbar^2 |\boldsymbol{k}|^2 / 2m$ is the free-state energy, with m the atomic mass.

The correlation function $C(\boldsymbol{\Delta r})$ has typical width σ, which is called the correlation length. As the scattering rate in direction $\boldsymbol{k}_{\text{dis}} = \boldsymbol{k'} - \boldsymbol{k_i}$ is proportional to $\tilde{C}(\boldsymbol{k'} - \boldsymbol{k_i})$, we identify a characteristic spatial frequency σ^{-1} that defines two scattering regimes. The first regime corresponds to low initial momentum $k_i \ll \sigma^{-1}$ (see first column in Fig. 2.1(b)). As $|\boldsymbol{k}_{\text{dis}}| \ll \sigma^{-1}$, $\tilde{C}(\boldsymbol{k'} - \boldsymbol{k_i})$ depends weakly on $\boldsymbol{k'}$. As a result, the scattering is isotropic. The other regime corresponds to the opposite case

---

[1] $\overline{\cdots}$ represents averaging over many realizations of disorder. Only in this chapter, we adjust the offset potential such that $\overline{V(\boldsymbol{r})} = 0$.

of large momentum $k_i \gg \sigma^{-1}$. $\tilde{C}(\boldsymbol{k'} - \boldsymbol{k_i})$ is negligible in all direction except for $|\boldsymbol{k'} - \boldsymbol{k_i}| \lesssim \sigma^{-1}$. As a result, the scattering is essentially concentrated in the forward direction. In this regime, the isotropization in the momentum distribution takes much longer time than τ_s. The isotropization time is equivalent to the transport time τ_B. In general, τ_B is related to τ_s according to [6, 67]

$$\tau_B = \frac{\tau_s}{1 - \langle \cos\theta \rangle}, \tag{2.4}$$

where θ the angle between $\boldsymbol{k_i}$ and $\boldsymbol{k'}$ and $\langle \cdots \rangle$ represents the averaging according to the scattering weight over all direction in space.

In addition, as discussed in Refs. [68–71], τ_s^{Born} behaves differently in the two regimes. For $k_i \ll \sigma^{-1}$, τ_s^{Born} is essentially constant for the isotropic scattering regime. In the opposite case, $k_i \gg \sigma^{-1}$, it starts to increase linearly in $k_i\sigma$. Hence, we see that $k_i\sigma$ is a pertinent parameter. Besides, we can remark a rather linear dependence of $\hbar/\tau_s^{\mathrm{Born}}$ on $C(\boldsymbol{\Delta r})$, from which we can define $V_R^2 \equiv C(\boldsymbol{\Delta r} = 0) = \overline{V^2(\boldsymbol{r})}$. This suggests another pertinent parameter V_R which represents the disorder strength[2].

One intuitive way to determine the validity of the Born approximation is to reason using a finite energy width $\Delta\epsilon = \hbar/\tau_s^{\mathrm{Born}}$ due to the finite lifetime τ_s^{Born}. The width $\Delta\epsilon$ should be much smaller than the initial energy ϵ_{k_i}. With $l_s^{\mathrm{Born}} = \frac{\hbar k_i}{m}\tau_s^{\mathrm{Born}}$, condition $\Delta\epsilon \ll \epsilon_{k_i}$ is equivalent to $k_i l_s^{\mathrm{Born}} \gg 1$. In the regime of Born approximation, the wave undergoes many oscillations between two scattering events. In general, dimensionless quantity kl_s (k : wave number, $k = k_i$ in presented case; $l_s = v\tau_s$) has been employed to characterize the scattering strength. The condition $k_i l_s^{\mathrm{Born}} \gg 1$ is compatible with the weak scattering regime whereby $k_i l_s \gg 1$. Furthermore, the criterion $kl_s \sim 1$ is widely accepted to set the limit between the weak and strong scattering regimes. It especially coincides with the Ioffe-Regel criterion[3] associated with Anderson localization.

2.1.2 Experiments related to scattering and transport properties with ultracold atoms

In our experiment, the elastic scattering time τ_s is determined from the measurements of the momentum distribution $n(\boldsymbol{k}, t)$, see Fig. 2.1(b). We usually perform the experiments in a quasi-two-dimensional configuration. The disordered potential is switched on at time $t = 0$. The atoms have initial momentum $\boldsymbol{k_i}$. The momentum distribution is directly obtained from time-of-flight imaging performed after propagation time t. Our experiment allows realizations of some theoretical studies related to the phenomena in momentum space (see for example Refs. [67, 72, 73]).

The initial momentum k_i is achieved by applying an external magnetic field gradient which is

---

[2] As discussed further in Chap. 4, we associate positive V_R to repulsive speckle potential (as depicted in Fig. 2.1(a)) and negative V_R to attractive speckle potential.

[3] It is usually defined for point-like scatterers ($\sigma \approx 0$) [8].

tunable. In our experiment, we can achieve an ultra-narrow momentum spread of the initial wave packet (typically $\Delta k = 0.15\ \mu\text{m}^{-1}$ corresponding to temperature as low as 150 pK) thanks to delta-kick cooling techniques [44, 45, 74]. The disorder realized with laser speckle can be either repulsive or attractive depending on its frequency [75]. Its strength, V_R, can be tuned by varying the laser intensity. These techniques provide excellent control of the parameters $k_i\sigma$ and V_R as mentioned in previous subsection.

In accordance with the theory depicted in Fig. 2.1(b), the wave packet is initialized at state $|\boldsymbol{k_i}\rangle$, we observe the ring formation in the momentum distribution, and we analyze the depletion of the initial peak. The depletion shows an exponential decay associated with time constant τ_s in accordance with Eq. 2.2 [50, 66]. Based on the speed of isotropization in the momentum space, we can also deduce the transport time τ_B [50, 67]. In the next section, we will see another related experiments on weak localization effect.

Experiments mentioned in this subsection are complement to our works related to the Anderson localization (see Figs. 1.1(a) and 1.2). They allow studies both in position and momentum spaces. Besides, the analyses can complement each other. As an example, the elastic scattering time τ_s is related to the width of the spectral function $A(E, \boldsymbol{k_i})$, that is discussed later in Chap. 5.

2.2 Weak localization

Weak localization is associated with the weak scattering regime. At time beyond τ_s or τ_B, the wave undergoes multiple scattering events. They form multiple scattering paths which can interfere among themselves. One important manifestation is the diminution of the diffusion constant,

$$D \to D - \delta D. \tag{2.5}$$

Diminution in diffusion constant results in decrease of conductivity. Weak localization effect requires time-reversal symmetry which is sensitive to perturbations caused by the presence of spin-orbit coupling or magnetic impurities. Negative magnetoresistivity of thin metallic films is one famous signature of weak localization in condensed matter physics [76].

For wave in general, weak localization manifests as appearance of coherent backscattering (CBS). It is the enhancement of the scattering probability in the backward direction due to a quantum interference of amplitudes associated with two opposite multiple scattering paths [6, 44]. This phenomenon has been reported for many kinds of classical waves such as light [77–79], sound [80, 81], and even seismic waves [82].

This section contains two subsections. In the first subsection, we discuss the weak localization correction and the dimensionality effect. In the second subsection, we discuss about the CBS signature and its observation with ultracold atoms.

2.2.1 Weak localization effect

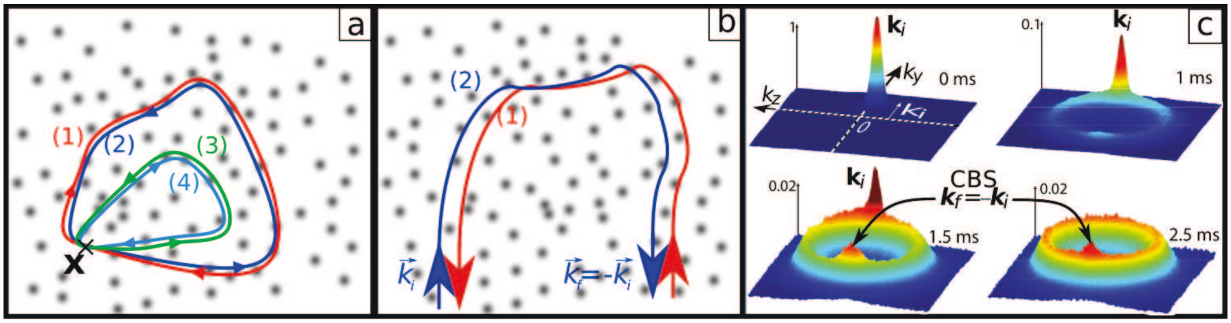

Figure 2.2: **Weak localization description.** (a) Loop mechanism: A loop can be associated with two opposite wave trajectories, which interfere constructively. The probability of returning to the origin (see point $\boldsymbol{x}$) is enhanced. (b) Coherent backscattering (CBS): in momentum space, for an incident wave with momentum $\boldsymbol{k_i}$ and final momentum $-\boldsymbol{k_i}$, two opposite multiple scattering paths interfere constructively, the scattering in backward direction ($-\boldsymbol{k_i}$) is enhanced. (c) CBS signature: in momentum distribution, the weak localization signature is the appearance of a peak at momentum $-\boldsymbol{k_i}$, opposite to the initial momentum.

Fig. 2.2 depicts the description of weak localization effect. The disorder is represented by the black point-like scatterers, and the colorful lines represent different multiple scattering paths. Fig. 2.2(a) depicts the description of weak localization using loop mechanism. This loop mechanism is robust, i.e. it survives disorder averaging. The weak localization effect results from the loop-like paths which increase the probability of return to the origin. As shown in Fig. 2.2(a), paths (1) and (2) form the same loop but have opposite direction; similar situation with paths (3) and (4). These loops start and end at point $\boldsymbol{x}$. Paths of each pair have equal length and accumulated phase. Therefore, they interfere constructively. Thus, the probability of return to the initial point is enhanced and the diffusion is slowed down.

The correction of the diffusion constant due to weak localization effect depends on the dimensionality of the system. Its expressions can be found in several references (as examples, [6,7]). They read

$$\delta D/D_B = \begin{cases} O\left(L/l_B\right) & \text{1D}, \\ O\left(\frac{1}{kl_B}\ln\left(\frac{L}{l_B}\right)\right) & \text{2D}, \\ O\left(\frac{1}{(kl_B)^2}\right) & \text{3D}, \end{cases} \tag{2.6}$$

where D_B is the classical diffusion rate and L the size of the system. These expressions hint certain nature of Anderson localization which is discussed in the next section. Firstly, the weak localization effect increases with L for 1D and 2D systems; the strong localization regime is attainable for large L. Secondly, weak localization effect increases with parameter $\frac{1}{kl_B}$. For 3D systems, the expression of the correction $\delta D/D_B$ suggests that the strong localization regime is attained for $kl_B \sim 1$. This can be related to the Ioffe-Regel criterion [83] for the Anderson localization, which reads

$$kl_B \lesssim 1. \tag{2.7}$$

As discussed in the next section, Anderson localization always happens for 1D and 2D systems whereas for 3D systems, there is transition between diffusive (metallic) and localized phases. Weak localization provides hints on the crossover between the classical Ohmic behavior and the Anderson localization, that also conform with the scaling theory [13].

2.2.2 Coherent backscattering

Fig. 2.2(b) depicts the schematic diagram of coherent backscattering. We consider an incoming plane wave with wave vector $\boldsymbol{k_i}$ and two opposite multiple scattering paths, colored in red and blue in the figure. Each path starts with direction $\boldsymbol{k_i}$ (the initial momentum) and ends with direction $-\boldsymbol{k_i}$ (the final momentum). We can see that the two paths have equal length and accumulated phase. As a result, the two paths interfere constructively and the scattering in the backward direction is enhanced.

Coherent backscattering (CBS) has been observed with ultracold atoms [44] in atom optics group in Palaiseau in 2012. The experimental procedure is similar to that of measurement of the elastic scattering time τ_s mentioned in subsection 2.1.2. Fig. 2.2(c) depicts the CBS signature in the momentum distribution. It manifests as appearance of a peak associated with momentum $\boldsymbol{k_f} = -\boldsymbol{k_i}$. The experiment is carried out in accordance with theoretical work presented in Ref. [72]. The peak appears at time beyond the transport time τ_B. In the experiment, the CBS peak is monitored up to $t \sim 10\tau_B$. Besides, work related to the time reversal symmetry of the CBS signature has also been carried out in 2014 [45]. These studies have confirmed the role of coherence of matter-wave propagation in the disorder. Besides, there have been other theoretical works related to the signatures of Anderson localization and Anderson transition in the momentum space, see Refs. [84–88], that could be realized with this experimental set-up.

2.3 Anderson localization

Anderson localization is associated with the strong scattering regime whereby the diffusion constant, D, vanishes. In this regime, the wave packet become localized and can be characterized by certain localization length ξ such that the wave function follows

$$|\psi|^2 \propto e^{-|\boldsymbol{r}|/\xi}. \tag{2.8}$$

As predicted by the scaling theory, the Anderson localization is imminent in 1D and 2D systems.

The expressions of $\delta D/D_B$ (Eq. 2.6) can give the typical localization length by evaluating L for $\delta D = D_B$, yielding

$$\xi \sim \begin{cases} l_B & \text{1D,} \\ l_B \exp\left(k l_B\right) & \text{2D.} \end{cases} \tag{2.9}$$

The localization length is related to the transport mean free path l_B.

We have mentioned earlier in the introduction several reported observations of the Anderson localization, including in ultracold atomic systems. In experiment of one-dimensional Anderson localization shown in Fig. 1.1(a), the localization length is approximately the length l_B at certain cut-off momentum $k_{\max}$ [89]; $k_{\max} \sim \sigma^{-1}$. For two-dimensional (2D) case, there is already attempt to observe the localization [90]. However, observation in the 2D system is proven more challenging. This is expected because the localization length can be very large due to the exponential dependence on kl_B.

The three-dimensional case is discussed in the following two subsections: the Anderson transition in the first subsection and several experimental observations in the second subsection.

2.3.1 Anderson transition

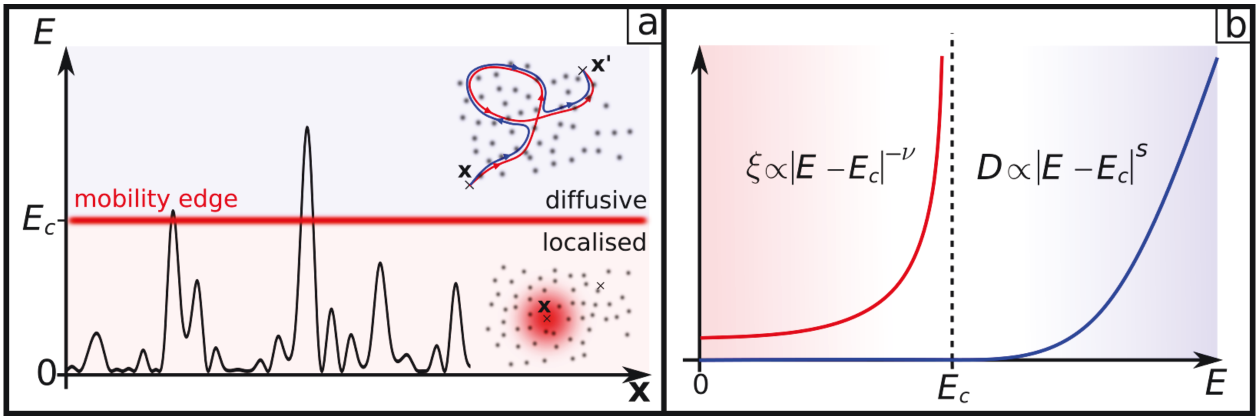

Figure 2.3: Anderson phase transition. (a) A critical energy E_c separates diffusive states ($E > E_c$) and localized states ($E < E_c$). (b) The diffusive constant $D(E)$ and localization length $\xi(E)$ associated with the diffusive states and the localized states have critical behavior around the mobility edge.

Fig. 2.3 depicts the Anderson transition at zero temperature. As predicted by the scaling theory, there exists a critical energy E_c (so-called the mobility edge) separating the localized states and diffusive states [13]. As depicted in Fig. 2.3(a), the diffusive states correspond to energy above E_c, characterized by their diffusion constant, D, whereas the localized states correspond to energy below E_c, characterized by their localization length, ξ.

Both D and ξ vary with the energy E. As depicted in Fig. 2.3(b), the diffusion constant vanishes for energy below the mobility edge while the localization length diverges near the mobility edge.

Around the critical energy, the dependences of D and ξ on the energy are given by

$$D \propto |E - E_c|^s \ , \ \xi \propto |E - E_c|^{-\nu} \,, \tag{2.10}$$

where s and ν are critical exponents.

The exponents s and ν are equal and they are not specific to any model of disorder. Till today, there is no exact theoretical model predicting the value of s and ν [91]. These numbers are usually studied numerically. Many works have agreed on values $s = \nu = 1.58$ [91–93]. These values are compatible with the experimental results obtained from cold atom experiment of kicked-rotor system [94].

2.3.2 Observations of the three-dimensional Anderson localization and the Anderson transition

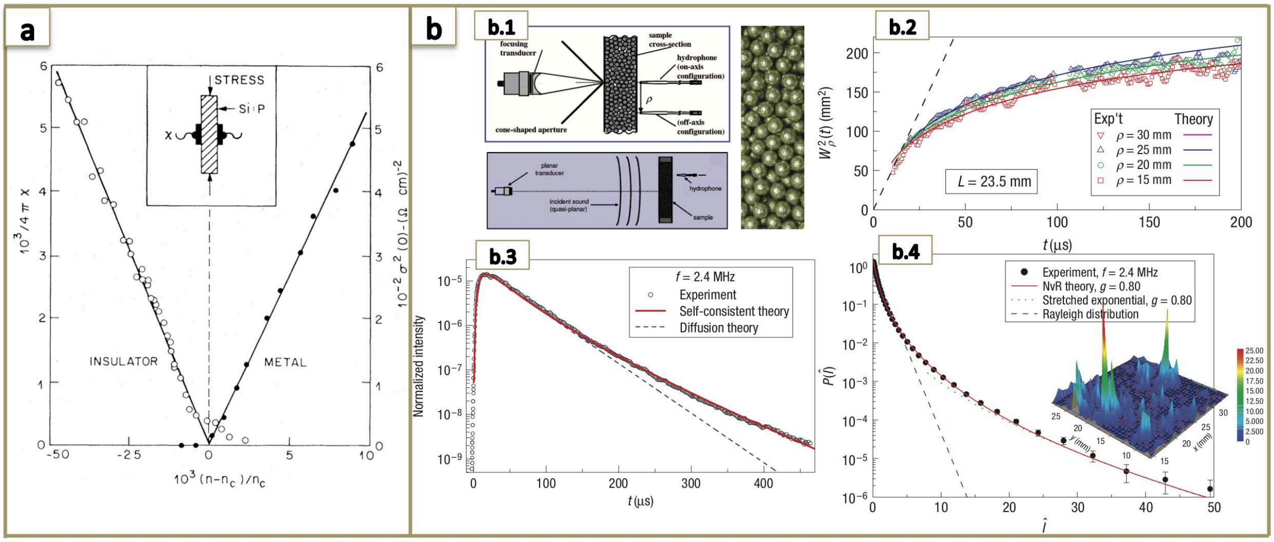

Figure 2.4: (a) Metal-insulator (Anderson) transition in phosphorous-doped silicon (Si:P), observed by varying the dopant density; figure is taken from Ref. [18]. (b) Observation of three-dimensional Anderson localization with ultrasound. Figures are taken from Refs. [7, 17]. (b-1) Either a quasi-point source of wave or a quasi-plane wave is sent across a random network made by brazing aluminum beads. Pulsed techniques are employed in measuring the amplitude transmission at various transverse positions $\boldsymbol{\rho}$. (b-2) Signature of transverse localization from measurements of the spatially and time-resolved transmitted intensity through the sample. (b-3) Averaged time-dependent transmitted intensity using the quasi-plane-wave source. Deviation from exponential tail at long times gives supporting evidence of localization. (b-4) For similar measurements using the quasi-plane-wave source, the normalized transmitted intensity is measured for a large number of individual transverse spots. The observed speckle pattern shows the intensity distribution deviating from usual Rayleigh distribution. The 3D figure shows observed speckle pattern with spikes of intensity.

For condensed matter system, Anderson transition manifests as metal-insulator transition. Fig. 2.4(a) shows the conductivity measurement on the metallic side and the dielectric susceptibility measurement on the insulating side of the transition in phosphorous-doped silicon (Si:P) [18]; The dopant density was tuned by applying uniaxial stress. The experiment shows exponent $\nu = 0.5$. However, subsequent experiments show discrepancies in the measured exponents, which are attributed to the finite temperature effect or interparticle interaction [8,95,96]. Unfortunately, such effects are usually unavoidable.

Unlike electrons, classical waves do not feature interparticle interaction. However, observations of Anderson localization signature with classical waves may be convoluted with absorption effect [97–99]. One study whereby the absorption effect can be ruled out is depicted in Fig. 2.4(b). The experiment consists of sending ultrasound wave across a disordered media and measuring the transmitted intensity at different transverse positions [17] (see Fig. 2.4(b-1)). Fig. 2.4(b-2) depicts the measured transverse widths $w_\rho(t)$ at different times t; a quasi-point wave source is used in this case. The localization signature is observed from the saturation of $w_\rho(t)$, which is a deviation from usual behavior described by the diffusion equation, $w_\rho^2(t) = 4Dt$. Investigation related to the longitudinal propagation consists of measuring the averaged time-dependent transmitted intensity associated with a quasi-plane wave source, depicted in Fig. 2.4(b-3). We can observe deviation from the expected exponential decay behavior, which can be described with wave diffusion theory. In addition, Fig. 2.4(b-4) depicts the observation of the near-field speckle patterns. The localization signatures manifest as the altered speckle pattern showing spikes of intensity (see the inset) and deviation of the intensity distribution from the Rayleigh distribution. In this experiment, several evidences of localization have been observed. However, localization signatures are rather associated with propagation in the transverse direction.

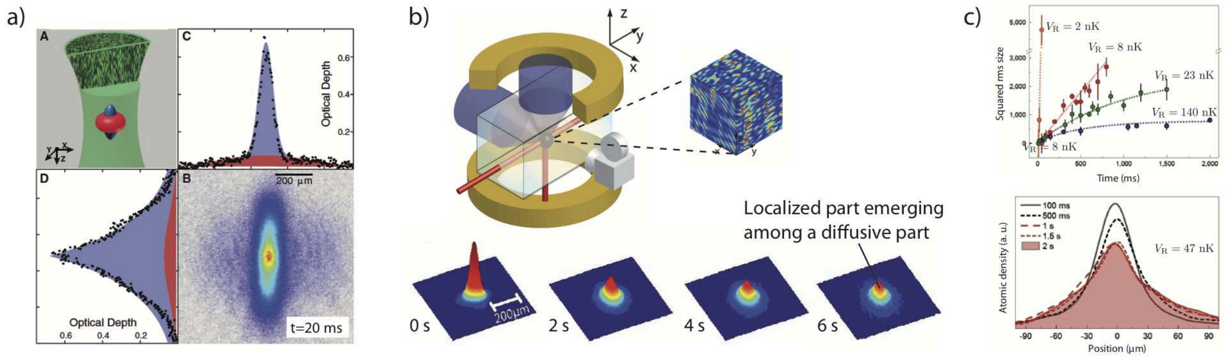

Figure 2.5: Observations of three-dimensional Anderson localization with ultracold atoms in (a) De Marco's group in Urbana-Champaign [40], (b) atom optics group in Palaiseau [41], and (c) the group of Modugno and Inguscio in Florence [42].

With ultracold atoms, Anderson localization can be directly observed by imaging the expansion of atomic cloud in the disorder. The wave function $|\psi|^2$ is directly proportional to the atomic density. For three dimensional configuration, the localization can be observed simultaneously from different directions. Dilute ultracold atomic cloud has also effectively zero interparticle interaction. Yet, the interaction can be tuned via Feshbach resonance [100], paving the way for studies related to many-body localization [37,101,102], Bose glass phase [103], etc. Fig. 2.5 depicts three observations of three-dimensional Anderson localization that are already mentioned earlier in the first chapter. These experiments have similarities of using speckle disorder and long-time-of-flight (TOF) imaging in presence of the disorder with long propagation time in order to distinguish the diffusive and the localized atoms. As shown in the Fig. 2.5(b), the propagation time can be as long as 6 s. The analyses of these experiments also have similarities of estimating the mobility edge based on the measured fraction of localized atoms. Details regarding these experiments are discussed in the next section.

2.4 Anderson transition with ultracold atoms: where is the mobility edge?

Currently, one major issue related to Anderson localization with ultracold atoms is the precise determination of the mobility edge. This is a crucial step towards studying the Anderson phase transition in the critical regime. For the experiments, we will consider the three experiments shown in Fig. 2.5. There exist numerical works which provide predictions of the mobility edge using self-consistent theory [68,70,104], Monte Carlo [105], and transfer-matrix technique [106]. In this section, we focus our attention to recent work by Pasek *et* al. [43], which provides direct comparison between the three experimental results and the numerical calculation[4].

Unlike the critical exponents, s and ν, the mobility edge depends on the details of the disorder. The speckle disorder features asymmetrical probability distribution resulting with non-trivial behavior of the mobility edge depending on whether the disordered potential is repulsive or attractive [107]. From the prediction for repulsive speckle disorder, the mobility edge lies below the average potential (the so-called “sea-level” which is set to be zero in this chapter).

This section comprises two subsections. In the first subsection, we discuss briefly the experimental analyses related to the estimation of the mobility edge. It involves broadened energy distribution due to introduction of the disorder, determination of the localized fraction, and the estimation of the mobility edge. We will exclude the Urbana Champaign experiment from the discussion due to lack of consideration for the energy broadening and also short propagation time (t) resulting in huge systematic error (t of only 20 ms as indicated in 2.5(a)). In the second subsection, we discuss the aforementioned numerical work which involves a non-trivial scaling. The scaling allows direct comparison between the experimental results, independently of the anisotropy of the disorder.

---

[4] Comparison is possible because all experiments have employed repulsive speckle disorder, i.e. $V_R > 0$.

2.4.1 Experimental determination of the mobility edge

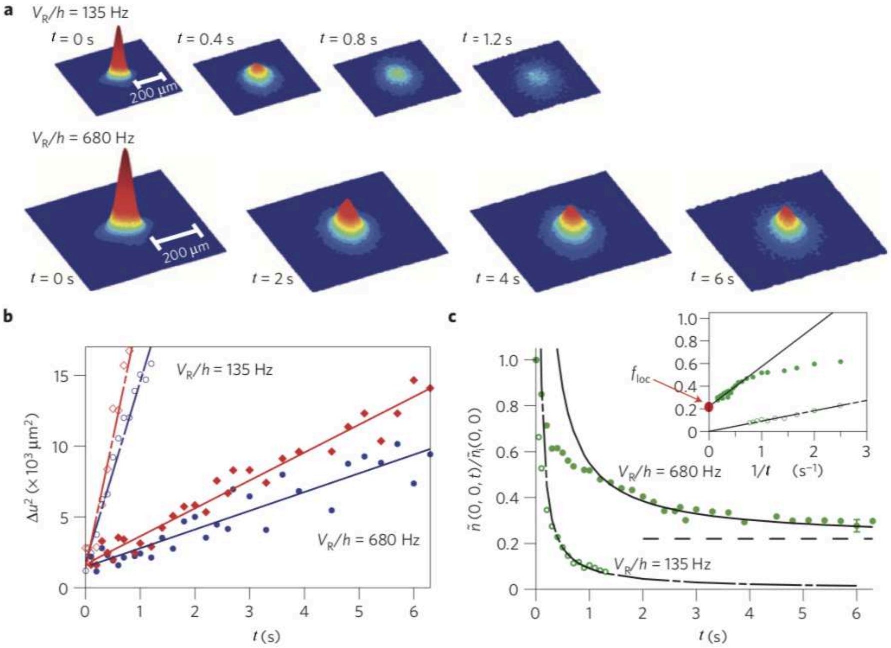

Figure 2.6: **3D Anderson localization experiment in Palaiseau in 2012.** (a) Evolution of atomic cloud at time t after the disorder quench, shown for two different disorder amplitudes, $V_R/h = 135$ Hz and $V_R/h = 680$ Hz. (b) Time evolution of the mean squared widths along the two axes. (c) The evolution of the column density at the center, normalized by its value at $t = 0$. The black lines show fittings according to $A + B/t$; plotted as a function of $1/t$ in the inset. The localized fraction corresponds to the value at the asymptotic limit at $t \to \infty$. Figures are taken from Ref. [41].

We are going to start with the experiment in Palaiseau (relevant results are shown in Fig. 2.6) since its theoretical description is relatively simpler than the others. The matter-wave was realized with Bose-Einstein condensation of rubidium-87, which can be associated to a quasi-plane wave at $\boldsymbol{k} = 0$. The disorder is quenched at time $t = 0$ and we are interested in the evolution of atomic density at time t, noted $n(\boldsymbol{r}, t)$; $n_0(\boldsymbol{r}) \equiv n(\boldsymbol{r}, t = 0)$. The analyses assume that the disorder quench does not affect the initial density. However, the disorder inevitably alters the energy distribution because the state $|\boldsymbol{k} = 0\rangle$ is not an eigenstate of the disordered system. The density at time $t > 0$ can be described as follows

$$n(\boldsymbol{r}, t) = \int \mathrm{d}\boldsymbol{r_0} \int \mathrm{d}E \; \mathcal{D}\left(\boldsymbol{r_0}, E\right) P\left(E, \boldsymbol{r} - \boldsymbol{r}_0, t\right), \tag{2.11}$$

where $P\left(E, \boldsymbol{r} - \boldsymbol{r}_0, t\right)$ is the probability distribution for a particle of energy E initially placed at point $\boldsymbol{r_0}$ to be found at point $\boldsymbol{r}$ at time t and $\mathcal{D}\left(\boldsymbol{r_0}, E\right)$ is associated with the semi-classical joint position-energy density after the disorder quench. When chemical potential μ and thermal energy $(k_B T)$ are smaller than the disorder strength V_R, $\mathcal{D}\left(\boldsymbol{r_0}, E\right)$ is given by

$$\mathcal{D}\left(\boldsymbol{r_0}, E\right) = A(E, \boldsymbol{k} = 0)\ n_0(\boldsymbol{r_0}), \tag{2.12}$$

where $A(E, \boldsymbol{k} = 0)$ is the so-called the spectral function associated with momentum $\hbar\boldsymbol{k} = 0$. Since the spectral function satisfies $\int \mathrm{d}E\ A(E, \boldsymbol{k}) = 1$, it can be interpreted as the energy distribution right after the quench.

The next step would be to deduce the localized fraction f_{loc}. Unlike atoms in the localized states, atoms in the diffusive states have non-zero diffusive constant such that they should be washed out from the system at large t. Mathematically, it can be written as [108]

$$\int \mathrm{d}\boldsymbol{r} \lim_{t\to\infty} P\left(E, \boldsymbol{r} - \boldsymbol{r}_0, t\right) = \Theta\left(E_c - E\right), \tag{2.13}$$

where E_c is the mobility edge. Given the total number of atoms $N = \int \mathrm{d}\boldsymbol{r_0} n_0(\boldsymbol{r_0})$, the localized fraction f_{loc} yields

$$f_{\mathrm{loc}} = \frac{1}{N}\int_{\Omega} \mathrm{d}\boldsymbol{r} \lim_{t\to\infty} n(\boldsymbol{r}, t) = \int_{-\infty}^{E_c} \mathrm{d}E\ A(E, \boldsymbol{k} = 0). \tag{2.14}$$

This result is intuitive because f_{loc} can be interpreted as the integration of the energy density for all E below E_c. Consequently, the determination of the mobility edge requires both knowledge of the spectral function and measurement of the localized fraction f_{loc} at extremely long propagation time t.

Experimentally, the imaging technique yields the atomic column density integrated along the imaging axis (see the $x-$axis in Fig. 2.5(b)). Fig. 2.6(a) depicts the density at increasing time t for two different disorder amplitudes. The images show propagation time t up to 6 s. From the snapshots, we can remark that the atomic diffusion is slower for the higher amplitude. This is confirmed from the plots of the mean squared widths, shown in Fig. 2.6(b). For $V_R/h = 680$ Hz, we can observe clear appearance of the localized atoms.

The localized fraction f_{loc} can be obtained by analyzing the evolution of the column density at its center, which is shown to be proportional to $A + B/t$. Fig. 2.6(c) shows the corresponding plot, the density is normalized by its initial value at $t = 0$. As discussed in Ref. [41], A is equivalent to the localized fraction f_{loc}. Systematic error due to finite time t can be avoided by associating f_{loc} to the asymptotic limit (see the inset). The analyses yield f_{loc} parameterized by the disorder amplitude V_R.

The mobility edge is deduced by applying Eq. 2.14. The spectral function was obtained numerically; details can be found in Ref. [109]. The experimental analyses have remarked that the determination of E_c was very sensitive to the spectral function. The analyses give the mobility edge $E_c = -1.75V_R^2/E_\sigma$, where $E_\sigma \sim \hbar^2/(m\sigma^2)$ is the correlation energy. The mobility edge is found below the “sea-level”, in accordance with the prediction mentioned earlier in this section.

Nonetheless, a more thorough error analyses of E_c would be desirable.

Three years after the experiment in Palaiseau, there was another experimental attempt to measure the mobility edge in Florence (see Fig. 2.5(c)). The experimental procedure is depicted in Fig 2.7(a). Similarities with the Palaiseau experiment include application of repulsive speckle disorder, broadening of the energy distribution due to the disorder and determination of the mobility edge based on measured f_{loc}. Several differences, the initial state could not be described as a plane wave and the energy distribution, noted $\mathfrak{D}_E(E)$, is not equal to the spectral function. The experiment also involves controlled energy-excitation which modifies the energy distribution. The localized fraction is measured after the excitation and also certain propagation time in the disorder (see inset II in Fig. 2.7(a)).

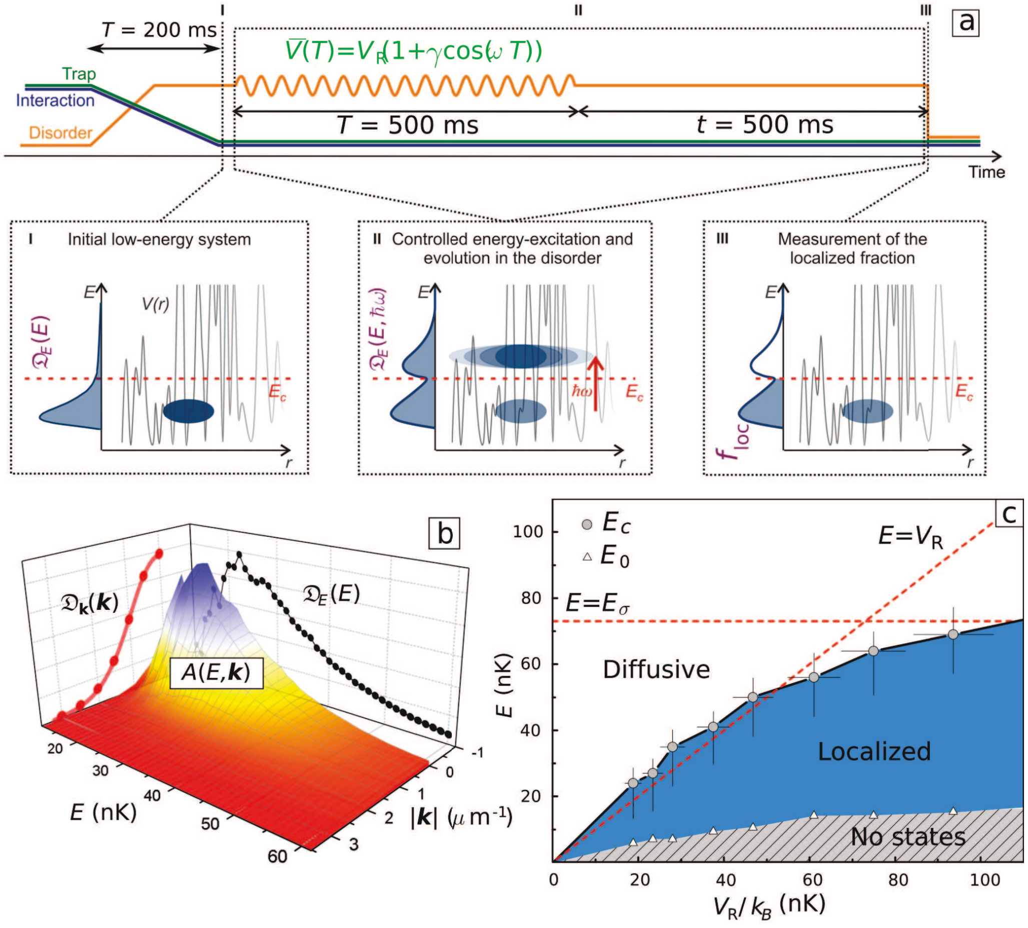

Figure 2.7: **3D Anderson localization experiment in Florence in 2015.** (a) Schematic diagram of the procedure: (inset I) preparation in quasi-localized states by disorder ramping accompanied with simultaneous ramping down of the trap strength and the interaction strength, (inset II) controlled excitation resulting in promotion of some atoms towards diffusive states, (inset III) measurement of the localized fraction. (b) Reconstruction of the energy distribution, $\mathfrak{D}_E(E)$, based on calculated spectral function $A(E,\boldsymbol{k})$ and measured momentum distribution $\mathfrak{D}_{\boldsymbol{k}}(\boldsymbol{k})$. (c) Measured mobility edge versus the disorder amplitude V_R. The "sea level" is shown as red-dashed line "$E = V_R$".

The energy distribution $\mathfrak{D}_E(E)$ requires knowledge of the spectral function. Time-of-flight measurements provide the momentum distribution $\mathfrak{D}_{\boldsymbol{k}}(\boldsymbol{k})$. $\mathfrak{D}_E(E)$ follows

$$\mathfrak{D}_E(E) = \int \mathrm{d}\boldsymbol{k}\ A(E, \boldsymbol{k})\mathfrak{D}_{\boldsymbol{k}}(\boldsymbol{k}). \tag{2.15}$$

Similar to the Palaiseau experiment, the spectral function $A(E, \boldsymbol{k})$ was numerically calculated (see Fig. 2.7(b)). Compared with the Palaiseau experiment, the energy distribution replaces the spectral function in the determination of the mobility edge.

Fig. 2.7(c) shows the deduced mobility edge for different disorder amplitudes V_R. Unlike the Palaiseau experiment which focuses only on V_R smaller than the correlation energy E_σ, the Florence experiment explores wider range of disorder amplitude V_R. In Fig. 2.7(c), the "sea-level" is represented by the red-dashed "$E = V_R$" line. The figure also shows that the mobility edge lies above the "sea-level" for lower disorder amplitudes with considerable asymmetric vertical error bars. The error analyses can be attributed to two effects. The first one originates from the application of the controlled excitation which results in symmetric error bar of few nK. The second one is attributed to the finite propagation time which results in the overestimation of the f_{loc}, and thus overestimation of the mobility edge. This systematic error results in asymmetric error bar of 6 nK. For low V_R/h of few tens of Hz, the uncertainties of the measured mobility edge become considerable. This renders measurement of the mobility edge with improved energy resolution desirable.

2.4.2 Comparison between experimental and numerical results

We would like to discuss the comparison between the experimental and the numerical results, presented in Ref. [43]. The repulsive speckle disorder employed in the experiments is anisotropic; the correlation length has dependence on axes in three dimension. As discussed in the Letter, the comparison must take into account the different degrees of anisotropy of the speckle disorder. From the three experiments, we can identify two configurations of speckle disorder: a single speckle configuration and two-crossed speckle configuration. A single speckle configuration realized in the Urbana-Champaign experiment results in a rather strong anisotropy; see inset A in Fig. 2.5(a) . The other two experiments use two-crossed speckle configuration which results in a rather isotropic disorder (as an example, see the two focused beams depicted in Fig 2.5(b)). In order to account for different cases, the authors consider anisotropic speckle disorder with correlation lengths σ_x, σ_y, and σ_z along three orthogonal directions. This leads to a redefinition of the correlation energy involving a geometrically averaged correlation length[5] $\sigma = (\sigma_x\sigma_y\sigma_z)^{1/3}$, yielding

$$E_\sigma = \frac{\hbar^2}{m\,(\sigma_x\sigma_y\sigma_z)^{2/3}}. \tag{2.16}$$

---

[5] See Ref. [110] for detailed justification.

As a main result, the mobility edge is shown to follow a non-trivial scaling,

$$\frac{E_c}{V_R} = \mathcal{F}\left(\frac{V_R}{E_\sigma}\right). \tag{2.17}$$

The scaling function $\mathcal{F}(x)$ has several known limits. For $x \ll 1$ which is associated with the quantum regime whereby the mobility edge converges to zero; $\lim_{x \to 0} \mathcal{F}(x) = 0$. For $x \gg 1$ which is associated with the classical regime whereby the mobility edge approaches the percolation threshold, which is very close to $-V_R$. Thus $\lim_{x \to \infty} \mathcal{F}(x) = -1$.

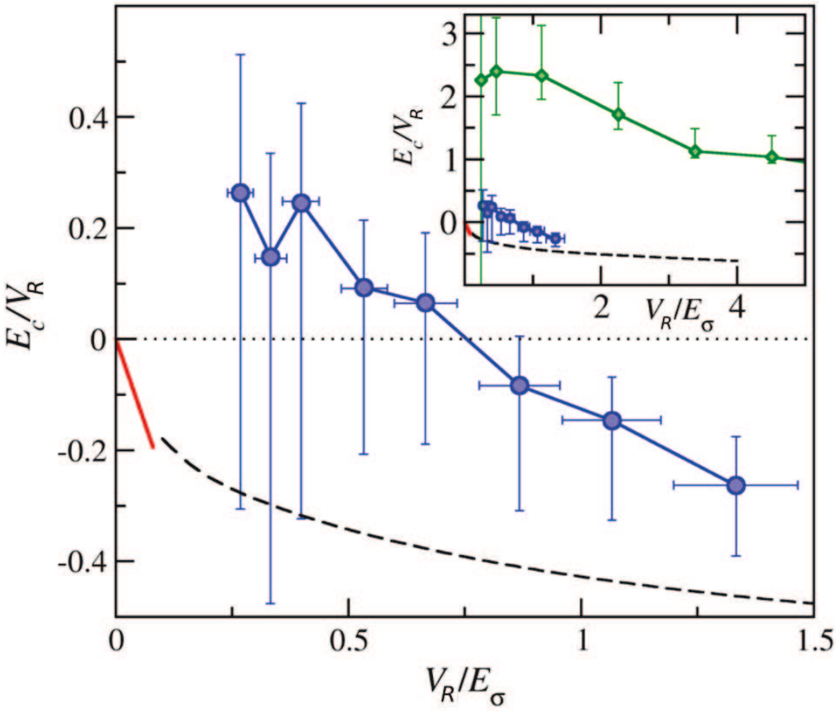

Figure 2.8: **Comparison of the mobility edge from experimental and numerical results**. Black dashed line obtained from numerical studies done in Delande's group in Paris; see Ref. [43] from which this figure is taken. Red solid line is obtained from the Palaiseau experiment. Blue points and blue line are obtained from the Florence experiment. Green points and green line (see inset) are obtained from the Urbana-Champaign experiment.

The comparison between different results are presented in Fig. 2.8. On the vertical axis, E_c/V_R represents the mobility edge normalized by the disorder amplitude. It is plotted against V_R/E_σ, the disorder amplitude normalized by the correlation energy. Here, the "sea level" corresponds to $E_c/V_R = 0$. The numerical result is plotted in black dashed line. The result from the Palaiseau experiment is plotted in red line. By taking into account the redefinition of the correlation lengths (in accordance with Refs. [43, 106]), this corresponds to $E_c/V_R = -2.24 V_R/E_\sigma$. The result from the Florence experiment is plotted in blue points which include their error bars. The vertical error bars of E_c/V_R appear larger for lower V_R. The result from the Urbana-Champaign experiment is plotted in green points in the inset. It shows large and positive value of mobility edge with great discrepancy compared with other results. As mentioned before, this may result from neglecting the broadening of the energy distribution and the extremely short propagation time (t). As argued in Ref. [111], the time is too short to detect the slow diffusion above the mobility edge, leading to an overestimation of the mobility edge.

2.5 Conclusion

In this chapter, we have reviewed concepts which are relevant to our work on the spectroscopic approach of Anderson transition. They include the elastic scattering time, the critical regime of Anderson transition, and the current problem in determination of the mobility edge in ultracold atomic experiments.

From the review of three experiments of three-dimensional Anderson localization with ultracold atoms and recent work on the mobility edge by Pasek et. al [43], we have demonstrated the critical role of the spectral function. We have remarked two problems. First, the spectral function was crucial for the determination of the mobility edge. Second, the measurement of the spectral function was absent while numerical calculations of spectral function were proven demanding. Measurement of the spectral function would be desirable to benchmark the numerical calculations.

Besides, we have learned the requirement of long observation time for observing the Anderson transition [108]. As an example, propagation time t of 0.5 s in the Florence experiment already results in systematic error of 6 nK which is shown sizeable for some weak disorder amplitudes. This leads to two important objectives for our research plan, improving the energy resolution and keeping the propagation time as long as possible. In Chap. 5, we present the measurements of the spectral function. From the experimental results, we show that our approach can give energy resolution as low as 0.5 nK ($\sim$ 10Hz in the spectroscopy), one order of magnitude lower compared to the Florence experiment. Lastly, in Chap. 6, we also present how long propagation time t can be realized.

Chapter 3

The exploitation of Bose-Einstein condensation

Contents

The production of Bose-Einstein condensates (BEC) relies on the techniques of laser cooling and trapping of atoms [112, 113]. These techniques have been developed since early 80s [114]. They have also been acknowledged with Nobel prize in physics in 1997 [115]. Furthermore, the Bose-Einstein condensation has been realized for the first time in 1995 in Boulder group with rubidium atoms [116] and in Ketterle group at MIT with sodium atoms [117]. These achievements have also been recognized with Nobel prize in physics in 2001 [118, 119]. Since then, BEC has been realized with various atoms ranging from alkali atoms, alkali-earth atoms and also rare earth atoms.

In the BEC state, the atoms occupy the lowest energy state. In order to obtain the BEC, we must cool down the atoms below certain critical temperature T_c. Without loss of generality, we consider atoms in a harmonic trap. The critical temperature is given by

$$T_c = \frac{\hbar\bar{\omega}}{k_B}\left(\frac{N}{1.202}\right)^{1/3}, \tag{3.1}$$

where $\bar{\omega} = (\omega_x\omega_y\omega_z)^{1/3}$ is the averaged trap frequency [120]. Towards the critical regime, wave packets of individual atoms start to overlap between each other. This corresponds to a phase space density $\mathcal{D}$ close to unity, i.e.

$$\mathcal{D} = n\lambda_{dB}^3 \sim 1, \tag{3.2}$$

with n the atomic density and $\lambda_{dB} = \frac{h}{\sqrt{2\pi m k_B T}}$ the de Broglie wavelength. This relation suggests that the BEC creation requires both cooling to extremely low temperature and sufficiently high atomic density. In most cases, such condition is achieved by applying evaporative cooling techniques [121].

In our experiment, the matter wave is realized with BEC of ^{87}Rb atoms[1]. The atoms must be cooled to temperature of a few nanoKelvins. For this purpose, we perform laser cooling techniques (Zeeman slowing, magneto-optical trap, etc) and trapping techniques (with magnetic field and with optical dipole trap). The atomic state can also be manipulated using radio-frequency fields. These processes are carried out in a vacuum system.

This chapter comprises three main sections. In the first section, we discuss some generalities related to the atomic structure, magnetic interaction, atom-light interaction, and detection method by imaging techniques. In the second section, we discuss the experimental sequences towards the production of Bose-Einstein condensates. Furthermore, we introduce the two spin states which can be used for the realization of the state-dependent disorder (see Fig. 1.3). In the third section, we discuss the radio-frequency transfer between these two states.

This experimental work is a continuation of previous works by Jérémie Richard [50] and Vincent Denechaud [52]. The details of the BEC production can also be found in the theses of Alain Bernard [47], Fred Jendrzejewski [48], and Kilian Müller [49].

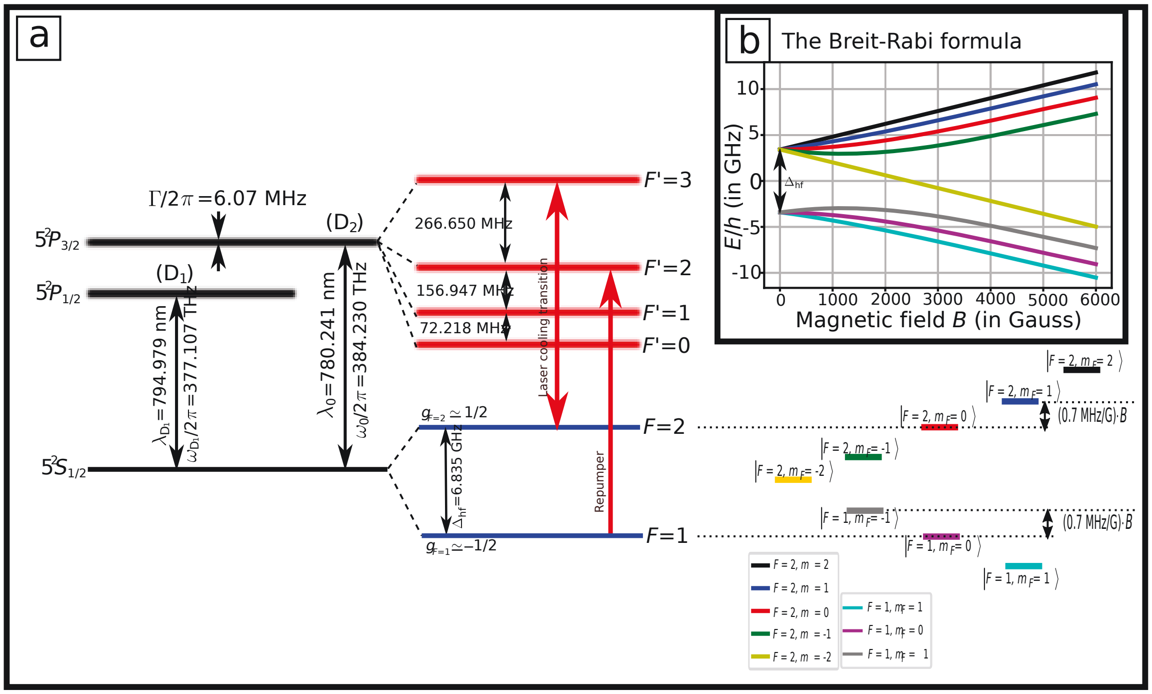

Figure 3.1: **Rubidium-87 D line and the energy shift due to magnetic field**. (a) Fine structure of rubidium 87 atom features the D_1 line and the D_2 line. The ground state has two hyperfine levels, $F = 1$ and $F = 2$. The laser cooling transitions and other transitions (repumper, etc) lie in the D_2 line. In this manuscript, $F \to F'$ transitions refer to the D_2 line by default. For weak magnetic fields, the energy shifts depend linearly on the magnetic field strength B as shown. (b) The energy shift dependence on the magnetic field strength B for the ground state according to the *Breit-Rabi* formula. (Data taken from Ref. [122])

3.1 Several essential tools

3.1.1 The atom: rubidium-87

Rubidium-87 is the second most abundant rubidium isotope after rubidium-85. It has nuclear spin of $I = 3/2$. Similar to many alkali atoms that have been cooled to quantum degeneracy, the D line is used for laser cooling transitions. Fig. 3.1 depicts the D line transitions; the fine structure features the D_1 line (or $5S_{1/2} \to 5P_{1/2}$ transition) and the D_2 line (or $5S_{1/2} \to 5P_{3/2}$ transition). As shown in the figure, we make use of the D_2 line for laser cooling transitions; in our work, most of the time, the D_1 line can be neglected. The ground state $5S_{1/2}$ has two hyperfine levels, $F = 1$ and $F = 2$ with hyperfine splitting of around 6.835 GHz. For the D_2 line excited states, there are four hyperfine levels, $F' = 0$, $F' = 1$, $F' = 2$, and $F' = 3$, mentioned from the lowest to the highest in energy. Each hyperfine level has $2F+1$ (or $2F'+1$) sublevels which are associated with quantum numbers $m_F = -F, ..., F-1, F$ (or $m_{F'} = -F', ..., F'-1, F'$). These sublevels are degenerate in

---

[1] Quantum gas of rubidium-87 follows bosonic statistics because its even number of constituent spin-1/2.

absence of magnetic field.

3.1.2 Magnetic interaction

The atomic interaction with an external magnetic field $\boldsymbol{B}$ is described by Hamiltonian

$$\hat{H}_B = \frac{\mu_B}{\hbar}\left(g_S\hat{\boldsymbol{S}} + g_L\hat{\boldsymbol{L}} + g_I\hat{\boldsymbol{I}}\right)\cdot\boldsymbol{B}, \tag{3.3}$$

where g_S, g_L, g_I are the electron spin, electron orbital, and nuclear $g-$factors. For weak magnetic fields, F and m_F (or F' and $m_{F'}$) are good quantum numbers. The energy shift (eigenvalues of $\hat{H}$) depends linearly on $B = |\boldsymbol{B}|$,

$$\Delta\, E_{F,m_F} = g_F m_F \mu_B B. \tag{3.4}$$

The g-factor for level $F = 1$ and $F = 2$ are approximately $g_F \simeq 1/2$ and $g_F \simeq -1/2$ respectively; see Fig. 3.1(a). This means that the energy shift of state $|1\rangle \equiv |F = 1, m_F = -1\rangle$ almost equals that of state $|2\rangle \equiv |F = 2, m_F = 1\rangle$. Thus, these states have similar magnetic susceptibility and their energy difference is nearly insensitive to external magnetic field. For strong magnetic field, the magnetic shift shows nonlinear behavior, that can be described by the *Breit-Rabi* formula, shown in Fig. 3.1(b). As discussed further in the following sections and chapters, we are interested in certain magic magnetic field $B = B_0^\star = 3.229$ G, whereby the states $|1\rangle$ and $|2\rangle$ have equal magnetic susceptibility. Besides, the magnetic shift also applies to the mechanism of magnetic trapping. The magnetic shift is equivalent to the potential energy.

3.1.3 Atom-light interaction

We consider two effects of atom-light interaction: the radiation pressure and the dipole force. The radiation pressure becomes important for near-resonance light, while the dipole force is usually relevant for off-resonant light. The formula presented in this subsection can be found, for example, in Refs. [112, 114].

Let us suppose an atom interacting with a laser beam associated with intensity I and wave vector $\boldsymbol{k}$, the radiation-pressure force is given by

$$\boldsymbol{F}_{\boldsymbol{k}} = \mathrm{Im}\,[\alpha]\,\frac{I}{\varepsilon_0 c}\boldsymbol{k}, \tag{3.5}$$

where α is the complex atomic polarizability. This force is related to the photon absorption rate by the atom, $\gamma_{\boldsymbol{k}}$, according to $\boldsymbol{F}_{\boldsymbol{k}} = \gamma_{\boldsymbol{k}}\hbar\boldsymbol{k}$. In average, the atom is pushed by the recoil momentum $\hbar\boldsymbol{k}$ of the absorbed photons at rate $\gamma_{\boldsymbol{k}}$. The rate is given by

$$\gamma_{\boldsymbol{k}} = \mathrm{Im}\,[\alpha]\,\frac{I}{\varepsilon_0 c\hbar} = \frac{\Gamma}{2}\frac{s}{1+s}, \tag{3.6}$$

where $s = \frac{I/I_{sat}}{1+(\delta/\Gamma)^2}$ is the saturation parameter with δ the detuning with respect to the transition and I_{sat} the saturation intensity of the transition. For laser cooling transition shown in Fig. 3.1, $I_{sat} = 1.67\ \mathrm{mW/cm^2}$.

The concept of radiation pressure is the underlying mechanism for the laser cooling technique, so-called Doppler cooling. For a moving atom with velocity $\boldsymbol{v}$, the Doppler effect modifies the laser beam frequency in the rest frame of the atom. The detuning with respect to the resonance becomes $\delta' = \delta - \boldsymbol{k} \cdot \boldsymbol{v}$, where δ is the initial detuning. For $\delta < 0$, the atom is repelled by any opposing laser beam, since that beam frequency is shifted towards the resonance ($\delta' = 0$). The force $\boldsymbol{F_k}$ acts a viscous damping force. Besides, the spontaneously emitted photons give zero average force because they are emitted in random direction. The Doppler cooling is usually realized by applying three pairs of counter-propagating laser beams in three orthogonal directions. It has characteristic Doppler temperature, $T_D = \hbar\Gamma/2k_B$.

In our experiment, there are three lasers for laser cooling purposes. The first laser is locked to the crossover resonance $F = 2 \to F' = 2 \times 3$ using saturated absorption spectroscopy. The second and the third laser are locked with respect to the first laser. The second laser addresses $F = 1 \to F'$ transitions; it is called the repumper laser. The third laser addresses $F = 2 \to F'$ transitions including the laser cooling transition ($F' = 3$); see Fig. 3.1. Details regarding the laser frequency locking, the optical amplification, and the modulation with acousto-optic modulators (AOMs) can be found in Alain Bernard's thesis [47].

Another force due to the atom-light interaction is the dipole force. This is a conservative force and is associated with an optical potential given by [75]

$$U = -\frac{\mathrm{Re}\,[\alpha]}{2}\frac{I}{\varepsilon_0 c}. \tag{3.7}$$

For far-off resonance, the polarizability is approximately real and independent of the light polarization, yielding

$$\alpha = \frac{6\pi\varepsilon_0 c^3}{\omega_0^2}\frac{\Gamma}{\omega_0^2 - \omega_L^2}, \tag{3.8}$$

where ω_0 and ω_L are the resonant frequency and the laser frequency respectively. In general, condition $\omega_L < \omega_0$ results in attractive potential, while $\omega_L > \omega_0$ results in repulsive potential.

In our experiment, we have a fiber laser at wavelength 1.064 μm used for the optical tweezer and the crossed-dipole trap (see subsections 3.2.5 and 3.2.6). Besides, we also have two lasers at wavelength around 780 nm for the implementation of speckle disorder (see Chap. 4 and Chap. 6).

3.1.4 Imaging of the atomic cloud

We apply two imaging techniques for the characterization of the cold atoms, absorption imaging and fluorescence imaging. Imaging is usually performed at the end of experimental sequence, after certain time-of-flight (TOF). In both techniques, the imaging provides the atomic cloud density integrated over the imaging axis, $n_{2D}(\boldsymbol{r})$. From this, the total number of atoms and the temperature can be obtained.

Absorption imaging. Fig. 3.2(a) shows the schema of absorption imaging. It consists of measuring the light intensity profiles in the imaging plane (the $y-z$ plane in Fig. 3.2(a)) in the presence of atomic cloud, $I(y,z)$, and in the absence of atomic cloud, $I_0(y,z)$. According to the Beer-Lambert law, the density $n_{2D}(y,z)$ corresponds to

$$\begin{aligned} n_{2D}(y,z) &= \int n(x,y,z)\ \mathrm{d}x \\ &= \frac{1}{\sigma}\ln\left(\frac{I_0(y,z)}{I(y,z)}\right), \end{aligned} \tag{3.9}$$

where σ is the scattering cross section. Ideally, the intensity should be weak compared with the saturation intensity, $s \ll 1$. In general, absorption imaging is a convenient technique for calibrating the number of atoms. In practice, we illuminate the atoms by a laser pulse probe resonant with the $F = 2 \rightarrow F' = 3$ transition. The typical pulse duration is 50 µs. In order to respect the condition $s \ll 1$, the laser power is kept below 100 μW. This probe falls on an EMCCD camera (see "EMCCD1" in the figure). Once the atoms are removed, another image with the probe is taken. An additional background image is also taken; this allows subtraction of the background noise.

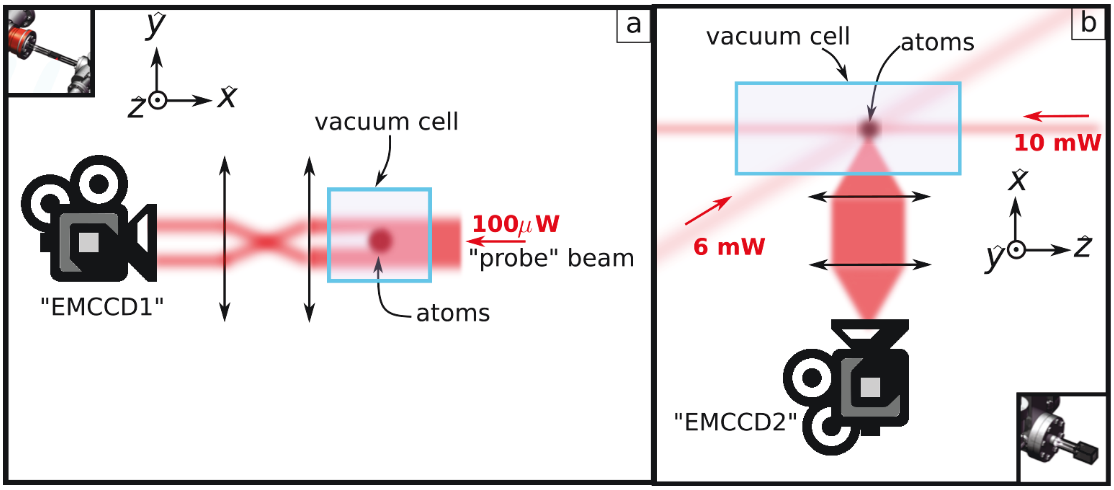

Figure 3.2: (a) **Absorption imaging.** A resonant probe pulse is sent to the atomic cloud, is partially absorbed, and is collected by camera "EMCCD1". The information on the cloud is obtained from the quantity of the light absorbed. (b) **Fluorescence imaging.** Several resonant probes are sent simultaneously to the atomic cloud. The atomic cloud emits fluorescent light which is partially collected by camera "EMCCD2". The information on the cloud is obtained from the estimation of the fluorescence light.

Fluorescence imaging. Fig. 3.2(b) shows one schema of fluorescence imaging[2]. It consists of measuring the light intensity profile in the imaging plane, $I_a(y,z)$, which is directly related to the density $n_{2D}(y,z)$ according to

$$I_a(y,z) = \frac{\Omega}{4\pi}\frac{s}{2(1+s)}\Gamma\hbar\omega_0 n_{2D}(y,z), \tag{3.10}$$

where $\Omega \approx \pi \mathrm{NA}^2$ is the solid angle of the collected fluorescent light, NA is the numerical aperture of the imaging system, and $s = \frac{I/I_{sat}}{1+(\delta/\Gamma)^2}$ is the saturation parameter (as introduced in Eq. 3.6). Ideally, it is better to perform imaging with at high probe power such that $s \gg 1$. Besides, fluorescence imaging is ideal for detecting small number of atoms. In practice, we illuminate the cloud with laser pulses resonant to the $F = 2 \to F' = 3$ transition. The typical pulse duration is 25 µs. In contrast with absorption imaging, the probes do not fall on the EMCCD camera (see "EMCCD2" on Fig. 3.2(b)). The camera collects a fraction of the fluorescence light emitted by the atoms. The intensity $I_a(y,z)$ is obtained from subtraction by an additional background image.

3.2 Experimental sequences of the BEC production

3.2.1 Overview of the experiment

Fig. 3.3 shows an overview of our experimental apparatus. Similar to many ultracold atom experiments, we have a source of atomic beam coming out from an oven containing a sample of rubidium heated at temperature 120 ˚ C. The experiment is carried in a vacuum system. It consists of two vacuum cells. The pressure inside these vacuum cells is maintained below 10^{-11} mbar thanks to the continuously working vacuum pumps; details of the vacuum system can be found in Alain Bernard's thesis [47]. Such low pressure is necessary to suppress collisions between the cooled atoms and the residual atoms in the vacuum cells.

In the first vacuum cell, we perform several experimental sequences consisting of capturing the atoms using Zeeman slower, magneto-optical trap, optical molasses, magnetic trapping, and evaporative cooling with radio-frequency field. Lastly, the atoms are loaded into a movable optical tweezer.

The tweezer allows transport of the cold atoms into the second vacuum cell. By having this additional vacuum cell, we have at our disposition a whole new optical and magnetic access for different experimental realizations. In this cell, the atoms are loaded into a crossed optical dipole trap and evaporative cooling technique is performed in order to realize the Bose-Einstein condensation. In addition, a system of magnetic levitation is implemented. It creates magnetic force which can hold the atoms against gravitational field. Furthermore, we also implement radio-frequency transfer

---

[2] The two schemas presented in Fig. 3.2 are performed in two different vacuum cells.

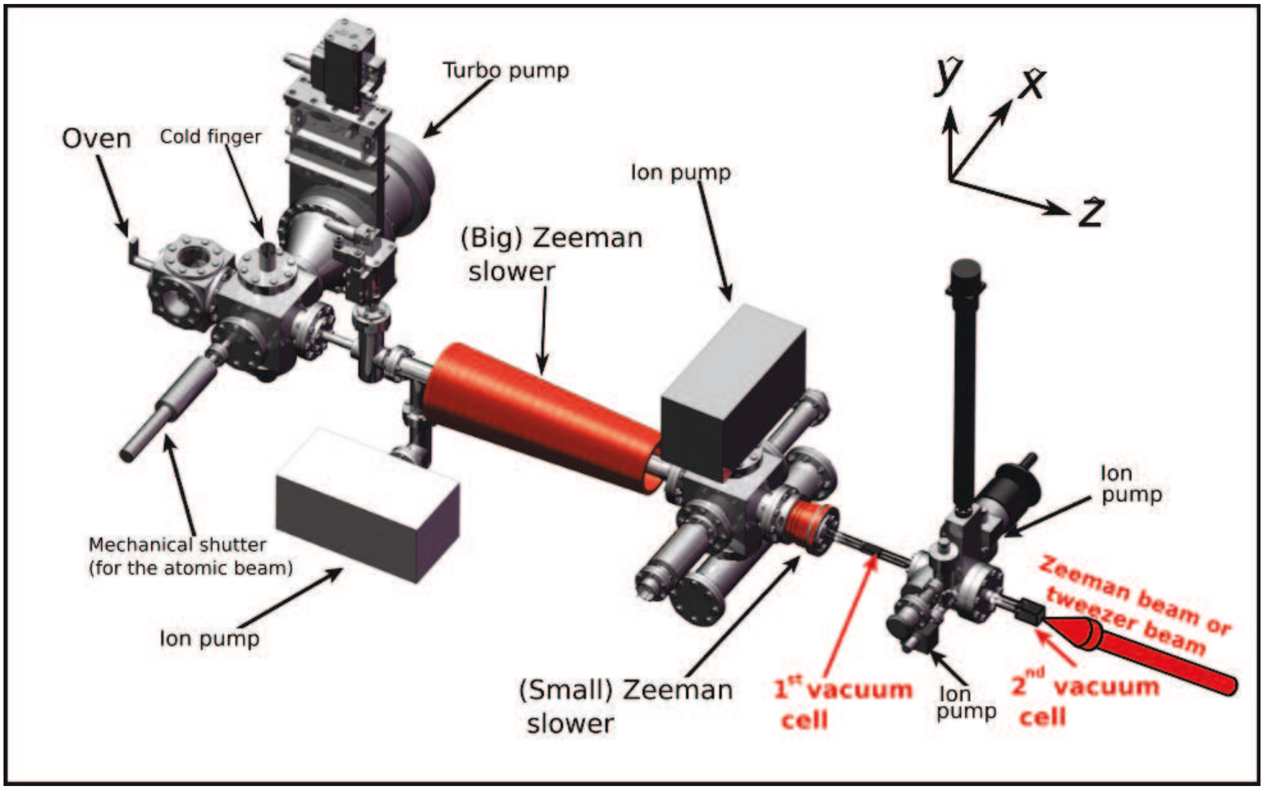

Figure 3.3: **Global view of the experimental apparatus**. Atomic beam coming out of the oven is guided towards the first vacuum cell and the second vacuum cell where the cold atoms are realized. Several vacuum pumps are employed to ensure pressure around 10^{-11} mbar inside the two vacuum cells. z-direction is defined by the axis of the Zeeman slower. y-direction is defined as the upward direction.

(see section 3.3) and speckle laser for the studies of Anderson localization (see Chap. 4). All these experiments would not be possible without an auxiliary vacuum cell.

"Writing" the experimental sequences Performing experimental sequences requires us to establish certain command signals to the lasers, optical modulators, magnetic coils, switches, etc. The command of these instruments are realized with modules sending synchronized analog and TTL signals. During this PhD studies, we have implemented new analog and TTL modules for the experiment. We have purchased them from *National Instrument*; they features 64 TTL channels and 64 analog channels. For our experimental purposes, at least 44 TTL channels and 14 analog channels are needed. All these channels can be synchronized using FPGA. The modules can receive sequences of commands which are written using software CICERO.

3.2.2 Zeeman slower

Zeeman slower decelerates the atomic jet such that the atoms become slow enough to be trapped inside a magneto-optical trap. The details of the Zeeman slower and the MOT can be found in

Ref. [123]. In short, the Zeeman slower consists of several magnetic coils (see “big Zeeman slower” and “small Zeeman slower” in Fig. 3.3) and a laser beam propagating against the atomic jet. The laser beam is σ^+-polarized and resonant to crossover resonance $F = 2 \rightarrow F' = 2 \times 3$. At the atomic referential frame, the laser frequency is shifted closer to $F = 2 \rightarrow F' = 3$ transition due to the Doppler effect. The atoms are slowed down after many cycles of light absorption and spontaneous emission. The Zeeman magnetic field gradient designed to compensate the velocity change such that the resonant condition is maintained. At the end of the slower, the atoms have typical speed of 20 m/s, which is slow enough to allow atom loading into the magneto optical trap (MOT).

The atom loading rate into the MOT is optimized thanks to the transverse molasses at the exit of the oven. It consists of two pairs of counter-propagating laser beams in the horizontal and in the vertical direction. The laser frequency is slightly red-detuned from the $F = 2 \rightarrow F' = 3$ transition, by around -8 MHz. The transverse cooling typically improves the loading rate by a factor of two.

3.2.3 Magneto-optical trap

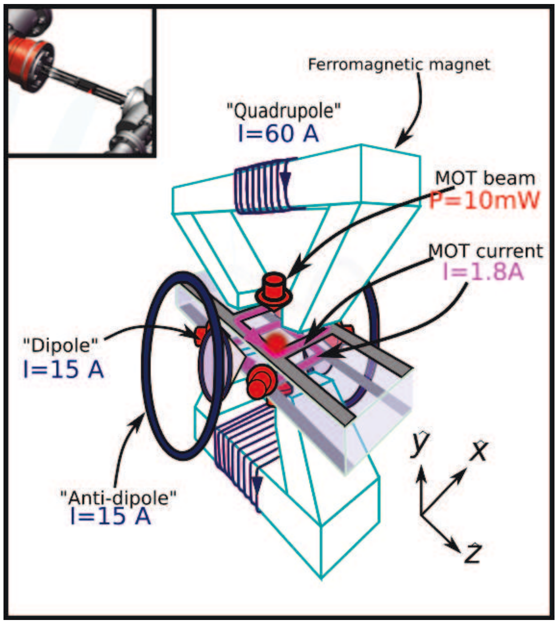

Figure 3.4: **Some experiments in the first vacuum cell**: Magneto-optical trap (MOT) and magnetic trap.

In magneto optical trap (MOT), we perform Doppler cooling technique by using three pairs of counter-propagating laser beam, two orthogonal pairs lie in the lateral direction and one pair is in the vertical direction. Each pair of beams has opposite polarizations, σ^+ and σ^- with respect to its axis. The laser beams are red-detuned with respect to the $F = 2 \rightarrow F' = 3$ transition, with detuning $\delta < 0$ (see Fig. 3.1). δ typically starts with -16 MHz. The power of each beam is typically

10 mW. The pair of MOT coils generates a quadrupole magnetic field. The magnetic field gradient is aligned with the direction of σ^+ beam creating additional restoring force for atoms deviating from the center of the trap. Besides, atoms falling into the level $F = 1$ can be brought back to the cooling transition, thanks to the repumper beams resonant with $F = 1 \rightarrow F' = 2$ transition (see "Repumper" in Fig. 3.1). In practice, the repumper beams are combined with the MOT beams. After 5 seconds of loading time, we have typically 10^9 atoms in the MOT.

In order to cool further the atoms, we switch off the MOT magnetic field and ramp the laser detuning to -60 MHz in typically 6 ms [124, 125], the so-called optical molasses step. With this technique, we can achieve temperature of around 15 μK. The final temperature is very sensitive to the compensation fields surrounding the vacuum cell. These fields are controlled using four pairs of compensation coils, three pairs for bias fields in all directions in space and one pair for compensation of quadrupole fields.

At the end of the MOT experiments, we transfer the atoms into a magnetic trap. The atom loading into the magnetic trap is sensitive to the position of the atomic cloud which can be adjusted thanks to three pairs of magnetic coils generating bias fields in three orthogonal directions. These fields have same current source as the MOT magnetic field. These bias fields allow fine tuning of the zero-point of magnetic field in which the MOT cloud is formed.

3.2.4 Magnetic trap

At the end of the MOT sequences, we load the atoms into the magnetic trap depicted in Fig. 3.4. We make use of Ioffe-Pritchard trap and the details regarding the coils and their characterization can be found in Ref. [123]. The magnetic trap potential, $U(\boldsymbol{r})$, is proportional to the magnetic field strength, $\boldsymbol{B}(\boldsymbol{r})$, according to

$$U(\boldsymbol{r}) = m_F g_F \mu_B \left|\boldsymbol{B}(\boldsymbol{r})\right|, \tag{3.11}$$

with μ_B the Bohr magneton, g_F the Landé factor and m_F the magnetic number. The magnetic field is superposition of dipole field and quadrupole field. The dipole field creates strong bias field along the x-axis which defines the quantization axis. In our experiment, the dipole field is created from two pairs of dipole coils (see "Dipole" and "Anti-dipole" in Fig. 3.4). The dipole field is given by

$$\boldsymbol{B_D} = B_0 \boldsymbol{e_x} + b'' \left(x^2 - \rho^2/2\right) \boldsymbol{e_x} - b'' x \boldsymbol{\rho}, \tag{3.12}$$

where $\boldsymbol{\rho}$ is the radial coordinates in $y - z$ plane. The parameters B_0 and b'' are linearly related to the "dipole" current and "anti-dipole" current. The quadrupole field is created using a pair of electromagnet (see "Quadrupole" in Fig. 3.4). The magnetic field is given by

$$\boldsymbol{B_Q} = b'(y\boldsymbol{e_y} - z\boldsymbol{e_z}). \tag{3.13}$$

The parameter b' depends on the "quadrupole" current. The total field is given by $\boldsymbol{B} = \boldsymbol{B_D} + \boldsymbol{B_Q}$. The field strength $|\boldsymbol{B}|$ has a minima which defines the center of the trap.

The minima of $|\boldsymbol{B}|$ becomes a potential minima for atomic states satisfying $m_F g_F > 0$. This condition implies three trapping states: $|F = 1,\ m_F = -1\rangle$, $|F = 2,\ m_F = 1\rangle$, and $|F = 2,\ m_F = 2\rangle$. In the experiment, we condense the atoms in the trapping state $|F = 1,\ m_F = -1\rangle$ before performing evaporative cooling. This is done by applying a pulse resonant to $F = 2 \rightarrow F' = 2$ transition in order to pump the atoms into the level $F = 1$, followed by an optical pumping pulse resonant to $F = 1 \rightarrow F' = 1$ transition to optimize the number of atoms in the state $|F = 1,\ m_F = -1\rangle$. While the first pulse is necessary, the second optical pumping allows optimization of the number of atoms by a factor of two. Typically we obtain around 10^9 atoms at temperature of 300 μK before the evaporative cooling. This high temperature is attributed to application of trap compression which is required for efficient evaporative cooling.

Evaporative cooling is realized by lowering the trap depth by applying so-called RF-knife. It consists of applying radio-frequency (RF) field, which induces spin flips between different states in the level $F = 1$ [126,127]. The RF frequency ν_{rf} becomes the cut-off energy $(h\nu_{rf})$ for the atoms to leave the trap. As the most energetic atoms leave the trap, the atoms with lower energy thermalize. The frequency is ramped down progressively; the sequence takes around 9.25 s. At the end, we obtain around 3×10^7 atoms with temperature of 20 μK. The phase density is typically increased from 10^{-8} to 10^{-4} .

3.2.5 Laser tweezer

The atoms are loaded into a laser tweezer at the end of the RF evaporative cooling. The tweezer consists essentially of a laser beam at 1.07 µm which is focalized around the atomic cloud (see Fig. 3.5). The laser frequency is far red-detuned from the rubidium D line, resulting in an attractive potential. This is called far-off resonant trap (FORT). A converging lens is mounted on a programmable linear translation stage (*Aerotech ABL80040*). As depicted in Fig. 3.5, atoms trapped around the focal point can be transported between the first vacuum cell and the second vacuum cell by applying a translation of 40 cm in the $+z$ direction.

The laser intensity profile can be described as Gaussian beam. Let us denote z as the distance from the focal point and r as the radial distance from the beam axis. In the transverse plane, the intensity has isotropic Gaussian distribution, $I \propto \exp\left(-2r^2/w^2(z)\right)$. $w(z)$ is defined as the beam waist which varies with z; it is also called $1/e^2$-radius. As depicted in the inset of Fig. 3.5, the beam waist has a minima at focal point, w_0. The waist $w(z)$ varies as $w(z) = w_0\sqrt{1 + z^2/z_R^2}$, where z_R is the Rayleigh length; $z_R = \pi w_0^2/\lambda$. Let us consider a beam with power P_L. By inserting the

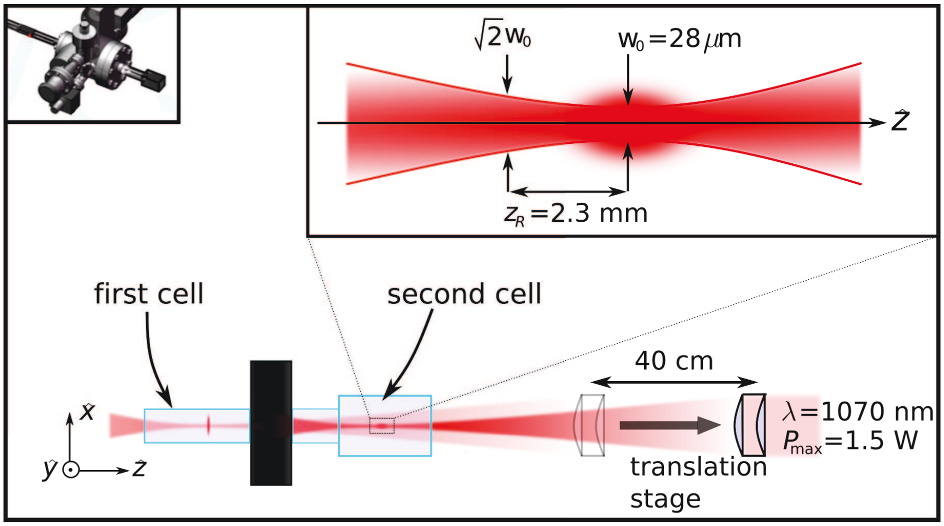

Figure 3.5: **Laser tweezer translation**. The tweezer consists of a focused laser (of wavelength $\lambda = 1070$ nm) whose focal point can be translated using a programmable translation stage. The atoms are trapped around the focal point of the tweezer. The transfer is done by focalizing the tweezer in the first vacuum cell, ramping the power of the tweezer up to $P_{\max} = 1.5$ W and translating the focal point into the second vacuum cell.

Gaussian intensity profile into Eq. 3.7, we obtain the following expression of optical potential

$$U(r,z) = -\frac{\mathrm{Re}\,[\alpha]}{\varepsilon_0 c}\frac{P_L}{\pi w_0^2}\left(\frac{w_0}{w(z)}\right)^2 \exp\left(-2\left(\frac{r}{w(z)}\right)^2\right). \tag{3.14}$$

We define optical trap depth as $U_L = U(r=0, z=0)$, yielding

$$U_L = -\frac{\mathrm{Re}\,[\alpha]}{\varepsilon_0 c}\frac{P_L}{\pi w_0^2}. \tag{3.15}$$

By approximating the potential to a three dimensional harmonic oscillator, we deduce the transversal and longitudinal trap frequencies, ω_r and ω_z respectively,

$$\omega_r = \sqrt{\frac{4U_L}{m w_0^2}}\ ,\ \omega_z = \sqrt{\frac{2U_L}{m z_R^2}}. \tag{3.16}$$

As shown in Fig. 3.5, the laser waist ($1/e^2-$radius) is 28 μm and its maximum power is $P_{\max} =$ 1.5 W. For $P_L = P_{\max} = 1.5$ W and $w_0 = 28\mu$m, we deduce the optical depth $k_B \times 86$ μK , $\omega_r/2\pi = 2$ kHz and $\omega_z/2\pi = 10$ Hz.

We control the power of the tweezer using a servo-loop system built with an acousto-optic modulator (AOM) and a photodiode (PD). Besides, we can also adjust the position of the tweezer using a piezoelectric inducer.

In order to transfer the atoms from the magnetic trap into the tweezer, we ramp down the quadrupole current to decompress the trap confinement and ramp up the tweezer power. Typically, we can achieve efficiency of 50%. The limitations come from the mismatch between the magnetic trap geometry and the tweezer trap geometry and 3-body losses due to high atomic density in the tweezer [128]. Furthermore, the translation takes typically 2 seconds. Details regarding the transfer optimization can be found in Ref. [47]. Typically we transfer around 5×10^6 atoms with temperature of 10 µK. This corresponds to around 40% of transfer efficiency with slight heating.

3.2.6 Crossed optical dipole trap

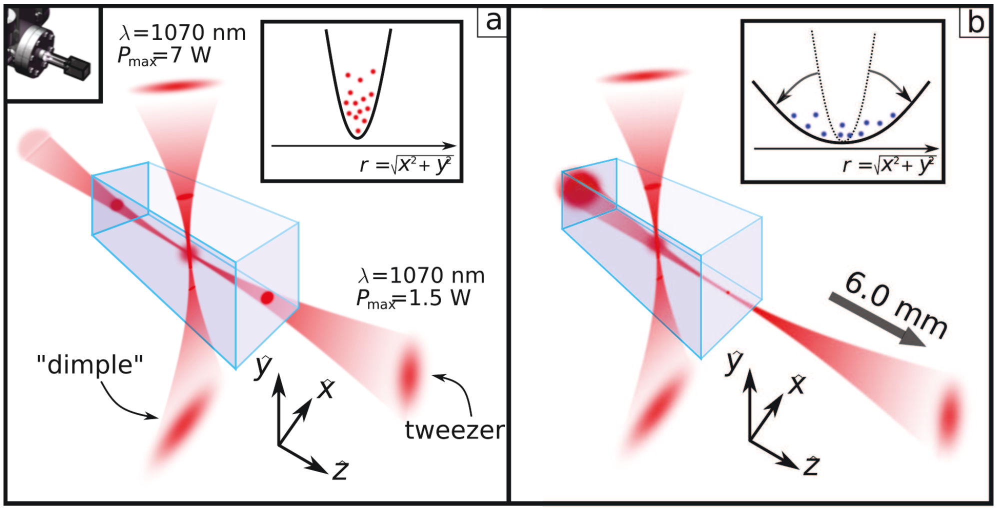

Figure 3.6: **All optical evaporative cooling in the crossed optical dipole trap**. (a) The atoms are trapped in the overlap between the tweezer beam and the “dimple” beam. During evaporative cooling, both the power of the tweezer beam and “dimple” beam are ramped down simultaneously. (b) Towards the end of the cooling, adiabatic opening is performed by translating the tweezer focal point by 6 mm in the z-direction. It simultaneously decreases the optical depth and the trap confinement.

The crossed optical dipole trap is considered as the first experimental realization in the second cell. Fig. 3.6(a) depicts the realization of the trap by superposing the tweezer beam and “dimple” beam. The trap has strong confinement in all direction. The dimple beam enhances confinement along the tweezer axis ($z-$axis), resulting in a quasi-isotropic confinement. Besides, the dimple beam has elliptic shape, the beam waist along x-axis, $w_x = 203$ µm, is wider than that along z-axis, $w_z = 91$ µm. The dimple beam has the same laser source as the tweezer. Its power is also controllable using a servo-loop system similar to that of the tweezer. Its maximum power is about 7W.

The dipole trap has effectively two parameters, the tweezer power and the dimple power. We perform all-optical evaporative cooling by ramping down simultaneously the tweezer power and dimple power. This lower the depth and the confinement of the trap. In addition, the magnetic levitation is switched on once the atoms are transferred into the second cell. As discussed further in the next subsection, it eliminates the sagging effect of the optical potential due to the gravitational field. In absence of the sagging effect, we can perform evaporative cooling to a very low optical depth. Furthermore, we also perform adiabatic opening. As shown in the Fig.3.6(b), it is done by translating the position of the focal by 6 mm in z-direction. It increases the tweezer beam waist at the crossed point and thus lowers the confinement. At the end of the sequence, we obtain shallow trap with typical characteristics, $\omega_x = \omega_y \approx \omega_{r,tweezer} = 2\pi \times 3.9$ Hz, $\omega_z \approx \omega_{r,dimple} = 2\pi \times 5.3$ Hz, and $U_0/k_BT = 15$ nK.

3.2.7 Magnetic levitation

Magnetic levitation has a critical role in our experiment. Its purpose is to levitate the atoms against gravitational field. This has two importances. First, it becomes feasible to prolong the TOF from typically 10 ms to several seconds! Second, the levitation eliminates potential sagging due gravitational field. As mentioned in previous subsection, it facilitates all-optical evaporative cooling to temperature of few nanoKelvins.

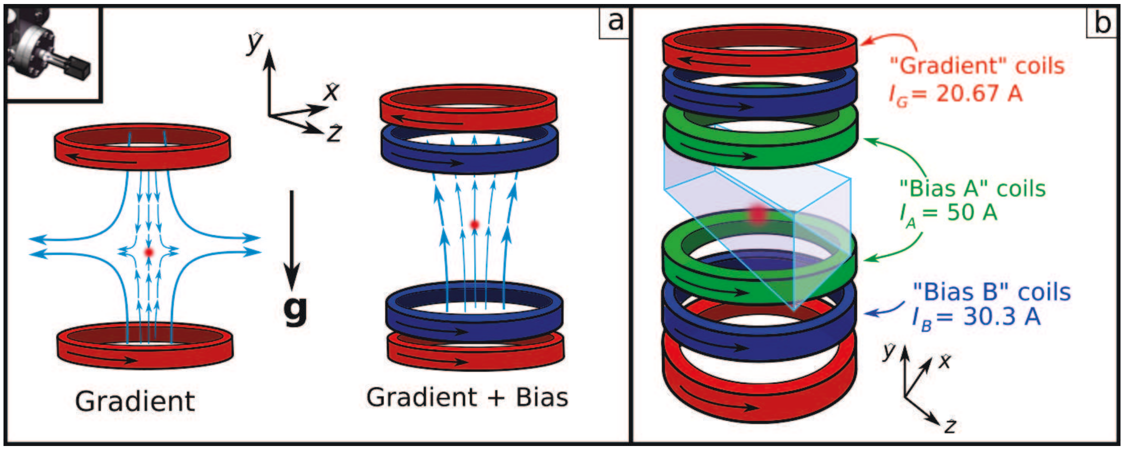

Figure 3.7: **Magnetic levitation**. (a) Left: the gradient magnetic field for levitation. Right: the gradient field combined with a bias field. (b) Our realization of magnetic levitation with three pairs of coils: one pair of coils generating gradient field (“Gradient” coils) and two pairs of coils generating bias magnetic field (“Bias A” and “Bias B”).

Fig. 3.7(b) depicts the schema of the magnetic levitation. More details regarding the magnetic levitation can be found in Ref. [47]. The magnetic field consists of a gradient magnetic field in y-direction which compensates the gravitational field and a bias field which sets the quantization axis. The gradient field is given by $\boldsymbol{B_G} = -b'(y\boldsymbol{e_y} - \boldsymbol{\rho}/2)$, where $\boldsymbol{\rho}$ is now a radial vector in $x - z$ plane. This field is generated by a pair of coils (see “Gradient” in Fig. 3.7(b)). The bias field is given by $\boldsymbol{B_B} = (B_0 + b''(y^2 - \rho^2/2))\,\boldsymbol{e_y} - b''y\boldsymbol{\rho}$. This field is generated by two pairs of coils (see “Bias A” and “Bias B” coils in Fig. 3.7(b)). These pairs have independent currents I_A and I_B respectively. The two variables allow independent control of the field parameters B_0 and b''.

The magnetic potential is given by $U_{mag}(y,\rho) = g_F m_F \mu_B B$, with $B = |\boldsymbol{B_G} + \boldsymbol{B_B}|$. Similar to the magnetic trap discussed in subsection 3.2.4, there are three states satisfying $g_F m_F > 0$. In particular, we are interested in the following two states with $g_F m_F \approx 1/2$:

$$\begin{aligned} |1\rangle &\equiv |F=1,\ m_F=-1\rangle \\ |2\rangle &\equiv |F=2,\ m_F=+1\rangle\,. \end{aligned} \tag{3.17}$$

These two states possess similar energy shift and magnetic force. In our experiment, the atoms are kept in one of these two states. These two states are the ones considered for the state-dependent disorder depicted in Fig. 1.3.

In order to provide force against gravity, we require $b' = mg/(g_F m_F \mu_B)$; here $g_F m_F$ can be replaced by 1/2. With approximation up to second order terms, we obtain

$$\begin{aligned} U_{\text{tot}}(y,\rho) &= g_F m_F \mu_B B_0 + \frac{1}{2} m\omega_y^2 y^2 + \frac{1}{2} m\omega_\rho^2 \rho^2, \\ \omega_y^2 &= \frac{2 g_F m_F \mu_B}{m} b'', \\ \omega_\rho^2 &= \frac{g_F m_F \mu_B}{m} \left(\frac{b'^2}{4B_0} - b'' \right). \end{aligned} \tag{3.18}$$

These relations imply that harmonic potential occurs when $b'' > 0$ and $b'^2 > 4B_0 b''$. Isotropic trap corresponds to $b'' = \frac{b'^2}{12B_0}$.

3.2.8 Obtention of Bose-Einstein Condensation

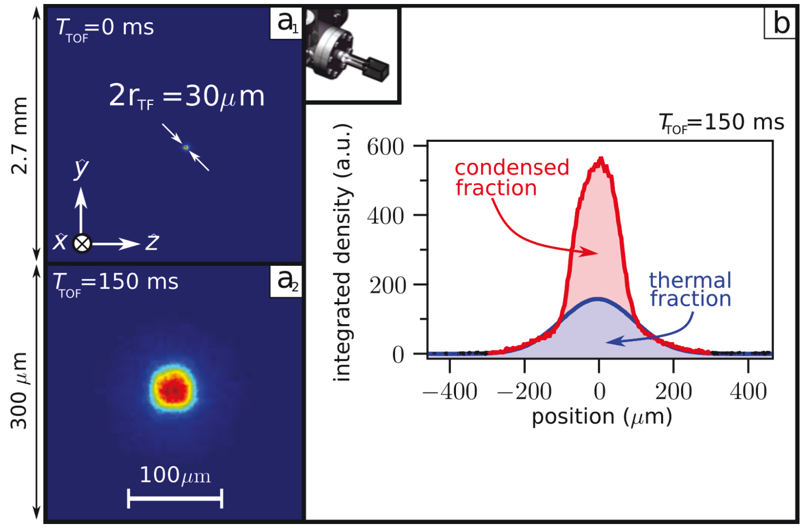

Figure 3.8: **BEC**. (a) Bose-Einstein condensation in the crossed optical dipole trap detected with fluorescence imaging (see Fig. 3.2(b)). (TOF = 0 ms for (a_1) and TOF = 150 ms for (a_2)). (b) The atomic density obtained from Fig. (a_2). It shows two components: the condensed (BEC) fraction and the thermal fraction.

At the end of the evaporative cooling in the crossed optical dipole trap, we obtain Bose-Einstein condensation containing around 200k atoms in spin state $|1\rangle = |F = 1,\ m_F = -1\rangle$. The critical temperature (see Eq. 3.1) is estimated at 11 nK. The atomic cloud contains condensed fraction and thermal fraction. The density of the thermal fraction follows Gaussian distribution. The density of the condensed fraction is approximately given by the solution of Gross-Pitaevskii equation in Thomas-Fermi regime, which follows

$$n(\boldsymbol{r}) = \max\left(\frac{\mu - V(\boldsymbol{r})}{g}, 0\right). \tag{3.19}$$

$\mu = \frac{1}{2}\left(15aN\hbar\bar{\omega}^3\right)^{2/5} m^{1/5}$ is the chemical potential, with $\bar{\omega} = \left(\omega_x\omega_y\omega_z\right)^{1/3}$ and $g = 4\pi a\hbar^2/m$. The condensed fraction has inverted parabolic shape as a result of harmonic trap. The de Broglie wavelength is in the same order of magnitude as the Thomas-Fermi radius, $r_{TF} \sim \lambda_{dB}$. This characteristic length also becomes the effective size of the BEC, which depends on the trap frequencies, $r_{TF,i} = \sqrt{\frac{2\mu}{m\omega_i^2}},\ i = x,\ y,\ \text{or}\ z$.

The BEC characterization consists of switching off the dipole trap and observing the expansion of the atomic cloud after relatively long TOF (time-of-flight). Fig. 3.8(a) depicts the images of the BEC obtained at two different TOFs, 0 ms and 150 ms. The Thomas-Fermi radius is around 15 µm. TOF as long as 150 ms can be realized thanks to the magnetic levitation. As depicted in Fig. 3.8(b), for TOF of 150 ms, we can observe two different components of the cloud, the BEC fraction and the thermal fraction. From the thermal fraction, we estimate the temperature which is about 5 nK. Lastly, with $a = 100\ a_0$ [129], we estimate the chemical energy, $\mu = h \times 40$ Hz.

3.3 Radio-frequency transfer

In addition to dimple beam and magnetic levitation, the experiments in the second vacuum cell also include radio-frequency (rf) transfer between states $|1\rangle = |F = 1,\ m_F = -1\rangle$ and $|2\rangle = |F = 2,\ m_F = 1\rangle$. With respect to the experimental scheme presented in Fig. 1.3, states $|1\rangle$ and $|2\rangle$ correspond to the initial and the final states respectively. Since they have difference of magnetic number $\Delta m = +2$, we implement the rf transfer based on mechanism of two-photon transition.

This section contains three subsections. In the first subsection, we discuss the principle of the two-photon transition and the implementation of the rf transfer. In the second subsection, we discuss the spectroscopy technique based on the rf transfer. In our experiment, the bias field B_0 is adjusted at $B_0 = B_0^\star$, where $B_0^\star$ is the magic magnetic field mentioned in subsection 3.1.2. This is critical for the robustness of our spectroscopy. The calibration is presented in the third subsection.

3.3.1 Rf transfer based on two-photon transition

Fig. 3.9 depicts the schema of the two-photon transition. It involves two electromagnetic fields, a microwave field and a radio-frequency field of frequencies ω_{mw} and ω_{rf} respectively. The fields couple the state $|1\rangle$ to the state $|2\rangle$ via an intermediate state $|\tilde{1}\rangle = |F = 2,\ m_F = 0\rangle$. The microwave drives the $|1\rangle \to |\tilde{1}\rangle$ transition with coupling constant Ω_{mw} and detuning $\delta_{\mathrm{mw}} \equiv \Delta_{1,\tilde{1}} - \omega_{\mathrm{mw}}$, where $\Delta_{1,\tilde{1}}$ represents the frequency of the $|1\rangle \to |\tilde{1}\rangle$ transition . The radio field drives the $|\tilde{1}\rangle \to |2\rangle$ with coupling constant Ω_{rf}.

Let us also introduce the frequency of the $|1\rangle \to |2\rangle$ transition $\Delta_{1,2}$, the two-photon frequency $\omega \equiv \omega_{\mathrm{mw}} + \omega_{\mathrm{rf}}$, and the two-photon detuning $\delta \equiv \omega - \Delta_{1,2}$. The multilevel system behave effectively as a two-level system (of states $|1\rangle$ and $|2\rangle$) under approximations [130]

$$\delta_{\mathrm{mw}} \gg \Omega_{\mathrm{mw}}, \Omega_{\mathrm{rf}}, \delta. \tag{3.20}$$

Under these conditions, the effective two-level system can be described by an effective detuning δ and an effective coupling

$$\Omega = \frac{\Omega_{\mathrm{mw}}\Omega_{\mathrm{rf}}}{2\delta_{\mathrm{mw}}}. \tag{3.21}$$

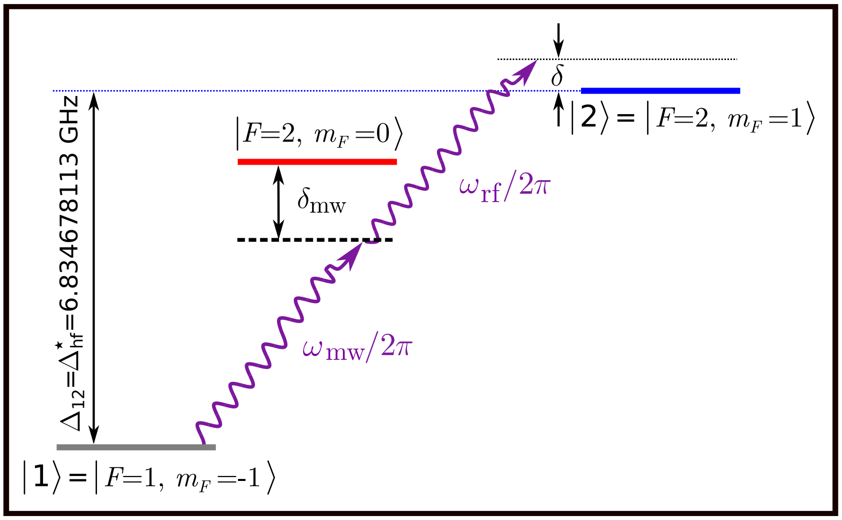

Figure 3.9: **Two-photon transition**. A microwave field of frequency ω_{mw} couples state $|1\rangle$ to an intermediate state $|\tilde{1}\rangle = |F = 2,\ m_F = 0\rangle$. A radio wave of frequency ω_{rf} couples the state $|\tilde{1}\rangle$ to the state $|2\rangle$. Under appropriate approximations, the atom-fields system behaves as an effective two-level system of states $|1\rangle$ and $|2\rangle$ interacting with an effective field of detuning δ and Rabi coupling $\Omega = \frac{\Omega_{\mathrm{mw}}\Omega_{\mathrm{rf}}}{2\delta_{\mathrm{mw}}}$; Ω_{mw} and Ω_{rf} are the coupling constants associated with the microwave and radio wave fields respectively.

Source of microwave and radio fields. Details regarding the radio-frequency circuit can be found in Ref. [52]. The microwave field is obtained by mixing a microwave generated by a synthesizer and a radio wave generated by a programmable DDS (Direct Digital Synthesizer). The synthesizer *BHE-BSVC14D* sends a microwave at fixed frequency $f_s = 6.910$ GHz. The DDS sends a radio wave at tunable frequency f_1 around 78.1 MHz. The mixed wave has frequency $\omega_{\mathrm{mw}} = 2\pi \times (f_s - f_1)$. It is then amplified and sent to an antenna located near the atomic cloud. The radio field for the two-photon transition is generated by another DDS. The frequency of the radio wave is set at $f_2 = \frac{\omega_{\mathrm{rf}}}{2\pi} = 2.8$ MHz. It is then amplified and sent to another antenna located near the atomic cloud.

3.3.2 Radio-frequency transfer: spectroscopy

The spectroscopy consists of performing the rf transfer at different detuning δ. Initially around $N \sim 2 \times 10^5$ atoms are in the state $|1\rangle$. When the fields are switched on, some atoms are transferred into the state $|2\rangle$. For transfer of duration t_0, the fraction of the transferred atoms is given by

$$p_2(t_0, \delta) = \frac{\Omega^2}{\Omega^2 + \delta^2} \sin^2\left(\frac{\sqrt{\Omega^2 + \delta^2}}{2} t_0\right) = \frac{\Omega^2 t_0^2}{4} \mathrm{sinc}^2\left(\frac{\sqrt{\Omega^2 + \delta^2}}{2} t_0\right), \tag{3.22}$$

i.e., Rabi oscillation at frequency $\sqrt{\Omega^2 + \delta^2}$. Fig. 3.10 depicts the typical oscillation obtained experimentally for $\delta = 0$. The oscillation decays with decoherence time $T_d = 62$ ms.

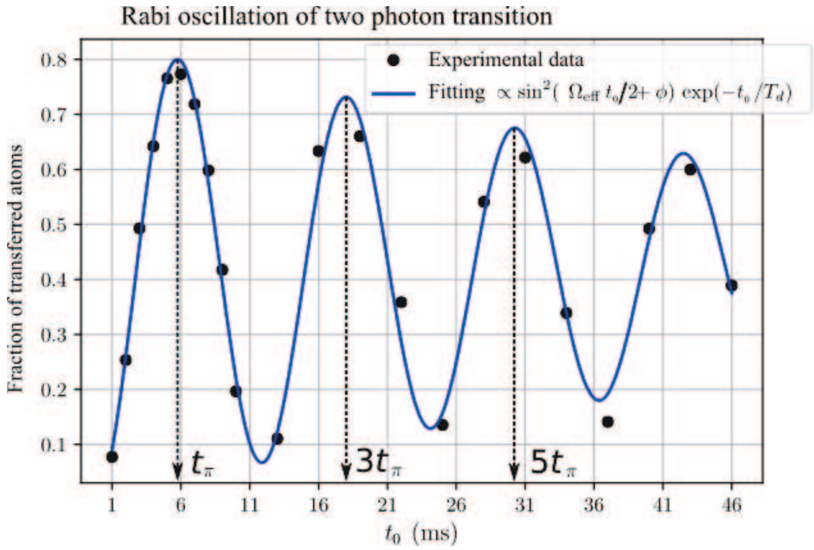

Figure 3.10: **Rabi oscillation of two-photon transition**. We measure the fraction of atom transferred from the state $|1\rangle$ into the state $|2\rangle$ resulting from the rf transfer of duration t_0. Experimental data are shown in black points and the fitting is shown in blue line. In this example, the fitting gives $\Omega_{\mathrm{eff}} = 2\pi \times 40$ Hz and $T_d = 62$ ms; $t_\pi = \pi/(2\Omega_{\mathrm{eff}}) \sim 5$ ms.

Spectroscopy. The rf spectroscopy is performed at a given transfer time t_0 and for a range of detuning δ. Ideally, it is performed in perturbative regime, i.e. $\Omega t_0 \ll 1$. In this regime, the excitation spectrum can be approximated by the squared sinus cardinal function in accordance with Eq. 3.22 at the limit $\Omega \to 0$. The excitation spectrum can also be related to the Fourier transformation of the rf-transfer pulse. As a result, the resolution width is approximately proportional to the inverse of the transfer time.

Fig. 3.11 shows the excitation spectrum corresponding to $t_0 = 5$ ms, $t_0 = 33$ ms, and $t_0 = 100$ ms respectively. For these cases, condition $\Omega t_0 \ll 1$ is respected. We remark that the spectrum width decreases as we increase the time t_0. We can remark that the excitation spectrum approaches the squared sinus cardinal profile for $t_0 = 33$ ms and $t_0 = 5$ ms, where $t_0 \lesssim T_d$. For $t_0 = 100$ ms, the effect of the finite lifetime T_d on the excitation spectrum starts to appear. Dependence $\exp(-t/T_d)$ of can be associated with Lorentzian spectrum of FWHM width $T_d^{-1} = \pi \times 5$ Hz. This limits the energy resolution of the spectroscopy. Overall, we have limit of energy resolution of around 10 Hz.

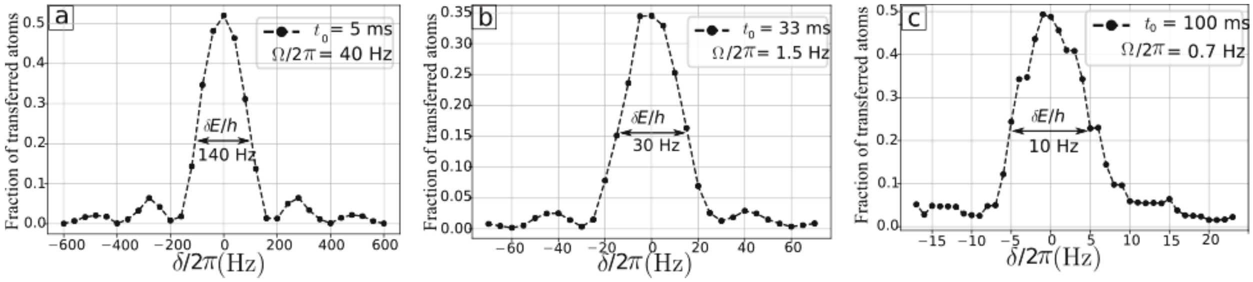

Figure 3.11: The excitation spectrums are obtained by varying δ, the detuning of two-photon resonance at a fixed applied time t_0. The plots corresponds to $t_0 = 5$ ms, $t_0 = 33$ ms, and $t_0 = 100$ ms respectively.

3.3.3 Two-photon transition: calibration of the bias field

The spectroscopy measurement presented in previous subsection can be vulnerable to any undesired fluctuation of magnetic field, especially for the finest energy spectrum. For this reason, the bias magnetic field is set at $B_0 = B_0^\star$, whereby there is zero difference between susceptibility of states $|1\rangle$ and $|2\rangle$. Around this value the energy difference $\Delta E_{1,2}$ becomes less sensitive to change in magnetic field; $\frac{\mathrm{d}\Delta E_{1,2}}{\mathrm{d}B_0} = 0$.

The nonlinear dependence of the energy shift on magnetic field has been discussed in subsection 3.1.2; see also Fig. 3.1 on the depiction of the *Breit-Rabi* formula. For convenience, we can assume that the atom is at the center of the magnetic levitation. The energy shifts of states $|2\rangle$ and $|1\rangle$ are

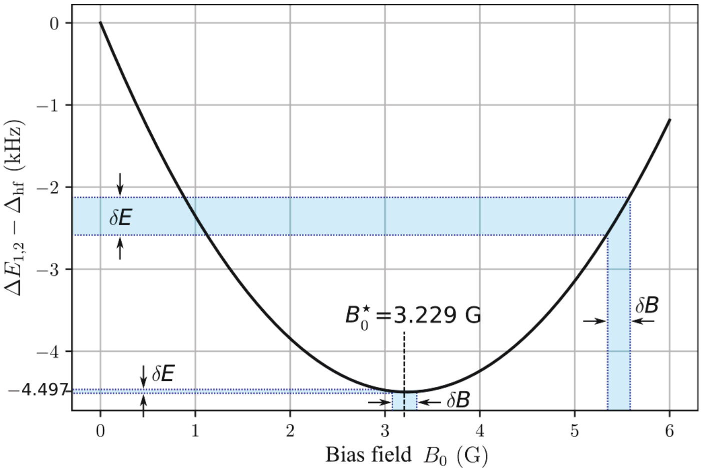

Figure 3.12: Dependence of the energy difference between states $|1\rangle$ and $|2\rangle$ on the applied bias field B_0. It is least sensitive to magnetic inhomogeneity when $\frac{\mathrm{d}\Delta E_{1,2}}{\mathrm{d}B_0} = 0$ corresponding to the minima. For field in the order of several gauss, the dependence is parabolic. The minima corresponds to $B_0 = B_0^\star = 3.229$ Gauss.

given by the *Breit-Rabi* formula,

$$\begin{aligned} E_2 &= \mu_B g_I m_{F,2} B_0 + \frac{h\Delta_{\mathrm{hf}}}{2}\sqrt{1 + m_{F,2}\beta + \beta^2}, \\ E_1 &= \mu_B g_I m_{F,1} B_0 - \frac{h\Delta_{\mathrm{hf}}}{2}\sqrt{1 + m_{F,1}\beta + \beta^2}, \end{aligned} \tag{3.23}$$

where $h\Delta_{\mathrm{hf}}$ is the hyperfine splitting of the ground state, $\beta = (g_J - g_I)\mu_B B_0/(h\Delta_{\mathrm{hf}})$, $m_{F,1} = -1$, and $m_{F,2} = 1$. In the weak field limit, $E_1 = -\frac{h\Delta_{\mathrm{hf}}}{2} + g_{F=1} m_{F,1}\mu_B B_0$, $E_2 = \frac{h\Delta_{\mathrm{hf}}}{2} + g_{F=2} m_{F,2}\mu_B B_0$; we find $g_{F=1} = -g_J/4 + 5g_I/4$ and $g_{F=2} = g_J/4 + 3g_I/4$. Developing $\Delta E_{1,2}$ to the third order yields

$$\Delta E_{1,2} \equiv E_2 - E_1 = h\Delta_{\mathrm{hf}} + 2g_I\mu_B B_0 + \frac{3\beta^2}{8} h\Delta_{\mathrm{hf}} + O(\beta^4). \tag{3.24}$$

As a result, we remark a parabolic dependence on the bias field B_0; see Fig. 3.12. By evaluating the solution for $\frac{\mathrm{d}}{\mathrm{d}\beta}(E_2 - E_1) = 0$, we obtain a minima corresponding to the aforementioned $B_0 = B_0^\star = -\frac{8}{3}\frac{g_I}{(g_J - g_I)^2}\frac{h\Delta_{\mathrm{hf}}}{\mu_B} = 3.229$ Gauss.

The magic bias field $B_0^\star$ corresponds to an effective splitting $\Delta_{\mathrm{hf}}^\star \equiv \Delta E_{1,2}/h|_{B_0 = B_0^\star}$. In practice, the bias current I_A generating the bias field is tunable; the bias field is proportional to the current I_A. This allows measurement of the frequency shift $\delta_0 = (\Delta_{1,2} - \Delta_{\mathrm{hf}}^\star)/2\pi$ depicted in Fig. 3.12; only "Bias A" was switched on for this characterization. Fig. 3.13 depicts the measured position of the shift δ_0 of excitation spectrum against the applied current I_A. The excitation spectrum is performed at $t_0 = 100$ ms. It shows expected parabolic dependence of δ_0 on I_A. As shown in the figure, the magic bias field corresponds to current $I^* = 0.975$ A.

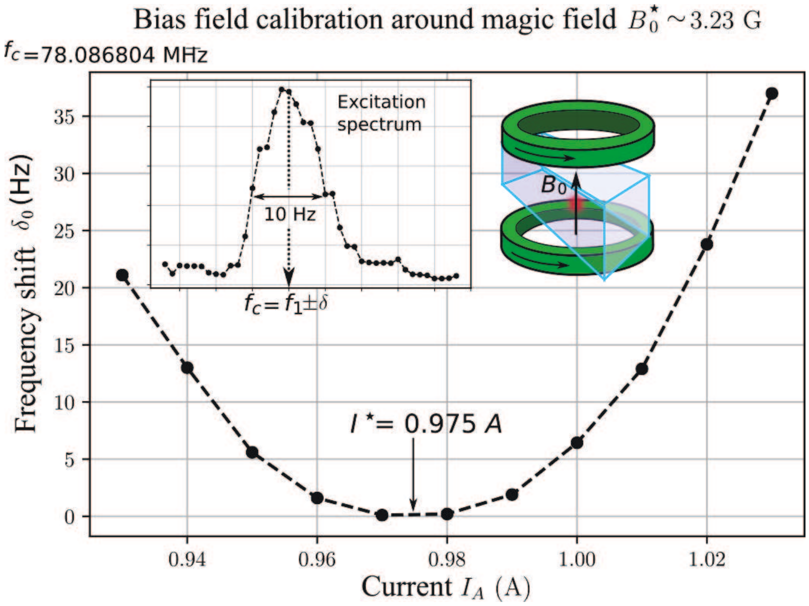

Figure 3.13: Resonance shift as function of the applied bias current generating the bias field. It shows parabolic dependence similar to the dependence on the bias field (see Fig. 3.12).

3.4 Conclusion

In this chapter, we have described the procedure of the matter-wave production from Bose-Einstein condensation (BEC) of rubidium-87 atoms. The BEC cloud contains around 10^5 atoms with a temperature of 5 nK; the ultracold atoms can be considered as a quasi-plane wave. In addition, the number of atoms would be sufficient for obtaining good signal to noise ratio.

Thanks to the magnetic levitation system, the atoms can be held against gravity for several seconds! This would be critical for observing the atomic cloud expansion in presence of disordered potential. Besides, the atoms can be either in states $|1\rangle = |F = 1,\ m_F = -1\rangle$ or $|2\rangle = |F = 2,\ m_F = +1\rangle$. For the realization of state-dependent disorder, spin state $|1\rangle$ will be the one which is insensitive to the disorder.

In section 3.3, we have presented the procedure of radio frequency transfer between the two states based on mechanism of two-photon transition. The spectroscopy measurements show limit of energy resolution of 10 Hz. Combined with state-dependent disorder, we could achieve energy-resolved matter wave. The energy inside the disorder is given by $\mathcal{E}_\delta = \hbar\delta$ and is tunable.

Chapter 4

State-dependent speckle disorder

Contents

In our experiment, we realize disordered potentials for ultracold atoms with laser speckle. Laser speckle has several advantages. Firstly, the properties are well understood [131, 132]. The applications of the speckle phenomena also present across different fields such as stellar speckle interferometry [133], imaging through scattering medium [134], and even detection of denaturation of milk [135]. Secondly, its implementation is relatively easy.

In this chapter, we present the realization of the state-dependent speckle disordered potential for the ultracold atoms. In the first section, we review certain properties of speckle disorder. In the second section, we present the implementation of the laser speckle. In the third section we discuss the state-dependent disordered potential created by the laser speckle.

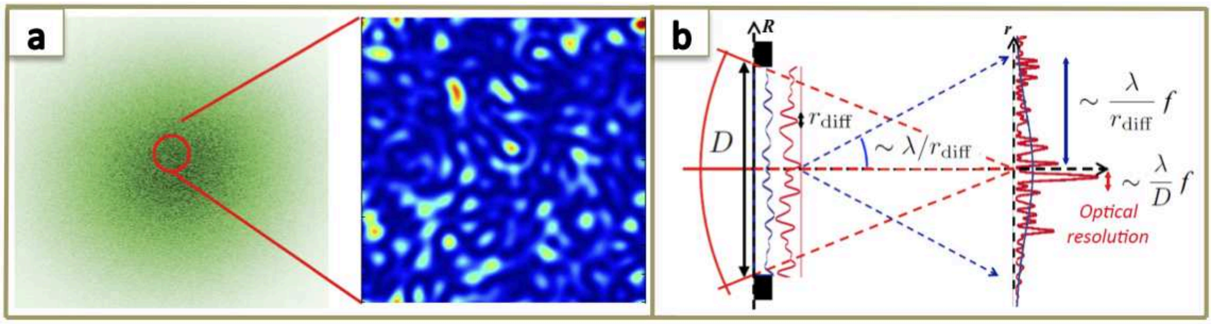

Figure 4.1: (a) Speckle pattern appears as randomly distributed intensity pattern. (b) Formation of speckle pattern from diffraction of a coherent incident field passing through a focusing lens and a diffusive plate. The size of the speckle grain is related to the optical resolution. The size of the speckle "halo" is related to the diffraction angle of the scatterers (with characteristic length r_{diff}). Figures are taken from Ref. [136].

4.1 Speckle disorder

Fig. 4.1(a) depicts typical speckle pattern. We are interested in the description of the speckle "halo", the speckle "grain", and the statistics of the random intensity pattern. We consider speckle pattern resulting from propagation of a coherent incident beam across a focusing lens and a diffusive plate. We consider speckle formation at the focal plane. Fig. 4.1(b) depicts the diffraction effect of the scattered fields at point $\boldsymbol{r}$ on the focal plane. In short, the halo size is related to the characteristic of the diffusive plate; it contains scatterers with characteristic length r_{diff}. The grain size is related to the optical resolution. The intensity distribution follows the Rayleigh distribution. These properties can be understood from the description of the diffraction effect of the incident field in presence of the random scatterers.

The focal plane can also be called "Fourier plane" since electric field at a point $\boldsymbol{r}$ on the focal plane is related to the scattered electric field at incident points $\{\boldsymbol{R}\}$ by certain Fourier transformation [136]. Scatterer at point $\boldsymbol{R}$ induces random transmission coefficient

$$t_{\text{diff}}(\boldsymbol{R}) = e^{i\phi(\boldsymbol{R})}. \tag{4.1}$$

The electric field $E(\boldsymbol{r})$ can be derived from Huygens-Fresnel principle in the Fraunhofer regime. We assume a uniform monochromatic incident field of amplitude E_0 and of wavelength λ. $E(\boldsymbol{r})$ yields [136, 137]

$$\begin{aligned} E(\boldsymbol{r}) &= -\frac{i}{\lambda}\frac{E_0}{f} e^{i\varphi_0(\boldsymbol{r})} \int P(\boldsymbol{R}) t_{\text{diff}}(\boldsymbol{R}) e^{-i2\pi \frac{\boldsymbol{r}\cdot\boldsymbol{R}}{\lambda f}} \mathrm{d}\boldsymbol{R} \\ &\equiv -\frac{i}{\lambda}\frac{E_0}{f} e^{i\varphi_0(\boldsymbol{r})} \cdot TF\left[P(\boldsymbol{R}) e^{i\phi(\boldsymbol{R})}\right](\boldsymbol{r}/\lambda f) \end{aligned} \tag{4.2}$$

where $P(\boldsymbol{R})$ is a function representing the aperture, which has value of either zero or one, and $\varphi_0(\boldsymbol{r}) = \frac{2\pi}{\lambda}(f + \frac{r^2}{2f})$ is certain global phase that has no role in our discussion. From this relation, we can remark a relation of Fourier transformation (denoted by $TF[...]$) in two dimension with appearance of conjugate variable[1] $\boldsymbol{r}/\lambda f$.

In this section, we split the discussion of this so-called Fourier speckle into three subsections. Certain statistical descriptions are involved. Subsection 4.1.1 concerns the characteristic of the scatterers. We deduce the characteristic length r_{diff} by evaluating the correlation function of the transmission $t_{\text{diff}}(\boldsymbol{R})$. The subsection 4.1.2 concerns the speckle pattern, its halo size and its grain size. Lastly, we derive the Rayleigh distribution for the intensity in subsection 4.1.3.

4.1.1 Statistical description of the scatterers

Description of the scatterers can be represented by random distribution of phase $\phi(\boldsymbol{R})$ for an arbitrary point $\boldsymbol{R}$ of the scatterers. The phase $\phi(\boldsymbol{R})$ depends on the refractive index n of the diffusive plate and its random thickness $l(\boldsymbol{R})$ at point $\boldsymbol{R}$. For thin-plate approximation, this yields

$$\phi(\boldsymbol{R}) = \frac{2\pi}{\lambda}(n-1)l(\boldsymbol{R}). \tag{4.3}$$

The random variables $\{l(\boldsymbol{R})\}$ are identically distributed. They follow a normal distribution centered at $\bar{l}$ with standard deviation σ_l. Consequently, the random variables $\{\phi(\boldsymbol{R})\}$ of the phase follow a normal distribution whose density is given by

$$p(\phi) = \frac{1}{\sigma_\phi\sqrt{2\pi}} e^{-(\phi-\bar{\phi})^2/(2\sigma_\phi^2)}, \tag{4.4}$$

where $\sigma_\phi = \frac{2\pi}{\lambda}(n-1)\sigma_l$ and $\bar{\phi} = \frac{2\pi}{\lambda}(n-1)\bar{l}$ (often set to zero by convention). For experimental purposes, we consider fully developed laser speckle associated with strong diffuser, that is $\sigma_\phi \gg 1$. The average transmission $\bar{t}_{\text{diff}} \equiv \overline{t_{\text{diff}}(\boldsymbol{R})} = \overline{e^{i\phi(\boldsymbol{R})}}$ is given by,

$$\bar{t}_{\text{diff}} = e^{-\sigma_\phi^2/2} \ll 1. \tag{4.5}$$

The random variables $\{l(\boldsymbol{R})\}$ are not independent. The roughness of the diffusive plate can be characterized by correlation function $\overline{l(\boldsymbol{R})l(\boldsymbol{R'})}$. It has dependence on $|\boldsymbol{R}-\boldsymbol{R'}|$ and maxima for $\boldsymbol{R}-\boldsymbol{R'}=0$; $\overline{l(\boldsymbol{R})l(\boldsymbol{R'}=\boldsymbol{R})} = \sigma_l^2$. The correlation function decreases around $|\boldsymbol{R}-\boldsymbol{R'}|=0$ with characteristic length r_l. For $|\boldsymbol{R}-\boldsymbol{R'}| \ll r_l$, $\overline{l(\boldsymbol{R})l(\boldsymbol{R'})}$ can be approximated as follows,

$$\frac{\overline{l(\boldsymbol{R})l(\boldsymbol{R'})}}{\sigma_l^2} \underset{|\boldsymbol{R}-\boldsymbol{R'}|\ll r_l}{\sim} 1 - \frac{|\boldsymbol{R}-\boldsymbol{R'}|^2}{2r_l^2}. \tag{4.6}$$

Nonetheless, correlation function $\overline{l(\boldsymbol{R})l(\boldsymbol{R'})}$ would not be sufficient for the description of the speckle pattern. As suggested by Eq. 4.2, transmission coefficients $\{t_{\text{diff}}(\boldsymbol{R})\}$ are more relevant for

---

[1] Analogous to wave vector $\boldsymbol{k} = -2\pi\boldsymbol{r}/(\lambda f)$

the characterization of the scatterers. The characteristic length r_{diff} is therefore associated with the following correlation function,

$$\begin{aligned} C_{\text{diff}}(\boldsymbol{R},\boldsymbol{R'}) &\equiv \overline{t_{\text{diff}}(\boldsymbol{R})t^*_{\text{diff}}(\boldsymbol{R'})}, \\ &= \overline{e^{i(\phi(\boldsymbol{R})-\phi(\boldsymbol{R'}))}}. \end{aligned} \tag{4.7}$$

Since $\{\phi(\boldsymbol{R})\}$ follow identical normal distribution and $\overline{\phi(\boldsymbol{R})\phi(\boldsymbol{R'})} = \sigma_\phi^2 \frac{\overline{l(\boldsymbol{R})l(\boldsymbol{R'})}}{\sigma_l^2}$, we deduce the following

$$\begin{aligned} C_{\text{diff}}(\boldsymbol{R},\boldsymbol{R'}) &= \exp\left(-\sigma_\phi^2 + \overline{\phi(\boldsymbol{R})\phi(\boldsymbol{R'})}\right), \\ &= \exp\left(-\sigma_\phi^2\left(1 - \overline{l(\boldsymbol{R})l(\boldsymbol{R'})}/\sigma_l^2\right)\right). \end{aligned} \tag{4.8}$$

This relation shows that $C_{\text{diff}}(\boldsymbol{R},\boldsymbol{R'})$ also has unique dependence on $|\boldsymbol{R}-\boldsymbol{R'}|$ like $\overline{l(\boldsymbol{R})l(\boldsymbol{R'})}$. This allows us to define the following correlation function

$$c_{\text{diff}}(\Delta\boldsymbol{R} = \boldsymbol{R}-\boldsymbol{R'}) \equiv C_{\text{diff}}(\boldsymbol{R},\boldsymbol{R'}). \tag{4.9}$$

Furthermore, we can see that $c_{\text{diff}}(\Delta\boldsymbol{R})$ also has maxima for $\Delta\boldsymbol{R} = 0$ and $c_{\text{diff}}(\Delta\boldsymbol{R} = 0) = 1$.

For $|\Delta\boldsymbol{R}| \ll r_l$, we have $c_{\text{diff}}(\Delta\boldsymbol{R}) \approx \exp\left(-\frac{|\Delta\boldsymbol{R}|^2\sigma_\phi^2}{2r_l^2}\right)$, i.e. a Gaussian function with standard deviation r_l/σ_ϕ. Besides, the Gaussian function decreases rapidly beyond several multiple of r_l/σ_ϕ; $r_l/\sigma_\phi \ll r_l$. As a result, the function $c_{\text{diff}}(\Delta\boldsymbol{R})$ can be approximated by a Gaussian with characteristic length r_{diff} as follows

$$c_{\text{diff}}(\boldsymbol{\Delta R}) = \exp\left(-\frac{|\boldsymbol{\Delta R}|^2}{2r_{\text{diff}}^2}\right) \quad , \tag{4.10}$$

where $r_{\text{diff}} = r_l/\sigma_\phi$. r_{diff} can be shown to be proportional to λ. The diffusive plate has parameter θ_{diff} defined as

$$\theta_{\text{diff}} \equiv \lambda/(\pi r_{\text{diff}}) = 2(n-1)\sigma_l/r_l, \tag{4.11}$$

which is independent of the wavelength λ.

Physically, r_l is much smaller than the optical aperture D. Consequently,

$$r_{\text{diff}} \ll r_l \ll D. \tag{4.12}$$

This relation justifies the discrete model that is discussed further in the subsection 4.1.3.

4.1.2 Statistical description of the speckle pattern

For the statistical description of the speckle pattern, it is convenient to introduce the autocorrelation function $\overline{E(\boldsymbol{r})E^*(\boldsymbol{r}+\boldsymbol{\Delta r})}$. Under approximations $r_{\text{diff}} \ll D$, we have shown in Appendix

B that

$$\overline{E(\boldsymbol{r})E^*(\boldsymbol{r}+\boldsymbol{\Delta r})} \approx \frac{|E_0|^2}{f^2\lambda^2} \cdot TF\left[c_{\text{diff}}(\boldsymbol{\Delta R})\right]\left(\frac{\boldsymbol{r}}{\lambda f}\right) \cdot TF\left[|P(\boldsymbol{R_0})|^2\right]\left(\frac{\boldsymbol{\Delta r}}{\lambda f}\right). \tag{4.13}$$

Two terms of Fourier transformation appear. They are related to the speckle halo and the speckle grain respectively

Speckle halo

The size of the speckle halo can be evaluated from the averaged intensity over realizations of disorder, $\overline{I(\boldsymbol{r})}$. This yields[2]

$$\begin{aligned} \overline{I(\boldsymbol{r})} &= \overline{|E(\boldsymbol{r})|^2}, \\ &= \frac{|E_0|^2}{f^2\lambda^2} \cdot TF\left[c_{\text{diff}}(\boldsymbol{\Delta R})\right]\left(\frac{\boldsymbol{r}}{\lambda f}\right) \cdot TF\left[|P(\boldsymbol{R_0})|^2\right]\left(\frac{\boldsymbol{\Delta r}=0}{\lambda f}\right). \end{aligned} \tag{4.14}$$

The size of the speckle halo is related to characteristic length of the function $TF\left[c_{\text{diff}}(\boldsymbol{\Delta R})\right]\left(\frac{\boldsymbol{r}}{\lambda f}\right)$. The term $S = TF\left[|P(\boldsymbol{R_0})|^2\right]\left(\frac{\boldsymbol{\Delta r}=0}{\lambda f}\right)$ equals to the area of the aperture.

From previous subsection, the function $c_{\text{diff}}(\boldsymbol{\Delta R})$ is a Gaussian. Thus, its Fourier transformation is a Gaussian too. We show

$$TF\left[c_{\text{diff}}(\boldsymbol{\Delta R})\right]\left(\frac{\boldsymbol{r}}{\lambda f}\right) = 2\pi r_{\text{diff}}^2 \exp\left(-2\frac{|\boldsymbol{r}|^2}{w_d^2}\right) \quad , \tag{4.15}$$

where w_d can be associated with the waist ($1/e^2-$radius) of the speckle field. The waist is given by

$$w_d = \frac{\lambda}{\pi r_{\text{diff}}} f = \theta_{\text{diff}} f. \tag{4.16}$$

This shows unique dependence of the waist on the characteristic angle θ_{diff} of the diffusive plate.

Speckle grain (transverse direction)

The size of the speckle grain in the transverse direction is equivalent to the correlation length of correlation function $\overline{\delta I(\boldsymbol{r})\delta I(\boldsymbol{r}+\boldsymbol{\Delta r})}$. By applying Wick theorem, this correlation function yields

$$\begin{aligned} \overline{\delta I(\boldsymbol{r})\delta I(\boldsymbol{r}+\boldsymbol{\Delta r})} &= \overline{I(\boldsymbol{r})I(\boldsymbol{r}+\boldsymbol{\Delta r})} - \overline{I(\boldsymbol{r})}.\overline{I(\boldsymbol{r}+\boldsymbol{\Delta r})}, \\ &= \left|\overline{E(\boldsymbol{r})E^*(\boldsymbol{r}+\boldsymbol{\Delta r})}\right|^2, \\ &\propto \left|TF\left[|P(\boldsymbol{R_0})|^2\right]\left(\frac{\boldsymbol{\Delta r}}{\lambda f}\right)\right|^2. \end{aligned} \tag{4.17}$$

---

[2] We impose $\frac{\varepsilon_0 c}{2} = 1$ such that the intensity is given by $I(\boldsymbol{r}) = |E(\boldsymbol{r})|^2$.

It shows that the intensity correlation function is directly related to the autocorrelation function $\overline{E(\boldsymbol{r})E^{*}(\boldsymbol{r}+\boldsymbol{\Delta r})}$. Considering the "halo" term of the autocorrelation function ($TF\left[c_{\text{diff}}(\boldsymbol{\Delta R})\right]$) to be a slowly varying function compared with the term $TF\left[|P(\boldsymbol{R_0})|^2\right]$, the "halo" term can effectively be treated as a constant. The correlation length can then be associated with the term $TF\left[|P(\boldsymbol{R_0})|^2\right]$.

Let us consider an aperture of diameter D, which yields numerical aperture $\text{NA} = D/(2f)$. The correlation length $\sigma_\perp$ of follows $D\frac{\sigma_\perp}{\lambda f} \sim 1$, yielding

$$\sigma_\perp \sim \frac{\lambda}{2\text{NA}}. \tag{4.18}$$

This shows unique dependence of the correlation length on the numerical aperture.

Speckle grain (longitudinal direction)

Let us consider $x-$axis as the longitudinal direction and $\boldsymbol{r}_\perp$ as coordinates on the focal plane. The size of the speckle grain along the longitudinal direction can be derived by considering the electric field $E(\boldsymbol{r})$ at position $\boldsymbol{r} = (x_l, \boldsymbol{r}_\perp = 0)$; we can simplify $E(\boldsymbol{r})$ and $I(\boldsymbol{r})$ with $E(x_l)$ and $I(x_l)$ respectively. In the Eq. 4.2, we replace the term $e^{-i2\pi\frac{\boldsymbol{r}\cdot\boldsymbol{R}}{\lambda f}}$ with $\exp\left(ik\left|\boldsymbol{R}\right|^2/x_l\right)$ in the integrand [131]. The size of the speckle grain along the longitudinal direction corresponds to the correlation length of the function $\overline{\delta I(x_l)\delta I(x_l+\Delta x_l)}$ and thus $\left|\overline{E(x_l)E^{*}(x_l+\Delta x_l)}\right|^2$. It yields

$$\sigma_\parallel \sim \frac{2\lambda}{\pi\text{NA}^2}. \tag{4.19}$$

This also shows unique dependence of the correlation length on the numerical aperture. Besides, we see that $\sigma_\perp/\sigma_\parallel \sim \text{NA}$.

Case of Gaussian laser beam

We can also have some analytical expressions for incoming field described as a Gaussian laser beam of waist w; the intensity of the incoming field follows $I \propto \exp\left(-2|\boldsymbol{R}|^2/w^2\right)$. Let us assume that the diffusive plate covers the full area lit by the Gaussian beam; aperture diameter much larger than the waist. In the paraxial approximation, the correlation function $\overline{\delta I(x_l,\boldsymbol{r}_\perp)\delta I(x_l+\Delta x_l,\boldsymbol{r}_\perp+\boldsymbol{\Delta r}_\perp)}$ is given by [70]

$$\overline{\delta I(x_l,\boldsymbol{r}_\perp)\delta I(x_l+\Delta x_l,\boldsymbol{r}_\perp+\boldsymbol{\Delta r}_\perp)} \propto \frac{1}{1+4x_l^2/\sigma_\parallel^2}\exp\left(-\frac{\left|\boldsymbol{r}_\perp\right|^2/\sigma_\perp^2}{1+4x_l^2/\sigma_\parallel^2}\right), \tag{4.20}$$

where $\sigma_\parallel = 4\lambda f^2/(\pi w^2)$ and $\sigma_\perp = \lambda f/(\pi w)$. Hence, $\sigma_\parallel$ and $\sigma_\perp$ can be interpreted as the speckle grain size in the longitudinal and transverse direction; $\text{NA} \sim w/(2f)$ and $\sigma_\perp/\sigma_\parallel = \text{NA}/4$.

4.1.3 Statistical description of the intensity distribution

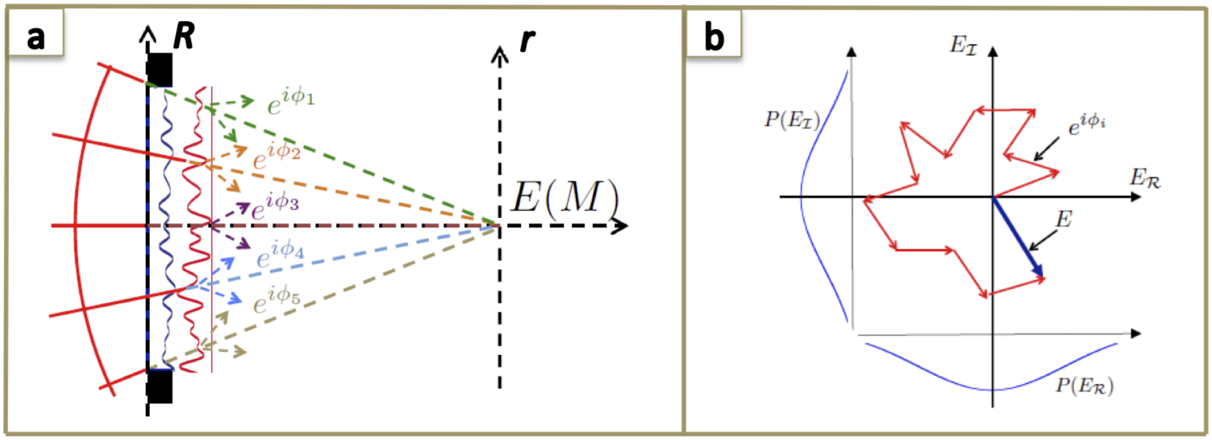

Figure 4.2: (a) The electrical field at any point M in the focal plane results from interference between the electric field emitted by scatterers. (b) Analogy of the interference with two-dimensional random walk.

The probability distribution can be derived by considering a simple discrete model of the electric field depicted in Fig. 4.2. The electric field $E(\boldsymbol{r})$ results from a summation of electric fields emitted by the all scatterers, yielding

$$E(\boldsymbol{r}) = \sum_i^N E_0 e^{i\phi_i}, \tag{4.21}$$

where $\{\phi_i\}$ is an ensemble of independent and identically distributed random phases, which are uniformly distributed over $[0, 2\pi]$. The typical size of each independent scatterer is r_{diff} which is much smaller than the size of the aperture; $r_{\text{diff}} \ll D$. As a result, we can consider N to be a huge number and we can apply the central limit theorem. The total electric field can be decomposed into two independent random variables associated with the its real and imaginary values,

$$\begin{aligned} E_R &= \operatorname{Re}\left[E(x)\right] = \sum_i^N |E_0| \cos(\phi_i), \\ E_I &= \operatorname{Im}\left[E(x)\right] = \sum_i^N |E_0| \sin(\phi_i). \end{aligned} \tag{4.22}$$

As depicted in Fig. 4.2(b), the representation in the complex plane of the resultant field is analogous to a two-dimensional random walk. According to the central limit theorem, variables variables E_R and E_I converge to the following normal distribution

$$P(E_R, E_I) = \frac{1}{2\pi\sigma_E^2} \exp\left(-\frac{E_R^2 + E_I^2}{2\sigma_E^2}\right), \tag{4.23}$$

where σ_E is the standard deviation and the normalization constant.

In order to obtain the distribution of the intensity, $I = E_R^2 + E_I^2$, we must introduce the following change of variables [131],

$$\begin{aligned} E_R &= \sqrt{I}\cos\varphi \\ E_I &= \sqrt{I}\sin\varphi. \end{aligned} \tag{4.24}$$

We obtain

$$P(I,\varphi) = \frac{1}{4\pi\sigma_E^2}\exp\left(-\frac{I}{2\sigma_E^2}\right), \tag{4.25}$$

which is independent of φ. Thus, the distribution of the intensity follows exponential (Rayleigh) distribution

$$p(I) = \frac{1}{\overline{I}}e^{-I/\overline{I}}. \tag{4.26}$$

The average intensity is given by $\overline{I} = 2\sigma_E^2$. The standard deviation is equal to the average intensity, $\sigma_I = \sqrt{\overline{I^2} - \overline{I}^2} = \overline{I}$.

4.2 The implementation of laser speckle

Fig. 4.3 depicts the implementation of laser speckle. It consists of three set-ups: laser source, optical manipulation, and speckle generation. In this section, we discuss the set-ups of laser source and optical manipulation in subsection 4.2.1, the set-up of speckle generation in subsection 4.2.2, and the speckle characterization in subsection 4.2.3. The details can also be found in Refs. [50,52,66,138].

4.2.1 Light source and optical manipulation

The aim of the set-ups laser source and optical manipulation is to have controlled incident beam for the speckle field generation. The laser beam comes from a laser (*Toptica TA-Pro*) at wavelength 780 nm. With an optical amplifier, the laser can produce up to 2 W of power. The laser beam is sent to an acousto-optic modulator (see AOM in set-up “laser source”) and we retrieve the -1 order of diffraction for speckle laser source. The AOM allows not only modulation of the diffracted beam but also fast switch for the beam. The diffracted beam is sent to the set-up optical manipulation using a polarization-maintaining optical fiber (*Thorlabs P3-780PM-FC-5*).

We account for possible sources of noise or fluctuations. The frequency of the *Toptica* laser is locked with respect to the second cooling laser discussed in subsection 3.1.3. It yields spectral accuracy of around 1 MHz. Besides, the laser wavelength is close to D_2 lines. This could result in parasite light for the BEC in the vacuum cell. For this, a mechanical shutter (*CC*) is place in front of the AOM to achieve excellent extinction ratio for the speckle field. Furthermore, the optical fiber has privileged polarization which minimizes optical fluctuation due to mechanical vibrations. For this, we control the incoming polarization with a half wave plate in front of the fiber coupler. The

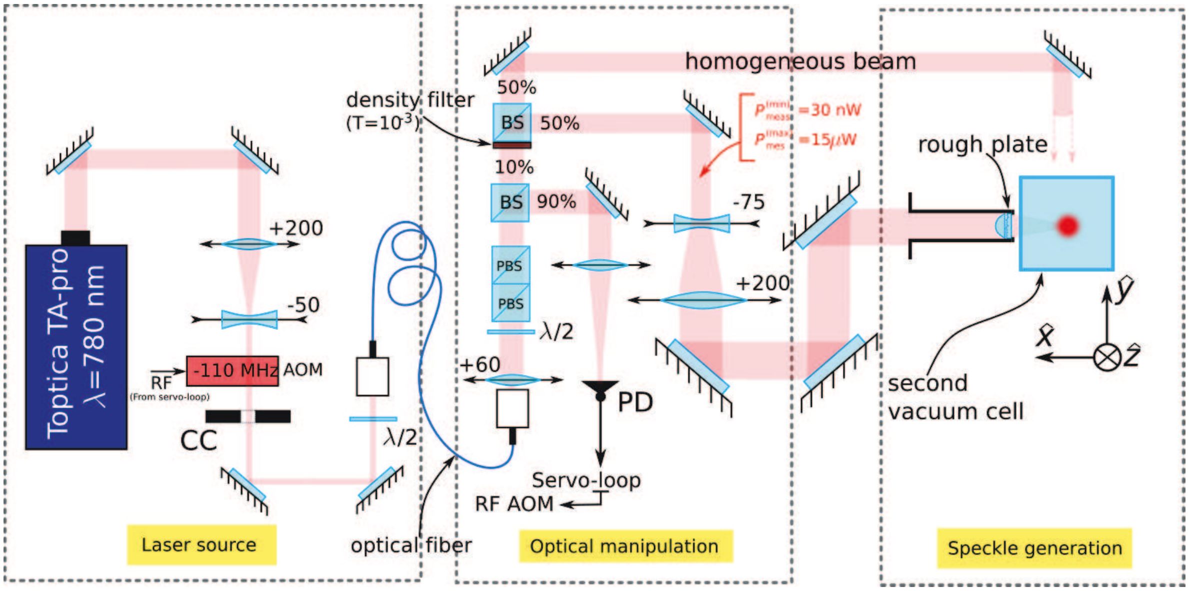

Figure 4.3: The implementation of speckle disorder consists of three set-ups: The laser source, the optical manipulation, and the speckle generation.

laser beam coming out of the fiber is further stabilized in polarization thanks to the two successive polarizing beam splitter (*PBS*); it results in extinction ratio of at least 1000:1.

As discussed in the next section, the optical power required for the laser speckle is much less than 1 mW because its frequency is not very far from the D_2 lines. In the optical manipulation set-up, the input beam is split into two beams by a 10:90 beam splitter (*BS*) and only the transmitted 10% is used for laser speckle. This beam is further attenuated with an optical density filter. The reflected beam is sent to a photodiode of a servo-loop system. The feedback signal is then sent to the RF input of the acousto-optic modulator (see "AOM" in Fig. 4.3). This servo-loop provides control and stability of the power of the laser speckle.

The transmitted beam is split further by a 50:50 beam splitter and we make use of the reflected beam for the laser speckle. In this work, we consider laser speckle from a single beam; it is called single speckle configuration in section 2.4. However, 50:50 beam splitter makes two-crossed speckle configuration conceivable. For current experimental purposes, the transmitted beam can be used as reference for a homogeneous beam.

Lastly, we shape the speckle laser beam. The waist ($1/e^2$ radius) of the beam is enlarged to 14.6 mm after a telescope. The beam has a polarization along e_y in the vacuum cell, parallel to the bias magnetic field of the magnetic levitation, i.e. π-polarization.

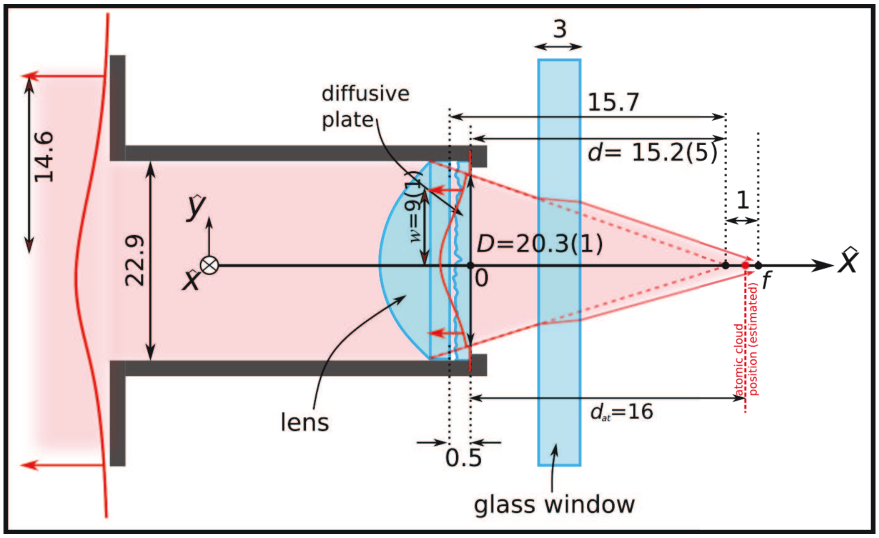

Figure 4.4: The speckle generation consists of a lens and a diffusive plate mounted in an optical tube. The incident beam is truncated Gaussian beam with final waist of $w = (9 \pm 1)$ mm and diameter of $D = (20.3 \pm 0.1)$ mm. The effective focal length is $d = (15.2 \pm 0.5)$ mm which gives numerical aperture NA $= (0.55 \pm 0.02)$

4.2.2 Speckle generation

Fig. 4.4 depicts the zoomed version of the speckle generation set-up shown in Fig. 4.3. It consists of an aspheric converging lens (*Thorlabs ACL2520-B*) and a diffusive plate (*Newport FSD10-3*) placed in a tube with diameter 22.9 mm. The lens and the diffusive plate have non-negligible thickness such that it is not trivial to determine the numerical aperture of the system. The distance between the focal point and the flat surface is 15.7 mm. The speckle optics is situated outside the vacuum cell. As shown in the figure, the glass window with thickness of 3 mm shift the position of the focal point further by 1 mm. The scattering sample is placed after the lens and the atomic cloud is situated around 16 mm from the scattering sample. From this, we ensure that the position of the atoms is within 0.5 mm of the focal point. The effective focal point defined with respect to the diffusive plate becomes $d = (15.2 \pm 0.5)$ mm. The diffusive plate has diffusion angle $\theta_{\mathrm{diff}} = 5.2\,^\circ \pm 0.1\,^\circ$. This results in speckle waist w_d,

$$w_d = \theta_{\mathrm{diff}} d = 1.38 \text{ mm}. \tag{4.27}$$

The incident beam is quasi-uniform, with waist ($1/e^2$ radius) of 14.6 mm, comparable to the diameter of the tube. The incident beam is best described by truncated Gaussian beam. After propagation through the thick lens and the diffusive plate, the diameter of the truncation slightly decreases to $D = (20.3 \pm 0.1)$ mm. The waist becomes $w = (9 \pm 1)$ mm. With with $\theta_{\mathrm{max}} =$

$\arctan\left(\frac{D}{2d}\right)$, the numerical aperture NA is given by

$$\mathrm{NA} = \sin\left(\theta_{\max}\right) = \left(0.55 \pm 0.02\right).$$

4.2.3 Speckle characterization

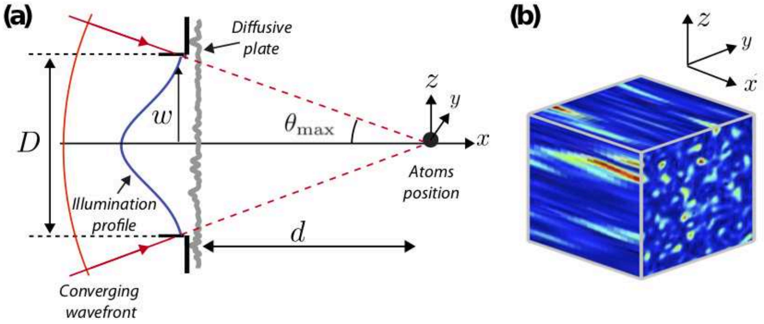

Figure 4.5: (a) Simplified schematic representation of the speckle generation. (b) 3D representation of the experimental laser speckle field. Figures are taken from Ref. [138].

The characterization of the speckle field consists essentially of measurement of intensity correlation discussed in subsection 4.1.2. The simplified schema of the speckle generation is depicted in Fig. 4.5(a). We are interested in the correlation measurement around the focal plane, which is also the position of the atoms. It is given by

$$c_{\exp}(\boldsymbol{\Delta r}) = \frac{\overline{\delta I(\boldsymbol{r})\delta I(\boldsymbol{r}+\boldsymbol{\Delta r})}}{\overline{\delta I^2}}, \tag{4.28}$$

with $\delta I = I - \overline{I}$. The random intensity pattern is recorded with a high-resolution optical microscope. Fig.4.5(b) depicts the 3D intensity pattern obtained from *ex-situ* measurement[3]. We can remark that the speckle grain is elongated along the propagation axis. The extracted two-point correlation functions in the transverse (z direction, same along y) and longitudinal (x direction) are shown as blue squares in Fig. 4.6.

For each experimental curve, we deduce the half-width-at-half-maximum (HWHM) lengths, noted $\sigma_\perp^{\mathrm{HWHM}}$ and $\sigma_\parallel^{\mathrm{HWHM}}$, associated with the transversal and longitudinal directions respectively. For consistency with the characteristic length defined in several theoretical references [43, 106], the transverse and longitudinal correlation lengths are given by $\sigma_{\perp,\parallel} = \sigma_{\perp,\parallel}^{\mathrm{HWHM}}/1.39156$, yielding

$$\sigma_\perp = (0.306 \pm 0.007)\ \mu\mathrm{m}, \text{ and } \sigma_\parallel = (1.45 \pm 0.04)\ \mu\mathrm{m}.$$

---

[3] Measurement was done outside the vacuum chamber with an exact replication of the geometrical configuration. See Ref. [50] for more details.

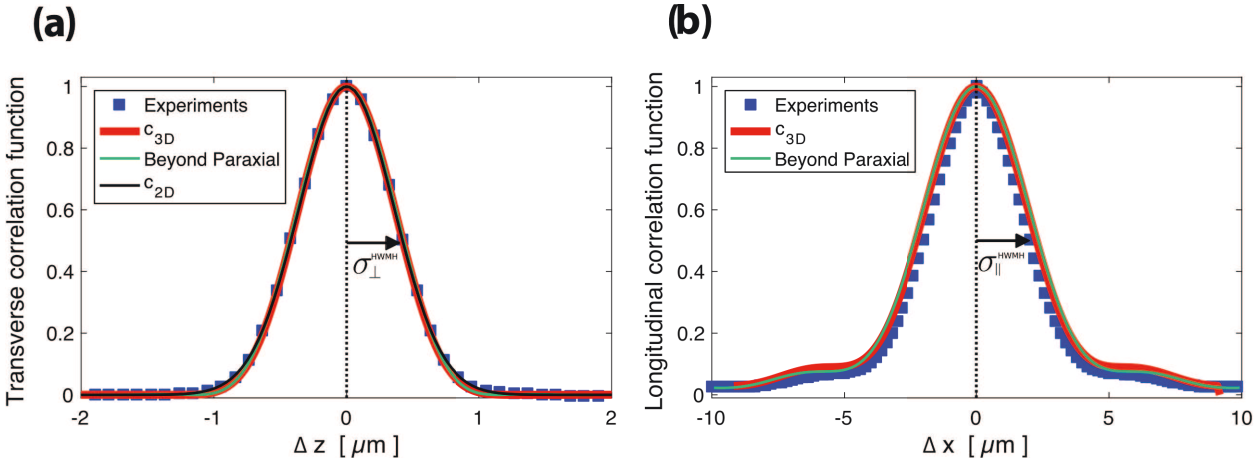

Figure 4.6: Transverse (a) and longitudinal (b) correlation functions of the laser speckle, respectively along the z (same along y) and x directions. Blue squares: experimental autocorrelation functions. Black solid line ($c_{2\mathrm{D}}$): transverse Gaussian fit, yielding $1/e-$radius of 0.50(1) μm. Red solid lines ($c_{3\mathrm{D}}$): effective paraxial calculations used in the Born prediction of elastic scattering time. Green solid lines: beyond paraxial calculations used in the calculation of the spectral functions of ultracold atoms in disordered potential, see Chap. 5. Horizontal black arrows indicate the half-width-at-half-maximum (HWHM) lengths of the correlation function: $\sigma_\perp^{\mathrm{HWHM}} = 0.42(1)$ μm and $\sigma_\parallel^{\mathrm{HWHM}} = 2.05(5)$ μm.

These values correspond to the correlation energy $E_\sigma = \frac{\hbar^2}{m(\sigma_\perp^2\sigma_\parallel)^{2/3}} = h \times 441$ Hz.

Due to large numerical aperture ($\mathrm{NA} = 0.55 \pm 0.02$), it is not easy to model the speckle field. We can remark that the transverse correlation function is fairly close to Gaussian in accordance with Eq. 4.20; see black solid line in Fig. 4.6(a). However, the longitudinal correlation function has a rather complicated shape. Thus, we need to go beyond paraxial approximation.

For the project of the measurement of the spectral functions (see section 5.2), our collaborators, M. Pasek and D. Delande, have developed realistic numerical disorder based on the geometry represented in Fig. 4.5(a); see Ref. [138]. It is then used for the calculation of of the spectral functions. It consists of generating the electric field at the focal point as a sum of modes with wave vector $\boldsymbol{k}$,

$$E(\boldsymbol{x}) = \sum_{\boldsymbol{k}} \mathcal{E}(\boldsymbol{k})\mathcal{P}(\boldsymbol{k})e^{i\boldsymbol{k}\cdot\boldsymbol{r}}, \tag{4.29}$$

with $\mathcal{E}(\boldsymbol{k})$ a complex amplitude whose real and imaginary parts are uncorrelated random Gaussian variables. $\mathcal{P}(\boldsymbol{k})$ is a phase mask expressed as,

$$\mathcal{P}(\boldsymbol{k}) = \delta(|\boldsymbol{k}| - k_L)\exp\left(-\frac{(\tan\theta)^2}{(w/d)^2}\right)\Theta\left(\frac{D}{2d} - \tan|\theta|\right), \tag{4.30}$$

where k_L is the modulus of the laser wave vector, $\theta \in [-\pi/2, \pi/2]$ is the angle between the optical axis and the vector $\boldsymbol{k}$. w is the beam waist, D is the diaphragm diameter, d is the position where the illumination field converges. The Heaviside function $\Theta\left(\frac{D}{2d} - \tan|\theta|\right)$ represents the truncation of the incident electric field due to the diaphragm. From the numerically generated speckle field, we can obtain the corresponding correlation functions, which are represented by solid green lines in Fig. 4.6. The best comparison with the experimental results was obtained for $D = 20.4$ mm, $d = 15.2$ mm, and $w = 9.9$ mm. These values are consistent with the experimental parameters; they lie within the experimental uncertainties.

For the Born prediction of the elastic scattering time, see Eq. 2.3, the correlation function corresponds to correlation $C(\boldsymbol{\Delta r})/\overline{V}^2$. For numerical calculation of the scattering time, we have developed a simpler model compared with the one used for the calculation of the spectral functions. It consists of introducing a global geometrical factor x_{scale} to tune the numerical aperture and calculating the correlation function using formula

$$c_{3D}\left(\Delta x, \boldsymbol{\Delta r}_\perp\right) \propto \left| TF\left[\Theta\left(\frac{|\boldsymbol{R}|}{D_{\text{eff}}} - 1\right)\exp\left(-2\frac{|\boldsymbol{R}|^2}{w_{\text{eff}}^2}\right)\exp\left(-i\pi\frac{|\boldsymbol{R}|^2\,\Delta x}{\lambda d}\right)\right]\left(\frac{\Delta r_\perp}{\lambda d}\right)\right|^2, \tag{4.31}$$

where $D_{\text{eff}} = x_{\text{scale}}D$ and $w_{\text{eff}} = x_{\text{scale}}w$. By setting $x_{\text{scale}} = 0.875 \pm 0.005$, we obtain the calculated correlation function whose plots along the transverse and longitudinal directions are shown as red solid lines in Fig. 4.6. This leads to an effective numerical aperture $\text{NA}_{\text{eff}} = 0.48 \pm 0.02$.

4.3 State-dependent disordered potentials

In this section, we study the disordered potentials associated with two “clock” states discussed in Chap. 3, $|1\rangle = |F = 1, m_F = -1\rangle$ and $|2\rangle = |F = 2, m_F = +1\rangle$. The disordered potentials result from the speckle intensity pattern discussed in previous section. In particular, we want to realize the so-called “state-dependent disorder” where the state $|1\rangle$ has zero potential $V_1(\boldsymbol{r})$ and the state $|2\rangle$ has controllable potential $V_2(\boldsymbol{r})$.

According to Eqs. 3.7 and 3.8, the optical potentials scale as $V_g(\boldsymbol{r}) \sim I(\boldsymbol{r})/\Delta_{|g\rangle}$, where $\Delta_{|g\rangle}$ is the laser detuning with respect to transitions of state $|g\rangle$; $g = 1$ or 2. Fig. 4.7 depicts the schema for the realization of state-dependent disorder. The laser is quasi-resonant with the $F = 2 \to F'$ transition; we choose $F' = 3$ as reference for the optical detuning Δ. The detuning Δ is chosen to be much smaller than the hyperfine splitting Δ_{hf} (similar to the “tune-in” scheme as described in Ref. [139]). As depicted in the figure, the detuning $\Delta_{|1\rangle} \approx -\Delta_{\text{hf}}$ is much larger than the detuning $\Delta_{|2\rangle} = \Delta$. Consequently, we have $V_{|1\rangle} \ll V_{|2\rangle}$.

Detailed analyses of the optical potentials require calculation of the atomic polarizability with taking into account all possible transitions. In subsection 4.3.1, we derive the atomic polarizabilities $\alpha_{|1\rangle}$ and $\alpha_{|2\rangle}$ of the states $|1\rangle$ and $|2\rangle$ respectively. As discussed in subsection 3.1.3, the real part of atomic susceptibility is related to the optical potential while the imaginary part is related to the dissipation. These calculations serve for the determination of parameter V_R of the disorder amplitude and the estimated lifetime of the atoms in the disorder (see subsection 4.3.2).

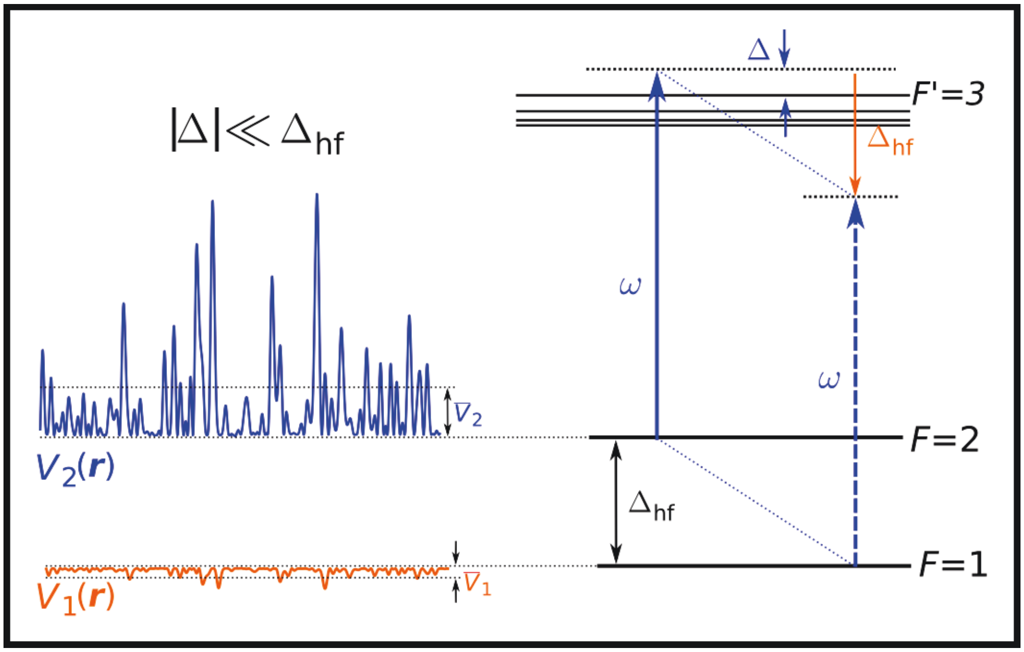

Figure 4.7: Schematic diagram of state-dependent disorder realized with a single monochromatic laser. The laser is quasi-resonant to the $F = 2 \rightarrow F' = 3$ transition (of detuning Δ) creating disordered potential for the spin-state $|2\rangle$. The laser detuning with respect to the $F = 1 \rightarrow F'$ transition is approximately $-\Delta_{\mathrm{hf}}$, much larger in absolute value than $|\Delta|$ such that the optical potential of spin-state $|1\rangle$ is negligible.

4.3.1 Calculation of the atomic polarizability

The atomic polarizability depends on three inputs: the state $|g\rangle$, the light frequency ω, and the light polarization $\boldsymbol{\epsilon}$. Let us consider $|g\rangle$ to be any the ground states of the D lines; $|g\rangle \equiv |F, m_F\rangle$. For the calculation of the atomic polarizability, we consider both D_1 and D_2 lines (see Fig. 3.1(a)). For the evaluation of the state-dependent disorder, we are only interested in the states $|1\rangle = |F = 1, m_F = -1\rangle$ and $|2\rangle = |F = 2, m_F = +1\rangle$, and we are only interested in the π-transitions since our laser speckle has linear polarization (parallel to the bias field).

General expression of the atomic polarizability. The atomic polarizability is a complex quantity. As shown in Eq. 3.7, the atomic polarizability $\alpha_{|g\rangle}$, associated with a state $|g\rangle$, is related to the optical potential, $V_g(\boldsymbol{r})$, according to

$$V_g(\boldsymbol{r}) = -\mathrm{Re}\left[\alpha_{|g\rangle}\right] I(\boldsymbol{r})/(2\varepsilon_0 c), \tag{4.32}$$

where $I(\boldsymbol{r})$ is the laser intensity. The real part, $\mathrm{Re}\left[\alpha_{|g\rangle}\right]$, is given by[4]

$$\mathrm{Re}\left[\alpha_{|g\rangle}(\omega,\boldsymbol{\epsilon})\right]=\frac{1}{\hbar}\sum_{f}\frac{2\omega_{gf}}{\omega_{gf}^{2}-\omega^{2}}\left|\langle f\left|e\hat{\boldsymbol{r}}\cdot\boldsymbol{\epsilon}\right|g\rangle\right|^{2}, \tag{4.33}$$

where $|f\rangle=|J',F',m_{F'}\rangle$ are the excited states of the D lines, ω_{gf} are the frequency of the transition between states $|g\rangle$ and $|f\rangle$, and $\langle f\left|e\hat{\boldsymbol{r}}\cdot\boldsymbol{\epsilon}\right|g\rangle$ are the dipole matrix elements respectively. The informations regarding the frequencies of the transitions are given in Ref. [122] and are listed in the Appendix A. Furthermore, the imaginary part is associated with the dissipative scattering rate and it is given by

$$\mathrm{Im}\left[\alpha_{|g\rangle}(\omega,\boldsymbol{\epsilon})\right]=\frac{1}{\hbar}\sum_{f}\left(\frac{2\omega_{gf}}{\omega_{gf}^{2}-\omega^{2}}\right)^{2}\left(\frac{\omega}{\omega_{gf}}\right)^{3}\left|\langle f\left|e\hat{\boldsymbol{r}}\cdot\boldsymbol{\epsilon}\right|g\rangle\right|^{2}. \tag{4.34}$$

Dipole matrix elements. Without loss of generality, we consider either π-polarization ($q=0$) or $\sigma_{\pm}$-polarization ($q=\pm1$). The matrix elements $\left|\langle J',F',m_{F'}\left|e\hat{\boldsymbol{r}}\cdot\boldsymbol{\epsilon}\right|J=1/2,F,m_F\rangle\right|^{2}$ follow

$$\left|\langle J',F',m_{F'}\left|e\hat{\boldsymbol{r}}\cdot\boldsymbol{\epsilon}\right|J,F,m_F\rangle\right|^{2}=\left|\langle J=1/2\left\|e\boldsymbol{r}\right\|J'\rangle\right|^{2}S_{FF'}\left|\langle F,m_F|F',1,(m_F+q),-q\rangle\right|^{2}, \tag{4.35}$$

where q represents the light polarization and $S_{FF'}$ represents the relative hyperfine transition strength factor. $\left|\langle J=1/2\left\|e\boldsymbol{r}\right\|J'\rangle\right|^{2}$ is the transition dipole matrix element; $J'=1/2$ and $J'=3/2$ correspond to D_1 lines and D_2 lines respectively. The dipole matrix elements for state $|1\rangle=|J=1/2,F=1,m_F=-1\rangle$ are summarized in the table 4.1 and the dipole matrix elements for state $|2\rangle=|J=1/2,F=2,m_F=1\rangle$ are summarized in the table 4.2.

D line	F'	Transition			$S_{FF'}$
		π	σ_-	σ_+	
D_2 line	2	$-\sqrt{1/8}$	$\sqrt{1/4}$	$\sqrt{1/24}$	5/12
	1	$-\sqrt{5/24}$		$\sqrt{5/24}$	5/12
	0			$\sqrt{1/6}$	1/6
D_1 line	2	$\sqrt{1/4}$	$-\sqrt{1/2}$	$-\sqrt{1/12}$	5/6
	1	$\sqrt{1/12}$		$-\sqrt{1/12}$	1/6

Table 4.1: Rubidium 87 dipole matrix elements for spin state $|1\rangle=|F=1,m_F=-1\rangle$, expressed either as multiples of $\langle J=1/2\left\|e\boldsymbol{r}\right\|J'=1/2\rangle$ for the D_1 line or as multiples of $\langle J=1/2\left\|e\boldsymbol{r}\right\|J'=3/2\rangle$ for the D_2 line.

---

[4] In other references, the factor $\frac{2\omega_{gf}}{\omega_{gf}^{2}-\omega^{2}}$ is often presented as $\frac{1}{\Delta_{gf}}=\frac{1}{\omega_{gf-\omega}}+\frac{1}{\omega_{gf+\omega}}$.

D line	F'	Transition			$S_{FF'}$
		π	σ_-	σ_+	
D_2 line	3	$-\sqrt{4/15}$	$\sqrt{1/10}$	$\sqrt{1/3}$	7/10
	2	$\sqrt{1/24}$	$-\sqrt{1/8}$	$\sqrt{1/12}$	1/4
	1	$\sqrt{1/40}$	$\sqrt{1/40}$		1/20
D_1 line	2	$\sqrt{1/12}$	$-\sqrt{1/4}$	$\sqrt{1/6}$	1/2
	1	$\sqrt{1/4}$	$\sqrt{1/4}$		1/2

Table 4.2: Rubidium 87 dipole matrix elements for spin state $|2\rangle = |F = 2, m_F = +1\rangle$, expressed either as multiples of $\langle J = 1/2 \,\| e\boldsymbol{r} \|\, J' = 1/2\rangle$ for the D_1 line or as multiples of $\langle J = 1/2 \,\| e\boldsymbol{r} \|\, J' = 3/2\rangle$ for the D_2 line.

4.3.2 Parameter of disorder amplitude V_R of the speckle disorder

The potential distribution of speckle disorder follows exponential distribution similar to the intensity probability density given by Eq. 4.26. From this, we can associate disorder amplitude V_R to the average potential of the state $|2\rangle$ at the center of the speckle potential[5] ($\boldsymbol{r} = \boldsymbol{0}$). As discussed in subsection 4.1.2, the speckle pattern has Gaussian profile with waist of $w_d = 1.38$ mm. By applying Eqs. 3.14 and 4.32, we obtain

$$V_R = -\frac{\mathrm{Re}\left[\alpha_{|2\rangle}\right]}{\varepsilon_0 c}\frac{P}{\pi w_d^2}, \tag{4.36}$$

where P is the power of the laser speckle.

Fig. 4.8 depicts the numerical calculation of disorder amplitude V_R as function of detuning Δ with respect to the $F = 2 \to F' = 3$ transition, calculated for $P = 1$ μW and $w_d = 1.38$ mm. We remark the divergence associated with the transitions $F = 2 \to F' = 1,\ 2,\ 3$. Around $\Delta = 0$, positive and negative detuning result in the repulsive and attractive disorder potential respectively. Examples shown in the figure are $\Delta = \Delta_\mathrm{r} = -2\pi \times 73$ MHz and $\Delta = \Delta_\mathrm{b} = 2\pi \times 81$ MHz, corresponding to attractive and repulsive disorders respectively. They result in the same magnitude of $|V_R|/P =$ 0.53kHz/μW, but opposite in sign.

From this calculation, disorder amplitude of around 5 kHz can be obtained with just 10 μW of laser power. This is due to the small detuning of tens of MHz. As discussed later in Chap. 5, we are interested in the interval of V_R between[6] $|V_R|/E_\sigma \sim 0.1$ and $|V_R|/E_\sigma \sim 10$. This corresponds roughly to the disorder amplitude between $|V_R|/h \sim 50$ Hz and $|V_R|/h \sim 5$ kHz which requires varying the laser power between 0.1 to 10 μW. It shows that only little amount of laser power is required.

The ratio of the optical potential V_1/V_2 equals to the ratio of the corresponding atomic polar-

---

[5] The atoms are supposed to be located at $\boldsymbol{r} = \boldsymbol{0}$.

[6] As discussed later in Chap. 5, $|V_R|/E_\sigma \ll 1$ corresponds to the quantum disorder regime while $|V_R|/E_\sigma \gg 1$ corresponds to the classical disorder regime.

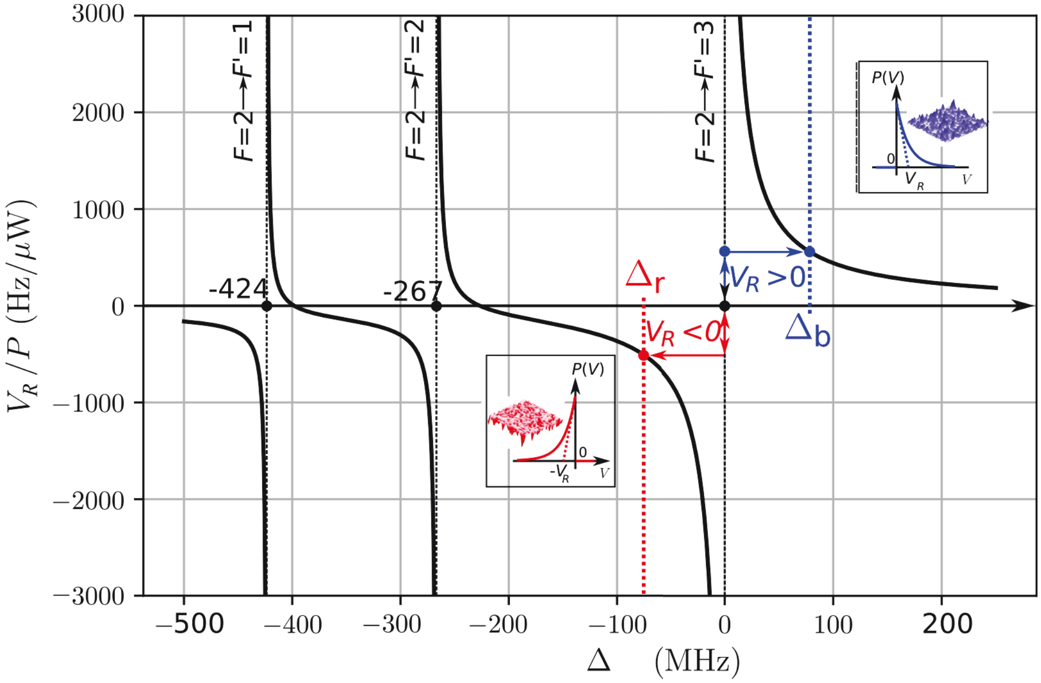

Figure 4.8: The estimated disorder amplitude $V_R = \bar{V}_2$ for power $P = 1$ µW and speckle waist of 1.38 mm. Around the $F = 2 \rightarrow F' = 3$ transition, positive (negative) detuning results in positive (negative resp.) V_R.

izability, $\alpha_{|1\rangle}/\alpha_{|2\rangle}$. Since α has typical $1/\Delta$-dependence on the optical detuning and $\Delta \ll \Delta_{\text{hf}}$, the potential associated with the state $|1\rangle$ is negligible. For the aforementioned examples of detuning, we have

$$|V_1/V_2| \sim 0.01. \tag{4.37}$$

However, we require potential V_1 to be smaller than the chemical potential which is about 40 Hz. This allow range of $|V_R|$ up to around 4 kHz.

Besides, estimation of the atomic lifetime in the disorder for $|V_R|/h = 4$ kHz is around 0.58 ms. Since the dissipation rate is proportional to the intensity like the optical potential, the lifetime is inversely proportional to the disorder amplitude V_R.

Lightshift measurement For experimental purposes, we keep detuning $\Delta = \Delta_{\text{b}} = 2\pi \times 81$ MHz for generating repulsive potential and $\Delta = \Delta_{\text{r}} = -2\pi \times 73$ MHz for generating attractive potential. In order to verify that the same power would give opposite disorder amplitude, we perform two-photon rf-spectroscopy of atoms in the presence of homogeneous light field produced (see Fig. 4.3) by the same laser used to generate the speckle disorder. From this, we obtain the lightshift. Fig. 4.9 depicts the spectrum excitations for the two values of the detuning Δ. As shown in the figure, the lightshifts measured are reasonably equal in magnitude, $\Lambda_r = -70$ Hz for the attractive case and $\Lambda_b = 71$ Hz for the repulsive case.

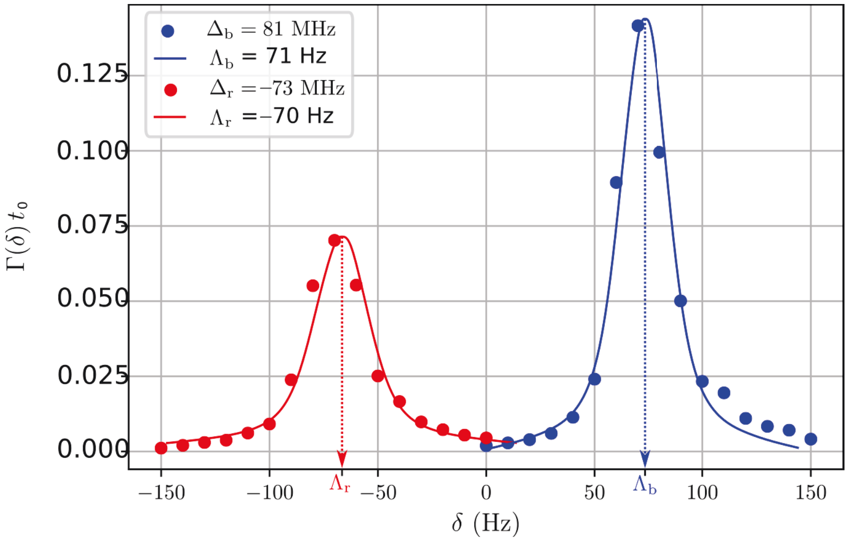

Figure 4.9: The spectrum excitations measured in the presence of homogeneous light resulting in lightshift. Blue points and line (red points and line) correspond to detuning $\Delta_b = 83$ MHz ($\Delta_r = -73$ MHz respectively) with respect to the $F = 2 \rightarrow F' = 3$ transition corresponding to repulsive (attractive respectively) optical potential. For laser power, $P_{\rm cal} = 200$ nW, the lightshifts measured are 71 Hz for the repulsive case and −70 Hz for the attractive case.

In our experiment, it is very complicated to measure the exact laser power experienced by the atoms. The laser power is measured *ex-situ*, see the "Optical manipulation" set-up in Fig. 4.3. We also estimate the power loss due to mirror reflections, lens transmission, etc. However, the real calibration of V_R will be commented in section 5.2.

4.4 Conclusion

In this chapter, we have discussed the realization of the state-dependent disordered potential for ultracold atoms introduced in Fig. 1.3. The disorder is realized with laser speckle. In the first section, we have discussed several relevant notions such as the waist of the speckle field, the correlation lengths (in transverse and longitudinal directions), and the Rayleigh probability distribution of the intensity. In the second section, we have presented the implementation of the laser speckle. In particular, we have characterized the correlation lengths from the correlation measurement. The disorder is shown to be anisotropic. In relation with Chap. 2, we have deduced the experimental value of the correlation energy (E_σ) (see Eq. 2.16). Furthermore, we have presented the implementation of the state-dependent potential in the third subsection. We have considered the optical potentials of the two "clock" states, $|1\rangle = |F = 1, m_F = -1\rangle$ and $|2\rangle = |F = 2, m_F = +1\rangle$. Effectively, only in the state $|2\rangle$ the disorder potential is realized. From this, we have introduced the parameter of disorder amplitude V_R which is equivalent to the average potential associated with the Rayleigh distribution. Lastly, we also show that it is possible to realize both attractive ($V_R < 0$)

and repulsive ($V_R > 0$) disordered potentials.

Combining the state-dependent disorder with the radio-frequency transfer (see subsection 3.3.1), it would be possible to load matter wave in the disorder with controllable energy. In Chap. 5, we present a proof of concept by measuring the spectral function of ultracold atoms in disordered potential. However, the dissipation is found to be high such that the atomic lifetime in the disorder is insufficient for the studies of Anderson transition. An upgraded version of the state-dependent disordered potential for such purpose is presented in Chap. 6.

Chapter 5

Spectral functions of ultracold atoms in disordered potentials

Contents

The spectral function is an essential tool for characterization of complex systems associated with interparticle interactions or random scatterers [140]. From this, we can extract information on the energy-momentum relation of one-particle excitations in the systems in order to describe their related phenomena. As an example, the spectral function of strongly correlated electronic system can be measured directly via angle-resolved photoemission spectroscopy (ARPES) [141]. This has many applications, such as for studies of high-T_c superconductivity of cuprate superconductors [142]. For ultracold atomic systems, the spectral functions are usually measured using radio-frequency spectroscopy [143], stimulated Raman spectroscopy [144], or Bragg spectroscopy [147,148]. For strongly interacting Fermi gases, the spectral function measurements lead to observations of pseudogap behavior associated with the pairing of fermions [145,146]. For Bose gases, the measurements allow novel approach for probing the superfluid-Mott insulator transition [147,148] and the dynamics of the quasiparticle in the Mott insulator regime [149].

As discussed in Chap. 2, the spectral function of cold atoms in disordered potential has been invaluable for the estimation of the mobility edge of the Anderson transition, yet its measurement was not available. In this chapter, we present our work on the direct measurement of the spectral functions of ultracold atoms in disordered potentials. The ultracold atoms can be considered as noninteracting particles at quasi-null momentum; see Chap. 3. The disordered potential is realized with three-dimensional speckle disordered potentials as presented in Chap. 4. In this chapter, we review several notions related to the spectral function in section 5.1 and we present the measurement results in section 5.2. We also highlight the compatibility of the spectral function measurement with previously measured elastic scattering time in section 5.3. As discussed further in the conclusion, this work would pave the way for spectroscopic approach of studying the Anderson transition.

5.1 Spectral function

The Hamiltonian $\hat{H}$ of a complex quantum system can be decomposed in two terms as follows

$$\hat{H} = \hat{H}_0 + \hat{V}, \tag{5.1}$$

where $\hat{H}_0$ is the free particle Hamiltonian and $\hat{V}$ is the perturbation Hamiltonian. Hamiltonian $\hat{H}_0$ has known basis. As an example, Hamiltonian $\hat{H}_0$ of an electron in a crystal is associated with the basis of wave-vectors inside the Brillouin zone. The basis is then used to describe the effect of the perturbation $\hat{V}$, which may result from interparticle interaction or disorder. For a matter wave in a disordered system, we consider a single-particle problem with $\hat{H}_0 = \boldsymbol{p}^2/(2m)$, the kinetic energy. The disordered potential acts as the perturbation $V(\boldsymbol{r})$. For disordered system, the plane waves $\{|\boldsymbol{k}\rangle\}$ form an appropriate basis to describe the system. Although the kinetic energy does not commute with the disordered potential, translation invariance emerges after the ensemble averaging. For this, one need to assume that the disordered potential is statistically homogeneous.

For a matter wave of energy E in a disordered potential, the spectral function follows [140]

$$A(E, \boldsymbol{k}) \equiv -\frac{1}{\pi}\mathrm{Im}\left[\overline{G}(E, \boldsymbol{k})\right], \tag{5.2}$$

where $\overline{\cdots}$ denotes the disorder averaging and G is the retarded Green's function.

In this section, we discuss several theoretical notions related to the spectral function that have not been thoroughly discussed in Chap. 2. It contains five subsections. In the first subsection, we review some generalities about the Green's function, including the so-called self-energy. In the second subsection, we introduce the definition of the spectral function. In the third subsection, we discuss the self energy in perturbative regime. In the fourth subsection, we consider a special regime of strong disorder, the so-called classical disorder. Lastly, we provide a short summary of these notions before presenting the experimental results in the next section.

5.1.1 The Green's function

The Green function is useful to describe the evolution of the system. It is represented by an operator[1] $\hat{\mathcal{G}}$,

$$\hat{\mathcal{G}}(t) = -i\Theta(t)e^{-i\hat{H}t/\hbar}, \tag{5.3}$$

where $\Theta(t)$ is Heaviside distribution. It can be represented in the position-temporal basis, $\mathcal{G}(\boldsymbol{r'}, \boldsymbol{r}, t) = \left\langle \boldsymbol{r} \left| \hat{\mathcal{G}} \right| \boldsymbol{r'} \right\rangle$, such that for an initial state $\Psi(\boldsymbol{r'}, t = 0)$, the evolved state $\Psi(\boldsymbol{r}, t)$ follows

$$\begin{aligned}\Psi(\boldsymbol{r}, t) = \langle \boldsymbol{r} | \Psi(t) \rangle &= \left\langle \boldsymbol{r} \left| \hat{\mathcal{G}} \right| \Psi(t = 0) \right\rangle \\ &= \int_{\mathbb{R}} \mathrm{d}\boldsymbol{r'}\, \mathcal{G}(\boldsymbol{r'}, \boldsymbol{r}, t)\Psi(\boldsymbol{r'}, 0).\end{aligned} \tag{5.4}$$

The Green's function, $\mathcal{G}(\boldsymbol{r'}, \boldsymbol{r}, t)$, can be interpreted as the "probability amplitude" for particle transition from point $\boldsymbol{r'}$ to point $\boldsymbol{r}$.

We are interested in the Green's function in the energy basis, $\hat{G}(E) = \frac{1}{\hbar}\int \mathrm{d}t\; e^{iEt/\hbar}\hat{\mathcal{G}}(t)$ which gives

$$\hat{G}(E) = \frac{1}{E - \hat{H} + i0^+}. \tag{5.5}$$

This Green's function also follows the following equation

$$\hat{G}(E) = \hat{G}_0(E) + \hat{G}_0(E)\hat{V}\hat{G}(E), \tag{5.6}$$

where $\hat{G}_0(E) = \frac{1}{E - \hat{H}_0 + i0^+}$ is the Green's function in the absence of hamiltonian $\hat{V}$. Upon iteration and ensemble averaging, we can obtain the following series,

$$\overline{\hat{G}(E)} = \hat{G}_0(E) + \hat{G}_0(E)\overline{\hat{V}}\hat{G}_0(E) + \hat{G}_0(E)\overline{\hat{V}\hat{G}_0(E)\hat{V}}\hat{G}_0(E) + \dots\,. \tag{5.7}$$

The self energy In many theoretical works (see Refs. [68, 140, 150] as examples), the averaged Green's function can be written as follows,

$$\overline{\hat{G}(E)} = \hat{G}_0(E) + \hat{G}_0(E)\hat{\Sigma}(E)\overline{\hat{G}(E)}, \tag{5.8}$$

---

[1] We consider the retarded Green function, defined for $t > 0$.

where $\hat{\Sigma}(E)$ is the (retarded) self-energy operator. This is known as the Dyson equation. The Green's function also can be rewritten as

$$\overline{\hat{G}(E)} = \frac{1}{\hat{G}_0^{-1}(E) - \hat{\Sigma}(E)}. \tag{5.9}$$

The self-energy operator contains all irreducible correlation function and can be shown as follows,

$$\begin{aligned}\hat{\Sigma}(E) &= \sum_{n=0}^{+\infty} \hat{\Sigma}_n, \\ &= \overline{\hat{V}} + \overline{\delta\hat{V}\hat{G}_0(E)\delta\hat{V}} + \dots ,\end{aligned} \tag{5.10}$$

where $\delta\hat{V} = \hat{V} - \overline{\hat{V}}$.

Before discussing the spectral function, we should represent the Green function in $|\boldsymbol{k}\rangle$-basis, which is given by $\overline{G}(E,\boldsymbol{k}) = \left\langle \boldsymbol{k} \middle| \overline{\hat{G}(E)} \middle| \boldsymbol{k} \right\rangle$. Similarly, the self-energy can be represented as $\Sigma(E,\boldsymbol{k}) = \left\langle \boldsymbol{k} \middle| \hat{\Sigma}(E) \middle| \boldsymbol{k} \right\rangle$. For $E_{\boldsymbol{k}}$ the kinetic energy associated with state $|\boldsymbol{k}\rangle$, we obtain,

$$\overline{G}(E,\boldsymbol{k}) = \frac{1}{E - E_{\boldsymbol{k}} - \Sigma(E,\boldsymbol{k})}. \tag{5.11}$$

Let us express the self-energy in terms of its real and imaginary components, $\Sigma(E,\boldsymbol{k}) = \Sigma_r(E,\boldsymbol{k}) - i\Sigma_i(E,\boldsymbol{k})$. Let us approximate functions $\Sigma_r(E,\boldsymbol{k})$ and $\Sigma_i(E,\boldsymbol{k})$ to be smooth functions of energy E around $E_{\boldsymbol{k}}$. In addition, we can also evaluate the Green's function $\overline{\mathcal{G}}(\boldsymbol{k},t) = \left\langle \boldsymbol{k} \middle| \overline{\hat{\mathcal{G}}(t)} \middle| \boldsymbol{k} \right\rangle$ as follows

$$\begin{aligned}\overline{\mathcal{G}}(\boldsymbol{k},t) &= \int \overline{G}(E,\boldsymbol{k}) e^{-iEt/\hbar} \frac{\mathrm{d}E}{2\pi} \\ &\sim \exp\left(-i\left(E_{\boldsymbol{k}} + \Sigma_r\right)t/\hbar\right) \exp\left(-\Sigma_i t/\hbar\right).\end{aligned} \tag{5.12}$$

From this expression, the real part of the self energy Σ_r can be associated with the dynamical phase. The imaginary part of the self energy, Σ_i, can be interpreted as the lifetime of the excitation[2], which is given by $\hbar/(2\Sigma_i)$.

5.1.2 The Spectral function

Based on the formalism described in previous subsection, we have at least two ways of expressing the spectral function. The first expression invokes the self-energy, which is a complex function. For

---

[2] The lifetime is associated with $\left|\overline{\mathcal{G}}(\boldsymbol{k},t)\right|^2$.

$\Sigma(E,\boldsymbol{k}) = \Sigma_r(E,\boldsymbol{k}) - i\Sigma_i(E,\boldsymbol{k})$, we obtain

$$\begin{aligned} A(E,\boldsymbol{k}) &= -\frac{1}{\pi}\mathrm{Im}\left[\overline{G}(E,\boldsymbol{k})\right] \\ &= \frac{1}{\pi}\frac{\Sigma_i(E,\boldsymbol{k})}{(E-E_{\boldsymbol{k}}-\Sigma_r(E,\boldsymbol{k}))^2+\Sigma_i^2(E,\boldsymbol{k})}. \end{aligned} \tag{5.13}$$

For a free particle, the spectral function would be a Dirac delta distribution at $E = E_{\boldsymbol{k}}$. For non-zero $\Sigma(E,\boldsymbol{k}) = \Sigma_r - i\Sigma_i$ as depicted in Fig. 5.1, the real part of the self energy is associated with the energy shift and the imaginary part is associated with the energy broadening.

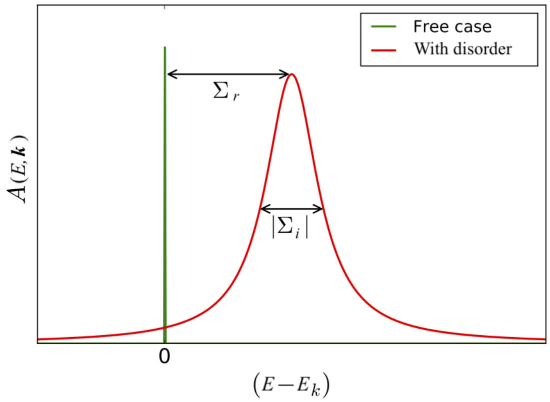

Figure 5.1: Spectral function associated with the self-energy $\Sigma = \Sigma_r - i\Sigma_i$ (in red line) and its comparison with the free particle case (in green line). Taken from Ref. [150]

Secondly, the spectral function can be expressed as follows

$$A\left(E,\boldsymbol{k}\right) = -\frac{1}{\pi}\mathrm{Im}\left\langle \boldsymbol{k}\left|\overline{\left(\frac{1}{E-\hat{H}+i0^+}\right)}\right|\boldsymbol{k}\right\rangle = \overline{\left\langle \boldsymbol{k}\left|\delta(E-\hat{H})\right|\boldsymbol{k}\right\rangle}. \tag{5.14}$$

If one introduces the eigenstates $|\psi_\alpha\rangle$, associated with energies $\mathcal{E}_\alpha$, of the Hamiltonian $\hat{H}$, Eq. 5.14 can be rewritten as:

$$A_{\boldsymbol{k}}\left(E\right) = \overline{\sum_\alpha |\langle \boldsymbol{k}|\psi_\alpha\rangle|^2\,\delta\left(E-\mathcal{E}_\alpha\right)}. \tag{5.15}$$

$|\langle \boldsymbol{k}|\psi_\alpha\rangle|^2$ is the overlap function between the state $|\boldsymbol{k}\rangle$ and state $|\psi_\alpha\rangle$ at energy $\mathcal{E}_\alpha$. Furthermore, it can be shown that $\int \mathrm{d}E\ A\left(E,\boldsymbol{k}\right) = 1$. Thus, the spectral function can be interpreted as the probability density for a plane-wave $|\boldsymbol{k}\rangle$ to have energy E in the disordered system. Besides, the spectral function can be related to the density of state[3], $\rho(E)$. Considering that the overlap function

---

[3] The density of state per unit volume, $\rho(E)$, follows

$$\rho(E) = \frac{1}{L^d}\mathrm{Tr}\left[\overline{\delta(E-\hat{H})}\right] = \int \frac{\mathrm{d}^d\boldsymbol{k}}{(2\pi)^d}A_{\boldsymbol{k}}\left(E\right).$$

$|\langle \boldsymbol{k}|\psi_\alpha\rangle|^2$ is a slow varying function upon disorder averaging, we obtain

$$A_{\boldsymbol{k}}(E) \sim |\langle \boldsymbol{k}|\psi_\alpha\rangle|^2 \rho(E). \tag{5.16}$$

5.1.3 The self energy within the Born approximation

In short, the Born approximation consists of considering only the first two terms of the self-energy (Eq. 5.10),

$$\Sigma(E,\boldsymbol{k}) \approx \left\langle \boldsymbol{k}\left|\overline{\hat{V}}\right|\boldsymbol{k}\right\rangle + \left\langle \boldsymbol{k}\left|\overline{\delta\hat{V}G_0(E,\boldsymbol{k})\delta\hat{V}}\right|\boldsymbol{k}\right\rangle. \tag{5.17}$$

The first term corresponds to average potential $\bar{V}$ which is real. The second term has non-zero imaginary part which is given by[4],

$$\begin{aligned}\Sigma_{1,i}(E,\boldsymbol{k}) &= -\mathrm{Im}\left[\left\langle \boldsymbol{k}\left|\overline{\delta\hat{V}G_0(E,\boldsymbol{k})\delta\hat{V}}\right|\boldsymbol{k}\right\rangle\right],\\ &= \pi\int \frac{\mathrm{d}^d\boldsymbol{k'}}{(2\pi)^d}\overline{\left|\left\langle \boldsymbol{k}\left|\delta\hat{V}\right|\boldsymbol{k'}\right\rangle\right|^2}\delta\left(E-E_{\boldsymbol{k}}\right).\end{aligned} \tag{5.18}$$

We can show that $\overline{\left|\left\langle \boldsymbol{k}\left|\delta\hat{V}\right|\boldsymbol{k'}\right\rangle\right|^2}$ is given by

$$\overline{\left|\left\langle \boldsymbol{k}\left|\delta\hat{V}\right|\boldsymbol{k'}\right\rangle\right|^2} = \tilde{C}(\boldsymbol{k}-\boldsymbol{k'}), \tag{5.19}$$

where $\tilde{C}(\boldsymbol{k}-\boldsymbol{k'})$ is the speckle intensity correlation in Eq. 2.3 and in subsection 2.1.1. From this, we deduce the scattering time τ_S within Born approximation,

$$\Sigma_{1,i}(E,\boldsymbol{k}) = \frac{\hbar}{2\tau_s^{\mathrm{Born}}}. \tag{5.20}$$

It can be shown that the real part of Σ_1 is small such that,

$$A_{\boldsymbol{k}}(E) \approx \frac{1}{\pi}\frac{\hbar/(2\tau_s^{\mathrm{Born}})}{\left(E-E_{\boldsymbol{k}}-\bar{V}\right)^2+(\hbar/(2\tau_s^{\mathrm{Born}}))^2}. \tag{5.21}$$

It has maxima at $E = E_{\boldsymbol{k}} + \bar{V}$ with full width at half maximum (FWHM) of $\hbar/(\tau_s^{\mathrm{Born}})$.

Validity of Born approximation. As the offset potential $\bar{V}$ has little importance, we show the validity of the Born approximation as

$$|\Sigma_1| = \hbar/(2\tau_S^{\mathrm{Born}}) \ll E_{\boldsymbol{k}}. \tag{5.22}$$

---

[4] By applying $\mathrm{Im}\left[\frac{1}{E-E_{\boldsymbol{k}}+i0^+}\right] = -\frac{1}{\pi}\delta\left(E-E_{\boldsymbol{k}}\right)$.

With $E_{\boldsymbol{k}} = \hbar^2 \boldsymbol{k}^2/(2m)$ and $l_s^{\text{Born}} = \frac{\hbar k}{m} \tau_s^{\text{Born}}$, we identify equivalent condition for the Born approximation, yielding

$$k l_s^{\text{Born}} \gg 1. \tag{5.23}$$

5.1.4 The spectral function in strong disorder regime

Strong disorder regime is also called classical disorder regime, whereby the non-commutativity of $\hat{\boldsymbol{r}}$ and $\hat{\boldsymbol{p}}$ can be neglected. This corresponds to the limit $|\delta V| / E_\sigma \to \infty$ that is sometimes noted as $\hbar \to 0$. The spectral function is approximated as follows

$$A(E, \boldsymbol{k}) = \overline{\left\langle \boldsymbol{k} \left| \delta(E - \hat{H}) \right| \boldsymbol{k} \right\rangle} \underset{\hbar \to 0}{\longrightarrow} A^{\text{cl}}(E, \boldsymbol{k}) = \overline{\delta(E - E_{\boldsymbol{k}} - \hat{V})}, \tag{5.24}$$

where $A^{\text{cl}}(E, \boldsymbol{k})$ is the spectral function in the classical limit. It yields

$$\begin{aligned} A^{\text{cl}}(E, \boldsymbol{k}) &= \overline{\delta(E - E_{\boldsymbol{k}} - \hat{V})}, \\ &= \int \mathrm{d}V \; P(V) \delta(E - E_{\boldsymbol{k}} - V), \\ &= P(E - E_{\boldsymbol{k}}), \end{aligned} \tag{5.25}$$

where $P(V)$ is the probability density of the disordered potential. $A^{\text{cl}}(E, \boldsymbol{k})$ corresponds to the "classical" probability for a particle to have energy $E = V + E_{\boldsymbol{k}}$, where $E_{\boldsymbol{k}}$ is the kinetic energy.

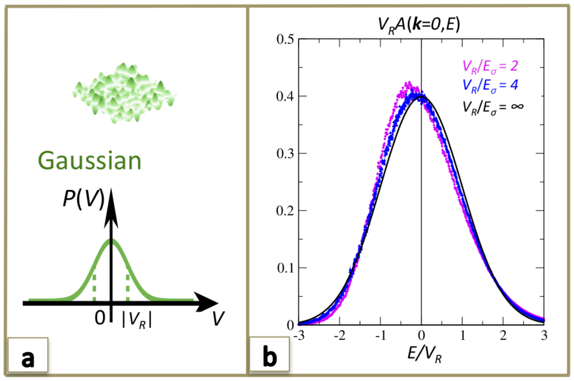

Figure 5.2: (a) Probability density of the Gaussian disorder with parameter V_R. (b) Numerical works of the spectral functions for Gaussian disorder for $V_R/E_\sigma = 2$, $V_R/E_\sigma = 4$ and the probability distribution ($V_R/E_\sigma = \infty$); taken from Ref. [151].

In many references on condensed matter physics, the Gaussian disorder is considered. Its probability distribution follows

$$P(V) = \frac{1}{\sqrt{2\pi} V_R} \exp\left(-\frac{V^2}{2V_R^2} \right), \tag{5.26}$$

where V_R corresponds to the standard deviation (see Fig. 5.2(a)). The parameter V_R can be associated with the disorder strength and we can also show that $V_R^2 = C(\boldsymbol{\Delta r} = 0)$. The convergence of the spectral function towards the classical probability distribution has been studied by Trappe et al. [151]. Fig. 5.2(b) depicts the calculated spectral functions for Gaussian disorder. The convergence of the spectral function towards the probability distribution can already be seen for $V_R/E_\sigma = 4$.

5.1.5 Conclusion

In this section, we have looked at many aspects of the spectral function. Its first importance is to characterize the energy-momentum relation as shown in Eq. 5.14. Secondly, the spectral function contains information on the evolution of the matter wave in the disorder as shown in Eq. 5.13. For spectral function with profile close to a Lorentzian, its width can be associated with certain characteristic lifetime. Fourthly, we have shown that in the limit of Born approximation, the width of the spectral function can be analytically derived based on Eqs. 5.20 and 2.3. Lastly, we have discussed the classical limit whereby the spectral function converges to the probability distribution.

Probability distribution of speckle disordered potential. As discussed in Chap. 4, the speckle disorder features Rayleigh distribution. The probability distribution for speckle disorder is given by

$$P(V) = \frac{\Theta\left(V/V_R\right)}{|V_R|} \exp\left(-\frac{V}{V_R}\right), \tag{5.27}$$

where V_R is the disorder amplitude which can be either positive or negative. Fig. 5.3 depicts the plots of the probability distribution for speckle repulsive potential ($V_R > 0$), speckle attractive potential ($V_R < 0$), and Gaussian disorder. Speckle potential has several peculiarities. Firstly, its probability density is asymmetrical. Secondly, the probability density has discontinuity at $V = 0$. Thirdly, the potential landscape depend on the sign of V_R. Repulsive speckle potential resembles mountainous landscape above zero level. In the contrary, attractive potential resembles a landscape full of calderas (or wells) below the zero level.

Classical disorder versus quantum disorder. As discussed in subsection 5.1.4, the classical disorder regime characterized by the convergence of the spectral function towards the probability density $P(V)$ in the limit of large $|V_R|/E_\sigma$. In the opposite limit, there exists the so-called "quantum" regime of weak disorder corresponding to $|V_R|/E_\sigma \ll 1$. In this regime, the spatial extension of typical eigenstates spans many disorder grains. As a consequence, the disorder potential is smoothened resulting in effective disorder strength

$$V_{R,\text{eff}} \sim \frac{V_R^2}{E_\sigma}, \tag{5.28}$$

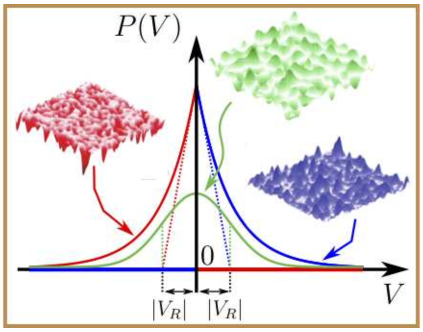

Figure 5.3: The probability density for attractive speckle (shown in red), repulsive speckle (shown in blue), and Gaussian speckle (shown in green); the standard deviation is $|V_R|$ for the three examples. For repulsive speckle, wave propagates between "mountains" whereas for attractive speckle, wave propagates between "wells".

which is much smaller than its initial strength $|V_R|$ [68,71]. In this extreme, the spectral function is a narrow function with a width $\sim V_{R,\text{eff}}$. Hence, we can see that the profile of spectral function has dependence on the ratio $|V_R|/E_\sigma$.

5.2 Measurement of the spectral functions

In this section, we present the direct measurement of the spectral functions of noninteracting ultracold atoms at quasi-null momentum in three-dimensional speckle disordered potentials. In the first subsection, we describe the measurement protocol. In the second subsection, we present the measurement results for both attractive (red-detuned) and repulsive (blue-detuned) laser speckle disorder. In particular, we discuss the crossover between the so-called "quantum" regime of weak disorder and the so-called "classical" regime of strong disorder.

5.2.1 Measurement protocol

Fig. 5.4 depicts the measurement scheme of the spectral functions. It combines the rf transfer scheme presented in section 3.3 and state-dependent disorder scheme presented in section 4.3. States $|1\rangle$ and $|2\rangle$ are the two "clock-states", $|F=1, m_F=-1\rangle \equiv |1\rangle$ and $|F=2, m_F=1\rangle \equiv |2\rangle$. Fig. 5.4(a) depicts the state-dependent disordered potential created using a near-resonant laser speckle as presented in subsection 4.3.2. The laser has detuning Δ with respect to the $F=2 \rightarrow F'=3$ transition, which is much smaller compared with the hyperfine splitting of around 6.8 GHz, $|\Delta| \ll \Delta^{\star}_{\text{hf}}$. Consequently, the optical potential of the state $|1\rangle$ becomes negligible. Red detuning, $\Delta < 0$ corresponds to attractive disordered potential ($V_R < 0$), while blue detuning, $\Delta > 0$ corresponds to repulsive one ($V_R > 0$) (see Fig. 4.8). Lastly, the laser intensity is proportional to the disorder strength $|V_R|$, it can be varied over 2 orders of magnitude (see Fig. 5.5).

Fig. 5.4(b) and (c) depicts the measurement scheme of the spectral function based on the rf

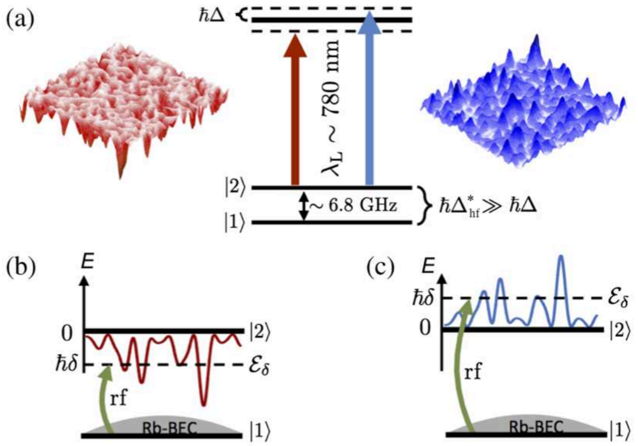

Figure 5.4: **Measurement scheme of the spectral function using a state-dependent disordered potential**. (a) Disordered potential is created using a near resonant laser speckle with detuning Δ with respect to the hyperfine $F = 2 \to F' = 3$ transition; red detuning, $\Delta < 0$, (blue detuning, $\Delta > 0$) corresponds to attractive (repulsive respectively) disordered potential. The optical potential experienced by atoms in the state $|1\rangle$ is negligible, since $\Delta^\star_{\text{hf}} \gg |\Delta|$. (b) and (c) A radio-frequency field at frequency $\Delta^\star_{\text{hf}} + \delta$ is applied to transfer a small fraction of atoms in a BEC in the state $|1\rangle$ to the state $|2\rangle$. The transfer rate measured in this experiment is proportional to the spectral function.

transfer scheme for attractive and repulsive disorders respectively. The experiment starts with the realization of a ^{87}Rb-BEC of about $n_1 = 2 \times 10^5$ atoms in the state $|1\rangle$. Then, the disordered potential for state $|2\rangle$ is turned on. At the same time, the transfer to the state $|2\rangle$ is performed during time interval t_0. The transfer rate, Γ_{rf}, is directly obtained by counting the atoms populating the state $|2\rangle$, n_2, via fluorescence imaging, according to $n_2(t_0) \simeq n_1(0)\Gamma_{\text{rf}} t_0$.

The transfer allows us to selectively populate eigenstates of the random potential around the resonant energy $E_f = E_i + \hbar\omega$ set by the rf frequency ω (here E_i and E_f correspond to the total energy of the initial and final states respectively). Because of the finite energy resolution of the transfer, energy levels in the disorder behave as an effective continuum, whose density of states ρ is equal to the density of states averaged over disorder realizations [51, 138]. According to the Fermi golden rule, one can thus define a transfer rate Γ_{rf}, proportional to the squared modulus of the transition amplitude from the initial state $|1\rangle$ to the targeted final states, which is directly linked to the spectral function of the disordered potential (see Eq. 5.29 below). The initial state of the BEC in a shallow trap very closely corresponds to a null momentum state $|\boldsymbol{k} = 0\rangle$. The total energy of the initial state can be taken equal to the internal energy E_1 [138]. The external energy of the final states is then given by $\mathcal{E}_\delta = \hbar\delta$, where $\delta = \omega - \Delta^\star_{\text{hf}}$ is the rf detuning from the bare resonant frequency corresponding to the hyperfine splitting between the respective internal energies $\Delta^\star_{\text{hf}}/2\pi = (E_2 - E_1)/h \simeq 6.8$ GHz (see Fig. 5.4)[5]. The rf transfer being associated with

---

[5] As discussed in section 3.3, the hyperfine splitting takes into account the magnetic shifts associated with the "magic" bias field $B_0^\star = 3.23$ G. This results in sharp resonance for the $|1\rangle \leftrightarrow |2\rangle$ transition.

a negligible momentum change, the transfer rate from state $|1\rangle$ to $|2\rangle$ is thus proportional to the spectral function $A\left(E=\hbar\delta, \boldsymbol{k}=0\right)$:

$$\begin{aligned}\Gamma_{\mathrm{rf}} \propto A\left(E=\hbar\delta, \boldsymbol{k}=0\right) &= \overline{\sum_{\alpha} \left|\langle\psi_{\alpha}|\boldsymbol{k}=0\rangle\right|^{2} \delta\left(\hbar\delta-\mathcal{E}_{\alpha}\right)} \\ &\sim \overline{\left|\langle\psi_{\delta}|\boldsymbol{k}=0\rangle\right|^{2}} \rho\left(E=\hbar\delta\right).\end{aligned} \tag{5.29}$$

Here, $|\psi_{\alpha}\rangle$ corresponds to the eigenstate of energy $\mathcal{E}_{\alpha}$ and $\overline{\cdots}$ denotes the averaging over disorder realizations. One can thus determine the spectral function by measuring the transfer rate as a function of the rf detuning δ. The spectral function $A(E=\hbar\delta, \mathbf{0})$ is finally obtained by repeating the measurement at various values of the detuning δ.

The measurements are performed in accordance with several conditions. Firstly, the rf coupling is weak enough such that the transfer rate Γ can be calculated via the Fermi golden rule as written in Eq. 5.29 [152–155]. The Fermi golden rule is valid provided that the Rabi coupling, Ω, is much smaller than the continuum width of the eigenstates of the random potential, Δ_w. Secondly, the duration t_0 is chosen short enough, i.e., $\Gamma_{\mathrm{rf}} t_0 \ll 1$, such that only a small fraction of atoms is transferred (a few percents at most). This assures the linear growth of the population in state $|2\rangle$ in t_0. Thirdly, the time t_0 is adapted such that the energy resolution, $\Delta\mathcal{E} \sim \hbar/t_0$ remains smaller than the typical energy span of the spectral function, i.e. Δ_w. These conditions are verified for each disorder amplitude, so that the observed profile is not affected.

Besides, additional disorder averaging is not necessary in the experiment. The finite energy resolution already provides an effective averaging over many energy states. In addition, the BEC initial extension which is given by the Thomas-Fermi radius is very large compared with the speckle grain size σ. Thus, the BEC "samples" efficiently the disordered potentials.

Comparison with numerical calculation. The experimental results are compared to the results of the numerical calculations. There are two important aspects. Firstly, the calculations take into account the detailed statistical properties of the speckle disorder used in the experiment, as discussed in subsection 4.2.3 (see the discussion which explains the "beyond paraxial" calculation of the correlation functions shown in Fig. 4.6). Secondly, the calculations of the spectral functions are based on the temporal representation (equivalent to the Eq. 5.14),

$$A\left(E, \boldsymbol{k}\right) = \frac{1}{\pi\hbar} \mathrm{Re}\left[\int_{0}^{\infty} \overline{\langle\boldsymbol{k}\left|e^{-iHt/\hbar}\right|\boldsymbol{k}\rangle} e^{iEt/\hbar} dt\right], \tag{5.30}$$

which amounts to evaluating the (disorder-averaged) scalar product between the initial plane-wave excitation $|\boldsymbol{k}\rangle$ (here, $|\boldsymbol{k}=0\rangle$) and the time-evolved state $\exp\left(-iHt/\hbar\right)|\boldsymbol{k}\rangle$, with H the disordered Hamiltonian. More details about the numerical calculation are presented in Refs. [51, 138].

5.2.2 Results

Fig. 5.5 shows the measured spectral functions, $A(E = \hbar\delta, \boldsymbol{k} = 0)$, as well as the results of their numerical calculations, for the cases of attractive (panel I on the top), and repulsive (panel II on the below) disordered potentials with amplitudes $|V_R|$ ranging from 60 Hz to 4 kHz. The area under the experimental curves is normalized in order to allow for a direct comparison with numerical calculations [51, 138]. Raw numerical results have been convolved by the experimental resolution function, yielding only minor corrections. The disorder strength has been precisely calibrated by adjusting the experimental and numerical curves of panel (I.b), leading to a 14% correction of the amplitude estimated from photometric measurements [51, 52]. This correction factor is then applied to all other measurements. The agreement is excellent over the whole range of disorder amplitudes.

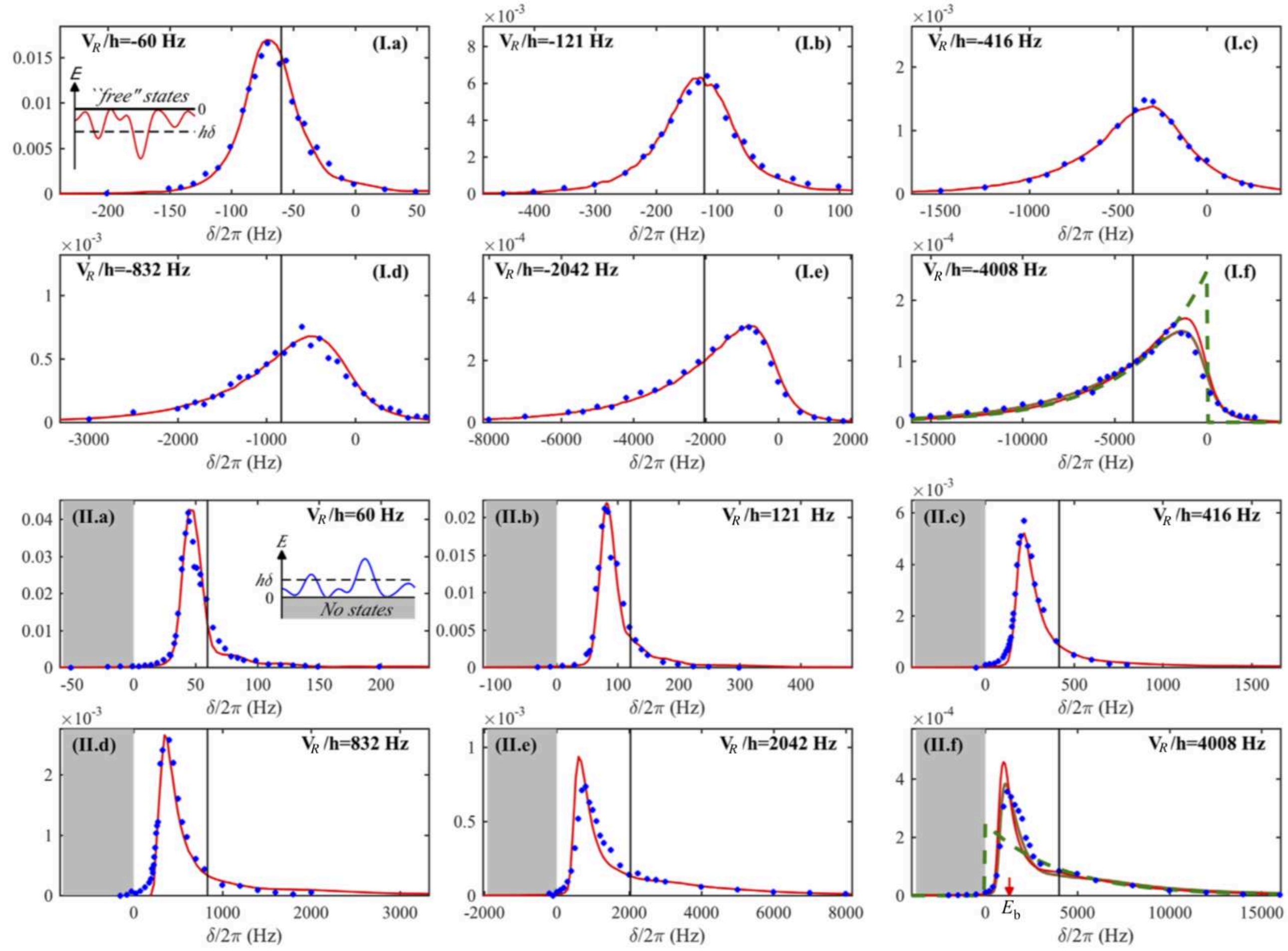

Figure 5.5: **Experimental results**. Measured (blue dots) and numerically calculated (red solid lines) spectral functions $A\,(E = \hbar\delta, \boldsymbol{k} = 0)$ of atoms in attractive (panel I on top) or repulsive (panel II) disordered potentials with various amplitudes. The solid brown lines in panels (I.f) and (II.f) are the results of numerical computations taking into account the residual effect of disorder in the initial state $|1\rangle$ [138]. In each panel, the black vertical lines indicate the average value V_R/h of the disorder. The small arrow in panel (II.f) indicates the estimated position of the average ground state energy in local minima, $E_\mathrm{b}/h = 1.3$ kHz. Insets in panel (I.a) and (II.a) illustrate the disorder potential for the corresponding configuration. The probability distribution $P(V)$ of the speckle potential is represented as a dashed green curve in panels (I.f) and (II.f). Figures are taken from Refs. [51]

In the attractive case (Fig. 5.5, panel I), we observe a smooth crossover from the weak disorder regime [panel (I.a)], where the spectral function is relatively narrow, symmetrical and centered closed to the averaged disorder amplitude V_R, to the strong disorder regime [panel (I.f)] where it becomes strongly asymmetrical. As discussed in the previous section, these two marginal regimes can be understood by comparing the disorder amplitude with the correlation energy, $E_\sigma = \frac{\hbar^2}{m(\sigma_\perp^2\sigma_\parallel)^{2/3}}$, associated with the finite spatial correlation lengths of the disordered potential. As discussed in subsection 4.2.3[6], in our experiment, $E_\sigma/h \approx 441$ Hz. Almost similar trend is observed for the repulsive case (Fig. 5.5, panel II) where the potential distribution is bounded from below. For this case, there is no state in the negative energy range (gray area) and the spectral function is strictly zero for negative energy. In following two subsubsections, we discuss more about the similarities and the differences between the attractive and the repulsive cases, in the quantum regime and in the classical regime.

5.2.2.1 The quantum regime

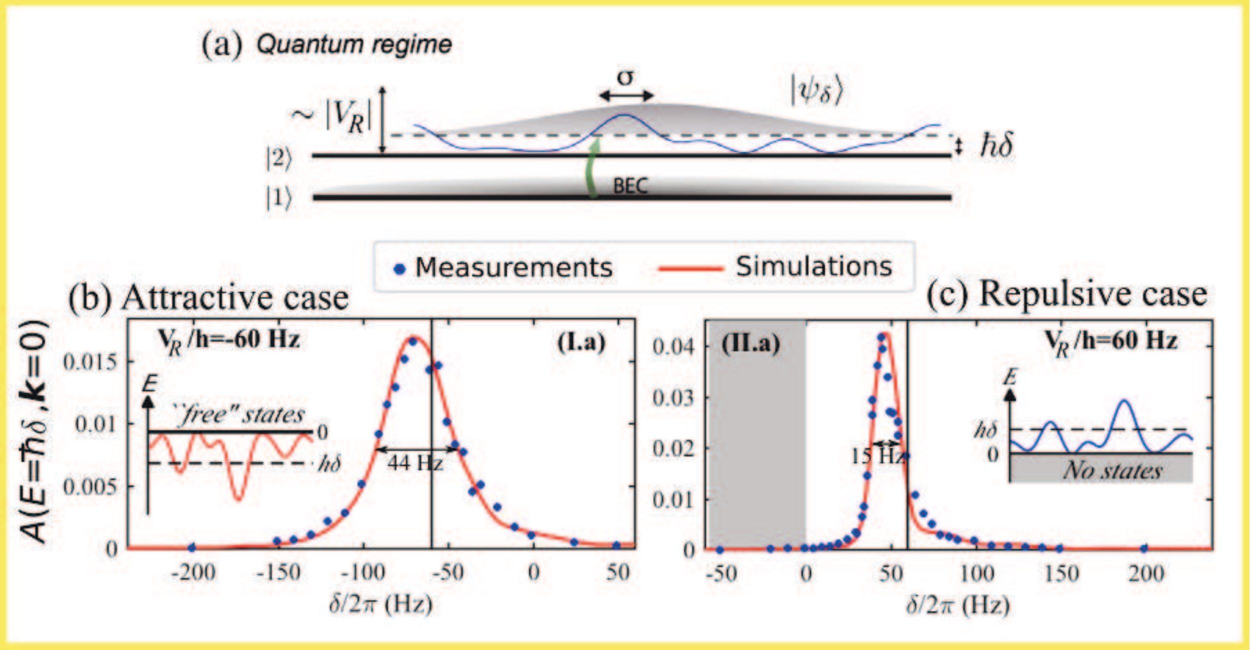

Figure 5.6: (a) Depiction of the quantum regime of weak disorder. The spectral functions measured at $V_R/h = \pm 60$ Hz correspond to this regime. (b) Case $V_R/h = -60$ Hz taken from panel (I.a) in Fig. 5.5. (c) Case $V_R/h = 60$ Hz taken from panel (II.a) in Fig. 5.5.

The quantum regime corresponds to disorder amplitude much weaker than the correlation energy, i.e. $|V_R|/E_\sigma \ll 1$ (see Fig. 5.6). In this regime, the amplitude of the disordered potential is too small to support bound states on the typical size $\sigma = (\sigma_\perp^2 \sigma_\parallel)^{1/3}$ of a speckle grain. Atoms with an energy of the order of $|V_R|$ have a large de Broglie wavelength compared to σ and their wave function extends over many speckle grains (see Fig. 5.6(a)). This leads to a smoothing of the disordered potential (see, e.g., Refs. [42,43]), whose rescaled effective amplitude corresponds to the width of the spectral function. Alternatively, a perturbative approach of scattering allows us to interpret this width as the inverse lifetime $\hbar/\tau_s$, where τ_s is the elastic scattering time, of the initial state

---

[6] By substituting m with the atomic mass, $\sigma_\perp \sim 0.306$ μm, and $\sigma_\parallel \sim 1.45$ μm.

$|\boldsymbol{k} = 0\rangle$ [44]. This approach predicts a Lorentzian shape for the spectral function, with a width $\sim \pi V_R^2/E_\sigma$ [21,25,43]. This explains the quasi-Lorentzian shape shown in Fig. 5.6(b).

Fig. 5.6 shows the measurement of spectral functions for $V_R/h = -60$ Hz and $V_R/h = 60$ Hz, corresponding to panels (I.a) and (II.a) in Fig. 5.5 respectively. Attempt of estimating the inverse lifetime $\hbar/\tau_S$ based on the FWHM-width gives $1/\tau_S = 2\pi \times 44$ Hz for the attractive case and $1/\tau_S = 2\pi \times 15$ Hz for the repulsive case. Clearly, for initial state $|\boldsymbol{k} = 0\rangle$, the Born approximation does not apply. However, we can compare these widths with that of the perturbative approach, which is given by $\hbar/\tau_S^B \sim \pi V_R^2/E_\sigma = h \times 25.6$ Hz [68,70,71]. The width of the repulsive case is 1.7 smaller than the perturbative case. In the contrary, the width of the attractive case is 1.7 larger than the perturbative case. While this shows that the measured widths have reasonable order of magnitude, this also shows consistency with the calculation of the third order of the self energy[7].

5.2.2.2 The classical regime

Contrary to the quantum regime, the classical regime corresponds to disorder amplitude much stronger than the correlation energy, i.e. $|V_R|/E_\sigma \gg 1$. The cases $V_R/h = \pm 4008$ Hz are approximately within this regime. The measured spectral functions are shown in Figs. 5.7(a) and (b). In these figures, the dashed green curves represent the probability distribution of the speckle potential towards which the spectral functions should converge[8]. The convergence is observed for both attractive and repulsive cases. However, around $|\mathcal{E}_\delta| \sim 0$, i.e. around the discontinuity of the potential distribution, the spectral functions remain smooth.

The classical regime can also be understood by using the so-called “Franck-Condon principle”. In this regime, atoms with an energy of the order of $|V_R|$ have a de Broglie wavelength small compared to σ, in opposite to the situation in the quantum regime. The corresponding wave functions have short spatial oscillations, except around the turning points r_j selected by the resonance condition $V(r_j) = \hbar\delta$, where atoms bounce classically on the disordered potential. This applies for both attractive case (see Fig. 5.7(c)) and repulsive case (see Fig. 5.7(d)). The overlap with the uniform initial state $|\boldsymbol{k} = 0\rangle$ is thus negligible except at these positions. The transfer rate—or, equivalently, the spectral function—is then a probe of the points where $V = \hbar\delta$, i.e., the probability distribution $P(V)$. This property was used in Ref. [132] to estimate the disorder amplitude V_R.

For speckle disorder, the convergence towards the probability distribution fails for energy around the zero level. However, the repulsive and the attractive cases show different trends. For the repulsive case whereby the spectral function is zero for negative energy, it shows a pronounced and narrow peak. Fig. 5.8 depicts the origin of the peak associated with the ground states of harmonic

---

[7] For speckle disorder, its correction to the τ_s scales as $1/V_R^3$, negative for the attractive case, positive for the repulsive case [66].

[8] Following discussion in subsection 5.1.4, by neglecting the kinetic energy term in Eq. 5.25, it yields directly $A(E, \boldsymbol{k} = 0) = P(V = E)$.

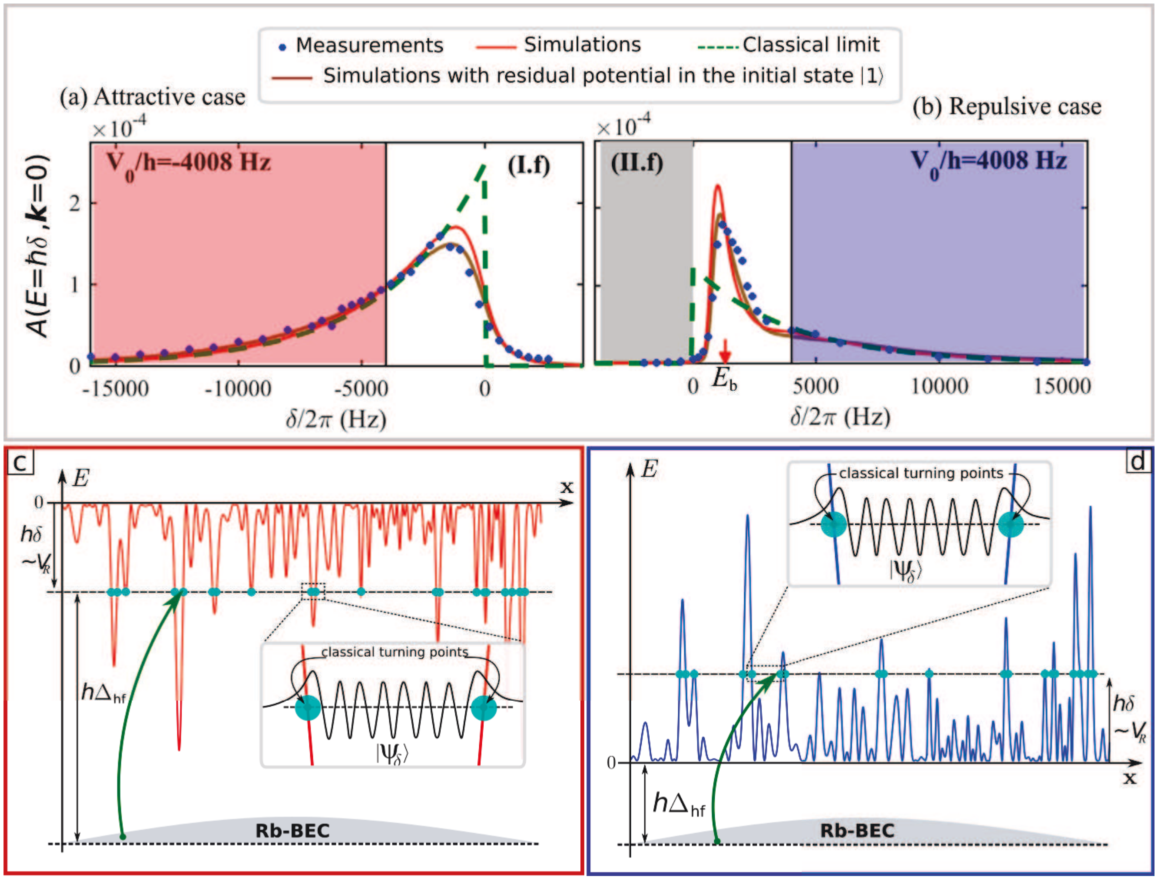

Figure 5.7: (a) and (b): The spectral functions measured for $V_R/h = -4008$ Hz and $V_R/h = 4008$ Hz respectively, which correspond to panels (I.f) and (II.f) in Fig. 5.5 respectively. (c) and (d): Depictions of the "Franck-Condon" principle for the regime of classical disorder for attractive and repulsive potentials respectively, which correspond to the shaded red area in Fig. (a) and to shaded blue area in Fig. (b) respectively.

oscillators around the local minima of the disordered potential. The ground states accumulate around typical energy[9] of $E_b \sim \sqrt{V_R E_\sigma}$ [151, 156]. As shown in Fig. 5.8(a) the peak is not far from $E_b = h \times 1.3$ kHz. Within the energy interval $[0, 2E_b]$, shown as the blue shaded area, both experimental data and numerical results of the spectral function show deviation from the classical limit.

Fig. 5.9 depicts the trend for the attractive case around the zero level. The red shaded area corresponds to interval $[-2E_b, 2E_b]$ where deviation from the classical limit is apparent; $E_b = \sqrt{|V_R|E_\sigma}$. For attractive speckle, the disordered potential features inverted harmonic potential below zero level. As discussed in Ref. [156], near zero level, the wave functions can tunnel between potential wells. As depicted in Fig. 5.9(b), the extension of the wave function near zero level can

---

[9] The typical frequency of the harmonic oscillator is given by $\omega_b = 2\sqrt{V_R/m}/\sigma$. Thus the energy of the first ground states is $E_b = \hbar\omega_b/2 = \sqrt{V_R E_\sigma}$

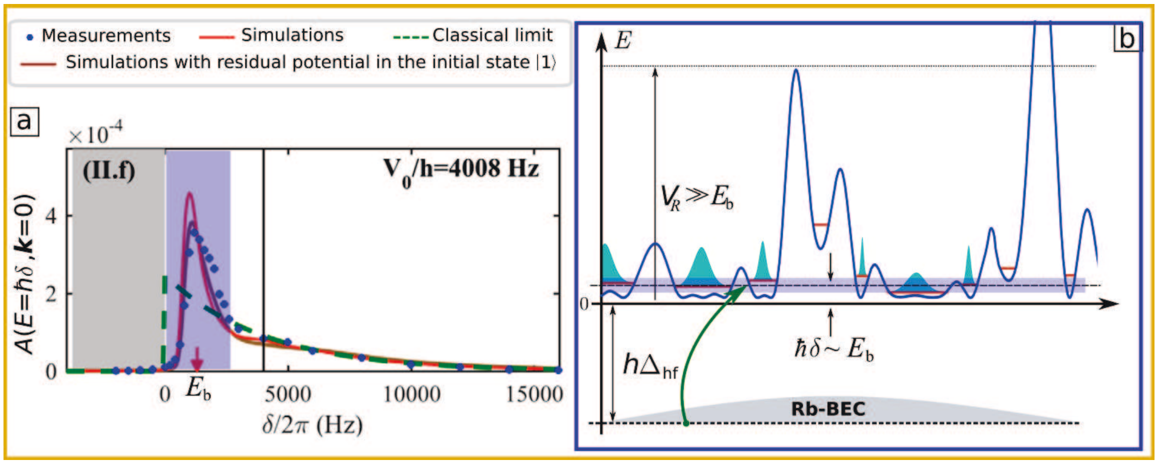

Figure 5.8: (a) Spectral functions measured for $V_R/h = 4008$ Hz with shaded area corresponding to interval $[0, 2E_b]$; $E_b = \sqrt{V_R \mathcal{E}_\sigma}$. (b) Depictions of the wave function of the states corresponding to δ in the interval $[0, 2E_b]$. The pronounced peak can be interpreted as a result of an accumulation of bound states around $\hbar\delta \sim E_b$.

span many speckle grains. Similar to the repulsive case[10], we can deduce similar characteristic energy $E_b = \sqrt{|V_R| E_\sigma}$.

For the largest disorder amplitudes, $V_R/h = \pm 4008$ Hz, we also consider the residual disorder on state $|1\rangle$. Since $V_{|1\rangle} \sim -0.01 \left| V_{|2\rangle} \right|$, we see that $V_{|1\rangle} \sim h \times 40$ Hz for the largest V_R which is about the same order of the chemical potential of the initial BEC. In order to take into account such effect in our numerical calculation, we performed a preliminary propagation of the initial state $|\boldsymbol{k} = 0\rangle$ in the presence of the same speckle disorder with amplitude $V_{|1\rangle}$ (which is always negative since the laser is always red detuned with $F = 1 \to F'$ transitions). Then, the perturbed state replaced the role of $|\boldsymbol{k}\rangle$ in the temporal representation (see Eq. 5.30). In general, this results in slight broadening of the measured spectral function [52], but its influence is shown to be marginal. The numerical computations taking into account the residual effect of disorder in the initial state $|1\rangle$ are shown in solid brown lines in Fig. 5.5 (see panels (I.f) and (II.f)) or Figs. (5.7, 5.8, and 5.9).

Concluding remarks

We have demonstrated a method that uses a state dependent disordered potential to probe the spectral functions of ultracold atoms in 3D laser speckle potentials. This allowed us to study the crossover from the quantum to the classical regime, the behavior being significantly different for red-detuned or blue-detuned laser speckles. In the latter case, a pronounced peak attributed to the lowest bound states in potential minima is observed, resulting in strong deviations from what we would expect using a weak-scattering perturbative approach.

---

[10] As an example, for a state of energy $E < 0$, it must be able to tunnel a distance $x_b \sim \sigma\sqrt{|E/2V_R|}$ with typical attenuation of $\gamma_b \sim \sqrt{2m|E|}/\hbar$. The tunneling is possible for $\gamma_b x_b \lesssim 1$, i.e. $|E| \lesssim \sqrt{|V_R| E_\sigma}$.

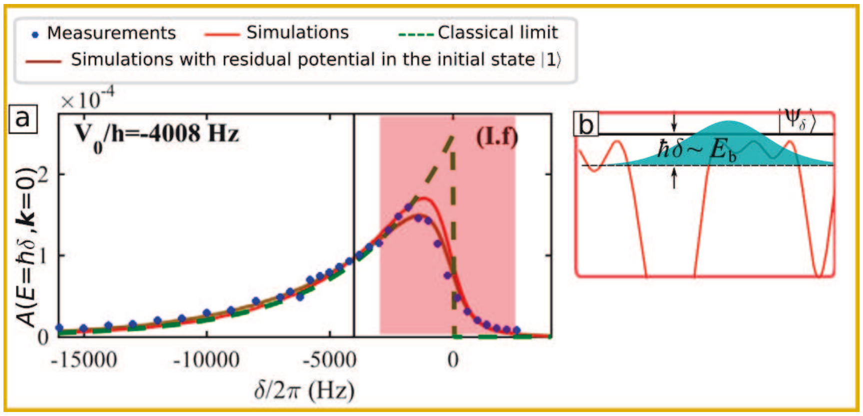

Figure 5.9: (a) Spectral functions measured for $V_R/h = -4008$ Hz with shaded area corresponding to interval $[-2E_b, 2E_b]$; $E_b = \sqrt{|V_R|E_\sigma}$. (b) Depictions of the wave function of the states corresponding to δ in the interval $[-2E_b, 2E_b]$. For δ around zero, the extension of the wave function spans many disorder grain and the spectral function smoothen the discontinuity associated with the classical limit, i.e. the potential distribution.

The present method, which yields the spectral function around zero momentum, could easily be generalized to finite values of $\boldsymbol{k}$ by, for instance, using stimulated Raman transitions effected by two laser beams whose angle allows one to select the desired value of $\boldsymbol{k}$ [144].

Furthermore, the measurement scheme of the spectral function presented here allows controlled transfer of atoms to well-defined energy states in the disorder. This feature represents well the rf transfer described in Fig. 1.3. The energy resolution set by the inverse of the transfer time can be made narrow compared with the typical spectral width. The achieved energy resolution ranging from 10 Hz to 100 Hz (which corresponds to a range between 0.5 nK and 5 nK) is strictly smaller than the typical error bar of the mobility edge estimation in previous experimental attempts [40–42]. While the employed disorder parameters have similar oder of magnitude, our spectroscopic approach would be promising for a direct and more precise measurement of the mobility edge.

5.3 Comparison with measurements of elastic scattering time

In this section, we present the measurements of the elastic scattering time and then we compare the results with the estimated lifetime obtained from the spectral function measurements.

5.3.1 Measurements of the elastic scattering time τ_s for ultracold atoms

As discussed in subsection 2.1.2, the elastic scattering time can be determined from the measurements of the momentum distribution $n(\boldsymbol{k}, t)$. The speckle disorder presented in Chap. 4 allows realization of a quasi-two-dimensional configuration. The speckle grain is elongated along x-axis. When atoms are initialized at momentum $\boldsymbol{k_i} = k_i\boldsymbol{e_y}$, their dynamics is essentially kept within the

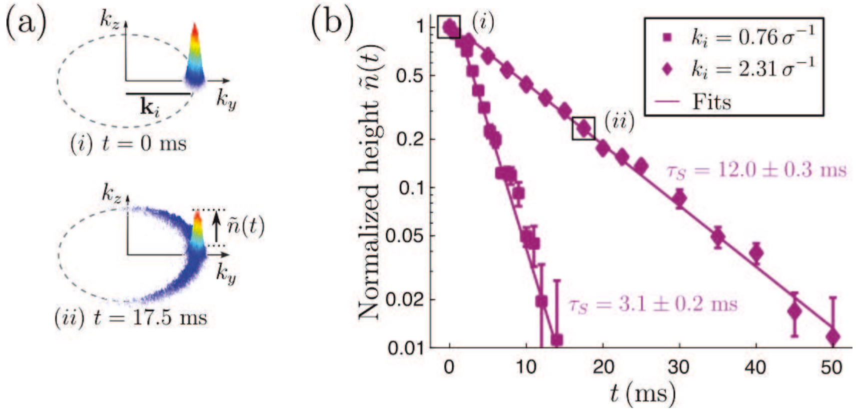

Figure 5.10: **Measurement procedure of the elastic scattering time τ_s.** (a) The momentum distributions $n(\boldsymbol{k}, t)$ are observed for different propagation times t in the disorder, here shown for the parameters $V_R/h = -104$ Hz (attractive case) and $k_i = 2.31\sigma^{-1}$. The normalized height $\tilde{n}(t)$ is determined from $n(\boldsymbol{k}, t)$ by a Gaussian fit of the radially integrated angular profile [66]. (b) When plotted as a function of time t, it shows an exponential decay from which τ_S is extracted, as illustrated for two different initial momentum $k_i = 0.76\sigma^{-1}$ and $k_i = 2.31\sigma^{-1}$, still at $V_R/h = -104$ Hz.

$y - z$ plane.

Since we consider a quasi-two-dimensional configuration, the speckle grain σ is naturally associated with the correlation length along the transverse direction. The correlation function shows an exponential shape from which we define the length σ according to $c_{2\text{D}} = \exp\left(-\left(y^2 + z^2\right)/\sigma^2\right)$. The correlation measurement gives $\sigma = 0.50(1)$ μm (see Fig. 4.6). Furthermore, the initial momentum k_i can be easily tuned by applying magnetic force generated by the "Gradient coils"(see Fig. 3.7) for certain short duration. With typical momentum spread as low as $\Delta k = 0.15$ μm^{-1} ($\Delta k\sigma = 0.08$) thanks to the delta-kick cooling techniques, we have excellent control of parameter $k_i\sigma$, allowing exploration from the isotropic scattering regime ($k_i\sigma \ll 1$) to the forward scattering regime ($k_i\sigma \gg 1$).

Similar to the spectral function measurements, the disorder amplitude V_R is a tunable parameter with $V_R > 0$ for repulsive disorder and $V_R < 0$ for attractive disorder. For elastic scattering time measurements, the detuning of the laser speckle with respect to the $F = 2 \rightarrow F'$ transition is typically 1 THz, much larger than that used for spectral function measurements, resulting in longer atomic lifetime in the disorder.

Fig. 5.10 depicts the measurement procedure of the elastic scattering time τ_s. It consists of analyzing the evolution of the peak in the momentum distributions associated with the initial momentum. The speckle potential is turned on at time $t = 0$. As t increases, the initial peak depletes accompanied with the ring formation in the momentum distribution. Fig. 5.10(a) depicts the momentum distributions observed for $t = 0$ and $t = 17.5$ ms, both correspond to parameters $V_R/h = -104$ Hz and $k_i = 2.31\sigma^{-1}$. For each time t, we measure the normalized height $\tilde{n}(t)$ of the peak; $\tilde{n}(t=0)=1$. Fig. 5.10(b) shows the plots of $\tilde{n}(t)$ in a semi-logarithmic scale, showing linear decreases. From the fitting according to Eq. 2.2, the elastic scattering time τ_s is deduced. The time τ_s corresponds to the time constant of the exponential decay.

5.3.2 Measurement results of the elastic scattering time

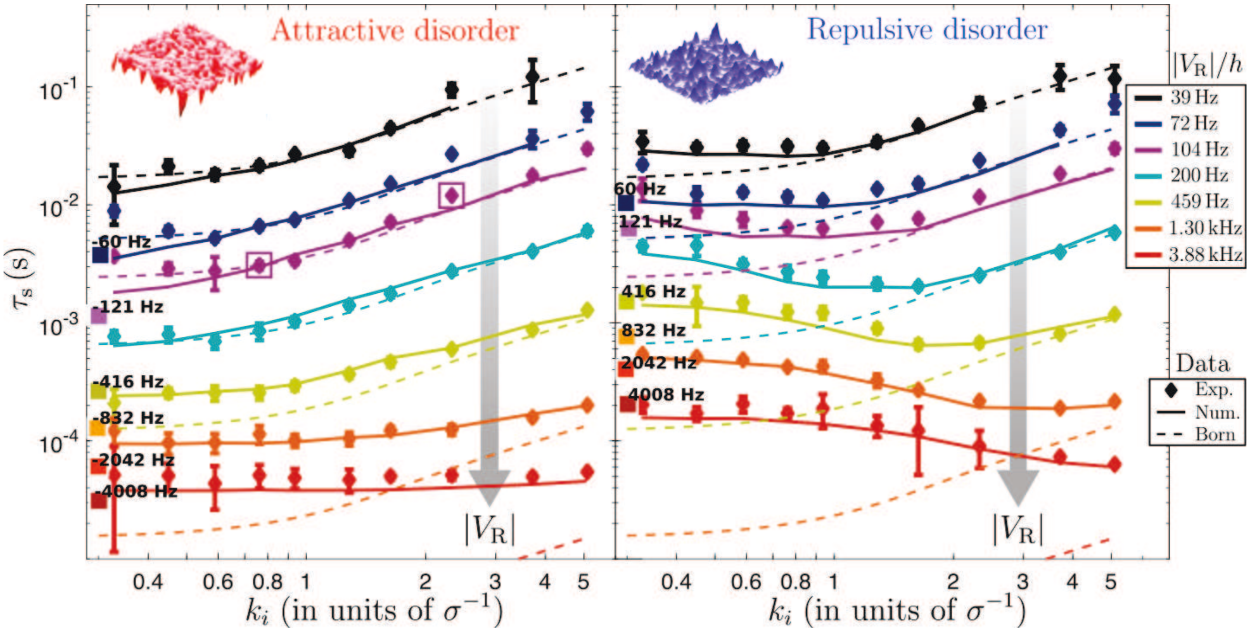

Figure 5.11: Experimental (diamonds) and numerical (solid lines) values of τ_s as a function of the initial momentum k_i for different values of the disorder amplitude $|V_R|$ for attractive disorder (left panel) and repulsive disorder (right panel). The initial momenta are shown in units of the characteristic frequency σ^{-1} of the disorder. Born predictions τ_s^{Born} are indicated by dashed lines. Note that the curves are just shifted down for the various disorder amplitudes due to the scaling $\tau_s^{\text{Born}} \propto 1/V_R^2$. The filled squares are the estimated lifetimes obtained from the spectral function measurements, indicated by their respective amplitude V_R; the colors are chosen based on the closest V_R of the τ_s-measurement.

Fig. 5.11 shows the measured values of the elastic scattering time τ_s for both the attractive and repulsive laser speckle disorder cases. The large set of disorder amplitude and momenta allows us to observe variations of τ_s from 40 μs to 100 ms. These observations are compared to 2D numerical calculations (solid lines) [66], showing remarkable agreement over the very broad data range, confirming the quasi-2D character of our configuration. Deviations are nevertheless observed in a small zone (very low momenta and disorder amplitudes, upper left part of the graphs) and may be attributed to technical difficulties to precisely measure τ_s in this regime due to the finite momentum resolution Δk [50].

The Born prediction (Eq. 2.3) is also shown in Fig. 5.11 (dashed lines). Note that τ_s^{Born} scales with the rms value $|V_R|$ as $1/V_R^2$, but does not depend on the specific form of the disorder amplitude distribution $P(V)$. As a consequence, the prediction is strictly identical for both attractive and repulsive speckles, since they possess the same frequency distribution $\tilde{C}(\boldsymbol{k}_{\text{dis}})$. In general, τ_s^{Born} shows a very good agreement with the data at low scattering strength, i.e., weak $|V_R|$ and large k_i (upper right part on Fig. 2.3), as expected for this first order perturbative approach. However, significant deviations appear already for the lowest disorder amplitude ($|V_R|/h = 39$ Hz, black dots) when considering the low initial momentum range, $k_i \lesssim \sigma^{-1}$. As the disorder strength $|V_R|$ increases, the deviations become more pronounced and extend to larger momenta. In strong scattering conditions, the two regimes previously mentioned, isotropic and forward scattering, are then not relevant anymore. Moreover, large differences are observed between attractive and repulsive disorders, another signature of the complete failure of the Born approximation.

Lastly, we can try to juxtapose the measured τ_s with the width of measured spectral functions. This is possible for two reasons. First[11], $n(\boldsymbol{k}=\boldsymbol{k_i},t) \approx \left|\overline{U}_{\boldsymbol{k_i}}(t)\right|^2$, where

$$\overline{U}_{\boldsymbol{k}}(t) = \left\langle \boldsymbol{k} \left| \overline{\exp\left(-itH/\hbar\right)} \right| \boldsymbol{k} \right\rangle = \int \mathrm{d}E e^{-iEt} A(E,\boldsymbol{k}). \tag{5.31}$$

As explained earlier in section 5.1, we can relate τ_s to the inverse of the width of the spectral function. This holds for spectral function with Lorentzian-shape. Nevertheless, τ_s should not differ much from the inverse of the spectral width. Secondly, the quasi-2D character of the experiment does no longer hold for small $k_i\sigma$. As a result, the measured τ_s for the smallest $k_i\sigma$ (here, $k_i\sigma = 0.33$) would approach the τ_s associated with three-dimensional configuration at $\boldsymbol{k} = 0$[12]. The estimated lifetimes from the measured spectral functions are shown as colored squares in Fig. 5.11, shown with their respective disorder amplitudes. We can see that for all amplitude V_R of the measured spectral functions, the estimated lifetimes are not very far from the measured τ_s at parameters $k_i\sigma = 0.33$ and similar amplitudes V_R. As an example, estimated lifetimes from the spectral function measurements at $|V_R|/h = 416$ Hz are not far from the measured τ_s at $|V_R|/h = \pm 459$ Hz and $k_i\sigma = 0.33$, for both attractive and repulsive case. Hence, the estimated lifetimes from the spectral function measurements are compatible with the measured elastic scattering time.

5.4 Conclusion

In this chapter, we have presented our work on the measurements of spectral functions of ultracold atoms in disordered potentials. In section 5.1, we have reviewed several notions including the regime of disorders (classical and quantum regime) and the relation between the spectral function and the elastic scattering time τ_S. In section 5.2, we have presented the measurement results which show excellent agreement with numerical calculations. We have also remarked the effect of the potential distribution on the spectral function profile. In section 5.3, we have compared our results

---

[11] In principle, $n(\boldsymbol{k}=\boldsymbol{k_i},t) = \overline{U^\dagger_{\boldsymbol{k_i}}(t)U_{\boldsymbol{k_i}}(t)}$, but for $t \sim \tau_s$, we can approximate $\overline{U^\dagger_{\boldsymbol{k_i}}(t)U_{\boldsymbol{k_i}}(t)} = \left|\overline{U}_{\boldsymbol{k_i}}(t)\right|^2$.

[12] For $\sigma_\parallel$ be the speckle grain size along the longitudinal axis, the system approaches 3D when $k_i\sigma_\parallel \lesssim 1$.

of the measurements of the spectral function with our results of the measurements of the elastic scattering time.

Besides the measurement of the spectral functions, a key feature of the method presented in section 5.2 is the controlled transfer of atoms to well-defined energy states in the disorder, the targeted energy being chosen by the resonance condition. It opens the possibility to probe the 3D Anderson transition, via a subsequent wave packet expansion, with an unprecedented energy resolution compared to earlier experimental attempts [40–42]. Nevertheless, we must circumvent the limitation of the short lifetime of the atoms in the disorder due to the application of the near resonant laser speckle. The solution is proposed in the next chapter.

Chapter 6

Bichromatic state-dependent speckle disorder

Contents

State-dependent speckle disorder scheme presented in Chap. 4 allows control of matter wave energy in the disorder and direct measurement of the spectral function. However, there is still a huge obstacle for further studies related to the critical regime of the Anderson transition. It is the short lifetime of the atoms in the disordered optical potential caused by the mechanism of spontaneous emission.

In this chapter, we propose a solution to circumvent this limitation by realizing state-dependent disorder with two laser speckles. In the first section, we present this scheme and evaluate the improved lifetime of the atoms in the disorder. The associated two speckle patterns have slight spatial mismatch due to small difference in wavelength. The resulting limitation is addressed in the second section. In the third section, we present the preliminary experimental implementation.

6.1 Bichromatic optical potential

In this section, we study the optical potential and the dissipation rate associated with two lasers. This section consists of three parts. First, we discuss the rationale for the two laser sources. Secondly, we will discuss the numerical calculations associated with the optical potential and the dissipation based on the calculation of atomic polarizability presented in the subsection 4.3.1. We show that the atomic lifetime in the disorder can be improved by three order of magnitude compared to the speckle laser presented in Chap. 4. Lastly, we present an additional technique allowing further improvement of the lifetime by about one order of magnitude.

6.1.1 Why two wavelengths are required?

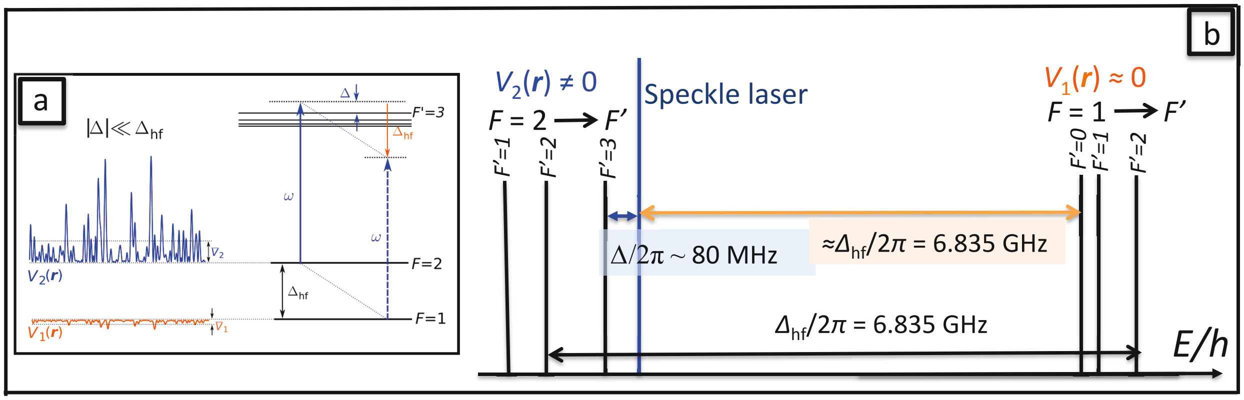

Figure 6.1: (a) Schematic diagram of state-dependent disorder as shown in Fig. 4.7. (b) Equivalent schematic diagram by showing the frequency of the laser speckle with respect to the D_2 transitions; the chosen example corresponds to repulsive disordered potential.

In order to show that one laser is not sufficient, we need to depict differently the schematic diagram of the state-dependent disorder which is shown earlier in Fig. 4.7. The equivalent schematic diagram is shown in Fig. 6.1(b). It represents the position of the laser frequency with respect to most relevant atomic transitions, i.e. the D_2 transitions. The $F = 1 \rightarrow F'$ transitions are separated from the $F = 2 \rightarrow F'$ transitions by around 6.8 GHz. The presented case is the repulsive one. It can be seen that the laser frequency is much closer to the $F = 2 \rightarrow F'$ transitions associated with state $|2\rangle$ than to the $F = 1 \rightarrow F'$ transitions associated with state $|1\rangle$. We recall Δ, the detuning of the laser with respect to the $F = 2 \rightarrow F' = 3$ transition; $\Delta = \Delta_b = 81$ MHz for the repulsive case. The potential V_R approximately follows $V_R \sim I/\Delta$. With Γ_{D2} the natural line width of the D_2 transition, the dissipation rate of the state $|2\rangle$, Γ_2, approximately follows $\Gamma_2 \sim \Gamma_{D2}\frac{I}{\Delta^2}$, such that

$$\Gamma_2 \sim \frac{1}{\hbar} |V_R| \frac{\Gamma_{D2}}{|\Delta|}. \tag{6.1}$$

The condition of low dissipation rate demands optical detuning in the order of several GHz. Let us suppose $|V_R|/h = 500$ Hz. Dissipation rate $\Gamma_2 = 1\mathrm{s}^{-1}$ corresponds to detuning $|\Delta|$ of about 19 GHz, whose order of magnitude is comparable to that of the hyperfine splitting Δ_{hf}. We have discussed in Chap. 4 that the state-dependent disorder realization with one laser requires the detuning Δ to be much smaller than the hyperfine splitting Δ_{hf}, i.e. $\Delta/\Delta_{\mathrm{hf}} \ll 1$. Hence, we find two contradictory conditions for Δ. This shows that we need more than one laser for the realization of state-dependent disorder.

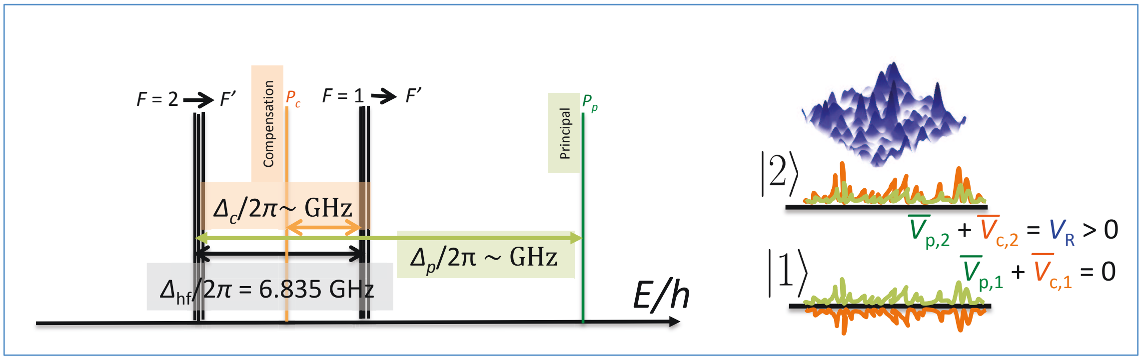

Figure 6.2: Schema of bichromatic state-dependent disordered potential for repulsive case. The principal laser (called $P-$laser, shown in green) is blue-detuned with respect to the $F = 2 \rightarrow F'$ transitions; $\Delta_p > 0$. The compensation laser (called $C-$laser, shown in orange) is red detuned with respect to the $F = 1 \rightarrow F'$ transitions, $\Delta_c < 0$, such that the resulting optical potential of the state $|1\rangle$ vanishes. The figure on the right shows the contribution of each laser to optical potential of the states $|1\rangle$ and $|2\rangle$. The powers of the lasers are chosen such that the potential of the state $|1\rangle$ vanishes while the potential of the state $|2\rangle$ is strictly positive.

As a solution, we consider realization of state-dependent disorder with two laser speckles. One intuitive solution is to far detune one laser frequency with respect to the $|2\rangle$'s transitions and to use a second laser to compensate the optical potential induced on the state $|1\rangle$. For these reasons, the first laser is called the principal laser (or $P-$laser) and the second laser is called the compensation laser (or $C-$laser). The solution for the repulsive case is depicted in Fig. 6.2. For the $P-$laser, let us define its detuning Δ_p with respect to the $F = 2 \rightarrow F'$ transition. To create a repulsive potential, we require $\Delta_p > 0$. For $\Delta_p > \Delta_{\mathrm{hf}}$, the $P-$laser creates repulsive potential for both states $|2\rangle$ and $|1\rangle$. For state $|1\rangle$, the $C-$laser must compensate the potential induced by the $P-$laser. Let us define its detuning with respect to the $F = 1 \rightarrow F'$ transition[1]. It is obvious that we need $\Delta_c < 0$ and $|\Delta_c| < \Delta_{\mathrm{hf}}$; otherwise, we would have a net attractive potential for the state $|2\rangle$. After take into account some redundancy[2], it is sufficient to consider the following range of detunings Δ_p and Δ_c:

$$\Delta_p > \Delta_{\mathrm{hf}} \text{ and } -\Delta_{\mathrm{hf}} < \Delta_c < -\Delta'_{02} \,(\text{repulsive disorder})\,, \tag{6.2}$$

---

[1] In practice, we consider $F' = 3$ for both Δ_p and Δ_c. Although the $F = 1 \rightarrow F' = 3$ transition does not exist, it does not prevent us to define the detuning Δ_c.

[2] We can exchange the $P-$laser and the $C-$laser.

where $\Delta'_{02} = 2\pi \times 229$ MHz is the hyperfine splitting between levels $F' = 0$ and $F' = 2$ of the D_2 excited states; $\Delta'_{02} \ll \Delta_{\mathrm{hf}}$ and can sometimes be considered as “zero”.

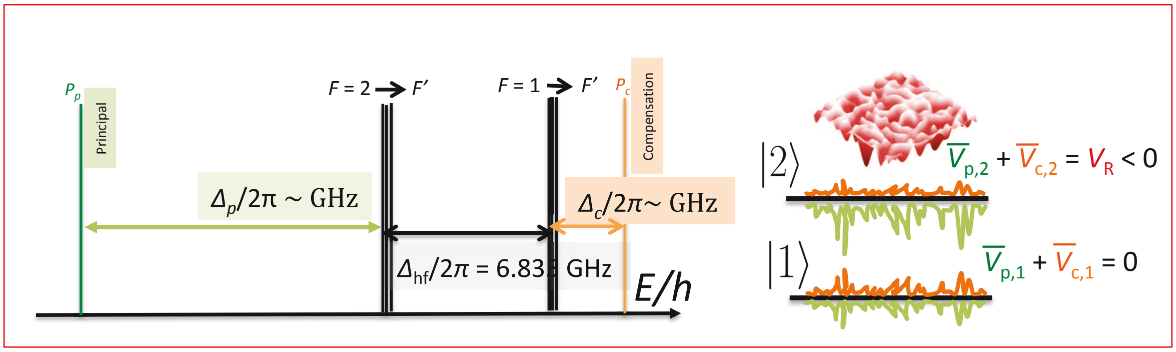

Figure 6.3: Schema of bichromatic state-dependent disordered potential for attractive case. The principal laser (called $P-$laser, shown in green) is red-detuned with respect to the $F = 2 \to F'$ transitions; $\Delta_p < 0$. The compensation laser (called $C-$laser, shown in orange) is blue detuned with respect to $F = 1 \to F'$ transitions, $\Delta_c > 0$, such that the resulting optical potential of the state $|1\rangle$ vanishes. The figure on the right shows the contribution of each laser to optical potential of the states $|1\rangle$ and $|2\rangle$. The powers of the lasers are chosen such that the potential of the state $|1\rangle$ vanishes while the potential of the state $|2\rangle$ is strictly negative.

Let us also treat the attractive case, depicted in Fig. 6.3. The $P-$laser is red-detuned with respect to the $F = 2 \to F'$ transitions, creating an attractive potential for both states $|2\rangle$ and $|1\rangle$. For state $|1\rangle$, the $C-$laser must have $\Delta_c > 0$ in order to compensate the attractive potential induced by the $P-$laser. Thus, the $C-$laser must be blue-detuned with respect to $F = 1 \to F'$ transitions; $\Delta_c > 0$. For the state $|2\rangle$, the potential created by the $C-$laser on state $|2\rangle$ is strictly weaker than the one created by the $P-$laser, resulting in net attractive potential. Hence, we consider the following range of detunings Δ_p and Δ_c:

$$\Delta_p < -\Delta'_{13} \text{ and } \Delta_c > 0\,(\text{attractive disorder})\,, \tag{6.3}$$

where $\Delta'_{13} = 2\pi \times 423.6$ MHz is the hyperfine splitting between levels $F' = 1$ and $F' = 3$ of the D_2 excited states; $\Delta'_{13} \ll \Delta_{\mathrm{hf}}$ and can sometimes be considered as “zero”. However, we shall see in the next subsection that for $\Delta_c \gtrsim \Delta_{\mathrm{hf}}$, the improvement of the atomic lifetime is marginal, such that the effective range for Δ_c becomes $0 < \Delta_c \lesssim \Delta_{\mathrm{hf}}$.

6.1.2 Estimation of atomic lifetime in the disorder

We aim to estimate the lifetime of the atom in the disorder, especially in the state $|2\rangle$, for a given disorder amplitude V_R. The atomic lifetimes in the states $|1\rangle$ and $|2\rangle$, noted τ_1 and τ_2 respectively, follow

$$\tau_1 = \Gamma_1^{-1}, \text{ and } \tau_2 = \Gamma_2^{-1}, \tag{6.4}$$

where Γ_1 and Γ_2 are the dissipation rate of the states $|1\rangle$ and $|2\rangle$ respectively. The disorder amplitude V_R is given by the average potential of the state $|2\rangle$. With vanishing potential for the state $|1\rangle$, we obtain the following conditions:

$$\begin{aligned} \overline{V}_1 &= \overline{V}_{p,1} + \overline{V}_{c,1} = 0, \\ \overline{V}_2 &= \overline{V}_{p,2} + \overline{V}_{c,2} = V_R, \end{aligned} \tag{6.5}$$

where $\overline{V}_{p,1}$ and $\overline{V}_{p,2}$ are the average potentials created by the $P-$laser on the states $|1\rangle$ and $|2\rangle$ respectively, and $\overline{V}_{c,1}$ and $\overline{V}_{c,2}$ are the average potentials created by the $C-$laser on the states $|1\rangle$ and $|2\rangle$ respectively (see Figs. 6.2 and 6.3).

Let us consider that $P-$laser and $C-$laser have same beam waist, w_d. By applying Eqs. 3.14 and 4.36, the potentials $\overline{V}_{p,1}$ and $\overline{V}_{p,2}$ are shown proportional to the power of the $P-$laser, P_p, as follows:

$$\begin{aligned} \overline{V}_{p,1} &= -\frac{\mathrm{Re}\left[\alpha_{p,1}\right]}{\varepsilon_0 c}\frac{P_p}{\pi w_d^2}, \\ \overline{V}_{p,2} &= -\frac{\mathrm{Re}\left[\alpha_{p,2}\right]}{\varepsilon_0 c}\frac{P_p}{\pi w_d^2}, \end{aligned} \tag{6.6}$$

where $\alpha_{p,1}$ and $\alpha_{p,2}$ are the atomic polarizability induced by the principal laser of the states $|1\rangle$ and $|2\rangle$ respectively. Similarly, the potentials $\overline{V}_{c,1}$ and $\overline{V}_{c,2}$ are proportional to P_c, the power of the $C-$laser, according to

$$\begin{aligned} \overline{V}_{c,1} &= -\frac{\mathrm{Re}\left[\alpha_{c,1}\right]}{\varepsilon_0 c}\frac{P_c}{\pi w_d^2}, \\ \overline{V}_{c,2} &= -\frac{\mathrm{Re}\left[\alpha_{c,2}\right]}{\varepsilon_0 c}\frac{P_c}{\pi w_d^2}, \end{aligned} \tag{6.7}$$

where $\alpha_{c,1}$ and $\alpha_{c,2}$, are the atomic polarizability induced by the compensation laser of the states $|1\rangle$ and $|2\rangle$ respectively. From Eqs. 6.5, 6.6, and 6.7, we deduce the followings

$$\begin{aligned} P_p &= \frac{\varepsilon_0 c \pi w_d^2 V_R \,\mathrm{Re}\left[\alpha_{c,1}\right]}{\mathrm{Re}\left[\alpha_{c,2}\right]\mathrm{Re}\left[\alpha_{p,1}\right] - \mathrm{Re}\left[\alpha_{c,1}\right]\mathrm{Re}\left[\alpha_{p,2}\right]}, \\ P_c &= -\frac{\varepsilon_0 c \pi w_d^2 V_R \,\mathrm{Re}\left[\alpha_{p,1}\right]}{\mathrm{Re}\left[\alpha_{c,2}\right]\mathrm{Re}\left[\alpha_{p,1}\right] - \mathrm{Re}\left[\alpha_{c,1}\right]\mathrm{Re}\left[\alpha_{p,2}\right]}. \end{aligned} \tag{6.8}$$

For numerical calculation, we use the waist $w_d = 1.4$ mm in accordance with the experimental value mentioned in subsection 4.2.2.

Numerical evaluations of the laser powers, P_p and P_c, and also the atomic lifetimes, τ_1 and τ_2, require the calculations of $\alpha_{p,1}$, $\alpha_{p,2}$, $\alpha_{c,1}$, and $\alpha_{c,2}$. Such calculations are already presented in subsection 4.3.1; we keep the same notation. Let us also consider that $P-$laser and $C-$laser have same polarization $\boldsymbol{\epsilon}$. Let ω_2 be the frequency associated with the $F = 2 \to F' = 3$ transition. The frequency of the $P-$laser becomes $\omega_2+\Delta_p$. $\alpha_{p,1}$ and $\alpha_{p,2}$ are given by

$$\begin{aligned}\alpha_{p,1} &= \alpha_{|1\rangle}\left(\omega_2+\Delta_p,\boldsymbol{\epsilon}\right),\\ \alpha_{p,2} &= \alpha_{|2\rangle}\left(\omega_2+\Delta_p,\boldsymbol{\epsilon}\right).\end{aligned} \tag{6.9}$$

Similarly for the $C-$laser, let ω_1 be the frequency associated with the imaginary $F=1\rightarrow F'=3$ transition. The frequency of the $C-$laser becomes $\omega_1+\Delta_c$. Hence, $\alpha_{c,1}$ and $\alpha_{c,2}$ are given by

$$\begin{aligned}\alpha_{c,1} &= \alpha_{|1\rangle}\left(\omega_1+\Delta_c,\boldsymbol{\epsilon}\right),\\ \alpha_{c,2} &= \alpha_{|2\rangle}\left(\omega_1+\Delta_c,\boldsymbol{\epsilon}\right).\end{aligned} \tag{6.10}$$

In the following subsection, the numerical results are presented for $\pi-$polarization.

The dissipations Γ_1 and Γ_2 result essentially from the mechanism of spontaneous emission. In case of single laser, the dissipation rate (in s^{-1}) is related to the atomic polarizability α, the power, P, and the beam waist, w_d, according to

$$\Gamma=\frac{2\mathrm{Im}\left[\alpha\right]}{\hbar\varepsilon_0 c}\frac{P}{\pi w_d^2}. \tag{6.11}$$

With similar relation, we can deduce Γ_1 and Γ_2. The total dissipation rate of the state $|1\rangle$, Γ_1, is a sum of contributions from the $P-$laser and the $C-$laser, yielding

$$\Gamma_1=\frac{2\mathrm{Im}\left[\alpha_{p,1}\right]}{\hbar\varepsilon_0 c}\frac{P_p}{\pi w_d^2}+\frac{2\mathrm{Im}\left[\alpha_{c,1}\right]}{\hbar\varepsilon_0 c}\frac{P_c}{\pi w_d^2}. \tag{6.12}$$

Similarly, the total dissipation rate of the state $|2\rangle$ yields

$$\Gamma_2=\frac{2\mathrm{Im}\left[\alpha_{p,2}\right]}{\hbar\varepsilon_0 c}\frac{P_p}{\pi w_d^2}+\frac{2\mathrm{Im}\left[\alpha_{c,2}\right]}{\hbar\varepsilon_0 c}\frac{P_c}{\pi w_d^2}. \tag{6.13}$$

Since P_p and P_c are proportional to V_R, the dissipation rates Γ_1 and Γ_2 are also proportional to V_R. However, we can show that Γ_1 and Γ_2 are independent of the waist w_d.

6.1.3 Results

We present numerical results for $V_R/h=\pm 4$ kHz, which also correspond to the strongest disorder amplitudes of the measured spectral functions (see Chap. 5). Besides, we recall $w_d=1.38$ mm. Results for arbitrary V_R and w_d can be easily obtained since $P_p, P_c\propto w_d^2 V_R$ and $\tau_1,\tau_2\propto V_R^{-1}$.

We recall that the main objective of the following numerical work is to improve the atomic lifetime τ_2. It was only 0.5 ms for $V_R/h=\pm 4$ kHz when considering the single laser speckle. While the atomic lifetime in the state $|2\rangle$ must be as long as possible, the lifetime in the state $|1\rangle$ must be long enough to allow the radio-frequency transfer. For $V_R/h=\pm 4$ kHz, we require $\tau_1>10$ ms; see subsection 3.3.1.

In this subsection, we present the numerical results for both repulsive and attractive cases. The repulsive case has particular importance because all experiments related to Anderson localization so far are carried out with repulsive disordered potential. For convenience purposes, several key results are presented in Tab. 6.1.

Repulsive case

Fig. 6.4 shows the main numerical results for the repulsive case. The schema is recalled in the first row, which shows the detunings Δ_p and Δ_c associated with the $P-$laser and the $C-$laser respectively. Atomic lifetimes τ_1 of the state $|1\rangle$ and τ_2 of the state $|2\rangle$ are shown in the second row (τ_1 on the left and τ_2 on the right). The powers P_p of the $P-$laser and P_c of the $C-$laser are shown in the third row. The calculations of these quantities are presented for range of detunings $\Delta_p/2\pi \in [6.9 \text{ GHz}, 100 \text{ GHz}]$ and $|\Delta_c|/2\pi \in [0.5 \text{ GHz}, 6.8 \text{ GHz}]$; $\Delta_c < 0$. For facilitating further discussion, we also represent the condition $\tau_1 = 10$ ms with dark red line in all colormaps.

The atomic lifetimes τ_1 and τ_2 are shown in logarithmic color scale. Both τ_1 and τ_2 vary more remarkably with Δ_c than with Δ_p. The lifetime τ_1 becomes shorter as Δ_c approaches zero, i.e. $C-$laser approaches resonance with respect to the state $|1\rangle$. Condition $\tau_1 > 10$ ms requires detuning $|\Delta_c|$ larger than $2\pi \times 1.6$ GHz (see the $\tau_1 = 10$ ms line at $\Delta_p/2\pi = 100$ GHz). Unfortunately, the lifetime τ_2 has negative relationship with the lifetime τ_1. τ_2 increases as $|\Delta_c| \to 0$ and it decreases as $|\Delta_c|$ approaches Δ_{hf}. When $|\Delta_c| \to \Delta_{\text{hf}}$, the $C-$laser is almost resonance to the $|2\rangle$'s transitions. For $\Delta_p/2\pi = 100$ GHz, $\tau_1 = 10$ ms is found at $|\Delta_c|/2\pi = 1.62$ GHz. At these detunings, we obtain $\tau_2 = 149$ ms (see Tab. 6.1).

The powers P_p and P_c are shown in linear color scale, in unit of mW. Compared with the colormap of the lifetimes, we can remark stronger variations with Δ_p. The power P_p of the $P-$laser increases with Δ_p. From the bar legend, the power P_p is considerably larger than power P_c. This is because we consider a much larger range of the detuning Δ_p compared with Δ_c. For $\Delta_p/2\pi = 100$ GHz and $\Delta_c/2\pi = -1.62$ GHz, we obtain $P_p = 5.16$ mW and $P_c = 69.6$ μW (see Tab. 6.1).

It would be interesting to understand the contribution of each laser to the resultant potentials. For state $|2\rangle$, contributions of the $P-$laser and the $C-$laser add up. For aforementioned detunings, $\Delta_p/2\pi = 100$ GHz and $\Delta_c/2\pi = -1.62$ GHz, we obtain $\overline{V}_{p,2}/h = 3.19$ kHz and $\overline{V}_{c,2}/h = 0.81$ kHz respectively. Besides, we obtain $\overline{V}_{p,1} = 3.41$ kHz; $\overline{V}_{c,1} = -\overline{V}_{p,1}$. It can be shown that the ratio $\overline{V}_{p,2}/V_R$ is independent of V_R and w_d, so does the ratio $\overline{V}_{p,1}/V_R$. Within the range of detunings considered for the repulsive case, the ratio $\overline{V}_{p,2}/V_R$ should lie between zero and one. Fig. 6.5 depicts the numerical results of the ratios $\overline{V}_{p,1}/V_R$ (on the left) and $\overline{V}_{p,2}/V_R$ (on the right) for range of detunings similar to that presented in Fig. 6.4. Both $\overline{V}_{p,1}/V_R$ and $\overline{V}_{p,2}/V_R$ are shown in linear color scale. For $\overline{V}_{p,1}/V_R$, it approaches zero for $|\Delta_c| \to \Delta_{\text{hf}}$ and it is about one around the $\tau_1 = 10$ ms

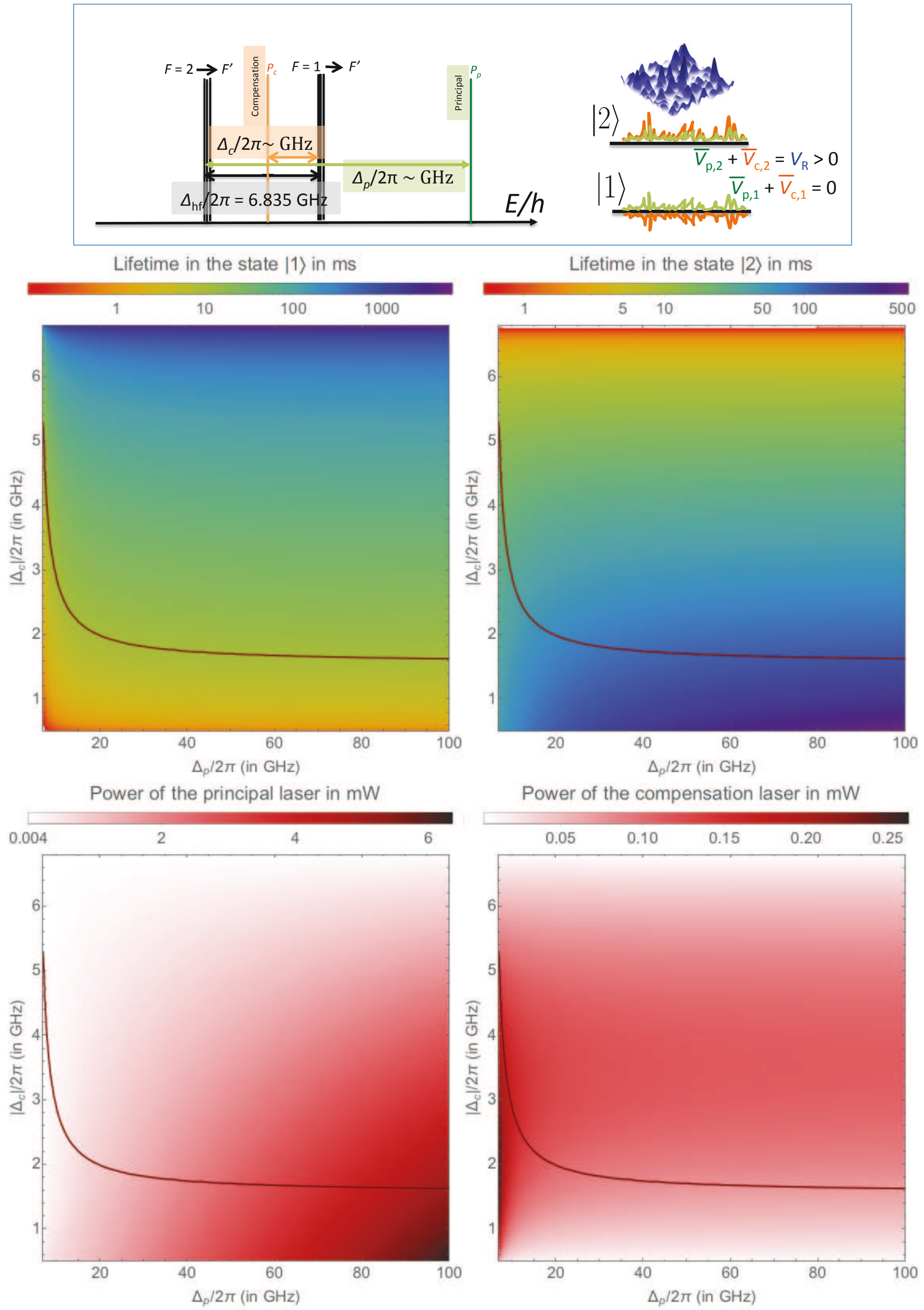

Figure 6.4: **Numerical results for repulsive case**; $V_R/h = 4$ kHz. First row: schema taken from Fig. 6.2. Second row: Atomic lifetimes in the states $|1\rangle$ (Left) and $|2\rangle$ (Right), shown in logarithmic color scale. The empty area on the left corresponds to $\tau_1 \leq 0.1$ ms; on the right, $\tau_2 \leq 0.5$ ms. Third row: The required power for the principal laser (P_p, left) and the compensation laser (P_c, right). The detunings Δ_p and $|\Delta_c|$ ($\Delta_c < 0$) are shown in horizontal and vertical axes respectively. Dark red line corresponds to situation where $\tau_1 = 10$ ms.

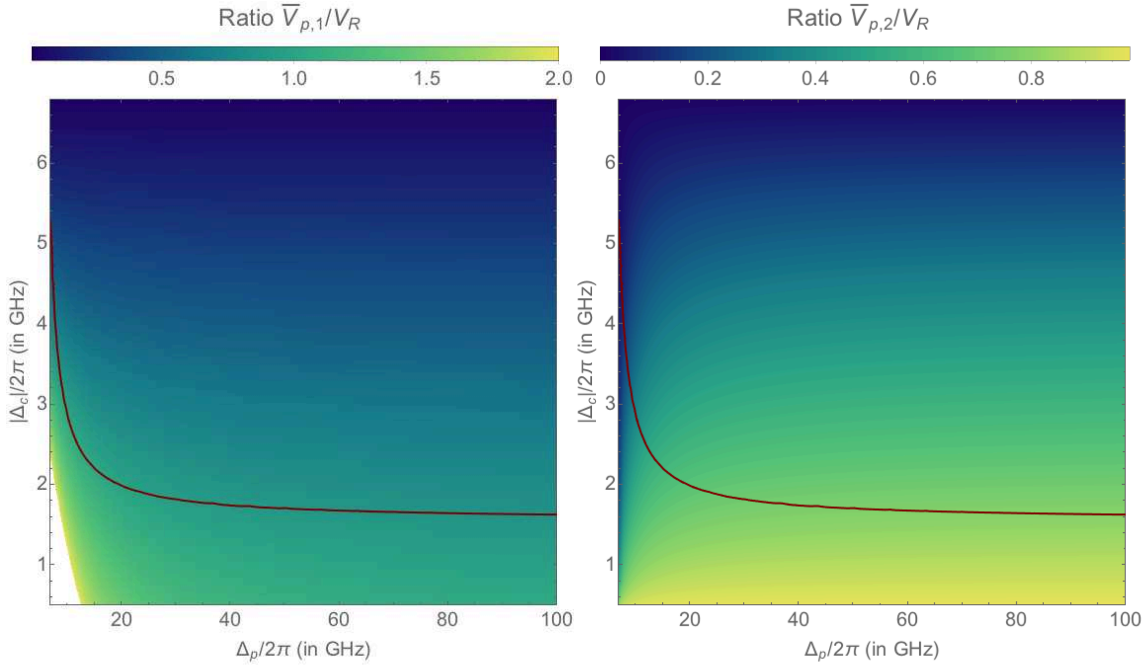

Figure 6.5: **Optical potentials induced by the $P-$laser for repulsive case**. (Left) The ratio $\overline{V}_{p,1}/V_R$ between the potential created on the state $|1\rangle$ and the disorder amplitude V_R. The empty area corresponds to $\overline{V}_{p,1}/V_R > 2$. (Right) The ratio $\overline{V}_{p,2}/V_R$ between the potential created on the state $|2\rangle$ and the disorder amplitude V_R. Both $\overline{V}_{p,1}/V_R$ and $\overline{V}_{p,2}/V_R$ are presented for detunings Δ_p and Δ_c similar to those shown in Fig. 6.4. Dark red line corresponds to $\tau_1 = 10$ ms.

line. For $\overline{V}_{p,2}/V_R$, it is about 0.8 around the $\tau_1 = 10$ ms line at relatively high Δ_p ($\Delta_p \gg \Delta_{\rm hf}$). We can see that $\overline{V}_{p,2}/V_R$ approaches one as Δ_c approaches resonances with the $|1\rangle$'s transitions and $\overline{V}_{p,2}/V_R$ approaches zero as Δ_c approaches resonances with the $|2\rangle$'s transitions.

For the atomic lifetimes in both states $|1\rangle$ and $|2\rangle$, we do not observe much improvement for $\Delta_p \gg \Delta_{\rm hf}$. At the same time, we expect the dissipation rates induced by the principal laser should diminish at high Δ_p. Thus, it would be interesting to evaluate the contribution of each laser to the total dissipation. For this, we are interested in the calculation of the ratio $\Gamma_{p,2}/\Gamma_2$, where $\Gamma_{p,2} = \frac{2{\rm Im}[\alpha_{p,2}]}{\hbar\varepsilon_0 c}\frac{P_p}{\pi w_0^2}$ is the dissipation rate due to the principal laser on the state $|2\rangle$. The ratio $\Gamma_{p,2}/\Gamma_2$ is shown in Fig. 6.6. It can be easily shown that the ratio $\Gamma_{p,2}/\Gamma_2$ is independent of the parameters V_R and w_d. As shown in the figure, the contribution of the principal laser decreases as Δ_p increases. The ratio $\Gamma_{p,2}/\Gamma_2$ typically below 0.17 for range of detunings where $\tau_1 > 10$ ms such as $|\Delta_c| > 1.7$ GHz at $\Delta_p \gg \Delta_{\rm hf}$. We can see that the dissipation Γ_2 is mainly contributed by the $C-$laser.

For convenience purposes, key numerical results related to the repulsive case are presented in the third column in Tab. 6.1.

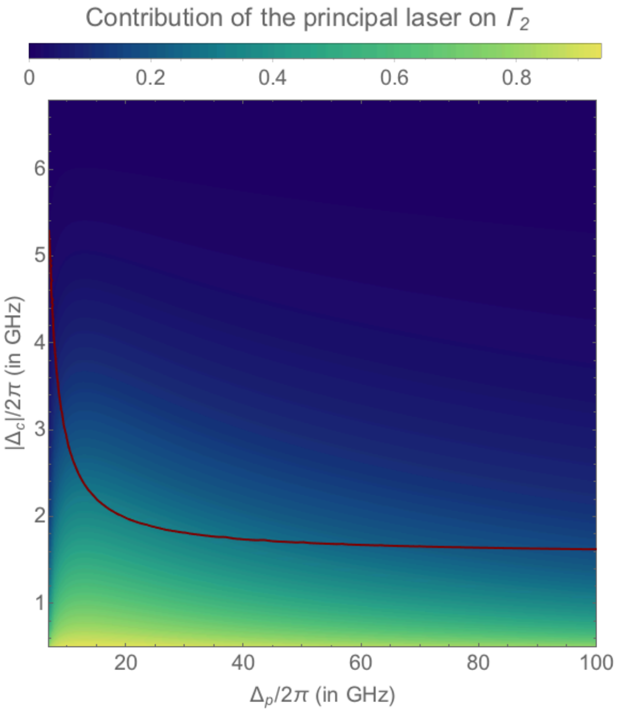

Figure 6.6: **Ratio $\Gamma_{p,2}/\Gamma_2$ for repulsive case**. The ratio between the dissipation rate of the state $|2\rangle$ due to the principal laser, $\Gamma_{p,2}$, and the total dissipation rate Γ_2. Ratio $\Gamma_{p,2}/\Gamma_2$ is presented for detunings Δ_p and Δ_c similar to those shown in Fig. 6.4. Dark red line corresponds to $\tau_1 = 10$ ms.

Attractive case

Fig. 6.7 shows the main numerical results for the attractive case. The schema is recalled in the first row, which shows the detunings Δ_p and Δ_c associated with the $P-$laser and the $C-$laser respectively. Atomic lifetimes τ_1 of the state $|1\rangle$ and τ_2 of the state $|2\rangle$ are shown in the second row (τ_1 on the left and τ_2 on the right). The powers P_p of the $P-$laser and P_c of the $C-$laser are shown in the third row. The calculations of these quantities are presented for range of detunings $|\Delta_p|/2\pi \in [0.5 \text{ GHz}, 100 \text{ GHz}]$ and $\Delta_c/2\pi \in [0.5 \text{ GHz}, 10 \text{ GHz}]$; $\Delta_p < 0$. For facilitating further discussion, we also represent the condition $\tau_1 = 10$ ms with dark red line in all colormaps.

The atomic lifetimes τ_1 and τ_2 are shown in logarithmic color scale. Similar to the results of the repulsive case, we remark negative relationship between τ_1 and τ_2. As Δ_p approaches zero, τ_1 increases and τ_2 decreases; $P-$laser approaches the $|2\rangle$'s transitions. The opposite situations happen when Δ_c approaches zero, τ_1 decreases and τ_2 increases; $C-$laser approaches the $|1\rangle$'s transitions. One non-trivial remark, τ_2 decreases as Δ_c increases. Hence, strategy of increasing detuning to lower the dissipation rate does not always work. At high $|\Delta_p|$ ($|\Delta_p| \gg \Delta_{\text{hf}}$), condition $\tau_1 > 10$ ms requires $\Delta_c/2\pi > 1.354$ GHz. (see the $\tau_1 = 10$ ms line at $|\Delta_p|/2\pi = 100$ GHz). For $|\Delta_p|/2\pi = 100$ GHz and $\Delta_c/2\pi = 1.354$ GHz, we find $\tau_1 = 10$ ms and $\tau_2 = 165$ ms (see Tab. 6.1).

The powers P_p and P_c are shown in linear color scale, in unit of mW. Compared with the colormap

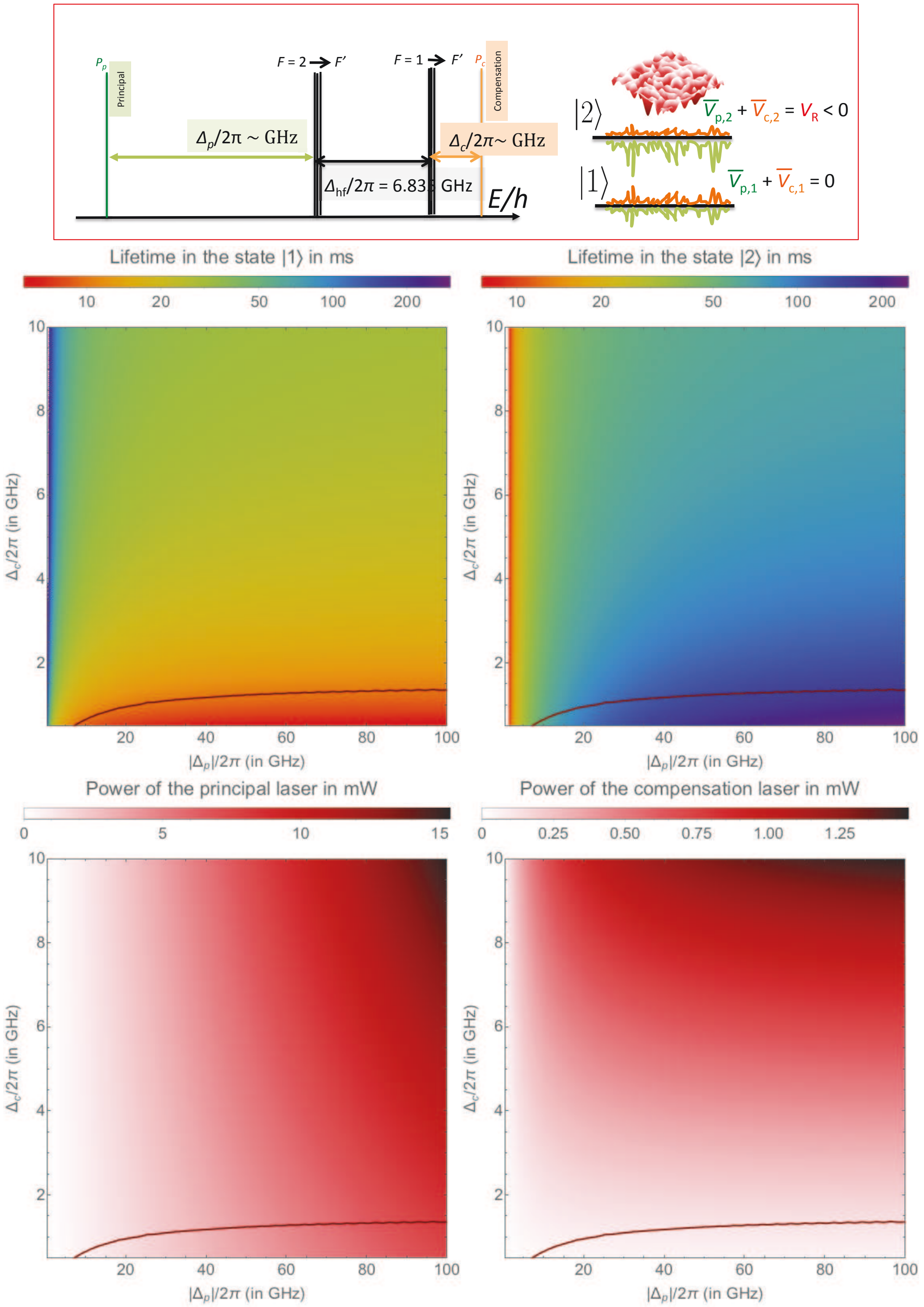

Figure 6.7: **Numerical results for attractive case**; $V_R/h = -4$ kHz. First row: schema taken from Fig. 6.3. Second row: Atomic lifetimes in the states $|1\rangle$ (τ_1, left) and $|2\rangle$ (τ_2, right), shown in logarithmic color scale. The empty area on the left corresponds to $\tau_1 > 0.3$ s; on the right, $\tau_2 < 7.5$ ms. Third row: The required power for the principal laser (P_p, left) and the compensation laser (P_c, right). The detunings $|\Delta_p|$ ($\Delta_p < 0$) and Δ_c are shown in horizontal and vertical axes respectively. Dark red line corresponds to situation where $\tau_1 = 10$ ms.

of the lifetimes, P_p and P_c show a rather positive relationship. Both of them increases with $|\Delta_p|$ and Δ_c. As the $P-$laser approaches the $|2\rangle$'s transitions, i.e. $|\Delta_p|$ approaches zero, both P_p and P_c decrease to near zero value. As the $C-$laser approaches the $|1\rangle$'s transitions, i.e. Δ_c approaches zero, both P_p and P_c decrease; P_c decreases to near zero value. These tendencies are rather obvious. The higher the detuning $|\Delta_p|$, the higher the power P_p is required to create potential of around V_R. The higher the detuning Δ_c, the higher the power P_c is required to compensate the potential created by the $P-$laser. For $|\Delta_p|/2\pi = 100$ GHz and $\Delta_c/2\pi = 1.354$ GHz, we obtain $P_p = 8.14$ mW and $P_c = 130$ μW (see Tab. 6.1).

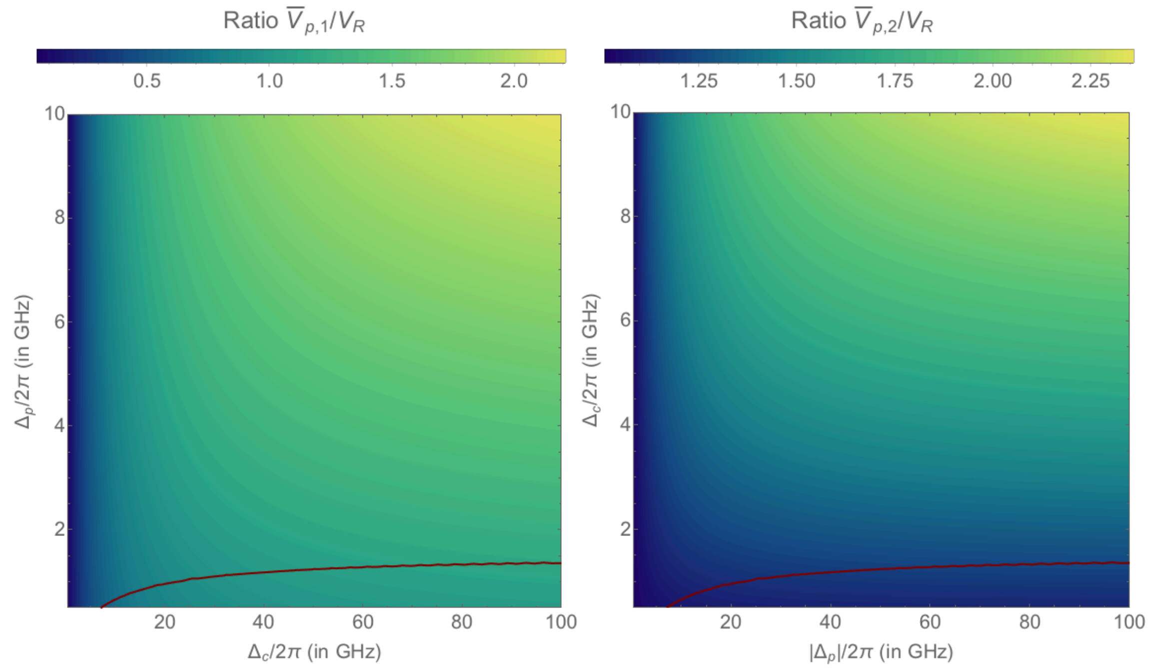

Figure 6.8: **Optical potentials induced by the $P-$laser for attractive case**. (Left) The ratio $\overline{V}_{p,1}/V_R$ between the potential created on the state $|1\rangle$ and the disorder amplitude V_R. (Right) The ratio $\overline{V}_{p,2}/V_R$ between the potential created on the state $|2\rangle$ and the disorder amplitude V_R. Both $\overline{V}_{p,1}/V_R$ and $\overline{V}_{p,2}/V_R$ are presented for detunings Δ_p and Δ_c similar to those shown in Fig. 6.7. Dark red line corresponds to $\tau_1 = 10$ ms.

Similar to the repulsive case, we evaluate the contribution of the $P-$laser to the resultant potentials, i.e. to evaluate the ratios $\overline{V}_{p,1}/V_R$ and $\overline{V}_{p,2}/V_R$. Contrary to the repulsive case, $\overline{V}_{p,2}$ and $\overline{V}_{c,2}$ have opposite signs (see the schema in Fig. 6.3 or 6.7). As a result, we expect the ratio $\overline{V}_{p,2}/V_R$ to be greater than one. Besides $\overline{V}_{p,2}/V_R > \overline{V}_{p,1}/V_R$ since the $P-$laser is closer to the $|2\rangle$'s transitions than to the $|1\rangle$'s transitions. For aforementioned detunings, $|\Delta_p|/2\pi = 100$ GHz and $\Delta_c/2\pi = 1.354$ GHz, we find $\overline{V}_{p,2}/V_R = 1.242$ and $\overline{V}_{p,1}/V_R = 1.166$ (see Tab. 6.1). The colormaps of the ratios $\overline{V}_{p,1}/V_R$ and $\overline{V}_{p,2}/V_R$ are presented in Fig. 6.8. Both ratios increase with $|\Delta_p|$ and with Δ_c.

Similar to the repulsive case, we can evaluate the contribution of the $P-$laser to the dissipation

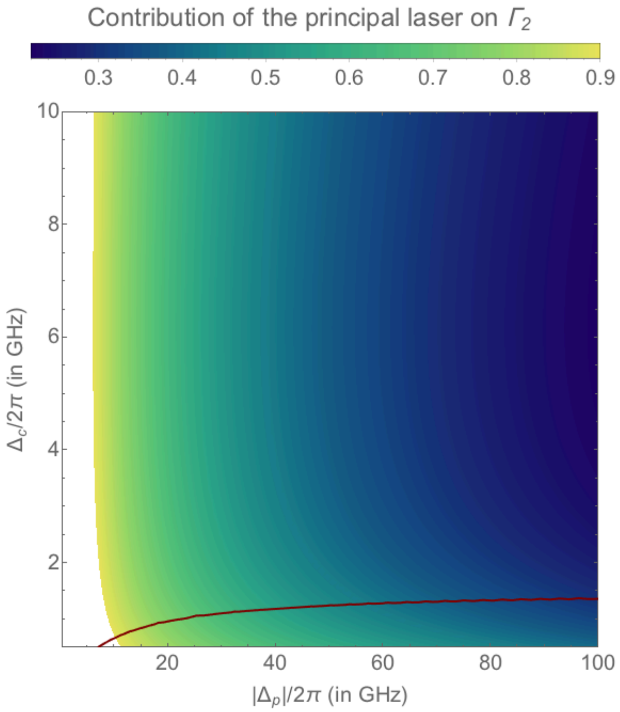

Figure 6.9: **Ratio $\Gamma_{p,2}/\Gamma_2$ for attractive case.** The ratio between the dissipation rate of the state $|2\rangle$ due to the principal laser, $\Gamma_{p,2}$, and the total dissipation rate Γ_2. The empty area corresponds to $\Gamma_{p,2}/\Gamma_2 > 0.9$. Ratio $\Gamma_{p,2}/\Gamma_2$ is presented for detunings Δ_p and Δ_c similar to those shown in Fig. 6.7. Dark red line corresponds to $\tau_1 = 10$ ms.

rate of the state $|2\rangle$, i.e. the ratio $\Gamma_{p,2}/\Gamma_2$. The ratio is expected to decrease as $|\Delta_p|$ increases and it is expected to be close to one as $|\Delta_p|$ approaches the $|2\rangle$'s transitions. The colormap of the ratio $\Gamma_{p,2}/\Gamma_2$ is presented in Fig. 6.9. We can see the variation with $|\Delta_p|$ confirms our predictions. We can also see that the $\Gamma_{p,2}/\Gamma_2$ decreases as Δ_c increases. For aforementioned detunings, $|\Delta_p|/2\pi = 100$ GHz and $\Delta_c/2\pi = 1.354$ GHz, we find $\Gamma_{p,2}/\Gamma_2 = 0.30$ (see Tab. 6.1). This also suggests that the dissipation rate of the state $|2\rangle$ is dominated by the contribution of the $C-$laser.

For convenience purposes, key numerical results related to the attractive case are presented in the second column in Tab. 6.1.

Concluding remarks

We have summarized several key values for both attractive and repulsive cases in Tab. 6.1. In general, the results are well understood. There is no peculiar value except around resonant conditions. In addition, we have also found that the laser powers required are reasonable and that none of the laser contribution is negligible. As we shall see in section 6.2, a new limitation arises from the fluctuation of the potential in the state $|1\rangle$, which is proportional to $\overline{V}_{p,1}$. Let us assume certain coefficient of 0.01 and consider the highest disorder amplitude ($|V_R|/h = 4$ kHz). For resultant fluctuation limited to 40 Hz, i.e. $0.01 \cdot \left|\overline{V}_{p,1}/h\right| \lesssim 40$ Hz, we would require $\overline{V}_{p,1}/V_R \lesssim 1$. For results shown in the table, this condition is more or less satisfied.

	Attractive case	Repulsive case
Fixed conditions:		
Disorder amplitude V_R	$-h \times 4$ kHz	$h \times 4$ kHz
Lifetime in the state $\|1\rangle$ (τ_1)	10 ms	10 ms
Detuning Δ_p	$-2\pi \times 100$ GHz	$2\pi \times 100$ GHz
Detuning Δ_c	$2\pi \times 1.354$ GHz	$-2\pi \times 1.622$ GHz
Lifetime in the state $\|2\rangle$ (τ_2)	165 ms	149 ms
Power of the principal laser (P_p)	8.14 mW	5.16 mW
Power of the compensation laser (P_c)	130.2 μW	69.6 μW
Ratio $\overline{V}_{p,1}/V_R$	1.166	0.853
Ratio $\overline{V}_{p,2}/V_R$	1.242	0.797
Ratio $\Gamma_{p,2}/\Gamma_2$	0.299	0.171
Optimized lifetime (τ_2')	0.68 s	0.69 s

Table 6.1: Summary of important numerical values for both attractive and repulsive cases mentioned in the text. The optimized lifetime follows $\tau_2' = \tau_2 \cdot \frac{\overline{V}_{p,2}/V_R}{\Gamma_{p,2}/\Gamma_2}$; see the scheme presented in Fig. 6.10.

We have evaluated the atomic lifetimes in the disorder associated with the states $|1\rangle$ and $|2\rangle$, noted τ_1 and τ_2 respectively. From the numerical results, it is not a straightforward matter to decide the best parameters of the laser detunings. For both repulsive and attractive cases, we have remarked certain negative relationship between τ_1 and τ_2. With conditions $|V_R|/h = 4$ kHz, $\tau_1 = 10$ ms, and $|\Delta_p|/2\pi = 100$ GHz, we have the lifetime τ_2 of around 0.15 s (see Tab. 6.1). Compared with one-laser configuration presented in Chap. 4, this constitutes improvement by three orders of magnitude.

Besides, we have remarked that the lifetime τ_2 does not improve much for high $|\Delta_p|$; we might expect τ_2 would increase linearly with $|\Delta_p|$ when $|\Delta_p| \gg \Delta_{\text{hf}}$. From numerical results of the ratio $\Gamma_{p,2}/\Gamma_2$, we can see that the dissipation is largely contributed by the compensation laser. For both repulsive and attractive cases, the optimum condition is surprisingly found for $|\Delta_c| \lesssim \Delta_{\text{hf}}$. This does not leave much room for optimization with respect to the parameter Δ_c. As a result, it is difficult to minimize the dissipation due to the $C-$laser.

6.1.4 Improving further atomic lifetime in the disorder

Would it be impossible to improve further the atomic lifetime? The answer turns out to be no! Once some atoms are transferred into the state $|2\rangle$, the atoms left in the state $|1\rangle$ become irrelevant and the condition of vanishing potential for the state $|1\rangle$ is no longer necessary. After the transfer, the atomic lifetime in the state $|2\rangle$ can still be optimized. However, the disorder amplitude V_R must be kept constant.

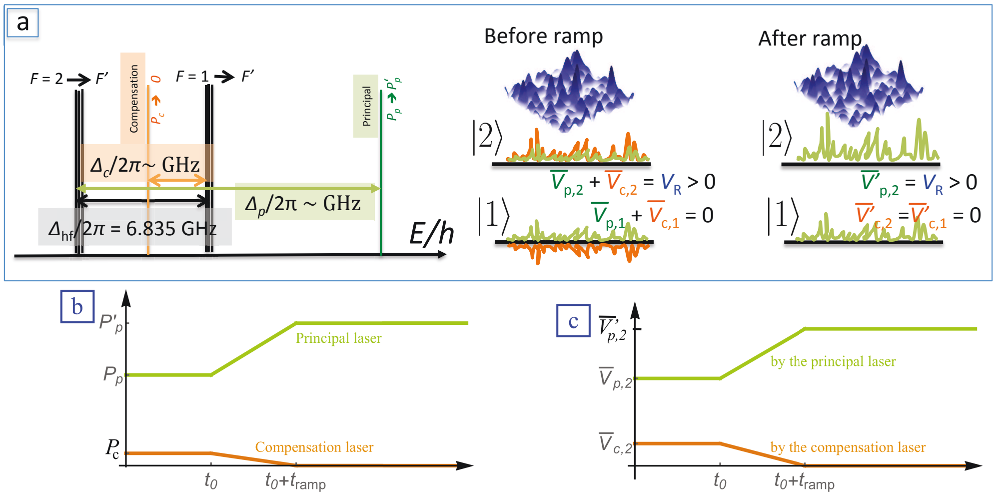

Figure 6.10: Scheme of optimization of lifetime in the disorder by ramping the laser power; example is given for repulsive disorder. (a) Effect of the ramp of the laser powers on the optical potentials. (b) The ramp of the laser powers. (c) The optical potentials induced by each laser on the state $|2\rangle$.

In practice, it is much more convenient to tune the laser powers P_p and P_c than the laser detunings. In addition, the optical potentials have linear dependence on the laser powers. Thus, we only consider solutions by ramping the laser powers. From the numerical results of the ratio $\Gamma_{p,2}/\Gamma_2$, we have remarked dominant contribution of the compensation laser to the dissipation rate Γ_2. As a solution, we ramp down the power of the compensation laser to zero. At the same time, the power of the principal laser is ramped to maintain the disorder amplitude V_R. The scheme for the repulsive case is depicted in Fig. 6.10. After the rf transfer sequence during time interval $[0, t_0]$, we apply linear ramp to both principal laser and compensation laser for a duration t_{ramp}. While the power P_c is ramped to zero, the power P_p is ramped to P_p'; the prime symbol denotes the corresponding values after the ramps. The power P_p' corresponds to average potential $\overline{V}'_{p,2} = V_R$.

The power P_p' can be deduced based on the value $\overline{V}_{p,2}/V_R$ shown in Fig. 6.5 for the repulsive case (or Fig. 6.8 for the attractive case). After the ramps, $\overline{V}'_{c,2} = 0$ and $\overline{V}'_{p,2} = V_R$. Hence $P_p' = P_p \times V_R/\overline{V}_{p,2}$. For aforementioned detunings of the repulsive case, $\Delta_p/2\pi = 100$ GHz and $\Delta_c/2\pi = -1.62$ GHz, we obtain $P_p' = 6.47$ mW (for the attractive case with $\Delta_p/2\pi = -100$ GHz and $\Delta_c/2\pi = 1.354$ GHz, $P_p' = 9.54$ mW). The improved lifetime in the disorder, τ_2', can be deduced based on the ratio $\Gamma_{p,2}/\Gamma_2$ presented in Fig. 6.6 (or Fig. 6.9 for the attractive case). It follows $\tau_2' = 1/\Gamma'_{p,2} = 1/\Gamma_{p,2} \times \overline{V}_{p,2}/V_R$, and thus $\tau_2' = \tau_2 \cdot (\Gamma_{p,2}/\Gamma_2)^{-1} \times \overline{V}_{p,2}/V_R$. For aforementioned detunings of the repulsive case, we find $\tau_2' = 0.69$ s (for the attractive case, $\tau_2' = 0.68$ s); see Tab. 6.1. Even though it is desirable to increase further the lifetime, for weaker disorder amplitude, for instance $V_R/h = 400$ Hz, the evaluated lifetime becomes longer than 6 s. For most disorder amplitudes associated with the previously measured spectral functions, the lifetime in the disorder is beyond one second!

Since we consider $|\Delta_p| \gg \Delta_{\mathrm{hf}}$, it is not hard to show that $\tau_2' \propto |\Delta_p|/V_R$. It seems that the lifetime τ_2' can be made even longer. However, increasing $|\Delta_p|$ would also increase the wavelength difference between the two lasers, $\delta\lambda/\lambda \sim |\Delta_p|/\omega_{\mathrm{D2}}$. This leads to another question: how large wavelength difference can be? It turns out, we need to consider the fluctuation of the potential in the state $|1\rangle$ resulting from the wavelength difference and this is discussed in the next section.

6.2 Bichromatic speckle disorder

The numerical results presented in previous section have assumed that the two lasers have identical speckle patterns. In this section, we attempt to examine the validity of such assumption. In subsection 4.1.2, we have identified several pertinent properties of speckle pattern[3], the speckle waist and the correlation lengths. The speckle waist is shown to be independent of the wavelength. Hence, the envelope of the intensity pattern is identical for both laser speckles. This has already been taken into account for the calculations presented in previous section. However, the correlation lengths, i.e. the speckle grain, are linearly proportional to the wavelength. More generally, the speckle pattern results from wave interference mechanism, resulting in the dependence on the wavelength.

In this section, we focus on the residual disordered potential in the state $|1\rangle$. For this, we generalize the condition of vanishing potential, $\overline{V}_{p,1} + \overline{V}_{c,1} = 0$, to $V_1(\boldsymbol{r}) = V_{p,1}(\boldsymbol{r}) + V_{c,1}(\boldsymbol{r})$ with $\overline{V_1(\boldsymbol{r})} = 0$. This problem is equivalent to evaluating the difference of two speckle intensity patterns. Hence, we further simplify the problem by replacing the potentials $V_{p,1}(\boldsymbol{r})$ and $V_{c,1}(\boldsymbol{r})$ with intensities $I_p(\boldsymbol{r})$ and $-I_c(\boldsymbol{r})$ such that

$$V_1(\boldsymbol{r}) \propto I_p(\boldsymbol{r}) - I_c(\boldsymbol{r}). \tag{6.14}$$

Intensities $I_p(\boldsymbol{r})$ and $I_c(\boldsymbol{r})$ can be considered as speckle patterns with difference only in their wavelength, λ_p and λ_c respectively. In particular, we are interested in the numerical result based on parameters presented in previous section; frequency difference of around 100 GHz at wavelength $\lambda = 780.24$ nm corresponds to $\delta\lambda = |\lambda_p - \lambda_c| = 0.2$ nm.

Estimation of the residual potential

We estimate the amplitude of the residual potential by evaluating the variance associated with the quantity $I_I(\boldsymbol{r}) = I_p(\boldsymbol{r}) - I_c(\boldsymbol{r})$. Furthermore, we introduce $I_p(\boldsymbol{r}) = \overline{I_p(\boldsymbol{r})} + \delta I_p(\boldsymbol{r})$ and $I_c(\boldsymbol{r}) = \overline{I_c(\boldsymbol{r})} + \delta I_c(\boldsymbol{r})$. Let us consider $\overline{I_p(\boldsymbol{r})} = \overline{I_c(\boldsymbol{r})} = I_0(\boldsymbol{r})$ and thus $\overline{I_I(\boldsymbol{r})} = 0$. Because of the speckle statistics, we have $\sigma^2_{I,p}(\boldsymbol{r}) = \sigma^2_{I,c}(\boldsymbol{r}) = I_0^2(\boldsymbol{r})$, where $\sigma^2_{I,p}(\boldsymbol{r}) = \overline{\delta I_p^2(\boldsymbol{r})}$ and $\sigma^2_{I,c}(\boldsymbol{r}) = \overline{\delta I_c^2(\boldsymbol{r})}$. The

---

[3] The waist follows $w_d = f \cdot \theta_{\mathrm{diff}}$. The correlation lengths in transverse and longitudinal directions follow $\sigma_\parallel \sim 2\lambda/(\pi \mathrm{NA}^2)$ and $\sigma_\perp \sim \lambda/(2\mathrm{NA})$.

variance $\sigma_I^2 \equiv \overline{\left(\delta I_p(\boldsymbol{r}) - \delta I_c(\boldsymbol{r})\right)^2}$ can be normalized as follows

$$\frac{\sigma_I^2(\boldsymbol{r}, \lambda_p, \lambda_c)}{I_0^2(\boldsymbol{r})} = 2\left(1 - \mathcal{R}(\boldsymbol{r})\right), \tag{6.15}$$

where $\mathcal{R}(\boldsymbol{r})$ is a dimensionless correlation function, which follows

$$\mathcal{R}(\boldsymbol{r}) \equiv \overline{\delta I_p(\boldsymbol{r})\delta I_c(\boldsymbol{r})}/I_0^2(\boldsymbol{r}). \tag{6.16}$$

The function $\mathcal{R}(\boldsymbol{r})$ has value between zero and one, from which we can conveniently quantify the degree of correlation between the two speckle patterns.

The case $\mathcal{R} = 1$ corresponds to the optimal correlation. The random variables $I_p(\boldsymbol{r})$ and $I_c(\boldsymbol{r})$ have linear relationship. This would describe exactly identical speckle patterns such that $\sigma_I^2(\boldsymbol{r}, \lambda_p, \lambda_c) = \left(\sigma_{I,p}(\boldsymbol{r}) - \sigma_{I,c}(\boldsymbol{r})\right)^2 = 0$, which is the ideal situation considered in section 6.1. However, this would be possible only if $\lambda_p = \lambda_c$.

Case $\mathcal{R} = 0$ can be associated to the incoherent limit. This would describe two completely independent speckle generations. In this case, the random variables $I_p(\boldsymbol{r})$ and $I_c(\boldsymbol{r})$ become independent. The constant term in Eq. 6.15 can then be called the “incoherent” term, which is equal to two.

The correlation function $\mathcal{R}(\boldsymbol{r})$ can be expressed as certain correlation between the electric fields of the two laser speckles. By applying the Wick's theorem[4], we deduce

$$\overline{\delta I_p(\boldsymbol{r})\delta I_c(\boldsymbol{r})} = \left|\overline{E_p(\boldsymbol{r})E_c^*(\boldsymbol{r})}\right|^2. \tag{6.17}$$

The correlation function $\mathcal{R}(\boldsymbol{r})$ can be determined from the following correlation function

$$c_E\left(\boldsymbol{r}, \lambda_p, \lambda_c\right) \equiv \overline{E_p(\boldsymbol{r})E_c^*(\boldsymbol{r})}. \tag{6.18}$$

The electric field $E_p(\boldsymbol{r})$ and $E_c(\boldsymbol{r})$ are obtained from the expression $E(\boldsymbol{r})$ used in Eq. 4.2 by replacing the wavelength λ by λ_p and λ_c respectively. The electric field follows

$$E(\boldsymbol{r}) \propto TF\left[P(\boldsymbol{R})e^{i\phi_\lambda(\boldsymbol{R})}\right](\boldsymbol{r}/\lambda f) \tag{6.19}$$

with $\phi_\lambda(\boldsymbol{R}) = 2\pi(n-1)l(\boldsymbol{R})/\lambda$. Intuitively, the speckle decorrelation should result from the dependence of $\phi_\lambda(\boldsymbol{R})$ on λ. With rms thickness of σ_l, we can identify a characteristic dephasing $\delta\phi = 2\pi(n-1)\sigma_l/l_c$ with $l_c = \lambda_p\lambda_c/\left|\lambda_p - \lambda_c\right|$ the coherence length[5]. Similar to the calculation of

---

[4] $\overline{I_p(\boldsymbol{r})I_c(\boldsymbol{r})} = \overline{E_p(\boldsymbol{r})E_p^*(\boldsymbol{r})E_c(\boldsymbol{r})E_c^*(\boldsymbol{r})} = \overline{E_p(\boldsymbol{r})E_p^*(\boldsymbol{r})}.\overline{E_c(\boldsymbol{r})E_c^*(\boldsymbol{r})} + \left|\overline{E_p(\boldsymbol{r})E_c^*(\boldsymbol{r})}\right|^2$.
The correlation function $\overline{E_p(\boldsymbol{r})E_c^*(\boldsymbol{r})}$ is similar to the expression $\left.\overline{E(\boldsymbol{r})E^*(\boldsymbol{r}+\boldsymbol{\Delta r})}\right|_{\boldsymbol{\Delta r}=0}$ discussed in subsection 4.1.2.

[5] We see $l_c \approx \lambda^2/\delta\lambda \approx \mathcal{N}\lambda$, where $\mathcal{N} = \lambda/\delta\lambda$ becomes the effective *finesse*.

the average transmission, we would expect coefficient $\mathcal{R}$ to follows $\mathcal{R} \sim \exp(-\delta\phi^2/2)$.

Besides, for speckle grain of size $\sigma \sim \lambda/(2\mathrm{NA})$ linearly proportional to λ, mismatch between two speckle patterns becomes significant after $\mathcal{N} = \lambda/\delta\lambda$ grains. This leads to typical characteristic length for decorrelation, $L = \mathcal{N}\sigma$, or

$$L \sim l_c/(2\mathrm{NA}). \tag{6.20}$$

More formally, the correlation function $c_E(\boldsymbol{r}, \boldsymbol{r'}, \lambda_p, \lambda_c)$ can be expressed as follows

$$c_E(\boldsymbol{r}, \lambda_p, \lambda_c) \propto \int \mathrm{d}\boldsymbol{R}\mathrm{d}\boldsymbol{R'}\; P(\boldsymbol{R})P^*(\boldsymbol{R'})\overline{t_p(\boldsymbol{R})t_c^*(\boldsymbol{R'})}\exp\left(i\frac{2\pi}{f}\boldsymbol{r}\cdot\left(\frac{\boldsymbol{R}}{\lambda_p} - \frac{\boldsymbol{R'}}{\lambda_c}\right)\right) \quad , \tag{6.21}$$

where $t_p(\boldsymbol{R}) = \exp\left(i\phi_{\lambda_p}(\boldsymbol{R})\right)$ and $t_c(\boldsymbol{R'}) = \exp\left(i\phi_{\lambda_c}(\boldsymbol{R'})\right)$. By applying similar derivation presented in subsection 4.1.1, the correlation function $\overline{t_p(\boldsymbol{R})t_c^*(\boldsymbol{R'})}$ is given by

$$\overline{t_p(\boldsymbol{R})t_c^*(\boldsymbol{R'})} = \exp\left(-\delta\phi^2/2\right)\exp\left(-\sigma_{\phi,p}\sigma_{\phi,c}\left(1 - \overline{l(\boldsymbol{R})l(\boldsymbol{R'})}/\sigma_l^2\right)\right), \tag{6.22}$$

where $\sigma_{\phi,p} = 2\pi(n-1)\sigma_l/\lambda_p$ and $\sigma_{\phi,c} = 2\pi(n-1)\sigma_l/\lambda_c$; $\delta\phi = |\sigma_{\phi,p} - \sigma_{\phi,c}|$. Furthermore, by applying the approximation $\frac{\overline{l(\boldsymbol{R})l(\boldsymbol{R'})}}{\sigma_l^2} \approx 1 - \frac{|\boldsymbol{R}-\boldsymbol{R'}|^2}{2r_l^2}$, we obtain

$$\overline{t_p(\boldsymbol{R})t_c^*(\boldsymbol{R'})} = \exp\left(-\delta\phi^2/2\right)\exp\left(-\frac{\pi^2\theta_{\mathrm{diff}}^2}{2}\frac{|\boldsymbol{R}-\boldsymbol{R'}|^2}{\lambda_p\lambda_c}\right), \tag{6.23}$$

which shows two exponential terms. The first term, $\exp\left(-\delta\phi^2/2\right)$, is associated with the dephasing due to the propagation through the diffusive plate. From the second term, we realize $\sqrt{\lambda_p\lambda_c}/\theta_{\mathrm{diff}} \sim r_{\mathrm{diff}}$ which is the effective size of the scatterers. We can see that the length r_{diff} is much smaller than the size of the aperture. The second term can be approached with a Dirac delta distribution. This leads to

$$c_E(\boldsymbol{r}, \lambda_p, \lambda_c) \propto \exp\left(-\frac{\delta\phi^2}{2}\right)\cdot TF\left[|P(\boldsymbol{R_0})|^2\right](\boldsymbol{\kappa_1}), \tag{6.24}$$

where $\boldsymbol{\kappa_1} = \frac{\boldsymbol{r}}{fl_c}$ becomes a scaling factor.

From the expression of $c_E(\boldsymbol{r}, \lambda_p, \lambda_c)$, we can deduce the dimensionless correlation function $\mathcal{R}(\boldsymbol{r}) \equiv \overline{\delta I_p(\boldsymbol{r})\delta I_c(\boldsymbol{r})}/I_0^2(\boldsymbol{r})$ which is given by

$$\begin{aligned}\mathcal{R}(\boldsymbol{r}) &= \frac{|c_E(\boldsymbol{r}, \lambda_p, \lambda_c)|^2}{I_0^2(\boldsymbol{r})}, \\ &= \exp\left(-\delta\phi^2\right)\cdot|\mathcal{F}(\boldsymbol{r})|^2,\end{aligned} \tag{6.25}$$

where $\mathcal{F}(\boldsymbol{r}) = TF\left[|P(\boldsymbol{R_0})|^2\right](\boldsymbol{\kappa_1})/TF\left[|P(\boldsymbol{R_0})|^2\right](\boldsymbol{0})$; $\mathcal{F}(0) = 1$ corresponds to the maxima of the function. The term $TF\left[|P(\boldsymbol{R_0})|^2\right](\boldsymbol{\kappa_1})$ is analogous to the term $TF\left[|P(\boldsymbol{R_0})|^2\right]\left(\frac{\boldsymbol{\Delta r}}{\lambda f}\right)$ in subsection 4.1.2 from which we have derived the size of the speckle grain. Here, the conjugate variable, i.e. the scaling factor, gives the characteristic length $L = l_c f/D = l_c/(2\text{NA})$ that is foreseen in Eq. 6.20. Furthermore the term $\exp\left(-\delta\phi^2\right)$ results in the maximum of the correlation $\mathcal{R}(\boldsymbol{r})$ at $\boldsymbol{r} = 0$, which is strictly less than one. The maxima of $\mathcal{R}(\boldsymbol{r})$ at $\boldsymbol{r} = 0$ also corresponds to the minima of $\frac{\sigma_1^2(\boldsymbol{r},\lambda_p,\lambda_c)}{I_0^2(\boldsymbol{r})}$ at $\boldsymbol{r} = 0$, which is given by

$$\frac{\sigma_1^2(\boldsymbol{r}=0,\lambda_p,\lambda_c)}{I_0^2(\boldsymbol{r}=0)} = 2\left(1-\exp\left(-\delta\phi^2\right)\right). \tag{6.26}$$

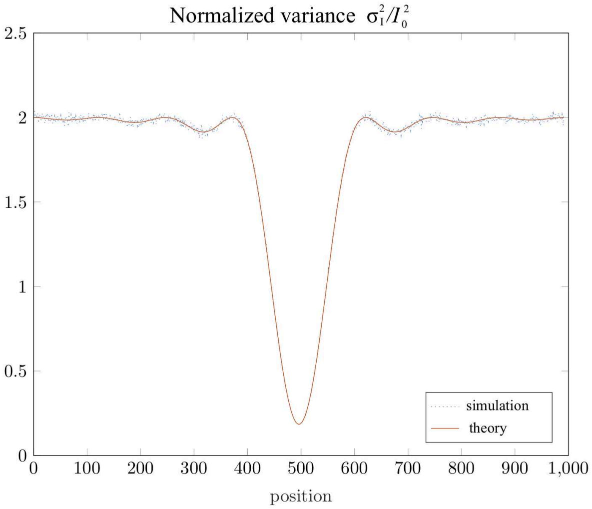

Figure 6.11: The normalized variance $\sigma_I^2/I_0^2 = 2(1-\mathcal{R})$ (see Eq. 6.15) calculated for $\delta\lambda/\lambda = 1/100$, obtained after averaging procedure. See App. C for details on the calculation.

Fig. 6.11 depicts the numerically calculated σ_I^2/I_0^2. It is obtained from the square of the subtraction between two speckle patterns. The shown plot corresponds to $\delta\lambda/\lambda = 1/100$. The plot confirms the dependence $2(1-\mathcal{R}(\boldsymbol{r}))$. At extremities, the two speckle patterns become completely uncorrelated ($\mathcal{R} = 0$), resulting in $\sigma_I^2/I_0^2 = 2$. Around the center, $\mathcal{R}$ is at maximum and thus σ_I^2/I_0^2 is at its minimum. We can see that the shape of the dip is approximately an inverted squared sinus cardinal function associated with the Fourier transform of a square function. The width can then be associated with the characteristic length $L = l_c f/D$, where D is the width of the aperture.

From the quantity σ_I^2/I_0^2, we can estimate the minimum fluctuation of the disordered potential at the state $|1\rangle$, noted σ_V. By assuming that the atomic cloud is around the center of the speckle fields, we have $\left|\sigma_V/\overline{V}_{p,1}\right| = \sqrt{\sigma_I^2/I_0^2}$, and thus

$$\begin{aligned}\left|\sigma_V/\overline{V}_{p,1}\right| &= \sqrt{2\left(1-\mathcal{R}(\boldsymbol{r}=0)\right)},\\ &= \sqrt{2\left(1-\exp\left(-\delta\phi^2\right)\right)}.\end{aligned} \tag{6.27}$$

This relation shows a unique dependence on $\delta\phi$ which is approximately proportional to the difference in the wavelength; we can show that $\delta\phi \propto |\lambda_p - \lambda_c|$. Under approximation $\delta\phi \ll 1$, we deduce

$$\sigma_V \approx \sqrt{2}\cdot\left|\overline{V}_{p,1}\right|\cdot\delta\phi \tag{6.28}$$

From this relation, in order to have reasonably small fluctuation σ_V, the wavelength difference must not be too large. At the same time, keeping σ_V below certain value results in constraint for $\overline{V}_{p,1}$ and thus V_R.

Experimentally realistic numerical results

In section, 6.1, we have considered frequency difference of around $|\Delta_p|/2\pi = 100$ GHz, which corresponds to $\delta\lambda = 0.2$ nm or $\mathcal{N}\lambda/\delta\lambda \approx 3900$. The coherence length $l_c = \mathcal{N}\lambda$ is 3 mm. With ON ≈ 0.5, we have the characteristic length[6] $L = l_c/(2\mathrm{ON})$ of 3 mm. This value is relatively large compared to the speckle field extension. As a result, we can neglect the spatial variation of the fluctuation, i.e. the factor $\mathcal{F}(\boldsymbol{r})$ in $\mathcal{R}(\boldsymbol{r})$. Hence, the fluctuation associated with the state $|1\rangle$ is effectively given by σ_V.

For the estimation of the residual potential, we have typical values $n \approx 1.5$, $\sigma_l \approx 10$ μm, and thus $\delta\phi \approx 0.01$; condition $2\pi(n-1)\sigma_l/l_c \ll 1$ holds. For σ_V limited to $h \times 40$ Hz, typical energy of the chemical potential of the BEC, we can see that $\left|\overline{V}_{p,1}\right|$ must be less than $h \times 2.8$ kHz.

We have presented the calculation of $\overline{V}_{p,1}$ (see Fig. 6.5 for the repulsive case and in Fig. 6.8 for the attractive case). In particular, for the repulsive case with $\Delta_p/2\pi = 100$ GHz and $\Delta_c/2\pi = -1.62$ GHz, we find $\overline{V}_{p,1}/V_R = 0.85$ and $\sigma_V = 0.012 V_R$ (see Tab. 6.1). For $V_R/h = 4$ kHz, we have $\sigma_V/h = 48$ Hz. For the attractive case with $\Delta_p/2\pi = -100$ GHz and $\Delta_c/2\pi = 1.354$ GHz, we find $\overline{V}_{p,1}/V_R = 1.166$ and $\sigma_V = 0.016|V_R|$ (see Tab. 6.1). For $V_R/h = -4$ kHz, we have $\sigma_V/h = 66$ Hz. Hence, for $|V_R|/h = 4$ kHz, we find the residual potential is about the same order of magnitude as the chemical potential. $|V_R|/h = 4$ kHz becomes typical limit for applicable disorder amplitude.

---

[6] We have L which is the same order of magnitude as the speckle waist w_d. In this case, the approximation we have applied to Eq. 6.23 does not hold. However this will only result in additional term $\exp\left(-4r^2/w'^2\right)$ to the correlation function $\mathcal{R}(\boldsymbol{r})$ (see Eq. 6.25), with $w' \approx w_d$; see App. B.2 for complete derivation.

6.3 Implementations

In this section, we present the preliminary implementation of the bichromatic speckle disorder. It constitutes an upgrade with respect to the implementation presented in section 4.2, where the experimental set-up was divided into three parts: "Laser source", "Optical manipulation", and "Speckle generation". Based on our presentation in previous two sections, the set-up "Speckle generation" would not require any change. However, there are now two laser sources for generating the speckle field. The set-up "Laser source" must incorporate the two lasers. Besides, we would like to keep change to the set-up "Optical manipulation" as little as possible.

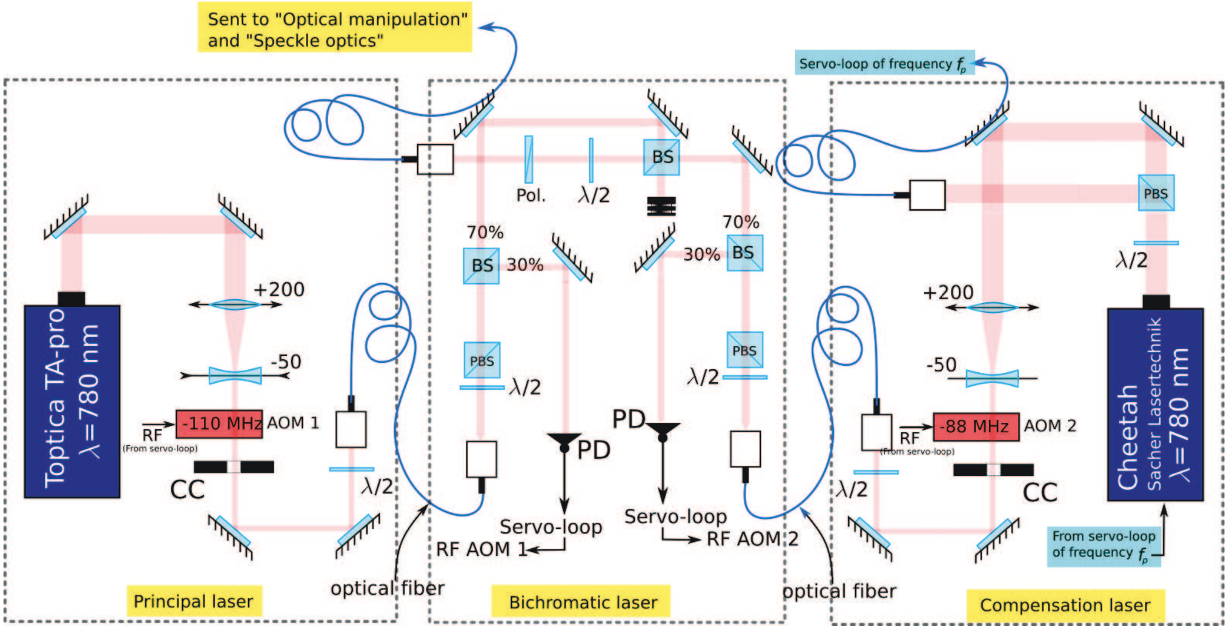

Figure 6.12: The upgraded set-up "laser source" consists of three set-up: laser source of the principal laser, laser source of the compensation laser and the source of bichromatic laser beam.

The new "Laser source" must involve combining the two lasers beams before the light enters the set-up "optical manipulation". This assures that the two beam will have identical beam characteristics. Fig. 6.12 depicts the upgraded set-up. It now consists of three separated parts: two set-ups associated with the principal laser and the compensation laser, and one set-up associated with the combination of the laser beams (see "Bichromatic laser").

The set-up "Principal laser" features is slightly modified from the set-up "Laser source" presented in Fig. 4.3. The principal laser beam is generated by the laser *Toptica TA-Pro* at wavelength 780.24 nm. The set-up "Compensation laser" is almost similar to "Principal laser". The principal laser will be detuned from the $F = 2 \to F'$ transitions by around 100 GHz, which is equivalent to 0.2 nm. The frequency of the laser *Toptica TA-Pro* employed for this is proven to be very stable. In addition, we can monitor easily the wavelength with a wavelength meter with resolution of a picometer. Hence, there would not be any need for servo-loop of frequency locking as shown in Fig. 4.3.

As depicted in Fig. 6.12, the compensation laser beam is generated by the laser Cheetah Sacher Lasertechnik at 780.24 nm. It is a compact Bragg grating stabilized ridge waveguide laser module which can produce up to 380 mW of laser power [157]. The compensation laser will be detuned by around few GHz from the $F = 1 \rightarrow F'$ transitions. The laser frequency must be locked to attain stability. It can be done conveniently with the frequency locking system previously used for the laser *Toptica TA-Pro*.

For each laser, the laser beam is sent to an acousto-optic modulator and the diffracted beam is sent to the set-up “Bichromatic laser” (see Fig.6.12) using an optical fiber. In the later set-up, the two beams are combined and sent to set-up “Optical manipulation” through another optical fiber. The power of each laser is controlled using servo-loop system of laser power previously presented in section 4.2. This allows independent control of the two laser powers. Both principal and compensation laser beam coming out of the fiber coupler are split by 70:30 beam splitter (BS). The reflected beams serve as inputs for the servo-loop systems. The feedback signals are sent to the acousto-optic modulators in each laser source set-up, AOM 1 for the principal laser and AOM 2 for the compensation laser (see Fig. 6.12). The transmitted beams from the 70:30 beam splitters are combined using a 50:50 beam splitter. Then, the combined beam pass through a polarizer and coupled to an optical fiber.

Similar to the set-ups presented in section 4.2, we put mechanical shutter (CC) in front of each AOM-diffracted beam to achieve excellent extinction ratio for each source of speckle field. To minimize fluctuations in polarization, we use polarization-maintaining optical fibers for the transport of the laser beams and polarization beam splitters in front of fiber out-couplers.

Fig. 6.13 depicts the set-ups “Bichromatic laser”, “Optical manipulation”, and “Speckle generation”. The output beam from “Bichromatic laser” is sent to “Optical manipulation”. While there is no modification for the “Speckle generation”, several minor changes are made for “optical manipulation”. As the typical power for the bichromatic laser beam is several mW, the optical density filter is no longer needed. Furthermore, the reflected beam from the 10:90 beam splitter would no longer be needed for a servo-loop system. Conversely, it would be difficult to control independently the laser powers once the two laser beams are combined.

6.4 Conclusions

In this chapter, we have presented the realization of bichromatic state-dependent speckle disorder. It involves two laser speckles to generate the disorder, that we have called the principal laser and the compensation laser. We have performed numerical studies to explore the best parameters associated with the two lasers. In particular, we evaluate the atomic lifetimes in the disorder, in both clock states $|1\rangle$ and $|2\rangle$. We have shown that it is possible to achieve atomic lifetime in the state $|2\rangle$ of

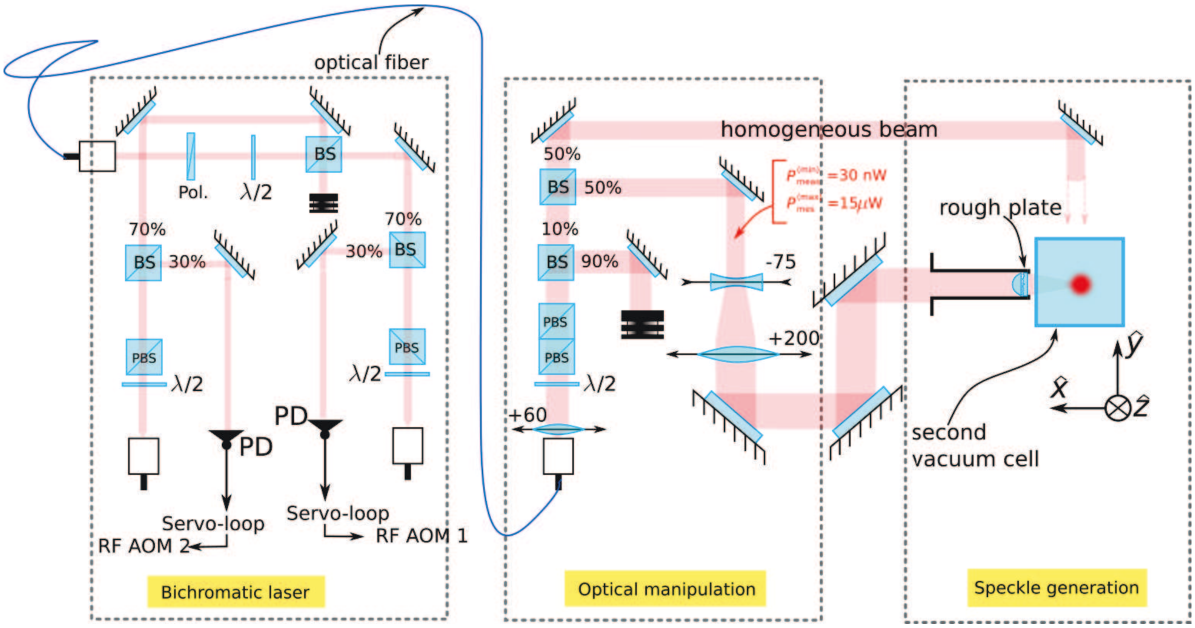

Figure 6.13: The set-up of bichromatic laser beam combined the principal and the compensation laser. This beam is sent to set-up "optical manipulation" and then "speckle optics" which are similar to those discussed in Chap. 4.

0.68 s for highest disorder amplitude used for the spectral function measurements ($V_R/h = \pm 4$ kHz); see Tab. 6.1.

However, a new limitation emerges from an effective residual potential in the state $|1\rangle$ due to mismatch between two speckle patterns at different wavelengths. Moreover, the longer the atomic lifetime, the larger the wavelength difference, and the stronger the residual potential. Hence, we need to find a balanced solution. We have evaluated theoretically and numerically the expected strength of the residual potential. Considering the proposed parameters and numerical results listed in Tab. 6.1, it is possible to perform experiment with range of disorder amplitude used in the spectral function measurements with improved atomic lifetime in the disorder by three order of magnitude[7]! Lastly, we have also presented the preliminary implementation of the bichromatic speckle disorder.

---

[7] From 0.5 ms for the single laser speckle to 0.68 s for the bichromatic laser speckle. Besides, ratio $\sigma_V/V_R \sim 0.01$ is similar to that in the previous state-dependent disorder scheme.

Chapter 7

Conclusions and current works

In this manuscript, we have presented our works towards realization of spectroscopic approach of the Anderson transition. We have developed techniques to control the energy of matter wave in disordered potentials, which allow scanning through the critical regime of the phase transition (see Chap. 2). Our techniques involve two distinct spin-states which are introduced in Chap. 3. Furthermore, we have presented the technique of radio-frequency transfer between the two states based on mechanism of two-photon transition. In Chap. 4, we have presented the realization of the disorder by using a single laser speckle. In particular, we have implemented the technique of state-dependent disordered potential, whereby the disorder is only significant for one of the two involved spin states. By combining these techniques, we have realized coherent transfer of matter wave from a disorder-free state into a state with controlled disorder. The corresponding energy in the disordered potential is tunable with resolution mainly limited by the Fourier transform associated with the rf transfer.

As a proof-of-principle, we have performed measurements of the spectral functions of matter wave in disordered potentials (see Chap. 5). The results show excellent agreement with numerical works carried out by our collaborators (Delande's group in LKB). This has opened up prospects for further studies of the Anderson transition. However, current realization of the state-dependent disorder does not allow long propagation time for the atoms in the disorder. For this, we have developed state-dependent disordered potential involving two laser speckles. From the numerical studies related to the lifetime and the residual potential of the disorder-free spin state, we show improvement of the atomic lifetime in the disorder. With this "upgraded" implementation, we expect to observe the mobility edge of the Anderson transition.

Spectroscopy of Anderson localization

Based on the research plan presented in Fig. 1.3, the next goal would be the direct measurement of the mobility edge (see Fig. 7.1(a)). In addition to the transfer procedure as being done for

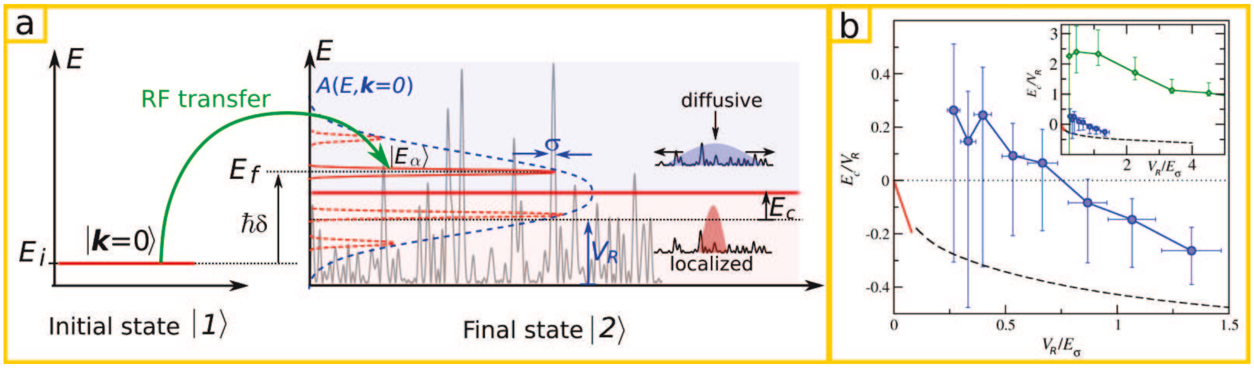

Figure 7.1: (a) Spectroscopic approach of Anderson transition; adapted from Fig. 1.3. The achieved energy resolution with our techniques is typically significantly smaller than the characteristic energies of the system such as disorder amplitude V_R, the correlation energy $E_\sigma = \hbar^2/(m\sigma^2)$, and the spectral function width. This would allow direct measurement of the mobility edge (see E_c) with improved precision. (b) Existing experimental and numerical results on the mobility edge determination, as shown in Fig. 2.8.

the spectral function measurement, we need to observe the expansion of the atomic wave packet in presence of the disorder. With the new scheme of the state-dependent disorder (see Chap. 6), the propagation time is reasonably long to allow differentiation between the diffusive states and the localized states. In order to observe the transition between the two phases, we need to scan the energy of the matter wave, i.e. the detuning δ of the rf transfer. Thanks to the fine energy resolution of the rf transfer, the transition should be more pronounced compared to earlier experimental attempts [40–42]. Thus, our method would allow not only direct measurement of the mobility edge, but also comparison with existing numerical predictions (see Fig. 7.1(b) or Refs. [43,107,158]).

Experimentally, it is possible to measure the diffusion rate or the localization length by analyzing the expansion rate of the atomic cloud. We are interested in the measurements of the diffusion rate D for energy above the mobility edge and the measurements of the localization length ξ for energy below the mobility edge. The behaviors of D and ξ around the mobility edge are predicted by the Eq. 2.10. The dependences of D and ξ on the energy are characterized by the critical exponents s and ν respectively. Since our experimental method allows controlled and well-defined energy in the disorder, it would be highly desirable to perform direct measurement of these exponents.

Signatures of Anderson transition in momentum space

As presented in section 5.3, the measurement of the elastic scattering time relies on observing the evolution of the wave packet in the momentum space. The experimental scheme has also been used to examine the signature of coherent backscattering (CBS) [44,45,72] (see section 2.2). Indeed, the scheme can also be applied to study the Anderson transition in momentum space. In recent work done in Delande's group, the width of CBS peak also shows signature of Anderson transition [84].

The width of the CBS peak width is shown to follow

$$k_i\Delta\theta_{\mathrm{CBS}}(t) \sim \begin{cases} 1/\sqrt{D(E)t} & E > E_c, \\ 1/t^{1/3} & E = E_c, \\ 1/\xi(E) & E < E_c. \end{cases} \tag{7.1}$$

We can gain some intuition on the behavior of $k_i\Delta\theta_{\mathrm{CBS}}(t)$ since the width of the CBS peak is approximately inversely proportional to the spatial extension of the wave packet; $\Delta x \sim (k_i\Delta\theta_{\mathrm{CBS}})^{-1}$.

In experiment, the measured width of CBS peak is affected by certain resolution Δk_{res} which depends mainly on the temperature and the imaging resolution. Even though Δk_{res} in aforementioned experiments is already very narrow thanks to the delta-kick cooling technique. Observing signature of Anderson transition from the CBS peak would require smaller Δk_{res} by around one order of magnitude. Thus, it would be extremely challenging to observe such signature of phase transition.

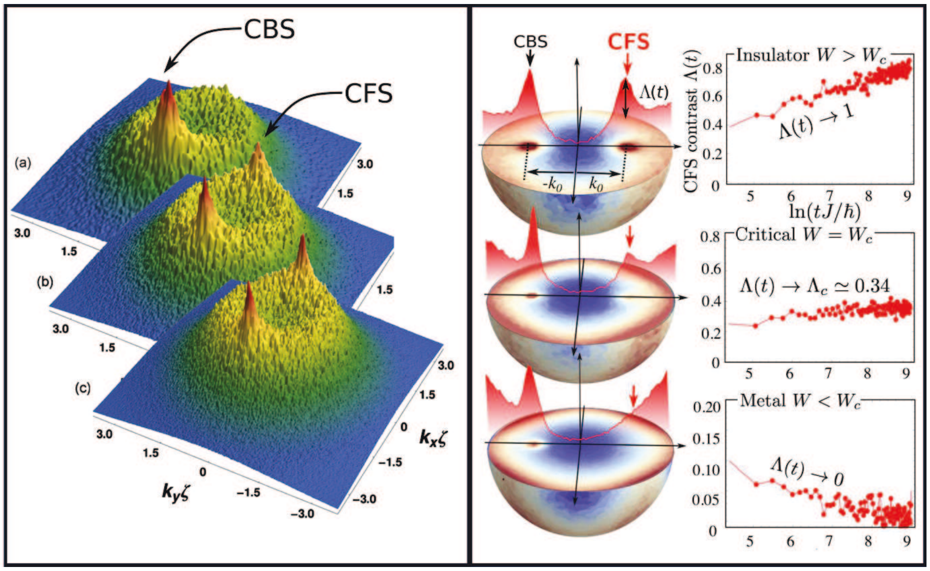

Figure 7.2: **Coherent forward scattering (CFS) signatures**. (a) CFS manifests as a peak complementary to the CBS peak in the momentum distribution, which appears at the initial momentum and at longer time [85]. (b) CFS peak constitutes signature of the Anderson transition [88]. It can be characterized by the contrast between the CFS peak and the CBS peak, noted as $\Lambda(t)$. For insulator (localized) phase, $\Lambda(t) \to 1$ at large t. For metallic (diffusive) phase, $\Lambda(t) \to 0$ at large t.

Another signature related to the momentum space is the so-called coherent forward scattering (CFS) [85]. It is characterized by formation of a peak at the initial momentum $h\boldsymbol{k_i}$ in addition the CBS peak. Subsequent related works suggest that the CFS peak is also a signature of Anderson localization [86, 87] and Anderson transition [88].

The phase transition can be observed from the contrast between the CFS peak and the CBS peak at long time. For diffusive states, the CFS peak vanishes whereas for localized states, the CFS peak and the CBS peak form twin peaks. The phase transition is characterized with parameter Λ, defined as the contrast between the CFS peak and the CBS peak. For diffusive states, $\Lambda(t) \to 0$, whereas for localized states, $\Lambda(t) \to 1$.

Experimentally, observing CFS demands several experimental improvements; to reduce the Δk_{res}. Firstly, the initial velocity distribution must be extremely narrowed. Although it is less stringent for CFS than for Anderson transition with CBS, we still need to cool the BEC to tens of picokelvins [159]. Secondly the resolution of the imaging system has to be optimized. In particular, we foresee implementation of optical tomoghraphic technique by introducing a spatially dependent condition for the resonant fluorescence imaging. Such technique can be realized using magnetic gradient [160] or with light-shift tomography [161]. Lastly, having such high-resolution imaging not only allows studies of localization signatures in momentum spaces, but also allows other possibility to probe multifractality [162, 163].

Localization and diffusion in tailored disorders

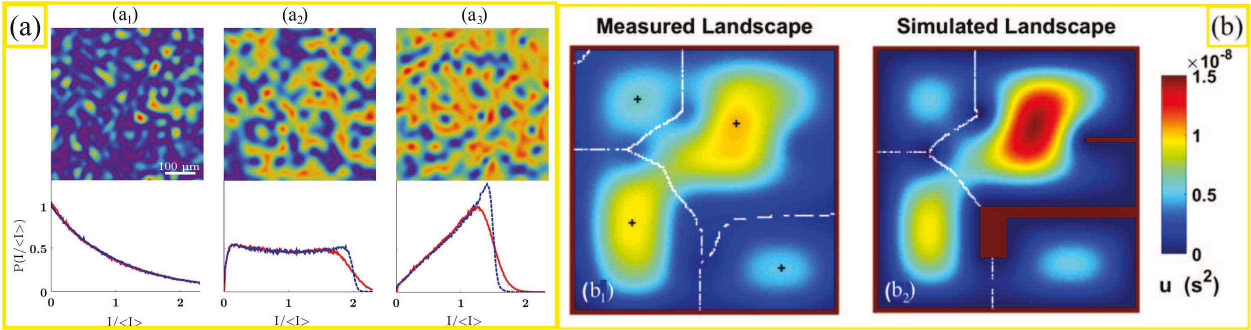

Figure 7.3: (a) **Customizing speckle intensity statistics**; figures are taken from Ref. [164]. (a$_1$) Usual Rayleigh speckle pattern and (a$_2$ and a$_3$) some customized speckle patterns with distinct intensity statistics. (b) **The hidden landscape theory**. (b$_1$) Measured vs (b$_2$) simulated landscape in a vibrating plate (figures are taken from Ref. [165]).

Throughout this manuscript, we have considered disordered potentials created using laser speckle. Such realization features tunable disordered amplitude V_R. On the other hand, tuning the correlation energy E_σ is proven more challenging. However, we can have further level of control by implementing a spatial light modulator (SLM) in place of a diffusive plate to generate the laser speckle. SLM has opened up prospects to tailor the spatial correlation of the disorder and even its probability density (see Ref. [164] or Fig. 7.3(a)).

In particular, we are interested in tailoring the disordered potential in order to study the hidden landscape theory. This recent theoretical approach is developed by Filoche and Mayboroda [166] with whom we envisage collaboration. They have demonstrated that both Anderson and weak localizations originate from the same universal mechanism, acting on any type of vibration, in any dimension, and for any domain shape. The proposed theory reveals inside any vibrating system a hidden landscape that divides the original domain into several weakly coupled vibrating subregions. The hidden landscape then allows predictions of both the regions of localization of eigenfunctions and the corresponding eigenvalues with remarkable accuracy (see Fig. 7.3(b)). The hidden landscape theory offers a possibility to speed up considerably the calculations [167]. It also opens the prospect to solve the inverse problem, i.e. to "engineer" specifically the disordered potential in order to obtain the desired localization properties for a given application.

Within the hidden landscape theoretical framework, the localization properties can be interpreted as a "classical" percolation problem in an effective potential (which is directly related to the landscape). We are interested in an effective percolation transition which emerges as the spatial correlation is varied from quasi-uncorrelated systems to strongly correlated ones. Experimentally, we aim to observe such crossover by varying the disorder amplitude across the correlation energy.

More generally, tailoring the disordered potential allows investigation of the Anderson transition for different types of distribution of disorder. Such study will test the universality of the phase transition (see Eq. 2.10). Besides, it is certainly more feasible to measure the spectral function and the mobility edge with disorder very different from speckle disorder; it would be interesting to identify the relevant microscopic details.

Other perspectives

In addition to the three aforementioned areas of further studies, there are still other possible studies that can be envisaged with our experiment. The measurement scheme of the spectral function could be implemented in a "reversed way," as proposed in Refs. [144, 168], where the ultracold atomic sample under investigation is in the disorder-sensitive state while the resonant transfer is driven to the "free" state. This configuration could be used to probe the complex excitation spectra of interacting and disordered quantum gases [144], for instance, to reveal the predicted gapless excitation spectrum in the Bose glass phase [169, 170]. Furthermore, we can also play with the interparticle interactions to investigate their effect on the Anderson transition [171] and their role in the thermalization of matter waves in disordered potentials [172]. Hence, our spectroscopic method would open multiple experimental prospects.

Bibliography

[1] Rotter, S. & Gigan, S. Light fields in complex media: Mesoscopic scattering meets wave control. *Reviews of Modern Physics* **89**, 015005 (2017). (page 15)

[2] Tourin, A., Fink, M. & Derode, A. Multiple scattering of sound. *Waves in Random Media* **10**, R31-R60 (2000). (page 15)

[3] Campillo, M. & Paul, A. Long-Range Correlations in the Diffuse Seismic Coda. *Science* **299**, 547 (2003). (page 15)

[4] Young, H. & Freedman, R. *University Physics with Modern Physics with MasteringPhysics (12th Edition).* (Addison Wesley, 2007). (page 15)

[5] Marder, M. P. *Condensed Matter Physics (2nd Edition).* (Wiley, 2010). (page 15)

[6] Akkermans, E. & Montambaux., G. *Mesoscopic Physics of Electrons and Photons.* (Cambridge University Press, 2007). (page 15, 23, 25, 26, 27, 28)

[7] Josse, V. *Propagation cohérente d'atomes ultra-froids: Laser à atomes guidé et localisation d'Anderson*, Université Paris Sud - Paris XI, (2015). (page 15, 16, 28, 31)

[8] Lagendijk, A., Tiggelen, B. v. & Wiersma, D. S. Fifty years of Anderson localization. *Physics Today* **62**, 24-29 (2009). (page 15, 16, 26, 32)

[9] Anderson, P. W. in *50 Years of Anderson Localization* 1-6 (WORLD SCIENTIFIC, 2010). (page 15)

[10] Anderson, P. W. Absence of Diffusion in Certain Random Lattices. *Physical Review* **109**, 1492-1505 (1958). (page 15)

[11] Thouless, D. in *50 Years of Anderson Localization* 7-25 (WORLD SCIENTIFIC, 2010). (page 15)

[12] Anderson, P. W. Local moments and localized states. *Reviews of Modern Physics* **50**, 191-201 (1978). (page 16)

[13] Abrahams, E., Anderson, P. W., Licciardello, D. C. & Ramakrishnan, T. V. Scaling Theory of Localization: Absence of Quantum Diffusion in Two Dimensions. *Physical Review Letters* **42**, 673-676 (1979). (page 16, 29, 30)

[14] Sapienza, L. et al. Cavity Quantum Electrodynamics with Anderson-Localized Modes. *Science* **327**, 1352 (2010). (page 16)

[15] Schwartz, T., Bartal, G., Fishman, S. & Segev, M. Transport and Anderson localization in disordered two-dimensional photonic lattices. *Nature* **446**, 52 (2007). (page 16)

[16] Mafi, A., Karbasi, S., Koch, K. W., Hawkins, T. & Ballato, J. Transverse Anderson Localization in Disordered Glass Optical Fibers: A Review. *Materials* **7**, 5520-5527 (2014). (page 16)

[17] Hu, H., Strybulevych, A., Page, J. H., Skipetrov, S. E. & van Tiggelen, B. A. Localization of ultrasound in a three-dimensional elastic network. *Nature Physics* **4**, 945 (2008). (page 16, 31, 32)

[18] Paalanen, M. A., Rosenbaum, T. F., Thomas, G. A. & Bhatt, R. N. Critical Scaling of the Conductance in a Disordered Insulator. *Physical Review Letters* **51**, 1896-1899 (1983). (page 16, 31, 32)

[19] Robins, N. P., Altin, P. A., Debs, J. E. & Close, J. D. Atom lasers: Production, properties and prospects for precision inertial measurement. Physics Reports **529**, 265-296 (2013). (page 16)

[20] Canuel, B. et al. in *i-DUST 2014 – Inter-Disciplinary Underground Science & Technology.* 01004. (page 16)

[21] Derevianko, A. & Katori, H. Colloquium: Physics of optical lattice clocks. *Reviews of Modern Physics* **83**, 331-347 (2011). (page 16)

[22] Eckel, S. et al. Hysteresis in a quantized superfluid 'atomtronic' circuit. *Nature* **506**, 200 (2014). (page 16)

[23] Cohen-Tannoudji, C. & Guéry-Odelin, D. *Advances in atomic physics: An overview.* (World Scientific Publishing, 2011). (page 16)

[24] Bloch, I., Dalibard, J. & Zwerger, W. Many-body physics with ultracold gases. *Reviews of Modern Physics* **80**, 885-964 (2008). (page 16)

[25] Bloch, I., Dalibard, J. & Nascimbène, S. Quantum simulations with ultracold quantum gases. *Nature Physics* **8**, 267 (2012). (page 16)

[26] Pitaevskii, L. & Stringari, S. in *Bose-Einstein Condensation and Superfluidity* (Oxford University Press, 2016). (page 16)

[27] Greiner, M., Mandel, O., Esslinger, T., Hänsch, T. W. & Bloch, I. Quantum phase transition from a superfluid to a Mott insulator in a gas of ultracold atoms. *Nature* **415**, 39 (2002). (page 16)

[28] Greiner, M., Regal, C. A. & Jin, D. S. Emergence of a molecular Bose–Einstein condensate from a Fermi gas. *Nature* **426**, 537 (2003). (page 16)

[29] Labuhn, H. et al. Tunable two-dimensional arrays of single Rydberg atoms for realizing quantum Ising models. *Nature* **534**, 667 (2016). (page 16)

[30] Clément, D. et al. Suppression of Transport of an Interacting Elongated Bose-Einstein Condensate in a Random Potential. *Physical Review Letters* **95**, 170409 (2005). (page 16)

[31] Fort, C. et al. Effect of Optical Disorder and Single Defects on the Expansion of a Bose-Einstein Condensate in a One-Dimensional Waveguide. *Physical Review Letters* **95**, 170410 (2005). (page 16)

[32] Schulte, T. et al. Routes Towards Anderson-Like Localization of Bose-Einstein Condensates in Disordered Optical Lattices. *Physical Review Letters* **95**, 170411 (2005). (page 16)

[33] Aspect, A. & Inguscio, M. Anderson localization of ultracold atoms. *Physics Today* **62**, 30-35 (2009). (page 16)

[34] Horak, P., Courtois, J.-Y. & Grynberg, G. Atom cooling and trapping by disorder. *Physical Review A* **58**, 3953-3962 (1998). (page 16)

[35] Diener, R. B., Georgakis, G. A., Zhong, J., Raizen, M. & Niu, Q. Transition between extended and localized states in a one-dimensional incommensurate optical lattice. *Physical Review A* **64**, 033416 (2001). (page 16)

[36] Gavish, U. & Castin, Y. Matter-Wave Localization in Disordered Cold Atom Lattices. *Physical Review Letters* **95**, 020401 (2005). (page 16)

[37] Choi, J.-y. et al. Exploring the many-body localization transition in two dimensions. *Science* **352**, 1547 (2016). (page 16, 33)

[38] Billy, J. et al. Direct observation of Anderson localization of matter waves in a controlled disorder. *Nature* **453**, 891-894 (2008). (page 16, 17, 19)

[39] Roati, G. et al. Anderson localization of a non-interacting Bose-Einstein condensate. *Nature* **453**, 895-898 (2008). (page 16, 17)

[40] Kondov, S. S., McGehee, W. R., Zirbel, J. J. & DeMarco, B. Three-Dimensional Anderson Localization of Ultracold Matter. *Science* **334**, 66-68 (2011). (page 17, 18, 32, 100, 104, 130)

[41] Jendrzejewski, F. et al. Three-dimensional localization of ultracold atoms in an optical disordered potential. *Nature Physics* **8**, 398-403 (2012). (page 17, 18, 19, 32, 34, 35, 100, 104, 130)

[42] Semeghini, G. et al. Measurement of the mobility edge for 3D Anderson localization. *Nature Physics* **11**, 554-559 (2015). (page 17, 18, 32, 100, 104, 130)

[43] Pasek, M., Orso, G. & Delande, D. Anderson Localization of Ultracold Atoms: Where is the Mobility Edge? *Physical Review Letters* **118**, 170403 (2017). (page 18, 33, 37, 38, 39, 73, 130)

[44] Jendrzejewski, F. et al. Coherent Backscattering of Ultracold Atoms. *Physical Review Letters* **109**, 195302 (2012). (page 19, 24, 27, 29, 130)

[45] Müller, K. et al. Suppression and Revival of Weak Localization through Control of Time-Reversal Symmetry. *Physical Review Letters* **114**, 205301 (2015). (page 19, 24, 27, 29, 130)

[46] Billy, J. *Quantum propagation of guided matter waves: Atom laser and Anderson localization,* PhD thesis, Université Paris Sud - Paris XI, (2010). (page 19)

[47] Bernard, A., *Quantum transport of ultracold atomic matterwaves: Anderson localization and guided atom laser,* PhD thesis, Université Pierre et Marie Curie - Paris VI (2010). (page 19, 42, 45, 47, 53, 54)

[48] Jendrzejewski, F., *Quantum transport of ultracold atoms in disordered potentials*, PhD thesis, Université Paris Sud - Paris XI (2012). (page 19, 24, 42)

[49] Müller, K. *Coherent transport of ultracold atoms in disordered potentials: Manipulation of time-reversal symmetry in weak localization experiments*, PhD thesis, Institut d'Optique Graduate School (2014). (page 19, 42)

[50] Richard, J., *Propagation d'atomes ultra-froidsen milieu désordonnée*, PhD thesis, Université Paris-Saclay (2015). (page 19, 24, 27, 42, 70, 73, 102)

[51] Volchkov, V. V. et al. Measurement of Spectral Functions of Ultracold Atoms in Disordered Potentials. *Physical Review Letters* **120**, 060404 (2018). (page 19, 92, 93, 94, 95)

[52] Denechaud, V., *Vers une étude spectroscopique de la transition d'Anderson avec des atomes froids*, PhD thesis, Université Paris-Saclay (2018). (page 20, 42, 58, 70, 94, 99)

[53] Rammer, J. *Quantum Transport Theory.* (Avalon Publishing, 2004). (page 23)

[54] Monteverde, M. et al. Transport and Elastic Scattering Times as Probes of the Nature of Impurity Scattering in Single-Layer and Bilayer Graphene. *Physical Review Letters* **104**, 126801 (2010). (page 24)

[55] Ando, T., Fowler, A. B. & Stern, F. Electronic properties of two-dimensional systems. *Reviews of Modern Physics* **54**, 437-672 (1982). (page 24)

[56] Bockelmann, U., Abstreiter, G., Weimann, G. & Schlapp, W. Single-particle and transport scattering times in narrow GaAs/Al$_x$Ga$_{1-x}$As quantum wells. *Physical Review B* **41**, 7864-7867 (1990). (page 24)

[57] Page, J. H. et al. Group Velocity in Strongly Scattering Media. *Science* **271**, 634 (1996). (page 24)

[58] Savo, R. et al. Observation of mean path length invariance in light-scattering media. *Science* **358**, 765 (2017). (page 24)

[59] Jacques, S. L., Wang, B. & Samatham, R. Reflectance confocal microscopy of optical phantoms. *Biomed. Opt. Express* **3**, 1162-1172 (2012). (page 24)

[60] Sevrain, D., Dubreuil, M., Leray, A., Odin, C. & Le Grand, Y. Measuring the scattering coefficient of turbid media from two-photon microscopy. *Opt. Express* **21**, 25221-25235 (2013). (page 24)

[61] Martin, C. & Ben-Yakar, A. Determination of scattering properties and damage thresholds in tissue using ultrafast laser ablation. *Journal of Biomedical Optics* **21**, 115004 (2016). (page 24)

[62] Shapiro, B. Large Intensity Fluctuations for Wave Propagation in Random Media. *Physical Review Letters* **57**, 2168-2171 (1986). (page 24)

[63] Emiliani, V. et al. Near-Field Short Range Correlation in Optical Waves Transmitted through Random Media. *Physical Review Letters* **90**, 250801 (2003). (page 24)

[64] Anache-Ménier, D., van Tiggelen, B. A. & Margerin, L. Phase Statistics of Seismic Coda Waves. *Physical Review Letters* **102**, 248501 (2009). (page 24)

[65] Obermann, A., Larose, E., Rossetto, V. & Margerin, L. Measuring the scattering mean free path of Rayleigh waves on a volcano from spatial phase decoherence. *Geophysical Journal International* **197**, 435–442 (2014). (page 24)

[66] Richard, J., Kim, L.-K., Denechaud, D., Volchkov, V. V., Lecoutre, B., Mukhtar, M., Jendrzejewski, F., Aspect, A., Signoles, A., Sanchez-Palencia, L., and Josse, V., Elastic scattering time of matter-waves in disordered potentials,. *Physical Review Letters* (in press, 2019). (page 24, 25, 27, 70, 97, 101, 102)

[67] Plisson, T., Bourdel, T. & Müller, C. A. Momentum isotropisation in random potentials. *The European Physical Journal Special Topics* **217**, 79-84 (2013). (page 26, 27)

[68] Kuhn, R. C., Sigwarth, O., Miniatura, C., Delande, D. & Müller, C. A. Coherent matter wave transport in speckle potentials. *New Journal of Physics* **9**, 161 (2007). (page 26, 33, 85, 91, 97)

[69] Piraud, M., Pezzé, L. & Sanchez-Palencia, L. Matter wave transport and Anderson localization in anisotropic three-dimensional disorder. *EPL (Europhysics Letters)* **99**, 50003 (2012). (page 26)

[70] Piraud, M., Pezzé, L. & Sanchez-Palencia, L. Quantum transport of atomic matter waves in anisotropic two-dimensional and three-dimensional disorder. *New Journal of Physics* **15**, 075007 (2013). (page 26, 33, 68, 97)

[71] Shapiro, B. Cold atoms in the presence of disorder. *Journal of Physics A: Mathematical and Theoretical* **45**, 143001 (2012). (page 26, 91, 97)

[72] Cherroret, N., Karpiuk, T., Müller, C. A., Grémaud, B. & Miniatura, C. Coherent backscattering of ultracold matter waves: Momentum space signatures. *Physical Review A* **85**, 011604(R) (2012). (page 26, 29, 130)

[73] Micklitz, T., Müller, C. A. & Altland, A. Echo spectroscopy of Anderson localization. *Physical Review B* **91**, 064203 (2015). (page 26)

[74] Ammann, H. & Christensen, N. Delta Kick Cooling: A New Method for Cooling Atoms. *Physical Review Letters* **78**, 2088-2091 (1997). (page 27)

[75] Grimm, R., Weidemüller, M. & Ovchinnikov, Y. B. in *Advances In Atomic, Molecular, and Optical Physics* Vol. 42 (eds Bederson Benjamin & Walther Herbert) 95-170 (Academic Press, 2000). (page 27, 45)

[76] Bergmann, G. Weak localization in thin films: a time-of-flight experiment with conduction electrons. *Physics Reports* **107**, 1-58 (1984). (page 27)

[77] Albada, M. P. V. & Lagendijk, A. Observation of Weak Localization of Light in a Random Medium. *Physical Review Letters* **55**, 2692-2695 (1985). (page 27)

[78] Wolf, P.-E. & Maret, G. Weak Localization and Coherent Backscattering of Photons in Disordered Media. *Physical Review Letters* **55**, 2696-2699 (1985). (page 27)

[79] Labeyrie, G. et al. Coherent Backscattering of Light by Cold Atoms. *Physical Review Letters* **83**, 5266-5269 (1999). (page 27)

[80] Bayer, G. & Niederdränk, T. Weak localization of acoustic waves in strongly scattering media. *Physical Review Letters* **70**, 3884-3887 (1993). (page 27)

[81] Tourin, A., Derode, A., Roux, P., van Tiggelen, B. A. & Fink, M. Time-Dependent Coherent Backscattering of Acoustic Waves. *Physical Review Letters* **79**, 3637-3639 (1997). (page 27)

[82] Larose, E., Margerin, L., van Tiggelen, B. A. & Campillo, M. Weak Localization of Seismic Waves. *Physical Review Letters* **93**, 048501 (2004). (page 27)

[83] Mott, N. F. Electrons in disordered structures. *Advances in Physics* **16**, 49-144 (1967). (page 29)

[84] Ghosh, S., Delande, D., Miniatura, C. & Cherroret, N. Coherent Backscattering Reveals the Anderson Transition. *Physical Review Letters* **115**, 200602 (2015). (page 29, 130)

[85] Karpiuk, T. et al. Coherent Forward Scattering Peak Induced by Anderson Localization. *Physical Review Letters* **109**, 190601 (2012). (page 29, 131)

[86] Micklitz, T., Müller, C. A. & Altland, A. Strong Anderson Localization in Cold Atom Quantum Quenches. *Physical Review Letters* **112**, 110602 (2014). (page 29, 131)

[87] Ghosh, S., Cherroret, N., Grémaud, B., Miniatura, C. & Delande, D. Coherent forward scattering in two-dimensional disordered systems. *Physical Review A* **90**, 063602 (2014). (page 29, 131)

[88] Ghosh, S., Miniatura, C., Cherroret, N. & Delande, D. Coherent forward scattering as a signature of Anderson metal-insulator transitions. *Physical Review A* **95**, 041602 (2017). (page 29, 131)

[89] Sanchez-Palencia, L. et al. Anderson Localization of Expanding Bose-Einstein Condensates in Random Potentials. *Physical Review Letters* **98**, 210401 (2007). (page 30)

[90] Robert-de-Saint-Vincent, M. et al. Anisotropic 2D Diffusive Expansion of Ultracold Atoms in a Disordered Potential. *Physical Review Letters* **104**, 220602 (2010). (page 30)

[91] Evers, F. & Mirlin, A. D. Anderson transitions. *Reviews of Modern Physics* **80**, 1355-1417 (2008). (page 31)

[92] Kramer, B. & MacKinnon, A. Localization: theory and experiment. *Reports on Progress in Physics* **56**, 1469 (1993). (page 31)

[93] Keith, S. & Tomi, O. Critical exponent for the Anderson transition in the three-dimensional orthogonal universality class. *New Journal of Physics* **16**, 015012 (2014). (page 31)

[94] Chabé, J. et al. Experimental Observation of the Anderson Metal-Insulator Transition with Atomic Matter Waves. *Physical Review Letters* **101**, 255702 (2008). (page 31)

[95] Thomanschefsky, U. & Holcomb, D. F. Metal-insulator transition in the compensated semiconductor Si:(P,B). *Physical Review B* **45**, 13356-13362 (1992). (page 32)

[96] Römer, R. A. & Schreiber, M. in *Anderson Localization and Its Ramifications: Disorder, Phase Coherence and Electron Correlations* (eds Tobias Brandes & S. Kettemann) 3-19 (Springer Berlin Heidelberg, 2003). (page 32)

[97] Wiersma, D. S., Bartolini, P., Lagendijk, A. & Righini, R. Localization of light in a disordered medium. *Nature* **390**, 671 (1997). (page 32)

[98] Scheffold, F., Lenke, R., Tweer, R. & Maret, G. Localization or classical diffusion of light? *Nature* **398**, 206 (1999). (page 32)

[99] Chabanov, A. A., Stoytchev, M. & Genack, A. Z. Statistical signatures of photon localization. *Nature* **404**, 850 (2000). (page 32)

[100] Chin, C., Grimm, R., Julienne, P. & Tiesinga, E. Feshbach resonances in ultracold gases. *Reviews of Modern Physics* **82**, 1225-1286 (2010). (page 33)

[101] Kondov, S. S., McGehee, W. R., Xu, W. & DeMarco, B. Disorder-Induced Localization in a Strongly Correlated Atomic Hubbard Gas. *Physical Review Letters* **114**, 083002 (2015). (page 33)

[102] Bordia, P. et al. Probing Slow Relaxation and Many-Body Localization in Two-Dimensional Quasiperiodic Systems. *Physical Review X* **7**, 041047 (2017). (page 33)

[103] D'Errico, C. et al. Observation of a Disordered Bosonic Insulator from Weak to Strong Interactions. Physical Review Letters 113, 095301 (2014). (page 33)

[104] Yedjour, A. & Van Tiggelen, A. B. Diffusion and localization of cold atoms in 3D optical speckle. *The European Physical Journal D* **59**, 249-255 (2010). (page 33)

[105] Pilati, S., Giorgini, S., Modugno, M. & Prokof'ev, N. Dilute Bose gas with correlated disorder: a path integral Monte Carlo study. *New Journal of Physics* **12**, 073003 (2010). (page 33)

[106] Delande, D. & Orso, G. Mobility Edge for Cold Atoms in Laser Speckle Potentials. *Physical Review Letters* **113**, 060601 (2014). (page 33, 38, 73)

[107] Pasek, M., Zhao, Z., Delande, D. & Orso, G. Phase diagram of the three-dimensional Anderson model for short-range speckle potentials. *Physical Review A* **92**, 053618 (2015). (page 33, 130)

[108] Müller, C. A., Delande, D. & Shapiro, B. Critical dynamics at the Anderson localization mobility edge. *Physical Review A* **94**, 033615 (2016). (page 35, 39)

[109] Piraud, M. *Anderson localization of matter waves in correlated disorder : from 1D to 3D*, Université Paris Sud - Paris XI, (2012). (page 35)

[110] Pasek, M., Orso, G. & Delande, D. (2017) Supplemental material for "Anderson Localization of Ultracold Atoms: Where is the Mobility Edge?" *Physical Review Letters.* [Online] Available: http://link.aps.org/ supplemental/10.1103/PhysRevLett.118.170403. (page 37)

[111] C.A. Müller and B. Shapiro, Comment on Three- Dimensional Anderson Localization in Variable Scale Disorder, *Physical Review Letters* **113**, 099601 (2014). (page 39)

[112] Metcalf, H. & van der Straten, P. *Laser Cooling and Trapping (Graduate Texts in Contemporary Physics).* (Springer, 1999). (page 41, 44)

[113] Dalibard, J. in *Chaire Atomes et Rayonnement* (ed Collège de France) (2015). (page 41)

[114] Gilbert Grynberg, A. A., Claude Fabre, Cohen-Tannoudji, C., Grynberg, G., Alain Aspect, & Fabre., C. in *Introduction to Quantum Optics* Ch. 8, (Cambridge University Press, 2010). (page 41, 44)

[115] Cohen-Tannoudji, C. N. Nobel Lecture: Manipulating atoms with photons. *Reviews of Modern Physics* **70**, 707-719 (1998). (page 41)

[116] Anderson, M. H., Ensher, J. R., Matthews, M. R., Wieman, C. E. & Cornell, E. A. Observation of Bose-Einstein Condensation in a Dilute Atomic Vapor. *Science* **269**, 198 (1995). (page 42)

[117] Davis, K. B. et al. Bose-Einstein Condensation in a Gas of Sodium Atoms. *Physical Review Letters* **75**, 3969-3973 (1995). (page 42)

[118] Cornell, E. A. & Wieman, C. E. Nobel Lecture: Bose-Einstein condensation in a dilute gas, the first 70 years and some recent experiments. *Reviews of Modern Physics* **74**, 875-893 (2002). (page 42)

[119] Ketterle, W. Nobel lecture: When atoms behave as waves: Bose-Einstein condensation and the atom laser. *Reviews of Modern Physics* **74**, 1131-1151 (2002). (page 42)

[120] Dalfovo, F., Giorgini, S., Pitaevskii, L. P. & Stringari, S. Theory of Bose-Einstein condensation in trapped gases. *Reviews of Modern Physics* **71**, 463-512 (1999). (page 42)

[121] Pethick, C. J. & Smith, H. *Bose–Einstein Condensation in Dilute Gases.* 2 edn, (Cambridge University Press, 2008). (page 42)

[122] Steck, D. A. *Rubidium 87 D Line Data* (2001). [Online] Available: http://steck.us/alkali-data/rubidium87numbers.pdf. (page 43, 77, 149, 150, 151)

[123] Fauquembergue, M. *Realization of a Bose-Einstein condensation setup and transport of a coherent cold atom cloud*, PhD thesis, Université Paris Sud - Paris XI, (2004). (page 49, 50)

[124] Dalibard, J. & Cohen-Tannoudji, C. Laser cooling below the Doppler limit by polarization gradients: simple theoretical models. *J. Opt. Soc. Am. B* **6**, 2023-2045 (1989). (page 50)

[125] Lett, P. D. et al. Observation of Atoms Laser Cooled below the Doppler Limit. *Physical Review Letters* **61**, 169-172 (1988). (page 50)

[126] Petrich, W., Anderson, M. H., Ensher, J. R. & Cornell, E. A. Stable, Tightly Confining Magnetic Trap for Evaporative Cooling of Neutral Atoms. *Physical Review Letters* **74**, 3352-3355 (1995). (page 51)

[127] Davis, K. B., Mewes, M.-O., Joffe, M. A., Andrews, M. R. & Ketterle, W. Evaporative Cooling of Sodium Atoms. *Physical Review Letters* **74**, 5202-5205 (1995). (page 51)

[128] Fedichev, P. O., Reynolds, M. W. & Shlyapnikov, G. V. Three-Body Recombination of Ultracold Atoms to a Weakly Bound s Level. *Physical Review Letters* **77**, 2921-2924 (1996). (page 53)

[129] Egorov, M. et al. Measurement of s-wave scattering lengths in a two-component Bose-Einstein condensate. *Physical Review A* **87**, 053614 (2013). (page 56)

[130] R. Anderson, *Non-equilibrium dynamics and relative phase evolution of two-component Bose-Einstein condensates*, PhD thesis, Swinburne University, (2010). (page 57)

[131] Goodman, J. W. *Speckle Phenomena in Optics: Theory and Applications.* (Roberts & Company, 2007). (page 63, 68, 70)

[132] Clément, D. et al. Experimental study of the transport of coherent interacting matter-waves in a 1D random potential induced by laser speckle. *New Journal of Physics* **8**, 165 (2006). (page 63, 97)

[133] Labeyrie, A. Attainment of diffraction limited resolution in large telescopes by Fourier analysing speckle patterns in star images. *Astron. Astrophys.* **6**, 85–87 (1970). (page 63)

[134] Katz, O., Heidmann, P., Fink, M. & Gigan, S. Non-invasive single-shot imaging through scattering layers and around corners via speckle correlations. *Nature Photonics* **8**, 784 (2014). (page 63)

[135] Verma, M., Singh, D. K., Senthilkumaran, P., Joseph, J. & Kandpal, H. C. Ultrasensitive and fast detection of denaturation of milk by Coherent backscattering of light. *Scientific Reports* **4**, 7257 (2014). (page 63)

[136] Libres savoirs: 0324 Statistical optics. [Online] Available: http://paristech.institutoptique.fr/cours.php?id=94 (page 64)

[137] Pérez, J. P. *Optique, Fondements et Applications*. (Dunod, 2004). (page 64)

[138] Volchkov, V. V. et al. (2018). Supplemental material for "Measurement of Spectral Functions of Ultracold Atoms in Disordered Potentials." *Physical Review Letters*. [Online] Available: https://journals.aps.org/prl/supplemental/10.1103/PhysRevLett.120.060404. (page 70, 73, 74, 92, 93, 94, 95)

[139] LeBlanc, L. J. & Thywissen, J. H. Species-specific optical lattices. *Physical Review A* **75**, 053612 (2007). (page 75)

[140] Bruus, H. & Flensberg, K. *Many-body quantum theory in condensed matter physics: an introduction*. (Oxford University Press, USA, 2004). (page 83, 84, 85)

[141] Andrea, D. Probing the Electronic Structure of Complex Systems by ARPES. *Physica Scripta* **2004**, 61 (2004). (page 83)

[142] Damascelli, A., Hussain, Z. & Shen, Z.-X. Angle-resolved photoemission studies of the cuprate superconductors. *Reviews of Modern Physics* **75**, 473-541 (2003). (page 83)

[143] Stewart, J. T., Gaebler, J. P. & Jin, D. S. Using photoemission spectroscopy to probe a strongly interacting Fermi gas. *Nature* **454**, 744 (2008). (page 83)

[144] Dao, T.-L., Georges, A., Dalibard, J., Salomon, C. & Carusotto, I. Measuring the One-Particle Excitations of Ultracold Fermionic Atoms by Stimulated Raman Spectroscopy. *Physical Review Letters* **98**, 240402 (2007). (page 83, 100, 133)

[145] Gaebler, J. P. et al. Observation of pseudogap behaviour in a strongly interacting Fermi gas. *Nature Physics* **6**, 569, (2010). (page 84)

[146] Feld, M., Fröhlich, B., Vogt, E., Koschorreck, M. & Köhl, M. Observation of a pairing pseudogap in a two-dimensional Fermi gas. *Nature* **480**, 75 (2011). (page 84)

[147] Clément, D., Fabbri, N., Fallani, L., Fort, C. & Inguscio, M. Exploring Correlated 1D Bose Gases from the Superfluid to the Mott-Insulator State by Inelastic Light Scattering. *Physical Review Letters* **102**, 155301 (2009). (page 83, 84)

[148] Ernst, P. T. et al. Probing superfluids in optical lattices by momentum-resolved Bragg spectroscopy. *Nature Physics* **6**, 56 (2009). (page 83, 84)

[149] Fabbri, N. et al. Quasiparticle Dynamics in a Bose Insulator Probed by Interband Bragg Spectroscopy. Physical Review Letters **109**, 055301 (2012). (page 84)

[150] Prat, T. *Anderson localization with cold atoms : dynamics in disorder and prospects from chaos*, Université Pierre et Marie Curie - Paris VI, (2017). (page 85, 87)

[151] Trappe, M. I., Delande, D. & Müller, C. A. Semiclassical spectral function for matter waves in random potentials. *Journal of Physics A: Mathematical and Theoretical* **48**, 245102 (2015). (page 89, 90, 98)

[152] Moy, G. M., Hope, J. J. & Savage, C. M. Born and Markov approximations for atom lasers. *Physical Review A* **59**, 667-675 (1999). (page 93)

[153] Jack, M. W., Naraschewski, M., Collett, M. J. & Walls, D. F. Markov approximation for the atomic output coupler. *Physical Review A* **59**, 2962-2973 (1999). (page 93)

[154] Gerbier, F., Bouyer, P. & Aspect, A. Quasicontinuous Atom Laser in the Presence of Gravity. *Physical Review Letters* **86**, 4729-4732 (2001). (page 93)

[155] Grynberg, G., Alain Aspect, & Fabre., C. in *Introduction to Quantum Optics* Ch. 1, (Cambridge University Press, 2010). (page 93)

[156] Prat, T., Cherroret, N. & Delande, D. Semiclassical spectral function and density of states in speckle potentials. *Physical Review A* **94**, 022114 (2016). (page 98)

[157] Rauch, S., Sacher, J. Compact Bragg grating stabilized ridge waveguide laser module with a power of 380 mW at 780 nm. *IEEE Photonics Technology Letters* **27**, 16 (2015). (page 126)

[158] Fratini, E. & Pilati, S. Anderson localization of matter waves in quantum-chaos theory. *Physical Review A* **91**, 061601 (2015). (page 130)

[159] Kovachy, T. et al. Matter Wave Lensing to Picokelvin Temperatures. *Physical Review Letters* **114**, 143004 (2015). (page 132)

[160] Köhl, M., Hänsch, T. W. & Esslinger, T. Measuring the Temporal Coherence of an Atom Laser Beam. *Physical Review Letters* **87**, 160404 (2001). (page 132)

[161] Brantut, J. P. et al. Light-shift tomography in an optical-dipole trap for neutral atoms. *Physical Review A* **78**, 031401 (2008). (page 132)

[162] Rodriguez, A., Vasquez, L. J., Slevin, K. & Römer, R. A. Critical parameters from a generalized multifractal analysis at the Anderson transition. *Physical Review Letters* **105**, 046403 (2010). (page 132)

[163] Werner, M. A., Demler, E., Aspect, A. & Zaránd, G. Selective state spectroscopy and multifractality in disordered Bose-Einstein condensates: a numerical study. *Scientific Reports* **8**, 3641 (2018). (page 132)

[164] Bender, N., Yılmaz, H., Bromberg, Y. & Cao, H. Customizing speckle intensity statistics. *Optica* **5**, 595-600 (2018). (page 132)

[165] Lefebvre, G. et al. One Single Static Measurement Predicts Wave Localization in Complex Structures. *Physical Review Letters* **117**, 074301 (2016). (page 132)

[166] Filoche, M. & Mayboroda, S. Universal mechanism for Anderson and weak localization. *Proceedings of the National Academy of Sciences* **109**, 14761 (2012). (page 132)

[167] Filoche, M., Piccardo, M., Wu, Y. R., Li, C. K., Weisbuch C., & Mayboroda, S. Localization landscape theory of disorder in semiconductors. I. Theory and modeling. *Physical Review B* **95**, 144204 (2017). (page 133)

[168] Pezzé, L. & Sanchez-Palencia, L. Localized and extended states in a disordered trap. *Physical Review Letters* **106**, 040601 (2011). (page 133)

[169] Giamarchi, T. & Schulz, H. J. Anderson localization and interactions in one-dimensional metals, *Physical Review B* **37**, 325 (1988). (page 133)

[170] Fisher, M. P. A., Weichman, P. B., Grinstein, G., & Fisher, D. S. Boson localization and the superfluid-insulator transition. *Physical Review B* **40**, 546 (1989). (page 133)

[171] Cherroret, N., Vermersch, B., Garreau, J. C. & Delande, D. How Nonlinear Interactions Challenge the Three-Dimensional Anderson Transition. *Physical Review Letters* **112**, 170603 (2014). (page 133)

[172] Cherroret, N., Karpiuk, T., Grémaud, B. & Miniatura, C. Thermalization of matter waves in speckle potentials. *Physical Review A* **92**, 063614 (2015). (page 133)

[173] Gibney, E. *Nature* **563**, 451(2018).

(page 149)

Appendix A

Physical constants and rubidium-87 D-lines

Throughout the manuscript, we can find several fundamental constants[1] and physical constants of rubidium 87. The fundamental constants are listed in table A.1 and the physical constants are listed in table A.2.

Speed of light	c	299 792 458 m/s (exact)
Permeability of vacuum	μ_0	$4\pi \times 10^{-7}$ N/A^2 (exact)
Permittivity of vacuum	ε_0	$(\mu_0 c^2)^{-1}$ (exact) $= 8.854187817 \times 10^{-12}$F/m
Planck's constant	h	$6.626\ 068\ 96(33) \times 10^{-34}$ J.s
	$\hbar$	$1.054\ 571\ 596 \times 10^{-34}$ J.s
Elementary charge	e_0	$1.602176462 \times 10^{-19}$ C
Bohr magneton	μ_B	$h \cdot 1.399\ 624\ 604(35)$ MHz/G
Atomic mass unit	u	$1.660\ 538\ 782(83) \times 10^{-27}$ kg
Electron mass	m_e	$9.109\ 382\ 15(45) \times 10^{-31}$ kg
Bohr radius	a_0	0.5291772083 Å
Boltzmann's constant	k_B	$1.380\ 6504(24) \times 10^{-23}$ J/K

Table A.1: Fundamental physical constants taken from Ref. [122].

---

[1] On November 16 2018 (at the end of the writing of this manuscript), the International Bureau of Weight and Measures has voted to redefine several base units in the International System of Units (SI), including the redefinition of the Planck's constant ($h = 6.626\ 070\ 15 \times 10^{-34}$ J.s) [173]. Although such resolution has not been taken into account in this work, the estimated correction is smaller than 1ppm which would not have any significance to the interpretation of the results presented in this manuscript.

Atomic number	Z	37
Total nucleons	$Z+N$	87
Atomic mass	m	86.909 180 520(15) u
Nuclear spin	I	3/2

Table A.2: Rubidium-87 physical properties from Ref. [122].

A.1 Properties of rubidium-87 D-lines

The D lines (transition $5s \to 5p$) consist of D_1 line ($5^2S_{1/2} \to 5^2P_{1/2}$ transition) and D_2 lines ($5^2S_{1/2} \to 5^2P_{3/2}$ transition). The properties of the D_2 lines are given in table A.3. The properties of the D_1 lines are given in table A.4.

Frequency	ω_{D2}	$2\pi \times 384.230\ 484\ 468\ 5(62)$ THz
Decay rate / natural line width (FWHM)	Γ_{D2}	$38.117(11) \times 10^6\ \mathrm{s}^{-1}$ $2\pi \times 6.0666(18)$ MHz
The dipole element	er_{D2}	$\langle J = 1/2\, \Vert \boldsymbol{er} \Vert\, J' = 1/2 \rangle = 4.22752 e_0 a_0$

Table A.3: Optical properties of rubidium-87 D_2 transition ($5^2S_{1/2} \to 5^2P_{3/2}$). Taken from Ref. [122].

Frequency	ω_{D1}	$2\pi \times 377.107\ 463\ 380(11)$ THz
Decay rate / natural line width (FWHM)	Γ_{D1}	$36.129(35) \times 10^6\ \mathrm{s}^{-1}$ $2\pi \times 5.7500(56)$ MHz
The dipole element	er_{D1}	$\langle J = 1/2\, \Vert \boldsymbol{er} \Vert\, J' = 1/2 \rangle = 2.9931 e_0 a_0$

Table A.4: Optical properties of rubidium-87 D_1 transition ($5^2S_{1/2} \to 5^2P_{1/2}$). Taken from Ref. [122].

The relation between decay rate and the dipole element is

$$\Gamma_D = \frac{\omega_D^3}{3\pi\hbar\varepsilon_0 c^3} \frac{2J+1}{2J'+1} \left| \langle J \, \Vert \boldsymbol{er} \Vert \, J' \rangle \right|^2 ; \ D = D1\ (J' = \frac{1}{2}) \text{ or } D2\ (J' = \frac{3}{2}). \tag{A.1}$$

Furthermore, the $g-$factors associated with the D lines are given in table A.5

A.2 Hyperfine structure of rubidium 87 D line

For the ground states ($5^2S_{1/2}$), there are two hyperfine states: $F=1$ and $F=2$. For the D_1 line excited states ($5^2P_{1/2}$), there are two hyperfine states: $F'=1$ and $F'=2$. For the D_2 line excited states ($5^2P_{3/2}$), there are four hyperfine states, $F' = 0,\ 1\ , 2\ ,$ and 3. The energies of these hyperfine levels are given by

$$E = \hbar\left(\omega_0 + \Delta\omega_F\right). \tag{A.2}$$

The values of ω_0 and $\Delta\omega_F$ for each level are given in table A.6.

Electron spin $g-$factor	g_S	2.002 319 304 3622(15)
Electron orbital $g-$factor	g_L	0.999 993 69
Fine structure Landé $g-$factor	g_J $(5^2S_{1/2})$	2.002 331 13(20)
	g_J $(5^2P_{1/2})$	0.666
	g_J $(5^2P_{3/2})$	1.3362(13)
Nuclear $g-$factor	g_I	$-0.000\ 995\ 141\ 4(10)$
Clock transition Zeeman shift	$\Delta\omega_{\text{clock}}/B^2$	$2\pi \cdot 575.15$ Hz/G^2

Table A.5: Rubidium-87 D transition magnetic and electric field interaction parameters. Taken from Ref. [122].

	Notation	J	F or F'	ω_0	$\Delta\omega_F/2\pi$ (in Hz)
ground	$5^2S_{1/2},\ F=1$	1/2	1	0	-4.271677×10^9
ground	$5^2S_{1/2},\ F=2$	1/2	2	0	2.563006×10^9
$D1$-excited	$5^2P_{1/2},\ F=1$	1/2	1	ω_{D1}	-509.05×10^6
$D1$-excited	$5^2P_{1/2},\ F=2$	1/2	2	ω_{D1}	305.43×10^6
$D2$-excited	$5^2P_{3/2},\ F=0$	3/2	0	ω_{D2}	-302.074×10^6
$D2$-excited	$5^2P_{3/2},\ F=1$	3/2	1	ω_{D2}	-229.852×10^6
$D2$-excited	$5^2P_{3/2},\ F=2$	3/2	2	ω_{D2}	-72.911×10^6
$D2$-excited	$5^2P_{3/2},\ F=3$	3/2	3	ω_{D2}	193.741×10^6

Table A.6: Hyperfine levels with their corresponding energies taken from Ref. [122].

Appendix B

Application of the Wick theorem for speckle correlation functions

The Rayleigh-Sommerfeld formula. Let us consider an incident field, $E(\boldsymbol{R})$, passing through an aperture and a converging lens; $\boldsymbol{R}$ represents the coordinates in the aperture. The electric field at point $\boldsymbol{r}$ around the focal point is given by

$$E(\boldsymbol{r}) = -\frac{i}{\lambda}\int E(\boldsymbol{R})\frac{e^{ik|\boldsymbol{R}-\boldsymbol{r}|}}{|\boldsymbol{R}-\boldsymbol{r}|}\frac{1+\cos(\theta)}{2}\mathrm{d}\boldsymbol{R}, \tag{B.1}$$

where λ is the wavelength, $k = 2\pi/\lambda$, and θ represents the angle between the ray and the longitudinal axis; $\theta \approx 0$ for Fraunhofer diffraction.

The Huygens-Fresnel formula. Let us consider a diffusive plate in addition to the converging lens. Let us also consider a uniform incident field E_0. It induces transmission $t(\boldsymbol{R})$. For $\boldsymbol{r}$ be coordinates with respect to the focal point, the electric field $E(\boldsymbol{r})$ is given by

$$\begin{aligned} E(\boldsymbol{r}) &= -\frac{i}{\lambda}\frac{E_0}{f}e^{i\frac{2\pi}{\lambda}\left(f+\frac{r^2}{2f}\right)}\int \mathrm{d}\boldsymbol{R}\ P(\boldsymbol{R})t(\boldsymbol{R})e^{-ik\frac{\boldsymbol{r}\cdot\boldsymbol{R}}{f}}, \\ &\equiv -\frac{i}{\lambda}\frac{E_0}{f}e^{i\frac{2\pi}{\lambda}\left(f+\frac{r^2}{2f}\right)}TF\left[P(\boldsymbol{R})t(\boldsymbol{R})\right](\boldsymbol{r}/\lambda f), \end{aligned} \tag{B.2}$$

where f is the focal length of the lens and function $P(\boldsymbol{R})$ represents the aperture.

Wick theorem. It is also called the Isserlis theorem. If $(X_1, ...X_{2n})$ is a zero-mean multivariate normal random vector, then

$$\begin{aligned} \overline{X_1 X_2 \cdots X_{2n}} &= \sum \prod \overline{X_i X_j}, \\ \overline{X_1 X_2 \cdots X_{2n-1}} &= 0, \end{aligned}$$

where the notation $\sum\prod$ means summing over all distinct ways of partitioning X_1, ..., X_{2n} into pairs X_i, X_j and each summand is the product of the n pairs. For $n = 2$,

$$\overline{X_1X_2X_3X_4} = \overline{X_1X_2}.\overline{X_3X_4} + \overline{X_1X_3}.\overline{X_2X_4} + \overline{X_1X_4}.\overline{X_2X_3}.$$

Electric field correlation function. Let us consider electric field $E_p(\boldsymbol{r})$ and $E_c(\boldsymbol{r})$ obtained from the expression $E(\boldsymbol{r})$ above by replacing the wavelength λ by λ_p and λ_c respectively. We define the following correlation function

$$C_E\left(\boldsymbol{r}, \boldsymbol{r'}, \lambda_p, \lambda_c\right) = \frac{\left|E_0\right|^2 e^{i\phi'}}{f^2 \lambda_p \lambda_c} \int \mathrm{d}\boldsymbol{R}\mathrm{d}\boldsymbol{R'}\ P(\boldsymbol{R})P^*(\boldsymbol{R'})\overline{t_p(\boldsymbol{R})t_c^*(\boldsymbol{R'})} \exp\left(i\frac{2\pi}{f}\left(\frac{\boldsymbol{r}\cdot\boldsymbol{R}}{\lambda_p} - \frac{\boldsymbol{r'}\cdot\boldsymbol{R'}}{\lambda_c}\right)\right) \quad , \tag{B.3}$$

where $\phi' = \frac{2\pi}{\lambda_p}\left(f + \frac{r^2}{2f}\right) - \frac{2\pi}{\lambda_c}\left(f + \frac{r'^2}{2f}\right)$, $t_p(\boldsymbol{R}) = \exp\left(i2\pi(n-1)l(\boldsymbol{R})/\lambda_p\right)$, and $t_c(\boldsymbol{R'}) = \exp\left(i2\pi(n-1)l(\boldsymbol{R'})/\lambda_c\right)$. We consider firstly $\lambda_p \neq \lambda_c$ that is relevant to Chap. 6. The case $\lambda_p = \lambda_c = \lambda$ is relevant to Chap. 4.

The correlation function $\overline{t_p(\boldsymbol{R})t_c^*(\boldsymbol{R'})}$ follows (by taking into account approximation $\frac{\overline{l(\boldsymbol{R})l(\boldsymbol{R'})}}{\sigma_l^2} \approx 1 - \frac{|\boldsymbol{R}-\boldsymbol{R'}|^2}{2r_l^2}$)

$$\begin{aligned} \overline{t_p(\boldsymbol{R})t_c^*(\boldsymbol{R'})} &= \exp\left(-\delta\phi^2/2\right)\exp\left(-\sigma_{\phi,p}\sigma_{\phi,c}\left(1 - \overline{l(\boldsymbol{R})l(\boldsymbol{R'})}/\sigma_l^2\right)\right) && \text{(B.4)} \\ &= \exp\left(-\delta\phi^2/2\right)\exp\left(-\frac{\pi^2\theta_{\text{diff}}^2}{2}\frac{\left|\boldsymbol{R}-\boldsymbol{R'}\right|^2}{\lambda_p\lambda_c}\right). && \text{(B.5)} \end{aligned}$$

where $\sigma_{\phi,p} = 2\pi(n-1)\sigma_l/\lambda_p$, $\sigma_{\phi,c} = 2\pi(n-1)\sigma_l/\lambda_c$, $\delta\phi = 2\pi(n-1)\sigma_l/l_c$, $l_c = \lambda_p\lambda_c/\left|\lambda_c - \lambda_p\right|$, $\theta_{\text{diff}} = 2(n-1)\sigma_l/r_l$.

B.1 Correlation function for monochromatic speckle field

Autocorrelation function of electric field

We are interested in the expression $\overline{E(\boldsymbol{r})E^*(\boldsymbol{r}+\boldsymbol{\Delta r})}$ which can be obtained by substituting $\boldsymbol{r'} = \boldsymbol{r} + \boldsymbol{\Delta r}$ and $\lambda_p = \lambda_c = \lambda$ in the expression $C_E\left(\boldsymbol{r}, \boldsymbol{r'}, \lambda_p, \lambda_c\right)$. With change of variables $\boldsymbol{R_0} = \boldsymbol{R_2}$ and $\boldsymbol{\Delta R} = \boldsymbol{R_2} - \boldsymbol{R_1}$, and approximation $P(\boldsymbol{R_0} - \boldsymbol{\Delta R})P(\boldsymbol{R_0}) \approx \left|P(\boldsymbol{R_0})\right|^2$, we deduce

$$
\begin{aligned}
\overline{E(\boldsymbol{r})E^*(\boldsymbol{r}+\boldsymbol{\Delta r})} &= \frac{|E_0|^2}{f^2\lambda^2}\int \mathrm{d}\boldsymbol{R_1}\int \mathrm{d}\boldsymbol{R_2}\; P(\boldsymbol{R_1})P(\boldsymbol{R_2})t(\boldsymbol{R_1})t^*(\boldsymbol{R_2})e^{-ik\frac{\boldsymbol{r}\cdot\boldsymbol{R_1}-(r+\boldsymbol{\Delta r})\cdot\boldsymbol{R_2}}{f}}, \\
&= \frac{|E_0|^2}{f^2\lambda^2}\cdot TF\left[|P(\boldsymbol{R_0})|^2\right]\left(\frac{\boldsymbol{\Delta r}}{\lambda f}\right)\cdot TF\left[c_{\text{diff}}(\boldsymbol{\Delta R})\right]\left(\frac{\boldsymbol{r}+\boldsymbol{\Delta r}}{\lambda f}\right).
\end{aligned}
\tag{B.6}
$$

The approximation $P(\boldsymbol{R_0}-\boldsymbol{\Delta R})P(\boldsymbol{R_0}) \approx |P(\boldsymbol{R_0})|^2$ is valid because the support of the function $c_{\text{diff}}(\boldsymbol{\Delta R})$ is typically r_{diff} which is much smaller than that of $P(\boldsymbol{R_0})$.

B.2 Correlation function for bichromatic speckle field

Lastly, by applying changement of variables, $\boldsymbol{R_0} = \frac{\boldsymbol{R}+\boldsymbol{R'}}{2}$ and $\Delta\boldsymbol{R} = \boldsymbol{R}-\boldsymbol{R'}$, and approximation $P(\boldsymbol{R})P^*(\boldsymbol{R'}) \approx |P(\boldsymbol{R_0})|^2$, we obtain the following,

$$
C_E\left(\boldsymbol{r},\boldsymbol{r'},\lambda_p,\lambda_c\right) = \frac{|E_0|^2\, e^{i\phi'}\exp\left(-\delta\phi^2/2\right)}{f^2\lambda_p\lambda_c}\cdot TF\left[|P(\boldsymbol{R_0})|^2\right](\boldsymbol{\kappa_1})\cdot TF\left[\exp\left(-\frac{\pi^2\theta_{\text{diff}}^2}{2}\frac{\Delta R^2}{\lambda_p\lambda_c}\right)\right](\boldsymbol{\kappa_2}),
\tag{B.7}
$$

where $\boldsymbol{\kappa_1} = \frac{1}{f}\left(\frac{\boldsymbol{r}}{\lambda_p}-\frac{\boldsymbol{r'}}{\lambda_c}\right)$ and $\boldsymbol{\kappa_2} = \frac{1}{2f}\left(\frac{\boldsymbol{r}}{\lambda_p}+\frac{\boldsymbol{r'}}{\lambda_c}\right)$. For $\boldsymbol{r}=\boldsymbol{r'}$, we have $\boldsymbol{\kappa_1} = \frac{\boldsymbol{r}}{fl_c}$ and $\boldsymbol{\kappa_2} = \frac{\boldsymbol{r}}{f\bar{\lambda}}$, where $\bar{\lambda} = 2\lambda_p\lambda_c/(\lambda_p+\lambda_c)$ and $c_E(\boldsymbol{r},\lambda_p,\lambda_c) \equiv C_E\left(\boldsymbol{r},\boldsymbol{r'}=\boldsymbol{r},\lambda_p,\lambda_c\right)$. The term $TF\left[|P(\boldsymbol{R_0})|^2\right](\boldsymbol{\kappa_1})$ is analogous to the term $TF\left[|P(\boldsymbol{R_0})|^2\right]\left(\frac{\boldsymbol{\Delta r}}{\lambda f}\right)$ from which we have derived the size of speckle grain. As a result, we obtain a characteristic length $L = l_cf/D = l_c/(2\text{NA})$. Secondly, the term $TF\left[\exp\left(-\frac{\pi^2\theta_{\text{diff}}^2}{2}\frac{\Delta R^2}{\lambda_p\lambda_c}\right)\right](\boldsymbol{\kappa_2})$ is equal to $2\pi\frac{\lambda_p\lambda_c}{\pi^2\theta_{\text{diff}}^2}\exp\left(-2r^2/w'^2\right)$ with $w' = w\bar{\lambda}/\sqrt{\lambda_p\lambda_c} \approx w$. The resulting characteristic length is approximately the speckle waist; 1.4 mm in our experiment.

More generally, from the expression of $C_E\left(\boldsymbol{r},\boldsymbol{r'},\lambda_p,\lambda_c\right)$, we can deduce the dimensionless correlation function $\mathcal{R}(\boldsymbol{r}) \equiv \overline{\delta I_p(\boldsymbol{r})\delta I_c(\boldsymbol{r})}/\left(\sigma_{I,p}(\boldsymbol{r})\sigma_{I,c}(\boldsymbol{r})\right)$ which is given by

$$
\begin{aligned}
\mathcal{R}(\boldsymbol{r}) &= \frac{\left|C_E\left(\boldsymbol{r},\boldsymbol{r},\lambda_p,\lambda_c\right)\right|^2}{\overline{I_p(\boldsymbol{r})}.\overline{I_c(\boldsymbol{r})}}, \\
&= \exp\left(-\delta\phi^2\right)\cdot\left|\mathcal{F}\left(\boldsymbol{r}\right)\right|^2\cdot\exp\left(-4\frac{r^2}{w'^2}\right),
\end{aligned}
\tag{B.8}
$$

where $\mathcal{F}\left(\boldsymbol{r}\right) = TF\left[|P(\boldsymbol{R_0})|^2\right](\boldsymbol{\kappa_1})/TF\left[|P(\boldsymbol{R_0})|^2\right](\boldsymbol{0})$; $\mathcal{F}\left(0\right) = 1$ corresponds to the maxima of the function.

Appendix C

Numerical work of bichromatic speckle disorder

With software MATLAB, we can generate speckle figures which take into account physical parameters such as wavelength (λ), diameter of the aperture D, etc. The program consists of creating a random matrix associated with the thickness $l(\boldsymbol{R})$ of the diffusive plate at all point $\boldsymbol{R}$ inside the aperture[1]. From this, the program calculates the corresponding matrix associated with the random phase $\phi(\boldsymbol{R}) = \frac{2\pi}{\lambda}(n-1)l(\boldsymbol{R})$ and performs discrete Fourier transform in order to generate the speckle pattern.

In case of bichromatic speckle pattern, we need to generate two speckle figures associated with different wavelengths and subtract them. For ΔX be the step associated with the discretization associated with the aperture coordinates. Based on the discrete Fourier transform, the spatial step in the focal plane, Δx, is given by

$$\Delta x = \frac{1}{N}\frac{f}{\Delta X}\lambda, \tag{C.1}$$

where N is the number of points along each axis. We can see that Δx is proportional to the wavelength λ. This results in mismatch of coordinates of the two speckle figures. To circumvent this problem, we have performed subsampling for each generated speckle pattern. For this, we need to choose $\delta\lambda$ such that $\lambda/\delta\lambda$ is a integer. Then, we only keep the points where the coordinates of the two numerically generated speckle patterns coincide. The effective spatial step Δx_{eff} becomes

$$\Delta x_{\text{eff}} = \frac{1}{N}\frac{f}{\Delta X}l_c, \tag{C.2}$$

with $l_c = \lambda(\lambda+\delta\lambda)/\delta\lambda$. The number of effective points are reduced, $N_{\text{eff}} \approx N\frac{\delta\lambda}{\lambda}$. Although many coordinate points are lost, it makes subtraction of the two speckle patterns possible and it provides

---

[1] In order to simulate the aperture, we create a matrix composed of 1 and 0; one for area inside the pupil and zero otherwise.

reliable numerical results. Thus, the number N at the beginning must be huge.

The numerical procedure involves fast Fourier transform algorithm[2]. For efficient calculation, the initial number of points N must be a multiple of small prime numbers. Nevertheless, the time required to generate two-dimensional patterns would be enormous without any significant importance compared with one-dimensional case. Hence, we only consider numerical study related to one-dimensional speckle patterns.

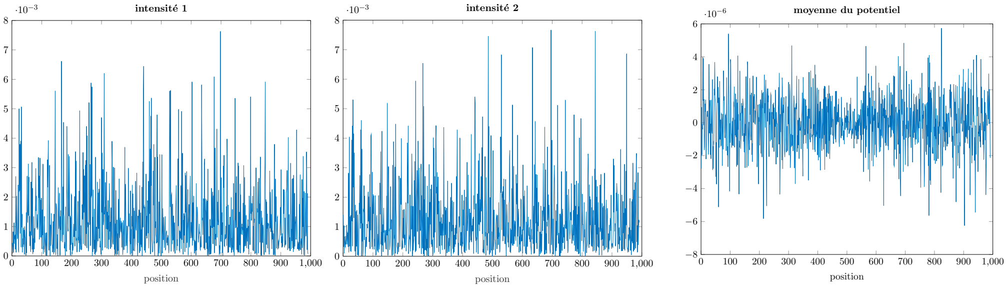

Figure C.1: Subtraction of two speckle figures of different wavelength obtained after subsampling. They share same step of $\frac{f\ l_c}{N\Delta X}$. The substracted speckle pattern shows much smaller variation around the middle point. The simulation is realized for $\delta\lambda/\lambda = 0.01$. Courtesy of Baptiste Lecoutre.

Fig. C.1 depicts the results of the substraction of the two speckle. The two speckle patterns are associated with $\delta\lambda/\lambda = 1/100$. Here, $N = 10^5$ but after the subsampling $N_{\text{eff}} = N\delta\lambda/\lambda = 1000$; the higher $\lambda/\delta\lambda$, the more number of points discarded because of the subsampling procedure.

From Fig. C.1, we can see that the fluctuation appears smaller around the middle point. After the averaging procedure, the intensity fluctuation diminishes greatly. The minima of the variance is found at the center of the coordinates in agreement to the theoretical analyses discussed in previous subsection. We also remark a non-zero residual variance as predicted. The analytical result of the variance is presented in red line.

For experimental purposes, we would be interested in the residual potential associated with the minima and the spatial width of the dip around the minima. Fig. C.2 depicts the influence of the parameters σ_l associated with the effective thickness of the diffusive plate and D associated with the numerical aperture ($\text{NA} = D/(2f)$). From previous subsection, we obtain the minima $2\left(1 - \exp\left(-\delta\phi^2\right)\right)$. Increasing the thickness σ_l of the diffusive plate results in the increase of the minima. This is confirmed by the numerical works shown in Fig. C.2. The curve 2 is obtained with σ_l twice compared with that of curve 1. Also, we expect width related with the numerical aperture (from term $\text{sinc}^2\left(\frac{2\pi x}{l_c}\text{NA}\right)$ for one-dimensional case),

$$L = l_c/(2\text{NA}). \tag{C.3}$$

This has been also confirmed with numerical works, from Fig. C.2, curve 3 obtained with numerical

---

[2] The calculation time scales as $O(N \log N)$

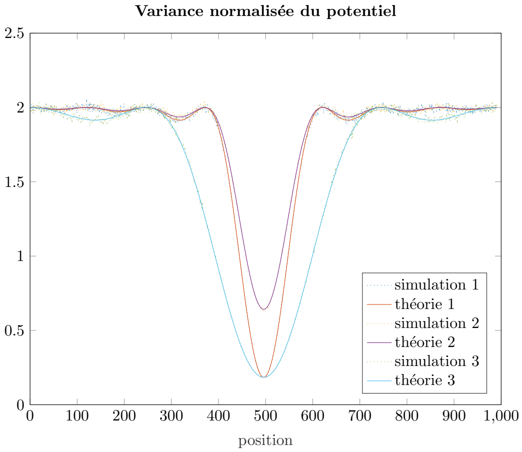

Figure C.2: The variance σ_V^2 dependence on the numerical aperture $(D/(2f))$ and the rough plate variance σ_l. Curve 1 is a reference, curve 2 obtained for σ_l twice the reference, and curve 3 obtained for diameter of the diaphragm (i. e. the numerical aperture) reduced by half. Increasing σ_l would increase the residual potential around the minima. Reducing the numerical aperture by half will double the width of the dip.

opening twice as that of curve 1 has wider dip with factor two.

université
PARIS-SACLAY

ÉCOLE DOCTORALE
Ondes et Matière
(EDOM)

Titre: potentiel désordonné sélectif en état de spin pour les études de la transition d'Anderson avec des atomes froids

Mots clés: Localization d'Anderson - Transition de phase - Seuil de mobilité - Speckle - Condensat de Bose-Einstein - Polarisabilité atomique

Résumé: Dans ce manuscrit, nous présentons notre avancement pour réaliser une méthode spectroscopique pour étudier la transition d'Anderson avec des atomes froids. Cela repose sur la réalisation d'un potentiel désordonné sélectif en état de spin, le désordre n'étant significatif que pour l'un des deux états de spin impliqués. En combinant cela avec la technique de transfert par radiofréquence d'un état insensible au désordre à un état exclusivement sensible au désordre, il devient possible de charger une onde de matière dans le désordre dans des états d'énergie bien définies. Pour prouver le concept, nous avons effectué des mesures des fonctions spectrales d'atomes ultra-froids dans des potentiels désordonnés, qui sont directement proportionnels au taux de transfert des atomes. Nous présentons les résultats en montrant un excellent accord avec les calculs numériques. Cela a ouvert des perspectives pour d'autres études sur la transition d'Anderson. En particulier, nous cherchons à observer la transition entre les états diffusifs et les états localisés séparés par une énergie critique, appelée le seuil de mobilité. Une telle étude nécessite la réalisation d'un désordre sélectif en état de spin qui permet un long temps de propagation dans le désordre afin de distinguer les deux phases. À cette fin, nous présentons un nouveau schéma du désordre sélectif en état de spin avec deux lasers du speckle (speckle bichromatique). Cela ouvre la voie à une approche spectroscopique de la transition d'Anderson avec des atomes froids avec une résolution en énergie bien supérieure à celles des expériences précédentes.

Title: State-dependent disordered potential for studies of Anderson transition with ultracold atoms

Keywords: Anderson localization - Phase transition - Mobility edge - Speckle - Bose-Einstein Condensate - Atomic polarizability

Abstract: In this manuscript, we present our progress towards realizing a spectroscopic method to study of Anderson transition with ultracold atoms. This relies on the realization of state-dependent disordered potential whereby the disorder is significant only for one of two involved spin-states. Combined with technique of radio-frequency transfer from the disorder-free state to the state with controlled disorder, it becomes possible to load a matter wave in the disorder in a well-defined energy states. As a proof of principle, we have performed measurements of the spectral functions of ultracold atoms in disordered potentials, which are directly proportional to the transfer rate of the atoms. We present the results showing excellent agreement with numerical calculations. This has opened up prospects for further studies of the Anderson transition. In particular we seek to observe transition between the diffusive and the localized states separated by a critical energy, the so-called mobility edge. Such study requires realization of state-dependent disorder which allows long propagation time in the disorder in order to distinguish the two phases. For this purpose, we present a new scheme of the state-dependent disorder with two laser speckles (bichromatic laser speckle). This paves the way towards spectroscopic approach of Anderson transition with ultracold atoms with energy resolution much higher than those in the previous experiments.

Université Paris-Saclay
Espace Technologique / Immeuble Discovery
Route de l'Orme aux Merisiers RD 128 / 91190 Saint-Aubin, France